WASHINGTON UNIVERSITY

SEVER INSTITUTE OF TECHNOLOGY

EXPERIMENTAL AND ANALYTICAL INVESTIGATIONS ON PUNCHING SHEAR OF THICK, LIGHTWEIGHT CONCRETE PLATES AND SHELLS

by

Long Thanh Phan

Prepared under the direction of Professor Thomas G. Harmon

A dissertation presented to the Sever Institute of
Washington University in partial fulfillment
of the requirements for the degree of

DOCTOR OF SCIENCE

August, 1988

Saint Louis, Missouri

WASHINGTON UNIVERSITY
SEVER INSTITUTE OF TECHNOLOGY

ABSTRACT

EXPERIMENTAL AND ANALYTICAL INVESTIGATIONS ON PUNCHING SHEAR OF THICK, LIGHTWEIGHT CONCRETE PLATES AND SHELLS

by Long Thanh Phan

ADVISOR: Professor Thomas G. Harmon

August, 1988

Saint Louis, Missouri

This study presents the results of the combined experimental and analytical study on the behavior of concrete structures under local, static transverse shear loads.

The experimental investigation focused on the punching shear behavior of heavily reinforced, lightweight concrete plates and shells. The 1/6-scale test specimens were designed to represent typical Arctic offshore structures. The amount of shear reinforcement and the curvature were found to have the largest effects on the punching shear capacity and the failure mechanisms of the test specimens. The ACI Code Provisions for punching shear were found to be very conservative with respect to the results obtained from this experimental program.

The analytical study focused on the development of a general material model for cracked concrete and method for implementing such model into a finite element computer program. The 2-dimensional crack material model was developed and quantified using the experimentally-obtained stress ratio and crack dilatancy laws. Cracked concrete strains were decomposed into crack strain and strain of solid concrete between cracks to facilitate implementation of the proposed crack material model and a nonlinear concrete model. Analyses of shear critical beams using the proposed models yielded encouraging results.

TABLE OF CONTENTS

LIST OF TABLES

LIST OF FIGURES

EXPERIMENTAL AND ANALYTICAL INVESTIGATIONS ON PUNCHING SHEAR OF THICK, LIGHTWEIGHT CONCRETE PLATES AND SHELLS

I. INTRODUCTION

I.1 BACKGROUND

Despite the harsh environmental conditions, the Arctic Ocean has been found to be potentially great source of oil and natural gas. Tapping these reserves requires permanent drilling platforms that can be used both as living facilities and for temporary oil storage in year-round operations. In the past several years, many designs of Arctic offshore structures with structural configurations and construction materials substantially different from standard construction have been proposed, built, and put into operation.

A typical Arctic offshore structure usually consists of an exterior wall, also known as ice wall, extending around the perimeter of the structure. This exterior wall consists mainly of either flat plate or curved structural elements, stiffened by a system of bulkheads and thrust beams. These elements are usually built segmentally and on-shore in temperate climates, with lightweight concrete as the construction material, and then transported through seas and assembled at installation sites in the Arctic Ocean. Concrete has been used extensively since it

parameters on the punching shear performance of these structures.

2. To examine the applicability of the provisions of the current ACI Code pertaining to the punching shear behavior of structures with increased thickness, high percentage of reinforcement, and curvature. This examination is necessary since the Code provisions were derived from tests conducted on thin and lightly reinforced sections.

3. To develop an improved 2-dimensional material model for cracked concrete that is general and quantifiable. The model will be incorporated into a finite element program which will be used to analyzed practical transverse shear deformations and failure problems. The validity of the 2-D model will be assessed by analyzing shear critical beams which have been investigated experimentally. This model will serve as basis for the eventual development of a 3-dimensional general material model that can be used to predict the load-deformation behavior of concrete plates and shells subjected to local transverse shear.

II.1 PUNCHING SHEAR TESTING PROGRAM

II.1.1 INTRODUCTION

This chapter describes the 1/6-scale experimental program which studied punching shear behavior in heavily reinforced, thick, lightweight concrete plates and shells subjected to high intensity concentrated loads. The experimental program included the testing of fifteen reduced-scale concrete specimens (1/6-scale) representative of portions of ice walls of Arctic offshore structures. In this experimental investigation, the following variables were investigated:

1. Area of loading,
2. Shell radius-to-thickness ratio (R/t),
3. Shear reinforcement ratio,
4. Effect of multiple span versus single span, and
5. Prestressing.

In the sections to follow, the selection of the following experimental factors are discussed:

1. Geometry, dimensions, and boundary conditions of the full-scale and the 1/6-scale specimens,
2. Scale factor and materials used for the 1/6-scale specimens,
3. Flexural and shear reinforcement ratios and prestress force to be used in the specimens,
4. Area and method of loading, and
5. Instrumentation, and data acquisition.

II.1.2 GEOMETRY OF TYPICAL FULL SCALE SPECIMENS

The geometries, dimensions, number of spans, and boundary conditions of the full scale specimens were determined based on: (1) typical dimensions and configurations of existing and proposed designs of Arctic

offshore concrete structures (Figure II.1) and (2) results of finite element analyses (see reference II.1.2). The exterior wall of an Arctic offshore structure is generally supported by a combination of vertical bulkheads and horizontal thrust beams to enhance its resistance to ice pressures. The concrete segments between two vertical bulkheads are either flat plates or arched shells. A review of the literature on Arctic offshore structures [II.1.1] indicates that these plate and shell concrete segments have typical thicknesses of 2 to 5 ft. This review also indicates a typical spacing of 15 to 25 ft (4.6 to 7.6 m) between two vertical bulkheads and a typical unsupported transverse wall length of at least 40 ft (12 m).

A full scale concrete model of these ice walls must not only have similar configurations and dimensions, but also have similar material properties and support conditions in order to ensure behavioral similarity. Two typical configurations were selected for the test specimens in this program, the flat plate and the arched shell configurations. The thickness of a full scale plate specimen was selected to be 3.5 ft, and the thickness of a full scale shell specimen is selected to be 2.5 ft. The results of linear elastic finite element analyses of centrally-loaded multi-span plates and shells with various boundary conditions [II.1.2] showed that flat ice walls can be best represented by three-span continuous, simply-supported flat plates, whereas curved ice walls can be best represented by pinned support, single-span open cylindrical shells. The three-span full scale plate specimens had a 20-ft central span and two 16-ft adjacent spans, and a 28-ft transverse length. The full scale single-span shells also had a 20-ft span length and 28-ft transverse length.

The large dimensions of the full scale specimens represented a problem in this experimental study. Thus reduced-scale specimens were tested to predict the behavior of the larger structure. A reduced-scale specimen had the advantages of being less costly to fabricate and test, and it did not require a large testing facility. In the following section, selections of scale factor and materials for the reduced scale specimens are discussed.

II.1.3 TEST SPECIMENS

II.1.3.1 Scale Factor And Dimensions Of Test Specimens

In modeling, the reduced scale specimen is related to the larger scale specimen by a set of similitude requirements. These requirements, if satisfied, allow a direct extrapolation of the behavior of the reduced scale specimen to the larger prototype structure. The set of similitude requirements governing the modeling of a reinforced concrete structure using a reinforced concrete specimen is given in References II.1.3 and II.1.4 and is reproduced in Table II.1.

It may be seen from Table II.1 that the similitude requirements for a reinforced concrete model are specified solely by the geometric scale factor S_1 since the stress-strain relationship of model concrete and its elastic modulus are assumed to be identical with those of the real structure. The choice of this geometric scale factor is governed by such factors as the capacity of the testing facilities, the practical dimensional limitations, and the cost of testing. Taking the above factors into consideration, a geometric scale factor S_1 of 6 was selected for this experimental study. The overall dimensions of the 1/6-scale specimens were obtained by directly scaling down the full scale dimensions by a factor of 6. The 1/6-scale three-span flat plate specimens thus had a uniform thickness of 7 in, a 40-in central span and

two 16-in adjacent spans, and a transverse length of 56 in. The 1/6-scale shell specimens thus had a uniform thickness of 5 in, a span length of 40 in, and a transverse length of 56 in. Figure II.2 shows the configurations, dimensions, and boundary conditions of the specimens in this experimental study.

II.1.3.2 Concrete Materials

In this study, the concrete and the reinforcement used for the 1/6-scale specimens were selected to have the same properties as the materials used for Arctic offshore structures. Information obtained from literature on Arctic offshore structures shows that high-strength lightweight concrete is used extensively as the principle building material for these structures. Lightweight concrete is required for economic and practical reasons, and is achieved by using lightweight coarse aggregate with a typical nominal maximum aggregate size of 3/4 in (19 mm). The use of many additives, including condensed silica fume, high-range water reducing agents or "superplasticizers", and air-entraining agents, is also reported. These additives are used to improve workability of the concrete mix and strength and durability of offshore structures. Based on this information, the following materials were selected for concrete:

1. North Carolina Solite lightweight aggregate with a nominal maximum size of 1/2 in (13 mm).
2. Acceptable proportions of condensed silica fume (10 percent replacement of cement), superplasticizer, and air-entraining agent.

The typical concrete mix design used for all specimens is listed in Table II.2. The mix design produced concrete with a compressive strength f'_c of at least 7,000 psi (48 MPa) and a mean density of 120-125

lb/cu.ft. This compressive strength was determined by testing 4x8 in (101x203 mm) cylinders according to recommendations of ACI Committee 444 [II.1.5].

II.1.3.3 Flexural Reinforcement

Available literature on the design of Arctic offshore structures indicates that flexural reinforcement ratios in these structures range from 1.5 to 2.5 percent [reference II.1.6]. This ratio represents the amount of flexural reinforcement in one direction on one face of the cross-sectional area of each specimen. A previous experimental investigation on punching shear [reference II.1.7] concluded that differences in punching shear strength due to varying the amount of flexural reinforcement in structures of this type is insignificant (an increase of 43% in flexural reinforcement caused only a 2% increase in punching shear strength). Therefore, flexural reinforcement was not considered as a variable in this study. Two flexural reinforcement ratios were selected for the 1/6-scale specimens, 1.75 percent and 2.5 percent. The high percentage of flexural reinforcement and the particular dimensions of the 1/6-scale models dictated the use of #4 (1/2 in diameter) deformed reinforcing bars for the flat plate specimens and #3 (3/8 in diameter) deformed bars for the shells. The bars were placed in groups of two in both directions of each layer of flexural reinforcement as shown in Figure II.3. A mean yield strength of 60 ksi (414 MPa) was specified for these reinforcing bars.

II.1.3.4 Shear Reinforcement

The contribution of shear reinforcement to punching shear resistance in offshore concrete structures is one of the variables examined in this study. No rational basis currently exists for the selection of shear reinforcement ratios in the design of Arctic offshore structures. Shear

reinforcement ratios as high as 1 percent have been suggested. To study the contribution of shear reinforcement to punching shear resistance, three ratios of shear reinforcement were selected: 0, 0.22, and 0.44 percent. There is a trend in industry toward using mechanically headed stirrups as shear reinforcement in Arctic offshore structures due to the congestion of reinforcement. To achieve similarity, T-headed bars, stamped out from steel plate, with a mean measured yield stress of 52 ksi (359 MPa) were selected for use as shear reinforcement in this study. The T-headed bars were anchored to the top and bottom layers of flexural reinforcement as shown in Figure II.4. Dimensions of the T-headed bars are given in Figure II.5.

II.1.3.5 Prestressing

Most Arctic offshore structures, due to their large dimensions, are built segmentally. The concrete wall segments are usually assembled at the site and connected by post tensioning. Tensioning values ranging from 300 to 1000 psi (2 to 7 MPa) have been reported in the design of Arctic structures. The tensioning force, by creating a state of triaxial compression in the prestressed walls, is expected to have an effect on the punching shear behavior of the walls. A prestressing force of 500 psi (3.5 MPa) in one and two directions for both plate and shell specimens was selected in this experimental program.

Finely-threaded bars, 7/8 in (22 mm) in diameter, with a yield strength of 125 ksi (862 MPa) were used as post-tensioning tendons. These tendons were equally spaced across the concrete section to provide uniform distribution of 500 psi (3.5 MPa) compressive stress in the specimens. Tendons with a fine pitch of thread were selected to minimize prestressing losses due to end anchorage slip, which otherwise can be significant due to the short length of the prestressing tendons.

Grouting of the post-tensioning ducts is usually performed in real Arctic structures to protect the post-tensioned tendons from being damaged by corrosion. However, it was believed that the absence of grout would not affect the punching shear strength of the post-tensioned structures. Therefore, to simplify the construction of the test specimens, the tendon ducts were not grouted in this study .

Prestress force in the tendons was applied sequentially and monitored using a strain gage mounted on each of the tendons. Sequential tensioning of the tendons helped reduce loss of prestress due to elastic shortening of concrete.

II.1.3.6 Area Of Loading & Loading System

a) Area Of Loading

The size of the loaded area in this test program was selected based on the following two criteria:

1. The size of the loaded area should be selected such that the contact pressure for punching shear failure to occur in the test specimens is within the range of realistic local ice pressures. The upper limit of a realistic ice pressure acting on an Arctic structure is approximately 3500 psi (24 MPa).
2. The size of the loaded area should be selected so that a punching shear failure will occur prior to flexural failure in all test specimens.

A relationship between the applied punching shear pressure and the loaded area was developed for different values of nominal ultimate shear stress as shown in Figure II.6. The ultimate shear stress was assumed to act on a critical section defined by the ACI Code. For a circular loaded area, the critical section is a circle with the perimeter located a distance equal to half of the effective depth away from the perimeter

of the loaded area. Figure II.6 shows that the size of the loaded area is inversely proportional to the ultimate applied pressure, i.e. if the area of loading becomes smaller, the required pressure for a punching shear failure will increase. If the area of loading is too small, the pressure at punching shear failure will become unrealistically large. However, if the loaded area is made too large, flexural failure of the specimen will occur instead of a punching shear failure.

Results of other punching shear studies indicated that the nominal ultimate shear stress acting on the ACI critical section of reinforced plates and shells with normal weight aggregate varied between $9\sqrt{f'_c}$ to $18\sqrt{f'_c}$. In order to satisfy the above stated criteria, a nominal shear strength of $15\sqrt{f'_c}$ was assumed for all specimens in this test program. This assumption is reasonable for lightweight concrete since the contribution of aggregate interlock in structures with this type of aggregate is anticipated to be less than that of a normal weight aggregate concrete structure. This assumed ultimate shear stress corresponds to a loaded area of 50 in^2 (see Figure II.6).

For this experimental program, a circular loaded area of 50 in^2 was selected for the majority of the specimens, although two specimens were tested with a circular loaded area of 100 in^2.

b) Loading System

A loading system designed to provide a uniformly distributed pressure on a circular area was selected for use in this testing program (Figure II.7). Load was applied through a solid steel piston contained in a steel cylinder. At the bottom of the steel piston, several layers of natural rubber and leather pads were placed. The rubber was used to simulate fluid behavior to impart a uniform pressure on the specimens. The leather pads were used to contain the rubber within the cylinder.

Molybdenum grease was applied on the inner surface of the steel cylinder to minimize friction between the piston and the cylinder. Calibration tests on the loading system showed that loss of applied load transmitted through the loading system due to friction was approximately 1 percent and therefore was considered negligible.

II.1.3.7 Testing Program

The list of the specimens in this test program is presented in Table II.3. The program consisted of fifteen 1/6-scale specimens. Of these, six were open cylindrical shells with two radius-to-thickness ratios (R/t of 6 and 12). The other specimens included eight three-span continuous flat plates and one single span flat plate (specimen FP1). Two of the three-span continuous plates (FP2-1 and IFP2-1) were duplicated to check the variability of test results. The specimens were different from each other either in configuration or properties. They were grouped as follows to facilitate the study of the influence on punching shear of the variables listed in section II.1.1:

1. Effect of area of loading: Specimens FP2-1 and FP2-2 versus IFP2-1 and IFP2-2.
2. Effect of radius-to-thickness ratio: Specimens FP1 vs. AS7 vs. AS8; Specimens AS10 vs. AS12.
3. Effect of shear reinforcement ratio: Specimens FP2s vs. FP3 vs. FP4; Specimens AS9 vs. AS7 vs. AS11.
4. Effect of multiple span: Specimens FP1 vs. FP3.
5. Effects of prestressing:
   a) One way prestressing: Specimens FP3 vs. FP5;

Specimens AS7 vs. AS10;
Specimens AS8 vs. AS12.

b) Two way prestressing: Specimens FP3 vs. FP6;
Specimens FP5 vs. FP6.

II.1.4 TEST SETUP

II.1.4.1 Plate Specimens

The test setup for the three-span plate specimens is shown in Figure II.8. Each three-span plate had one pin and three roller supports. The plate specimens were set on top of two interior supports, spaced 40 in. on center. Each support consisted of a 4x1 in steel bearing plate, a 3 in-diameter half-round steel bar, and a W8x67 beam. At one of the two interior supports, two layers of Teflon were placed between the bearing plate and the half-round bar to provide a friction-free surface. Similarly, the assembly of the exterior supports consisted of a 4x1 in bearing plate, Teflon layers, a 3 in-diameter half-round bar, and a W12x53 beam. These exterior supports were placed on top of the specimens, 32 in. away from the interior supports. They were tied down to the test floor to prevent vertical displacement of the specimen at the exterior supports. Half-round steel bars and Teflon were used to allow rotational and horizontal displacements at the supports, simulating a roller support condition. In the one interior support where Teflon was not used, friction was assumed to prevent horizontal displacement and allow only rotational displacement, thus simulating a pin support.

II.1.4.2 Shell Specimens

A steel test bed was used for testing the arched shell specimens. A schematic of the test setup is shown in Figure II.9. The test bed consisted of three wide flange beams (W10x60), 78 in long, placed parallel

to the span direction of the shell specimens. Two cut-off beams (W8x58), cut with two different angles to accommodate two R/t ratios of the shell specimens, were bolted onto the top flange of each of the wide flange beams by eight 7/8 in-diameter bolts to accommodate the thrust forces. The wide flange beams were tied down to the test floor at the center to prevent upward displacement of the test bed. A 2x12 in steel plate, 56 in long, was placed against the three cut-off beams on each side of the test bed to provide continuous supports along the straight edges of the shells.

II.1.5 INSTRUMENTATION

Monitoring the behavior of the specimens during testing included making the following observations and measurements:

1. Ultimate failure load and mode of failure.
2. Strain in the shear and flexural reinforcement and in the prestressing tendons in the vicinity of the loaded area.
3. Crack development and crack patterns.
4. Deflections under the load and at points along the major axes of the test specimens.
5. Support rotation in the shells.

The test load was applied to the specimens incrementally using a 12,000 kip capacity universal testing machine and monitored by both the load indicator on the testing machine and a 400 kip-capacity load cell. Strains in the reinforcement and specimen displacements were recorded at each increment of load using an electronic data acquisition system capable of scanning and recording 128 data channels in 1/100 of a second.

Electrical resistance foil strain gages were used to measure strain in the shear and flexural reinforcement and in the prestressing tendons. All gages were temperature-compensating gages. The gages were mounted on the reinforcement using an M-bond 200 adhesive and protected from

moisture with layers of protective coating. Strain in the shear reinforcing steel (T-headed bars) was measured using small strain gages attached to the stem section of the bars. Two gages were mounted at mid-height and on opposite sides of each T-headed bar. Four T-headed bars with gages were placed along the two major axes of each specimen at a distance of half of the effective depth away from the edge of the loaded area (8 in from center of specimen), and an additional four gaged shear bars were placed at a distance equal to the effective depth (12 in from center) in specimens with shear reinforcement. These gaged shear bars were greased after they were placed so that bond stresses on the bars would be minimized. Strain readings from the T-headed bars and the flexural reinforcement were used to determine the initiation of cracking and the strain profiles in each specimens.

Strain gages were also used in monitoring the tension force in the post-tensioning tendons. One strain gage was mounted on each tendon. These gages indicated loss of prestress in the post-tensioning process and also indicated any stress changes in the tendon during testing, although it was expected that little change would occur.

Deflections of the test specimens were measured using linear variable differential transformers (LVDTs). Measurements were taken on the underside of the test specimens at distances of 0 and 12 in (30 cm) away from the center of the specimens in both directions, and at the supports.

Locations of strain gages in the shear reinforcement are shown in Figures II.10a and b.

Externally-mounted dial gages were used to monitor the support rotations of the shell specimens during testing. Monitoring of the support rotations provided information on the behavior of the test setup.

Cracks and crack patterns in the specimens were visually monitored during testing. After testing to failure, the specimens were to be removed and sectioned in both directions, and the cracks were highlighted and recorded.

II.1.6 SUMMARY

1/6-scale three-span continuous, simply-supported flat plates and single-span, arched shells were selected to represent typical Arctic ice walls. The plate had a 40 in central span, two 32 in adjacent spans, and an uniform thickness of 7 in. The shell was pin supported along the straight edges (transverse direction) and had an uniform thickness of 5 in and a span length of 40 in. Both the plates and the shells specimens had 56 in transverse lengths.

Lightweight aggregate (North Carolina Solite) with a nominal maximum size of 1/2 in (13 mm) was used to produce lightweight concrete. Condensed silica fume, an air-entraining agent, and a superplasticizer were also used to achieve similarity with the material of real Arctic offshore structures.

Reinforcing bars, with 3/8 and 1/2 in diameters (#3 and #4) and a specified yield stress of 60 ksi (414 MPa), were used as flexural reinforcement. Two flexural reinforcement ratios of 1.75 and 2.5 percent were selected. T-headed bars with a measured yield strength of 52 ksi (359 MPa) were used as shear reinforcement. Three ratios of shear reinforcement, 0, 0.22, and 0.44 percent, were selected.

Two circular loaded areas of 50 and 100 in^2 (300 and 600 cm^2), with the majority of specimens have 50 in^2 loaded area, were selected.

II.2 TEST RESULTS

II.2.1 INTRODUCTION

A considerably large volume of raw data was obtained in this test program. These data were reduced to engineering units and plotted to facilitate examination of the performance of each specimen. For each specimen, the results are shown by the following plots:

1. Load-center deflection relationship.
2. Load-strain relationships for the gaged T-headed bars.
3. Flexural strain profiles, plotted for the tension reinforcement in both span and transverse directions. For the arched shell specimens, strain profiles of the compression reinforcement in the span direction are also provided.

Discussion regarding the performance of each specimen is based largely on the above plots and the observations made during testing. In addition, pictures of crack patterns on the underside and on the cross sections of the specimens are also shown.

Descriptions of the test specimens in this test program are summarized in Table II.3, and the test results of all specimens are given in Table II.4.

II.2.2 RESULTS OF PLATE TESTS

II.2.2.1 Plate Specimens Without Shear Reinforcement

a) Specimens FP2-1 and FP2-2

Specimens FP2-1 and FP2-2 were identical in every aspect except for their concrete compressive strengths at testing. They were designed to provide some measure of the variability of the test results in this test program. The difference in concrete compressive strengths of the

specimens at testing was taken into account by normalizing the loads with respect to the square root of the measured compressive strengths. Four gaged shear bars were placed along the two major axes of each of these specimens at locations of 12 inches away from their centers to monitor internal shear cracking.

For specimen FP2-1, the flexural strain profiles were not obtained, therefore only the load-deflection curve and the load-strain curves for the gaged shear bars are shown in Figures II.11 and II.12.

The first indication of internal shear cracking in this specimen was registered by the two gaged shear bars on the transverse axis at approximately 90 kips (78% of ultimate load) as seen in Figure II.12. At this load level, a slight deviation of the load-deflection curve from the original linear relationship was observed (see Figure II.11), indicating a degradation of stiffness due to cracking.

Cracks continued to develop and completion of the circumferential crack was estimated at 100 kips (87% of ultimate), as evidenced by the sudden increase of strain in the two gaged shear bars on the span axis. Ultimate load was recorded at 114.9 kips, at which point the strain in all four gaged bars increased rapidly. The applied load dropped slightly at 114.9 kips before climbing back to the same peak of 114.9 kips (Figure II.11).

The specimen was cut in both span and transverse directions after failure and the cross-sections are shown in Figures II.13a and b. From these cross sections, it was observed that cracking was in the form of multiple shear cracks which were not necessarily parallel to each other. The primary shear cracks were determined as those with the largest width. Measurements of the angles of these primary cracks with respect to a horizontal plane gave angles of approximately 27^{o} in the span direction

and 28° in the transverse direction. However, it should be noted that these measurements are approximate since there were many cracks on the cross-sections.

For specimen FP2-2, the load-deflection curve, load-strain curves for gaged shear bars, and flexural strain profiles are shown in Figures II.14, 15 and 16.

The load-strain curves for the gaged shear bars (Figure II.15) of this specimen indicate that internal shear cracking occurred first in the transverse direction as in specimen FP2-1 at 98 kips (77% of ultimate load). The flexural strain profiles of the tension reinforcement in both directions of this specimen (Figures II.16a and II.16b) show proportional increases in strain with increasing load up to 90 kips. However, at the initial cracking load of 98 kips, redistribution of flexural strain in both directions of the specimen was observed. Smaller increase of strain was recorded at the center of the specimen compared with the increase of strain at 8 inches from the center of the specimen in both directions. This is an indication of shear cracks intersecting with the tension reinforcement in the region of 8 inches away from the center of the specimen. At 113 kips, a decrease in flexural strain at the center of the specimen was seen on the transverse strain profiles (Figure II.16b). At this same load level, significant increase of strain in all gaged shear bars developed (Figure II.15), indicating the completion of circumferential crack and an increase of crack width. Further opening of cracks at 113 kips is also evidenced by the drop of the applied load while the center deflection was still increasing (see Figure II.14).

Load then climbed up again and the ultimate capacity of FP2-2 was recorded at 126.9 kips. Flexural strain profiles at ultimate show that there was further decrease in flexural strains at the center of FP2-2 in

both directions while the strains at locations of 8 inches and further away from the center continued to increase (Figures II.16a and II.16b).

Crack patterns on the span and transverse cross sections and on the underside of FP2-2 are shown in Figures II.17a, b and c. Cracks, almost in circular form, can be observed on the underside of FP2-2. The two cross sections also show similar crack patterns as was observed in specimen FP2-1.

Essentially similar load-deflection behavior was observed for specimens FP2-1 and FP2-2. Both specimens displayed the same stiffness up to ultimate. The difference between ultimate loads of these two specimens, when normalized with respect to $\sqrt{f'_c}$, was small ($4.8\sqrt{f'_c}$ and $5.4\sqrt{f'_c}$, respectively). Yielding of the tension steel did not occur in either specimens.

b) Specimens IFP2-1 and IFP2-2

Similar to specimens FP2-1 and FP2-2, these two specimens were not reinforced in shear. However, both of these specimens had larger amounts of flexural reinforcement and loaded areas than the rest of the specimens tested in this program. Specimen IFP2-1 had a flexural reinforcement ratio of 2.5 percent and an area of loading of 138 in^2, and specimen IFP2-2 had the same amount of flexural reinforcement and an area of loading of 100 in^2. The larger loaded area of 138 in^2 in specimen IFP2-1 resulted from load being transferred by friction to the outer cylinder of the loading system. This problem was corrected for specimen IFP2-2 by applying lubricant at the interfaces of the loading system. Since these two specimens were designed to provide guidances for the overall test program, they were not monitored to the same extent that the rest of the specimens in the testing program were. The test results for

strain curves (Figure II.20). At this load level, gradual degradation of stiffness, indicated by the deviation of the load-deflection relationship from the original linear relationship, was observed on the load-deflection curve (Figure II.19). Shortly after 90 kips, redistribution of flexural strains occurred in both directions of the tension reinforcement (Figures II.21a and II.21b), seen in specimen FP2-2 (Figures II.16a and II.16b). The flexural strain profiles in both directions of FP3 show a smaller increase of strain at the center of the specimen and a larger increase in the region of 8 inches away from the center. The inflection points seen in both directions before 90 kips disappeared.

The strain redistribution process in this specimen, however, was less extensive when compared with the redistribution process seen in FP2-2. The flexural strain at the center of FP3 continued to increase with increasing load up to ultimate at a slower and no longer proportional rate, but it never decreased as happened in FP2-2. This is due to the presence of the shear reinforcement in FP3. The shear reinforcement bridging the crack surfaces provided restraint from further crack opening and therefore slowed down the rate of crack propagation. Additional load had to be applied to overcome this restraining force before ultimate failure could occur, thus increasing the load carrying capacity of the specimen and making the failure process of FP3 more gradual than that of FP2-2. The more gradual progression of shear cracks in FP3 is also evidenced by the fact that the sudden development of strain in different gaged shear bars in this specimen occurred at significantly different load levels (from 90 kips to approximately 160 kips).

The ultimate capacity of FP3 was recorded at 195.1 kips. Yielding did not occur in the tension reinforcement prior to ultimate failure.

Also, greater strains carried in the span direction of the specimen indicates that the stiffness in the span direction was greater than in the transverse direction. This observation is consistent with the behavior displayed in the flexural strain profiles of specimen FP2-2 and with the fact that cracks always occurred first in the transverse direction.

Similar to specimens FP2-1 and FP2-2, multiple cracks formed in the region local to the failure surface as shown on the cross-sections of FP3 (Figures II.22b and II.22c). Cracking on the underside of the specimen was diffused and included many fine cracks (Figure II.22a). The slope of the shear cracks appeared to be steeper in the transverse direction than in the span direction with primary crack angles of 27^{o} in the span direction and 32^{o} in the transverse direction.

b) Specimen FP4

The load-deflection curve, load-strain curves for gaged shear bars, flexural strain profiles, and crack patterns of specimen FP4 are shown in Figures II.23, 24, 25a and b, 26a, b and c.

Internal shear cracking was first evidenced by the sudden increase of strain of two gaged shear bars, one on the span and one on the transverse direction (Figure II.24), at approximately 100 kips (40% of ultimate).

Beside the fact that this specimen displayed higher punching shear strength than specimen FP3 (ultimate load was recorded at 251.9 kips) and yielding occurred in the tension reinforcement shortly after 180 kips (Figures II.25a and b), the failure process of this specimen was essentially similar to the failure process observed in specimen FP3.

Deviation of the load-deflection relationship from the original linear relationship, evidence of the degradation of stiffness due to

cracking, was seen shortly after internal shear cracking was detected by the gaged shear bars. Beginning of the flexural strain redistribution in the tension reinforcement in both directions also became evident around this load level. The wide range of loads at which sudden development of strain in all the gaged shear bars occurred (from 100 kips to approximately 230 kips as seen in Figure II.24) indicated that the failure process of FP4 was even more gradual than that of FP3. The load dropped slightly at 246 kips while the center deflection was still increasing, indicating the development of major crack openings at 246 kips. This load drop-off also implied that most, if not all, the shear reinforcement crossing the cracks might have failed at this load level, thus allowing a less restricted opening the of cracks. The load then increased again to the indicated peak load of 251.9 kips (see Figure II.23). Figures II.26a, b and c show the crack patterns on the cross sections and underside of this specimen. Cracking on the underside of this specimen was also diffused, similar to the cracking in specimen FP3. The primary shear crack angles were approximately 27° in the span direction and 36° in the transverse direction.

II.2.2.3 Plate Specimens With Prestressing

Two specimens, FP5 and FP6, were constructed to study the effects of prestressing on punching shear behavior in the plate specimens. Like specimen FP3, each of these two specimens contained 0.22 percent of shear reinforcement. The only difference between these two specimens and specimen FP3 was the presence of prestress. For specimen FP5, a prestress of 500 psi was applied uniformly in the transverse direction of the specimen. For specimen FP6, the same value of prestress was applied in both span and transverse directions.

a) Specimen Prestressed In Transverse Direction: FP5

The test results of this specimen and pictures of crack patterns on the span and transverse cross-sections and on the underside are shown in Figures II.27, 28, 29a and b, and 30a, b and c.

Internal shear cracking occurred first in the span direction of FP5 at 87 kips (43% of ultimate load) as indicated on the load-strain curves for the shear reinforcement (Figure II.28). Due to the effect of prestressing in the transverse direction, this cracking was different from the non-prestressed specimens in which cracking began in the transverse direction. After initiation of cracking at 87 kips, radial and circumferential cracks propagated gradually down and outward. Major crack openings, marked by the sudden increases of strain in the gaged shear bars, developed at approximately 150 kips (74% of ultimate).

On the load-deflection curve (Figure II.27), evidence of the initiation of internal shear cracking was observed by the gradual degradation of stiffness beginning at 87 kips. The development of major shear cracking was confirmed by a sudden shift of the load-deflection relationship at 150 kips.

The flexural strain profile in the span direction of FP5 indicates the beginning of the strain redistribution process at 90 kips (Figure II.29a and b). Yielding of tension reinforcement in the span direction occurred shortly before ultimate. These strain profiles also indicates that more load was carried in the span direction of this specimen. Ultimate punching shear capacity of FP5 was recorded at 202.2 kips.

The underside and cross-sections of specimen FP5 are shown in Figures II.30a, b and c. Cracks on the underside were diffused, but not as much as was observed in specimens FP3 and FP4. The primary crack angle in the span direction (perpendicular to the direction of prestress)

was approximated as 42°. This angle was much steeper than the angles observed in specimens FP3 and FP4. In contrast, cracks in the transverse direction were at angles of approximately 16° and 23°, which were flatter than the angles observed in the transverse directions of FP3 and FP4.

The behavior of specimen FP5 was similar to that of specimen FP3. Internal shear cracking initiated in both specimens at almost the same load level, 90 kips for FP3 and 87 kips for FP5 (46% and 43% of ultimate loads, respectively). Sudden development of strain in all gaged shear bars, an indication of major crack opening, occurred at 160 kips for FP3 and at 150 kips for FP5. This was also marked by the shifts in the load-deflection relationships in both specimens at these load levels. The punching shear strength of specimen FP5, however, was 8 percent higher when compared to that of FP3.

b) Specimen Prestressed In Both Directions: FP6

A prestress of 500 psi was applied uniformly in both directions of specimen FP6. Information from strain gages mounted on the tension reinforcement was not obtained for this specimen, therefore the flexural strain profiles for FP6 are not presented. The load-center deflection curve and the load-strain curves for the shear reinforcement are shown in Figures II.31 and 32.

The load-strain curves (Figure II.32) show that internal shear cracking first developed at 85 kips (38% of ultimate). Around this load level, gradual degradation of stiffness was observed on the load-deflection curve (Figure II.31). The load-deflection behavior of this specimen was essentially similar to that of FP3 and FP5. Ultimate load was recorded at 221.3 kips for FP6.

Figures II.33a, b and c show the crack patterns on the cross-sections and on the underside of specimen FP6. The primary shear crack

angles were measured as 37° in the span direction and 23° in the transverse direction. In both specimens FP5 and FP6, the locations of the post-tensioning ducts were seen to have influenced the formation of the cracks.

II.2.2.4 Single Span Flat Plate Specimen

In a three-span specimen, the two adjacent spans provide the center span with restraint that makes the specimen stiffer in the span direction. The lack of this restraint in a single span specimen makes it more flexible, which may affect the load carrying mechanism. To better understand the influence of this restraint condition on the punching shear behavior of the specimens in this test program, a single-span plate specimen, FP1, was tested. Except for being a single-span specimen, FP1 was identical to FP3 (0.22 percent of shear reinforcement). The test results for this specimen are shown in Figures II.34, 35, 36a and b.

The flexibility of specimen FP1 is reflected in its load-deflection curve and its flexural strain profiles (Figures II.34, II.36a and b). The load-displacement relationship of this specimen deviated more from the original linear relationship at a much lower load than in any three-span plate specimens, and the flexural strain profiles show that there was more bending action, especially in the span direction, in FP1 than in its three-span counterpart FP3. Yielding of the tension reinforcement in the span direction was observed at approximately 140 kips (65 percent of ultimate load). Yielding also occured in the transverse tension reinforcement at ultimate.

Ultimate load was recorded at 216.8 kips. Internal shear cracking occurred at approximately 76 kips (35% of ultimate) as indicated by the load-strain curves for the shear reinforcement. Shortly after the

initial cracking load was reached, redistribution of strain was seen in the span direction as indicated by the larger increase of strain at locations of 8 inches away from the center of the specimen compared with the increase of strain at the center.

Even though yielding in the tension reinforcement occurred at a fairly low load level in this specimen (at 65 percent of ultimate load), the initiation of internal shear cracking at relatively low load level (35 percent of ultimate load), and the distributions of strain in the tension reinforcement indicate that punching shear was the primary mode of failure.

The measured punching shear strength of FP1 was 20 percent higher than that of FP3. This increase in punching shear strength can be attributed to the flexibility of this specimen. Since FP1 was more flexible in the span direction than FP3, its ability to deform with increasing load was greater than that of FP3. The greater deformability allowed FP1 to deflect more than FP3 or any other three-span specimen after cracking had formed. This deflection helped reduce the tensile stress in the shear reinforcement crossing the crack. Additional applied load was required to fail this shear reinforcement, resulting in a higher load-carrying capability in the single-span specimen. This is further confirmed by the significantly wider range of loads at which sudden strain developments in the gaged shear bars occured in FP1 (from 76 kips to ultimate) as seen in Figure II.35.

Crack patterns on the underside and on the span cross-section of this specimen are shown in Figures II.37a and b. The underside of this specimen shows extensive flexural and shear cracks, and the cross-sections show primary crack angles of approximately 27^{o} in the span direction and 24^{o} in the transverse direction.

II.2.3 RESULTS OF TESTS ON SHELLS WITH R/t RATIO OF 12

II.2.3.1 Shell Specimen Without Shear Reinforcement

For all shell specimens, the strain profiles of the compression reinforcement in the span direction are provided, in addition to the load-deflection curve, the load-strain curves for shear reinforcement and the strain profiles of the tension reinforcement. The test results of specimen AS9, which had an R/t ratio of 12 and contained no shear reinforcement, are shown in Figures II.38, 39, 40a, b and c, and 41a, b and c.

Only information from three of the four gaged shear bars, placed on the two major axes of this specimen, was obtained, as shown in the load-strain curves for the shear reinforcement (Figure II.39). According to these load-strain curves, internal shear cracking initiated at approximately 92 kips. However, the beginning of the strain redistribution processes in both directions took place at approximately 85 kips (Figures II.40a and b), indicating that internal shear cracking might have occurred at this load level rather than at 92 kips as given by the load strain curves. The load-deflection curve (Figure II.38) shows a linear relationship up to the level of the initial shear cracking load (92 kips). Gradual degradation of stiffness, marked by the decrease of the slope of the load-deflection relationship, occurred shortly after that load level. The ultimate punching shear capacity was recorded at 124.3 kips. The sudden developments of strain in the gaged shear bars, an indication of the extension of crack at their locations, occurred between 85 kips to approximately 118 kips (Figure II.39).

The flexural strain profiles (Figures II.40a, b and c) show that bending action was equally distributed in both directions. Yielding of either tension or compression reinforcement did not occur at ultimate.

More importantly, these strain profiles show a similar strain redistribution process as seen in the plate specimen without shear reinforcement FP2-2. As load continued to increase after 85 kips, a decrease of strain in the tension reinforcement near the center of the specimen and a large, unproportional increase of strain in the portion of the tension reinforcement approximately 8 inches away from the center were observed. This indicates that shear cracks intersected the tension reinforcement approximately 8 inches from the center of the specimen. This behavior, which is similar to the behavior displayed by the plate specimen FP2-2, may be explained as follows:

> As a shear crack extended downward and intersected the tension reinforcement, additional tension created by the opening of crack was introduced into the portion of the tension reinforcement local to the crack. This resulted in an increase of tensile strain in that portion. At the same time, compression created by the decrease in volume of the solid concrete between the cracks due to crack opening was introduced to the tension reinforcement between the cracks (at the center of the span specimen), thus releasing some tension in this portion. This is evidenced by the decrease of tensile strain at the center of the specimen.

More information on how this specimen behaved is offered in the strain profiles of the compression reinforcement (Figure II.40c). These profiles show a steady, almost proportional increase of compressive strain in the compression reinforcement under increasing load up to 120 kips (96 percent of ultimate load). This compressive strain was evidence of the existence of a compressive zone, or more correctly a compressive dome, extending from the top surface of the specimen to the two supports.

Figures II.41a ,b and c show the crack patterns on the underside and on the cross-sections of AS9. Again, multiple shear cracks developed prior to the final collapse of the specimen (Figures II.40b and c). Evidence of crushing of concrete was observed in the region near to the top of the specimen. The primary shear crack angles were approximated to be 25° and 18° in the span direction and 22° in the transverse direction.

II.2.3.2 Shell Specimens With Shear Reinforcement

Two specimens, AS7 and AS11, were constructed to study the influence of shear reinforcement on punching shear capacity and failure mechanism of the shell specimens. Both AS7 and AS11 had the same R/t ratio of 12. The only difference between these two specimens and specimen AS9 was the inclusion of shear reinforcement. AS7 contained 0.24 percent of shear reinforcement and AS11 contained 0.48 percent.

a) Specimen AS7

A total of eight gaged shear bars were placed along the two major axes of AS7, four were placed on the two major axes at the same distance of 8 inches from the center of the specimen and the other four were placed at 12 inches from the center. Test results for this specimen are shown in Figures II.42, 43, 44, and 45.

Despite visual observation made during the test which indicated a sudden failure, the load-strain curves for the gaged shear bars (Figure II.43) revealed a gradual process of crack development. Initiation of internal shear cracking was detected at approximately 93 kips (49 percent of ultimate load) by a gaged shear bar placed at 8 inches from the center of the specimen in the span direction. Cracking then slowly propagated circumferentially and radially, evidenced by the development of strain in the gaged shear bars placed further from the center at higher loads

(see Figure II.43). In one of the gaged shear bars placed 12 inches from the center of the specimen, this development of strain did not occur, indicating that at least some of the shear reinforcement crossing the crack was not fully activated at ultimate.

The flexural strain profiles (Figures II.44a and b) showed that redistribution of strain in the transverse direction of this specimen occurred shortly after 90 kips. The strain redistribution process in this specimen was less extensive when compared with the strain redistribution process that occurred in the specimen without shear reinforcement, AS9. Strains in the tension reinforcement in the transverse direction were greater than they were in the span direction, and yielding of the tension reinforcement in the transverse direction occurred at approximately 150 kips.

The strain profiles for the compression reinforcement (Figure II.44c) showed a steady, proportional increase of compressive strain with increasing load. Yielding due to compression almost occurred in the compression reinforcement at ultimate.

The load-deflection curve of this specimen (Figures II.42) displayed an essentially linear relationship between load and center displacement. No clear sign of degradation of stiffness due to cracking was offered from this relationship. The ultimate punching shear capacity of this specimen was recorded at 190.6 kips.

Crack patterns on the underside and on the cross-sections of AS7 are shown in Figures II.45a, b and c. Cracking on the underside was in the form of a single, circular crack. Multiple cracks also formed on the cross-sections with evidence of concrete crushing on top of the specimen. The primary crack angles were estimated as 31^{o} in both the span and transverse directions.

b) Specimen AS11

AS11 contained 0.48 percent of shear reinforcement, twice the amount contained in AS7. The test results of this specimen are shown in Figures II.46, 47, 48 and 49.

The load-strain curves for the gaged shear bars (Figure II.47) showed that internal shear cracking developed first at the location of the four inner gaged shear bars (8 inches from center) at 95 kips. Internal shear cracking propagated radially outward, and at 133 kips reached the four outer gaged shear bars (12 inches from the center). The development of strain in all gaged shear bars was much more gradual compared with that of AS7 and AS9, indicating a more restrictive crack opening in AS11. This was due to the larger amount of shear reinforcement crossing the cracks. The fact that cracks were less free to open and propagate is also evidenced in the strain profiles (Figures II.48a, b and c). These profiles show an even less extensive strain redistribution process when compared with the process seen in specimen AS7. Like AS7, the load-strain curves for the gaged shear bars in this specimen also indicated that some shear reinforcement bridging the crack did not fail when the ultimate load was achieved.

Yielding of the tension reinforcement occurred in the span direction shortly after 120 kips, and in the transverse direction shortly after 150 kips, as indicated in Figures II.48a and b. Yielding of the compression reinforcement in the compression zone occurred at ultimate (Figure II.48c). The strain profiles in the tension reinforcement also showed that bending action was more equally distributed in both directions of this specimen than it was in specimen AS7. The strain profiles of the compression reinforcement showed a steady, proportional increase of compressive strain in the compression zone up to ultimate.

The load-deflection behavior of AS11 is almost identical with that of AS7. Essentially, a linear relationship between load and center displacement was observed throughout the loading history. No clear sign of degradation of stiffness due to crack was indicated by the curve. Sudden rupture observed during test marked the ultimate failure of this specimen; and the ultimate load was recorded at 192.4 kips, almost the same load level with AS7.

Crack patterns on the cross-sections of the failed specimen are shown in Figures II.49a anb b. Formation of circular cracks was seen on the underside of AS11. Similar to AS7 and AS9, cracks on the cross-sections of AS11 were in the form of multiple cracks with evidence of concrete crushing on top of the specimen. The primary crack angles were measured as 34^{o} in the span direction and 37^{o} in the transverse direction.

II.2.3.3 Shell Specimen With Prestressing

The influence of prestressing on the punching shear behavior of the shell specimens was examined in specimen AS10. Except for the prestress of 500 psi applied uniformly in the transverse direction of this specimen, AS10 was identical to AS7. It contained 0.24 percent of shear reinforcement and had an R/t ratio of 12. The test results of AS10 are shown in Figures II.50, 51, 52, and 53.

Unlike specimen AS7, in which cracking was seen to propagate slowly (internal shear cracks initiated at 93 kips at locations of the inner gaged shear bars and did not reach the locations of the outer gaged shear bars until 143 kips), the propagation of cracks in AS10 was rapid. Initial shear cracking load in AS10 was determined as approximately 87 kips, and extension of cracks to the outer gaged shear bars (12 inches from center) was recognized at approximately 100 kips (Figure II.51).

Shortly after reaching the initial cracking load of 87 kips, redistributions of strain in the tension reinforcement in both directions of AS10 were observed on the flexural strain profiles as shown on Figures II.52a and b. The distributions of strain in the compression reinforcement were proportional to the applied load up to approximately 120 kips. Beyond this load level, redistribution of compressive strain in the compression reinforcement occurred as observed in the strain profiles shown in Figure II.52c.

At the initial cracking load (87 kips), the load-deflection curve (Figure II.50) showed a slight deviation from the original linear relationship. Ultimate punching shear capacity was recorded at 152.1 kips.

Crack patterns on the underside and on the cross-sections of AS10 are shown in Figures II.53a, b and c. Cracking was in a circular form on the underside, and multiple cracks developed on the cross-sections prior to complete failure of the specimen. The primary shear crack angles were 47^{o} and 36^{o} in the span direction and 31^{o} in the transverse direction. Influence of the locations of the post-tensioning ducts on the formation of cracks was also visible on the cross-sections.

II.2.4 RESULTS OF TESTS ON SHELLS WITH R/t RATIO OF 6

The influence of compressive membrane action (arching action) on punching shear behavior of the test specimens was further studied by testing two shell specimens with larger curvature, AS8 and AS12. Both specimens had an R/t ratio of 6. AS8 contained no shear reinforcement and AS12 contained 0.24 percent of shear reinforcement.

II.2.4.1 Specimen AS8

Except for the larger curvature, this specimen was identical to specimen AS9. The test results of this specimen are shown in Figures II.54, 55, 56, and 57.

Internal shear cracking was recognized at 108 kips by three gaged shear bars, two on the transverse axis and one on the span axis (Figure II.55). The completion of the circumferential crack, indicated by the development of strain in the remaining gaged shear bar, was recorded at 128 kips. The beginning of the flexural strain redistribution process, which was similar to that seen in AS9, was observed on the strain profiles of the tension reinforcement in both directions (Figures II.56a and b) shortly after the initial cracking load was reached. Proportional increases of compressive strain in the compression reinforcement up to ultimate were observed on the strain profiles for the compression reinforcement (Figure II.56c). Ultimate load was recorded at 152.0 kips. The load-deflection curve showed an essentially linear relationship between the applied load and the center deflection up to ultimate.

Crack patterns on the underside of this specimen are shown in Figure II.57. Crack patterns on the cross-sections are not shown here due to the difficulty in cutting this specimen.

II.2.4.2 Specimen AS12

The only difference between AS12 and AS7 was the larger curvature in specimen AS12. The test results of this specimen are shown in Figures II.58, 59, 60, and 61.

Like in other specimens with shear reinforcement, the development of strain in the gaged shear bars in AS12 was gradual, with the development of strain in the inner gaged shear bars occurring first (Figure II.59). The initial shear cracking load was recorded at 106 kips

(62 percent of ultimate). Like in specimen AS7, one of the gaged shear bars of AS12 did not fail at ultimate, indicating that ultimate failure of this specimen occurred prior to complete failure of all shear reinforcement crossing the crack.

The strain profiles of the tension reinforcement (Figures II.60a and b) showed that yielding did not occur prior to ultimate load. Redistribution of strain in the tension reinforcement in both directions was evidenced shortly after 106 kips. The strain redistribution in this specimen was also less extensive than that of specimen AS8, which contained no shear reinforcement. Compressive strain in the compression reinforcement increased proportionally with increasing load up to ultimate as shown in Figure II.60c.

The load-deflection curve (Figure II.58) displayed an essentially linear relationship between the applied load and the center deflection, with no clear sign of degradation of stiffness due to internal shear cracking. Ultimate load was recorded at 170.1 kips for AS12.

Crack patterns on the underside of AS12 are shown in Figure II.61. Primary crack angles were estimated to be 60^{o} in the span direction and 30^{o} in the transverse direction.

II.2.5 SUMMARY

Experimental results and general observations obtained from this test program have been presented in the above sections. Discussion regarding the behavior of each specimen was given with respect to load history. Test results of all specimens were summarized and presented in Table II.4. The behavior of the specimens in this testing program is summarized here:

1. In most cases, the load level at which internal shear cracking was first detected by the gaged shear bars was lower or almost the same

as the load level at which the redistribution of flexural strain was observed. This established confidence in relying on the gaged shear bars to determine the initial cracking loads.

2. The strain redistribution process, marked by the unproportional increases of strain in the flexural reinforcement at locations near the cracks and the unproportional decreases of strain at center of the specimens, was more extensive in specimens without shear reinforcement than in those with shear reinforcement. This process was also more extensive in the shell specimens than in the plate specimens.

3. Failure in the plate specimens that contained shear reinforcement was more gradual than in those without shear reinforcement. In the latter specimens, sudden rupture occurred shortly after internal shear cracking, while in the former specimens the final collapse did not occur until significant increase of load and center deflection had been achieved. The ductility of the specimens increased with increasing amount of shear reinforcement.

4. Not all the shear reinforcement crossing the crack in the shell specimens (AS7, AS11, and AS12) was fully activated at ultimate, especially those shear bars at locations further away from the center of the specimen. This indicates that failure in these specimens occurred mainly due to the failure of concrete in the compression zone.

5. The rate of radial propagation of shear cracks was much slower in the shell specimens than in the plate specimens, indicating the influence of the compressive membrane forces in restraining the cracks opening.

6. In all shell specimens, the strain profiles of the compression reinforcement showed a steady, proportional increase of compressive strain with increasing applied load up to ultimate. This increase in

strain indicates that a compressive dome existed in all shell specimens throughout the loading process. In the shell specimens with 0.24 and 0.48 percent of shear reinforcement (AS7 and AS11), yielding of the top flexural reinforcement due to compression occurred prior to failure of the specimens.

7. Deviation of the load-center deflection relationship from the original linear relationship, an indication of the degradation of stiffness in the specimen due to internal shear cracking, was more apparent in the plate specimens than in the shell specimens.

8. Increasing shell curvature resulted in a slower rate of crack propagation and less extensive flexural strain redistribution. Furthermore, increasing shell curvature also resulted in higher punching shear capacity.

9. Increasing shell curvature resulted in an increase of normalized shear cracking stress. The mean shear cracking stress was $3.3\sqrt{f'_c}$ for plates, $7.4\sqrt{f'_c}$ for shells with R/t ratio of 12, and $9.0\sqrt{f'_c}$ for shells with R/t ratio of 6.

10. Normalized shear cracking stress V_{cr} is not affected by the amount of shear reinforcement.

11. In all specimens, the primary shear crack angles were flatter than 45^{o}.

II.3 FAILURE MECHANISMS OF THE TEST SPECIMENS

II.3.1 INTRODUCTION

Experimental results are used in this chapter to identify the failure mechanisms of the test specimens and to explain the processes that led to their ultimate failures. Since more complete information was obtained for the shell specimens, the failure mechanisms of the shells are explained first.

II.3.2 FAILURE MECHANISMS OF SHELL SPECIMENS

Substantial empirical evidence indicated that shear-compression was the mechanism of failure in all the shell specimens. This mechanism of failure can be better explained if the progression of internal shear cracks in the shell specimens is understood.

The region where internal shear cracks first occurred was determined by examining the strain profiles of both the tension (bottom flexural steel) and compression reinforcement (top flexural steel). These profiles indicated that there existed a dome-like compression zone, extending from the supports to the top layer of the shell specimens as idealized in Figure II.62, throughout the loading history of the shells. The strain profiles of the compression reinforcement of all shells showed steady and proportional increases of compressive strain up to ultimate load. Redistribution of strain in the compression reinforcement was minor and occurred only shortly before ultimate load was achieved. The proportional increase of compressive strain up to ultimate in the compression reinforcement clearly indicated that internal shear cracking could not have initiated first in the region close to the top of the specimens, where this reinforcement was located. If this had occurred,

a major strain redistribution in the compression reinforcement would have resulted. The strain profiles of the tension reinforcement showed significant redistribution of strain shortly after internal shear cracking was detected by the gaged shear bars. As explained in chapter II.2, the redistribution of strain in the tension reinforcement was caused by the intersection of shear cracks with the bottom steel layer. The redistribution of strain in the tension steel only occurred in most cases after internal shear cracking had been detected by the shear bars. This also ruled out the possibility that shear cracks initiated first at the bottom of the specimens. Consequently it is clear that internal shear cracking first developed in the mid-depth region of the specimens.

Having determined the region where internal shear cracks first developed, the progression of shear cracks in the shells can now be explained by examining the behavior of one typical shell specimen, specimen AS7. AS7 had an R/t ratio of 12 and 0.24 percent of shear reinforcement. Two layers of gaged shear bars were placed on the two major axes of the specimen, the inner layer 8 inches away from the center and the outer layer 12 inches away from the center. The following successive events describe the failure process of AS7.

During the period before any internal shear cracks developed in AS7 (from 0 to 93 kips), the gaged shear bars experienced only minor compressive or bending stresses as a result of elastic deformation in the specimen. This resulted in a very small amount of either tensile or compressive strain as can be seen on the load-strain curves (Figure II.43). Elastic bending action was evidenced in this period by the proportional distributions of flexural strain with respect to the applied load in both the tension and compression reinforcement (Figures II.45a, b and c). Furthermore, a dome-like compression zone, extending from the

supports to the top layer of the specimen, was clearly indicated by the strain profiles of both the tension and the compression reinforcement.

At 93 kips and shortly thereafter, sudden development of tensile strain in the shear reinforcement, an indication of internal shear cracks, was detected by the inner layer gaged shear bars (Figure II.43). As discussed earlier, these internal shear cracks first initiated in the mid-depth region of the specimen. These cracks then propagated outward, as evidenced by the detection of cracks at 143 kips by an outer layer gaged shear bar placed in the span direction. The shear cracks also propagated downward and intersected the tension reinforcement, evidenced by the redistribution of strain in the tension reinforcement (Figures II.45a and b). This redistribution was marked by a sudden increase of strain at crack locations (approximately 8 inches from the center of the specimen) and by a decrease in rate of strain increase at the center of AS7. The increase of strain at locations local to the shear crack in the tension reinforcement was caused by the opening of cracks. This opening also resulted in a release of tension in the concrete portion in between the cracks, as reflected by the decrease of tensile strain at the center of the specimen (see Figure II.63).

During the period when strain redistribution was taking place in the tension reinforcement, the strain profiles of the compression reinforcement still showed a proportional distribution (Figure II.45c). This proportional distribution persisted until ultimate load was reached, indicating that shear cracks were not present in the compression region of AS7. Similar indications were observed for all other shell specimens.

Redistribution of strain in the tension reinforcement continued to take place until ultimate failure occurred at 190.6 kips. The failure appeared to be very sudden, even though the detection of shear cracks at

much lower load (93 kips) indicated a more gradual development of shear cracks.

At failure, one interesting observation was made on the load-strain curves of the gaged shear bars (Figure II.42). These load-strain curves showed that some of the shear bars crossing the cracks did not yield at ultimate. Similar observations were made for other shell specimens with shear reinforcement, AS11 and AS12 (Figures II.47 and II.59). This suggests that the failure in the shell specimens was controlled by the failure of concrete in the compression zone. Pictures of crack patterns on the cross-sections of this specimen (Figures II.45a, b, and c) also suggest that failure was controlled by failure of concrete in the compression zone. This crushing failure occurred in region immediately under the loaded area, where the area of the compression zone was smallest. The inclined cracks which had developed earlier created a tied-arch system, where compression was resisted by the compression dome and tension was resisted mainly by the tension reinforcement. Yielding of more shear bars on the crack surfaces resulted in continuing reduction of compression area in the compression zone as the shear crack opened wider. This reduction of area eventually led to the overloading in of the compression zone which caused a crushing failure of concrete on top of the specimen. It should also be noted that in specimens containing shear reinforcement, AS7 and AS11, yielding in compression at the center of the top reinforcement occurred prior to the ultimate load being achieved.

II.3.3 FAILURE MECHANISMS OF THE PLATE SPECIMENS

Unlike the shells where failure occurred due to crushing of concrete in the compression zone without the complete failure of the shear reinforcement, the plate specimens failed in a different mode due to the lack of membrane compressive forces.

The difference between the behavior of the plates and the shells was disclosed in the load-strain curves of the gaged shear bars. Figures II.20, 24, 28, and 32 show the load-strain curves of specimens FP3, FP4, FP5, and FP6. All these specimens contained shear reinforcement with ratios of 0.22 to 0.44 percent. These load-strain curves show that most if not all the shear bars had yielded at load levels much lower than ultimate load. For example, both layers of gaged shear bars in specimen FP3 yielded at appoximately 150 kips, while FP3 did not fail until 195 kips (Figure II.20). The complete yielding of shear reinforcement at significantly low load levels suggests that failures in the plate specimens were caused by the successive failures of the shear reinforcement, the interface shear transfer, and the dowel action. In other words, the failures in the plates were due mainly to shear. The applied shear force overcame the combined action of the three basic shear resistance mechanisms, namely the axial restraint provided by the shear reinforcement, the dowel action, and the interface shear transfer, and ultimately led to final collapses.

II.3.4 SUMMARY

The progression of shear cracks and the causes of failures of the test specimens were explained using experimental results obtained from this test program. The presence of in-plane compression in shell specimens resulted in crushing failures of concrete in the compression zone without the complete failure of shear reinforcement. Thus, the

failure mechanism of the shells was identified as that of shear-compression type. The lack of this in-plane compressive force in the plates resulted in failures due to failure of the shear resistance mechanisms.

II.4 EFFECTS OF TEST PARAMETERS ON PUNCHING SHEAR STRENGTH

II.4.1 INTRODUCTION

The effects of different parameters on punching shear strength of specimens in this test program are investigated in this chapter. Direct comparisons of normalized shear strengths are provided in order to examine the effects of the following test parameters:

1. Shear reinforcement ratio,
2. Radius-to-thickness ratio (R/t),
3. Span continuity,
4. Prestressing, and
5. Size of area of loading.

II.4.2 EFFECT OF SHEAR REINFORCEMENT RATIO

Plotted in Figure II.64 are the normalized punching shear strengths of the test specimens versus the shear reinforcement index. Three curves are shown in this figure. The first curve is made up of the normalized shear strengths of four plate specimens, FP2-1, FP2-2, FP3 and FP4. As indicated, the only difference between these specimens was the amount of shear reinforcement (0.0 to 0.44 percent). The second curve includes data of three shell specimens with R/t ratio of 12. These specimens, AS9, AS7 and AS11, contained 0, 0.24 and 0.48 percent of shear reinforcement, respectively. The third curve includes data of two shell specimens with R/t ratio of 6, AS8 and AS12, which contained 0 and 0.24 percent of shear reinforcement. The reinforcement index was used to account for the slight difference in the yield strength of the T-headed bars used in the plate and the shell specimens.

From the curve for the plate specimens, it is apparent that within the range of 0 to 0.44 percent of shear reinforcement, the punching shear

strength of the plate specimens increased proportionally with increasing shear reinforcement ratio (or reinforcing index), with a rate of increase of approximately $1.3\sqrt{f'_c}$ per every additional 0.1 percent of shear reinforcement. The linear relationship between the punching shear strength and the shear reinforcing index suggests that, within the indicated range of shear reinforcement ratio, the shear reinforcement in the plate specimen was effectively utilized. This relationship further confirms that ultimate failure in the plate specimens was the result of complete failures of all three basic shear resistance mechanisms, i.e. the restraint provided by the shear reinforcement, the interface shear transfer, and the dowel action. It is anticipated that at some point, the benefit from increasing the amount of shear reinforcement in the plate specimen would diminish. However, it is difficult to assess the optimum level of shear reinforcement in the plate specimens without testing plates with shear reinforcement ratios higher than 0.44 percent.

Different from the plate specimens, the curve for the shell specimens with an R/t ratio of 12 shows an initially larger contribution of shear reinforcement to the punching shear strength of the shells, with a mean rate of increase in punching shear capacity of $1.9\sqrt{f'_c}$ for every 0.1 percent increase of shear reinforcement up to 0.24 percent. The rate of increase in punching shear strength in these shells, however, decreased significantly as the shear reinforcement ratio increased from 0.24 percent to 0.48 percent. This decrease, coupled with the fact that not all the shear bars bridging the cracks in specimens AS7 and AS11 failed when failure occurred, is consistent with the explanation given for the failure mechanism of the shells. That is complete failures in the shells were controlled by crushing of concrete in the compression zone. Since not all the shear bars in specimen with 0.24 percent of shear

reinforcement failed at ultimate, the effective level of shear reinforcement for shells with R/t ratio of 12 must be smaller than 0.24 percent. This effective level of shear reinforcement can be considered as the optimum level beyond which the contribution of shear reinforcement in punching shear strength is no longer significant.

For the shells with R/t ratio of 6, only two data points were obtained as shown in Figure II.64. However, if a linear relationship can be assumed between these two data points, then the rate of increase in punching shear strength with increasing shear reinforcement ratio in these shells is almost equal to the rate obtained for the plate specimens ($1.2\sqrt{f'_c}$ to compare with $1.3\sqrt{f'_c}$ in the plates). As in shells with R/t ratio of 12, the shear reinforcement ratio of 0.24 percent in these shells also exceeds the optimum level since some of the shear bars bridging the cracks in specimen AS12 did not fail at ultimate.

II.4.3 EFFECT OF CURVATURE

The normalized shear strengths of four sets of data are plotted against the inverse of R/t ratios as shown in Figure II.65 to facilitate examination of effects of shell curvature on punching shear strength. The four curves shown in Figure II.65 correspond to data obtained from specimens with: (1) no shear reinforcement (FP2's, AS9, and AS8), (2) 0.22 and 0.24 percent of shear reinforcement (FP3, AS7 and AS12), (3) 0.44 and 0.48 percent of shear reinforcement (FP4 and AS11), and (4) 0.22 and 0.24 percent of shear reinforcement and a prestress of 500 psi (FP5 and AS10).

In general, the curves that correspond to the cases of 0 and 0.44 percent of shear reinforcement show a consistent increase of $5\sqrt{f'_c}$ in punching shear strength as the curvature (t/R ratio) increases from 0 to 0.0833 (R/t of 12). Within this range of curvature, however, the curve

for specimens with prestress shows a lesser increase of approximately $4\sqrt{f'_c}$ and the curve for 0.22 percent of shear reinforcement shows a larger increase in punching shear strength of $6.7\sqrt{f'_c}$. This inconsistency appears to be caused by the high normalized shear strength obtained for specimen AS7.

Examination of curves corresponding to 0 and 0.22 percent of shear reinforcement revealed that higher punching shear strength can be achieved by increasing curvature of the specimens. However, the rate of increase in punching shear strength appears to decrease as the curvature increases. Further, in one of the shell specimens with larger curvature, specimen AS8, a somewhat different crack pattern was observed. Lines of cracks developed on top and bottom of this specimen, parallel to the lines of supports. This appears to be the result of a combined in-plane compression and bending action. This development, which occurred only in AS8, coupled with the observation that the rate of increase in punching shear strength decreases with increasing curvature, suggests that further increase of shell curvature beyond the R/t ratio of 6 would result in different mode of failure in the shell and no significant benefit in terms of shear strength could be achieved.

II.4.4 EFFECT OF SPAN CONTINUITY

The effect of span continuity is examined by comparing test results of the single span plate specimen FP1 and its three-span counterpart FP3. The single span plate specimen FP1 had a normalized punching shear strength that was approximately 20 percent higher than that of specimen FP3. This is due to the greater flexibility in the span direction of FP1. As explained in chapter II.2, the greater flexibility in the span direction allowed FP1 to deform more with load. This deformation helped reduce the stress in the shear reinforcement bridging the cracks. Higher

load was therefore required to fail the shear reinforcement in this specimen in order to achieve complete failure, resulting in a higher punching shear capacity.

From this comparison, it is apparent that the relative stiffness in a specimen has an important influence on its shear carrying capability and the results obtained from the single span specimen must be considered as being unconservative when applied to the real multi-span structures.

II.4.5 EFFECT OF PRESTRESSING

Prestressing achieved little in improving the punching shear capacity of the specimens in this test program. Three comparisons were made regarding the effects of prestressing: (1) effect of one-way prestressing in plates, specimens FP3 and FP5, (2) effect of two-way prestressing in plates, specimens FP3 and FP6, and (3) effect of one-way prestressing in shells, specimens AS7 and AS10.

The test results in Table II.4, show that the initial cracking loads for specimens with and without prestressing were nearly the same. This indicates that the concrete shear cracking load was not affected by the 500 psi prestress. In terms of punching shear capacity, one-way prestressing resulted in an increase in strength of approximately 9 percent and two-way prestressing resulted in an increase of approximately 19 percent in the plate specimens. However, one-way prestressing in shells resulted in a 14 percent less in punching shear strength.

Examination of the crack patterns on the cross-sections of the prestressed specimens revealed the influence of the tendon ducts on the orientation of shear cracks. The angle of cracks in the direction parallel to the direction of prestressing was steeper than the crack angle in the other direction. The primary shear cracks in all cases intersected the post-tensioning ducts.

II.4.6 EFFECT OF SIZE OF LOADED AREA

The normalized shear strengths of four plate specimens, FP2-1, FP2-2, IFP2-1, and IFP2-2, were plotted against the area of loading to facilitate the examination of the influence of size of loaded area on punching shear strength, as shown on Figure II.66. It can be seen that the normalized shear strength decreased with increasing area of loading. This is probably due to the complex interaction between beam shear and punching shear in the two initial plate specimens, IFP2-1 and IFP2-2, which resulted in lower normalized shear strengths in these two specimens.

II.5 COMPARISON OF TEST RESULTS WITH ACI PREDICTIONS

II.5.1 INTRODUCTION

The applicability of the ACI code provisions for punching shear on high-strength lightweight concrete structures is examined in this chapter. To facilitate comparison of the test results and the ACI predictions, key provisions for punching shear of the ACI 318-83 building code are summarized. Discussions regarding its limitations are given in the following section.

II.5.2 SUMMARY OF THE ACI PROVISIONS FOR PUNCHING SHEAR

A summary of the ACI 318-83 provisions for punching shear is given in Table II.5. Discussed here are the important clauses concerning the treatment of punching shear in reinforced and unreinforced concrete structures that are considered relevant to this study:

1. The ACI 318-83 building code regards the nominal shear strength V_n of reinforced concrete structures as the sum of two independent quantities, the shear strength provided by the concrete V_c, and the shear strength provided by the shear reinforcement V_s. Such treatment ignores the interaction between the concrete and the shear reinforcement. This interaction is evidenced by the restraining action of the shear reinforcement to growth of inclined cracking. This action leads to larger interface shear transfer capability along cracked surfaces, and ultimately to higher shear strengths.
2. The concrete shear strength component V_c is not to exceed $2\sqrt{f'_c}$ for concrete with shear reinforcement, and $4\sqrt{f'_c}$ for concrete without shear reinforcement. The strength of the reinforcement, V_s, is computed by summing the force in the shear reinforcement

crossing a 45° failure surface defined by the ACI code. This provision in effect limits the concrete strength in slabs with shear reinforcemnt to half that of the concrete strength in slabs without shear reinforcment. Further, the code also specifies an upper limit of $6\sqrt{f'_c}$ on the nominal punching shear strength of all reinforced slabs, regardless of the amount of shear reinforcement.

3. The benefit of the curvature-induced membrane compression that exists in curved members is not yet recognized by the code.

II.5.3 COMPARISON WITH ACI 318-83

The component shear strengths, V_c and V_s, and the predicted nominal shear strength V_n, of the specimens in this test program using the ACI code provisions are given in Table II.6. To facilitate an examination of the ACI predictions, the code-specified upper limits of V_n are plotted with the measured normalized shear strengths of specimens against the shear reinforcement index as shown in Figure II.67. The predicted concrete strength component V_c is multiplied by a strength reduction factor of 0.85 to account for sand-lightweight concrete.

The thickened line in Figure II.67 represents the upper limit of normalized shear strength V_n allowed by the code for reinforced and unreinforced slabs. By placing the an upper limit of $6\sqrt{f'_c}$ on the nominal shear strength of reinforced slabs, the code neglects any benefit from the additional shear reinforcement when the shear reinforcement ratio exceeds an effective level. For the specimens in this test program, the effective level of shear reinforcement is corresponded to a shear reinforcing index of 393 psi (or a shear reinforcing ratio of 0.75 percent). Since the largest amount of shear reinforcement tested

was 0.44 percent in the plate specimens (corresponding to a reinforcing index of 228 psi), and the shear strength of the plates increased linearly with increasing shear reinforcing index within the range examined, it is difficult to make a conclusive statement regarding the effective level of shear reinforcement implied by the code for reinforced slabs. More tests on plate with larger shear reinforcing index may be needed to further examine this code-implied upper limit.

It is apparent from Figure II.67 that the code predictions are very conservative for the specimens of this test program, especially for those with shear reinforcement. This conservatism is due the limit of $2\sqrt{f'_c}$ imposed on V_c of slabs with shear reinforcement. By reducing the contribution of V_c from $4\sqrt{f'_c}$ to $2\sqrt{f'_c}$ when shear reinforcement is included, the code does not recognize any contribution of shear reinforcement unless a minimum amount of shear reinforcement is provided. For these specimens, this minimum amount is 0.31 percent (corresponding to a shear reinforcing index of 160 psi). In contrast, the test results for the plate specimens show that even with a modest increase of shear reinforcing index (less than 160 psi), the benefit in terms of increasing the punching shear strength can clearly be observed.

The conservativeness of the code can be quantitatively examined by comparing the measured component shear strengths and the component shear strengths predicted by the code.

The measured shear strengths of specimens in this test program, denoted as V_{test}, were divided into two components V_c and V_s. V_c was determined as the measured punching shear strength of the unreinforced specimen, and V_s was computed as the difference between V_{test} and V_c. There are three reasons that led to this treatment. Firstly, since more than one shear crack developed on the cross-sections of all specimens and

because the failure surfaces were not exactly conical, the area of the failure surfaces could not be accurately computed. Therefore the total amount of shear reinforcement on the failure surface of a specimen could not be reliably determined. Second, it was observed that an undetermined amount of shear reinforcement in the shells did not yield at ultimate. This makes it more difficult to estimate the exact amount of shear reinforcement activated at failure. Third, such treatment ignored the interaction between the shear reinforcement and the concrete, making comparisons of experimental results and the ACI predictions more appropriate since similar treatment was used by the code.

The measured component shear strengths of the test specimens are listed in Table II.7. Listed also in Table II.7 are the ratios of the measured to code-predicted component shear strengths, and ratios of the measured shear strength V_{test} to shear strengths predicted by ACI V_n. Several conclusions were drawn by examining these ratios:

1. In reinforced and unreinforced slabs, the ratios V_c/V_{cACI} and V_s/V_{sACI} show that the code was more conservative in predicting the concrete shear strength V_c than in predicting the shear strength provided by the shear reinforcement. This is the direct result of the minimum shear reinforcement requirement implied in the provision for concrete shear strength of reinforced slab. For the unreinforced slabs (specimens FP2-1 and FP2-2), V_c/V_{cACI} was equal to 1.5. However, this ratio doubled ($V_c/V_{cACI} = 3.0$) when shear reinforcement was present. The ratio V_s/V_{sACI} for slabs with shear reinforcement showed that the code underestimated the strength provided by the shear reinforcement by a factor of approximately 2.1 (FP3 and FP4). This was 30 percent less conservative than the prediction for

concrete strength V_c. However, when the effects of prestressing and single span were accounted for, the V_s/V_{sACI} ratio increased to 2.7.

2. The code predictions for concrete strength were even more conservative for the shells. This conservatisn was due to the fact that there is no provision in the code which recognizes the benefit of the curvature-induced membrane compression. In unreinforced shells, the concrete strength components V_c of specimens with R/t ratio of 12 were underestimated by ACI by a factor of 3.0. This factor increased to 3.6 when the curvature of the shell was doubled (R/t of 6). In reinforced shells, a mean V_c/V_{cACI} ratio of 5.9 was obtained for shells with R/t of 12, and a ratio of 7.1 was obtained for shells with R/t of 6. By comparing the rate of increase of these ratios with respect to increasing curvature, it is apparent that the code became less conservative with increasing curvature. An average V_s/V_{sACI} ratio of 2.3 was obtained for all shell specimens with shear reinforcement. This ratio was slightly smaller than that of the plates (2.7), which reflects the fact that not all the shear reinforcement crossing the crack in the shell specimens yielded at ultimate.

3. The underestimation of the contribution of shear reinforcement to the punching shear strength by ACI can be attributed to the assumption by ACI that shear cracks are at a 45^o angle with the horizontal plane and to the disregard of the influence the shear reinforcement might have on the growth of inclined cracking. The presence of a shear reinforcement across the crack results in larger interface shear transfer capacity, which ultimately

enhances the shear strength. In addition, it was observed from the cross-sections of the specimens that the crack angles on the failure surface in all cases were flatter than 45°. This means that more shear reinforcement had been activated to resist the applied shear stress than the amount recognized by ACI.

4. The ratio V_{test}/V_{nACI} was 1.5 for unreinforced plates, 3.0 for unreinforced shells with R/t of 12, and 3.6 for unreinforced shells with R/t of 6. For specimens with shear reinforcement, this ratio is 2.8 for plates, 4.1 for shells with R/t of 12, and 4.2 for shells with R/t of 6.

II.5.4 SUMMARY

Quantitative comparisons of the experimentally-obtained normalized shear strengths and the ACI predictions are provided in this chapter. In most cases, the code was more conservative in predicting the shear strength provided by the concrete (V_c) than the strength provided by the shear reinforcement (V_s). The conservatism of the code is amplified by the provision which implied a minimum effective ratio of shear reinforcement (0.31 percent) for reinforced slabs. The lack of consideration for the contribution of membrane action in the code resulted in more conservative estimates for curved specimens. Finally, the assumption of a 45° angle shear crack and the disregard of the ability of crack to transfer shear, especially when shear reinforcement is present, were identified as the reasons for the underestimations of shear strength provided by the shear reinforcement.

II.6 SUMMARY AND CONCLUSIONS OF THE EXPERIMENTAL PROGRAM

II.6.1 SUMMARY

A total of fifteen specimens, nine flat plates and six arched shells, were tested to study the punching shear behavior of lightweight concrete plates and shells. Two distinct modes of punching shear failure resulted in the plates and the shells. In the plates, failure was due to the failure of all three basic shear resistance mechanisms and very little evidence of membrane compression was observed. In the shells, the presence of membrane compression associated with the curvature of the shell resulted in a mode of failure similar to the shear-compression mode in deep beams. Final collapse in the shells was controlled the crushing failure of concrete in the compression zone.

For all specimens, substantial empirical evidence indicated that internal shear cracking developed first in the mid-depth region of the specimens. The redistribution of flexural strain in specimens not reinforced in shear was more extensive than that in specimens with shear reinforcement, indicating the influence of shear reinforcement in restraining growth of inclined shear cracks. Visual observation made during tests of shell specimens indicated a brittle mode of failure in the shells. However, empirical evidence indicated that cracks developed gradually in these specimens.

II.6.2 CONCLUSIONS

The following conclusions regarding the ACI code provisions for punching shear and the effects of major variables studied in this program were drawn from the test results:

1. The ACI code provisions are very conservative with respect to the results obtained from this test program. Further, the code

is more conservative in predicting the shear strength of concrete than in predicting the shear strength provided by the shear reinforcement. Underestimation of shear strength provided by the concrete is amplified by the reduction of V_c by half when shear reinforcement is included. This reduction implies that the code does not recognize the contribution of shear reinforcement until a minimum amount is provided, corresponding to 0.31 percent in this test program. In contrast, test results showed that significant increases in shear strength can be achieved even with a modest increase of shear reinforcement. Underestimation of V_s was due to the steeper crack angle assumed by the code (45^o) and the disregard of the concrete-shear reinforcement interaction.

2. Within the range of shear reinforcing ratios examined in this test program (0 to 0.48 percent), any increase in the amount of shear reinforcement will result in a proportional increase in punching shear capacity of the plates. In the shells, the rate of increase in punching shear strength decreases with increasing amount of shear reinforcement.

3. The upper limit of shear strength imposed by the code ($6\sqrt{f'_c}$) is not particularly meaningful with respect to this study, since all specimens with shear reinforcement displayed much higher punching shear capacities.

4. Punching shear strength is greatly enhanced when membrane compression due to curvature is present. However, the rate of increase in punching shear strength due to membrane compression decreases with increasing curvature. The presence of curvature in the specimens resulted in a failure mode controlled by the

crushing failure of concrete in the compression zone, without complete yielding of the shear reinforcement on the failure surface.

5. Failures in the shells appeared to be very sudden. However, substantial empirical evidence suggested that the processes of crack development in the shells were gradual.

6. Internal shear cracking initiated first in the mid-depth region of the specimens.

7. Prestressing with 500 psi achieved very little in terms of improving the punching shear capacity of the specimens in this testing program.

III.1 RELEVANT STUDIES IN INTERFACE SHEAR TRANSFER

III.1.1 INTRODUCTION

This chapter reviews both experimental and analytical studies related to the ability of cracks to transfer shear force in cracked concrete. These studies provide not only qualitative knowledge on the nonlinear behavior of cracked concrete but also a quantitative assessment of this nonlinearity. Information obtained from these studies will be used in chapter III.2 for the development of a general material model for cracked concrete that can be incorporated by the finite element method.

III.1.2 EXPERIMENTAL STUDIES ON INTERFACE SHEAR TRANSFER

In general, the transmission of shear forces across a crack in reinforced concrete is achieved through three related shear transfer mechanisms, namely the interface shear transfer (IST) mechanism, the dowel action, and the axial restraint provided by the steel reinforcement crossing the crack. These mechanisms have been the subject of experimental investigation by many researchers in the last several years. In most of these experimental investigations, the specimens have been of push-off type. Each specimen would be cast solid and then split in halves along a predetermined plane to produce a natural crack plane between the two halves. Direct shear loads would be applied parallel to the crack plane to produce the relative displacements of the two concrete blocks.

One of the early direct shear test programs to study IST was conducted by Paulay and Loeber [III.1] on unreinforced concrete specimens. All specimens had the same area of crack plane of 33.7 in^2 (217 cm^2) and mean cube compressive strength at testing of 5300 psi (37

N/mm^2). In the majority of the tests, the crack width of the specimen was kept constant during testing. The main objective was to study the effects of crack width, aggregate shape and size on the interface shear shear stiffness (through the shear stress-slip relationships). Three nominal crack widths of 0.005 in, 0.01 in and 0.02 in (0.13, 0.25 and 0.51 mm, respectively) and three types of coarse aggregates, being 3/8 in (9.5 mm) and 3/4 in (19 mm) round maximum size and 3/4 in (19 mm) crushed maximum size, were examined. Direct shear loads were applied incrementally in the direction parallel to the crack plane. The test frame was designed such that the crack width could be adjusted to within 2% of the specified value before each load increment. Since constant crack width was maintained in these tests, the restraint condition in the direction normal to the crack plane can be considered as being infinitely stiff.

The results of this study were presented in the form of shear stress-shear slip relationships and are shown in Figure III.1. The authors concluded that, within the shear stress range of approximately 100 psi to 1000 psi, the crack width is approximately inversely proportional to the interface shear stiffness of the crack (or proportional to the shear slip), and that neither the shape nor size of aggregate particles affect the shear stress-slip relationship.

Houde and Mirza [III.2] also conducted direct shear tests with constant crack width to develop a force-displacement relationship in cracked concrete. The primary purpose of this investigation was to study the effects of crack width, concrete compressive strength, and aggregate size on the crack shear stiffness. The area of shear plane used in this test program was 16 in^2 (103 cm^2), approximately half as large as that used by Paulay and Loeber. Four crack widths ranging from 0.005 in to

0.02 in and three concrete compressive strengths ranging from 2370 psi to 7390 psi were specified.

The results of Houde and Mirza's tests were presented using the same format as Loeber and Paulay's to facilitate comparison (see Figure III.2). The authors concluded that within certain limits of shear displacements (the upper limit was determined as 40 to 65% of the crack width), the relationship between applied shear stress and shear displacement for a given crack width is linear. However, different from Paulay and Loeber who observed an approximately linear relationship between the crack shear stiffness and the inverse of crack width, Houde and Mirza found a nonlinear relationship between these two quantities as shown in Figure III.3. In addition, the authors concluded that an increase in concrete compressive strength would result in an increase of crack shear stiffness (Figure III.4).

Tests with constant crack width conducted by Loeber, Houde and other researchers have provided both qualitative and quantitative measures of the shear deformability of the crack surfaces. However, these tests did not realistically represent the true behavior of cracked concrete in practical situations since the crack width was kept constant throughout the loading process (which is equivalent to imposing an infinitely stiff constraint condition in the direction normal to the crack plane). In practical situations, due to the rough nature of the crack surface, it is more likely that the relative shear displacement (or shear slip) of the two opposing crack faces will be always accompanied by their relative normal displacement. Indeed, in all the direct shear tests with constant crack width reviewed so far, the crack width increased with increasing shear displacement (or increasing shear load) and had to be readjusted to the initially specified width after every load increment. This

dilitant nature of crack in reinforced concrete affects the state of stress in the reinforcement crossing the crack as the reinforcement is subjected to additional shear and axial stresses caused by further crack opening.

The internal relationships between the normal and tangential crack displacements and the normal and shear stresses, which characterize the natural behavior of cracks, have been studied by many researchers who conducted direct shear tests with constant normal restraining stiffness that allowed the crack width to continuously increase as the shear load was applied. Either external bars with known extensional stiffness or steel reinforcement was used to provide restraint in the direction normal to the crack plane. Among the most comprehensive experimental studies are works conducted by Laible [III.3], White [III.4] and Walraven [III.5].

Laible [III.3] performed direct shear tests with constant normal restraining stiffness on a total of thirty precracked specimens. Two areas of shear plane of 150 in^2 and 300 in^2 were considered. Cyclic loading was applied and each specimen was subjected to 15 cycles of loading. The majority of tests were cycled at a shear stress value of 180 psi. The initial crack width ranged from 0.01 in to 0.03 in. The study was confined to only the IST mechanism as the other shear transfer mechanisms were excluded. The clamping stiffness of the reinforcement was represented by placing external restraining bars in the direction normal to the crack plane.

Laible observed that during the initial cycle of loading, crack width, slip, and the resulting forces in the restraining bars increased at a slightly increasing rate whereas in the successive cycles, crack width and the bar forces increased at a decreasing rate. Degradation of

interface shear stiffness was also found with successive cycling. For a given cycle, the unloading stiffness was found to be larger than the loading stiffness and residual shear slip was observed in the unloading process of every specimen even when the shear stress was completely reduced to zero. Typical shear stress-slip relationships obtained from this program are shown in Figure III.5, which showed an approximately linear relationship between applied shear stress and slip in the first loading cycle within the stress range of 0 to 180 psi.

Based on this observation, Laible suggested two essential modes of shear resistance which make up the interface shear transfer mechanism, the bearing of adjacent pieces of aggregate and mortar and the friction due to the normal restraining forces. The bearing mode, which depended largely on the crack width, essentially occurred during the initial cycle of loading when the crack width was still small and the major actions were those of crushing of concrete and degradation of the local roughness of the crack surfaces. The deterioration of the local roughness on the crack surface after the first loading cycle resulted in larger shear slip in the subsequent cycle even though the shear stress was not increased. As cycling continued, overriding of the two opposing crack surfaces would widen the crack width, thus resulting in an increase in the normal restraining force, and consequently an increase of frictional resistance. This resistance was identified by Laible as the frictional mode of the IST mechanism and was found to be the dominant mode of shear resistance in cracked concrete when the crack width was large. The bearing mode would predominate in the initial stage during which the crack width was smaller.

Jimenez-Peres, White and Gergely [III.4] conducted a direct shear test program on block-type concrete specimens with area of shear plane

as large as those used in Laible tests (225 in^2). The large area of shear plane was used to eliminate possible size effects. The specimens were reinforced by conventional steel reinforcement with sizes ranging from #7 to #14 and were subjected to fully reversing cyclic shear stresses of approximately 200 psi. Cracks were formed by axially stressing the embedded reinforcing bars and the extensional stiffness of the bars was determined by applying the axial loads incrementally and measuring the corresponding crack widths. The stresses in the bars were then adjusted until the desired initial crack width was achieved. Two test series were conducted. The first series consisted of 8 specimens with reinforcement ratios ranging from 0.0107 to 0.02 percent. The purpose of this series of tests was to study the shear transfer by the combined action of IST and dowel action. The second series of tests consisted of 5 specimens and was conducted to study shear transfer by dowel action alone. The IST mechanism was studied by contrasting the results of these two test series.

In the first test series, all specimens had initial crack widths of 0.015 in to 0.02 in, except for one specimen with an initial crack width of 0.01 in. Typical results of this test series are presented in Figure III.6. Similar to observations made from Laible's tests, the first cycle shear stress-shear slip relationship for positive loading of the specimens in this test series could be approximated as being linear. For the subsequent cycles, an initially soft response was observed between the shear stress range of 0 to 50 psi. After this stress level was exceeded, the shear stiffness could be approximated by a linear function. Also, within a load cycle, the unloading stiffness was always larger than the loading stiffness and residual shear slip was observed during the unloading process in all specimens. Furthermore, the shear stiffness of

the first cycle was found to increase with increasing steel ratio at the shear plane, and for a given steel ratio with decreasing crack width. The rate of increase in either crack width or shear displacement with cycling was larger for specimens with the lower reinforcement ratios. The authors suggested that increasing the reinforcement ratio on the crack plane would result in larger axial and dowel stiffness that would restrict the rate of increase of the shear and normal displacements. The authors found a negligible increase of crack width as the shear load was increased, probably due to the large normal restraining stiffness provided by reinforcing bars crossing the crack plane. Finally, the shear slip obtained in these combined action tests was found to be less than that obtained from Laible's tests, indicating the contribution of dowel action in resisting shear deformation.

In the dowel action test series, 5 specimens reinforced either by 4 #9 or 2 #14 bars were tested. All but one specimen were axially stressed to approximately 30 Ksi/bar and subsequently subjected to cyclic shear stresses up to the occurrence of failure. From this test series, the authors concluded that the size of the reinforcing bars and the tensile stress in the bars have an effect on the shear stiffness of the crack. The use of lesser numbers of larger size bars may result in smaller dowel stiffness due to the larger concrete deterioration caused by the stiffer bars as they transfer the dowel forces to the concrete. Further deterioration of concrete surrounding the bars, which also leads to smaller dowel stiffness, would result if large tensile stress is applied to the bars.

The results of the above mentioned tests clearly indicated that the shear dilatancy in a crack, which can be represented by the relationship between the crack width and shear slip, is influenced by the normal

restraining stiffness. This influence is further explored by Walraven [III.5].

Walraven [III.5] conducted direct shear tests on a total of 83 push-off type specimens. All specimens had the same area of shear plane of 55.8 in^2 (360 cm^2). The specimens were divided into two groups. The first group included specimens externally restrained in the normal direction. The second group included specimens with embedded reinforcement. The specimens were placed on roller bearings and shear load was applied on top by a knife hinge (see Figure III.7) so that the shear plane would be subjected only to shear stress. Load was applied monotonically and tests were stopped when the shear slip had reached a value of approximately 0.08 in (2 mm). Prior to testing, the specimens were cracked along the predetermined shear plane by splitting forces in the grooves on their front and rear faces and the cracked width was measured so that the desired crack width could be achieved.

In tests with externally restraint bars, different initial crack widths ranging from 0 to 0.016 in (0 to 0.4 mm), in combination with different normal restraining stiffnesses and concrete compressive strengths, were considered. These tests were conducted to study the influences on crack behavior by such factors as the initial crack width, the concrete compressive strength, and the normal restraint stiffness. The advantage of these tests is that the normal stresses acting on the crack plane could be measured directly on the restraint bars. The test results of this series are shown in Figures III.8, 9 and 10. Figure III.8 shows the averaged shear stress as a function of shear slip, Figure III.9 shows the relation between crack width and shear slip, and Figure III.10 shows the normal restraint stress as a function of crack width. Increasing the initial crack width resulted in larger shear displacement

at the same shear stress level and a larger crack width at constant normal stress. Also the crack opening path, which characterizes the shear dilatancy, was influenced by the normal restraint stiffness. A small difference in restraint stiffness would lead to another crack opening path.

The typical results of tests with embedded bars are shown in Figure III.11. Reinforcing bars with diameters ranging from 0.236 to 0.63 in (6 to 16 mm) in the form of closed stirrups were embedded in the specimens in this test series. Reinforcement ratios selected for study were varied between 0.56 and 2.24 percent. The initial crack widths in this test series were controlled to be smaller than 0.0016 in (0.04 mm). The normal stress acting across the crack plane could not be measured for this test series. The experimental results showed that the crack opening path, i.e. the crack width-shear slip relationship, was not significantly influenced by the reinforcement ratio. This is contrary to the results obtained from tests with external restraint, which found that the crack opening path was sensitive to the change of normal restraining stiffness. The shear strength, however, increased with increasing reinforcement ratio.

In summary, the shear deformability of rough crack surfaces and factors affecting the ability of cracks to transfer shear have been quantitatively investigated by examining various direct shear test programs. The ability of cracks to transfer shear diminishes with increasing crack width and decreasing concrete compressive strength. Cycling was found to cause degradation of interface shear stiffness which also reduces the ability of cracks to transfer shear force. In most of these tests, and more specifically in Walraven's tests, the dependency

of the crack opening path upon the amount of external restraint could be clearly observed.

III.1.3 ANALYTICAL STUDIES RELATED TO INTERFACE SHEAR TRANSFER

Over the years, efforts have been made by many researchers to represent cracks and the subsequent transfer of shear forces in mathematical models that can be implemented by the finite element techniques. In representing cracks, two general approaches have been developed: the discrete crack approach and the smeared crack approach.

The discrete crack approach has the advantage of being able to offer realistic representation of cracks in concrete; that is, a crack represented by a discontinuity in the strain field. This approach was first introduced by Ngo and Scordelis [III.6] who used a predefined crack pattern to study bond stresses and stresses in concrete and in the reinforcing steel for a particular crack pattern. Cracks were modelled by seperating the nodal points in the finite elements. This model was later refined by Ngo, Scordelis and Franklin [III.7] to include the effect of interface shear transfer. The IST mechanism was simulated in this study by placing a special linkage element with known stiffness across the crack.

Instead of having to preselect a crack pattern, which is unrealistic, Nilson [III.8] modified this approach to allow the model to generate the locations of cracks by separating the nodal points between two adjacent elements once the averaged stress in these elements exceeds the tensile strength of concrete. The accuracy of this procedure, however, is mesh dependent as large element size would cause overestimation of crack length.

Mufti et al [III.9] and later, Al-Mahaidi [III.10] further refined the finite element method of representing discrete cracks by defining

either two or four nodes at a single nodal point, connected by stiff linkage elements until cracking occurs. The stiffness of the linkage element was varied as a measure to account for interface shear transfer.

The problems with representing cracks using the discrete crack appoach are the constant change of the finite element topology associating with the development of cracks and the fact that crack propagation is constrained by the placement of element boundaries. These problems were solved by Saouma and Ingraffea [III.11] by employing automatic mesh regeneration and bandwidth minimization methods. In their study, linear elastic fracture mechanics principles were used to govern the mixed-mode crack propagation (opening and shearing modes). The interface shear transfer problem was treated using a simplified model that allows the shear modulus G of the crack element to be reduced by a shear retention factor β. The authors recognized that the shear retention factor β should be inversely proportional to the crack width, and therefore took advantage of the discrete nature of crack to directly compute the crack opening, and evaluate the shear stiffness along the crack using the empirical equation derived by Fenwick and Paulay [III.12].

The "βG" method has also been used to account for interface shear transfer in the smeared crack approach. In this approach, a crack is assumed to contain many parallel microcracks and local discontinuities due to cracking are modelled as being distributed over some tributary area within the finite element, the material model for cracked concrete thus can be derived in terms of stress-strain relations. One of the earliest attempts to incorporate the βG model in the smeared crack approach is the study conducted by Hand, Pecknold and Schnobrich [III.13], who introduced a layered finite element procedure for

determining the load-deflection history of reinforced concrete plates and shells up to failure. In this study, the shear retention factor was assumed to be constant ($\beta = 0.4$), the reinforcing steel was considered to be elastic-plastic material and the concrete was considered to be isotropic bilinear elastic-perfectly plastic material with a limited tensile strength. The stress-strain relation for concrete with a crack oriented at an angle with respect to the reference coordinate system is presented as:

$$\{ \sigma \} = [D] \{ \epsilon \} \qquad \text{(III.1.1)}$$

Where $\{ \sigma \}^T = [\sigma_x, \sigma_y, \tau_{xy}]$

$\{ \epsilon \}^T = [\epsilon_x, \epsilon_y, \gamma_{xy}]$

And
$$[D] = [T]^{-1} \begin{vmatrix} E & 0 & 0 \\ 0 & 0 & 0 \\ 0 & 0 & \dfrac{\beta E}{2(1+\nu)} \end{vmatrix} [T]^{-T}$$

T is the transformation matrix from the rotated coordinate system to the reference system and $^{-T}$ indicates the inverse transformed.

In a similar study, Suidan and Schnobrich [III.14] used the same approach of introducing the constant shear retention factor β into the material property matrix of a three-dimensional isoparametric cracked concrete element in order to account for interface shear transfer. The steel reinforcement was in effect smeared out throughout the element thus enabled the incorporation of orthotropic reinforcement into the "cracked reinforced concrete" material matrix.

The "βG" approach, however, does not provide an accurate treatment for the interface shear transfer problem since it implies that the shear stiffness of cracked concrete is independent of the crack width, which is contrary to experimental results. To account for this, many researchers like Al-Mahaidi [III.10], Ingraffea [III.11] and Buyukozturk [III.15] have proposed models in which β is a function of crack width. Buyukozturk proposed that the IST stiffness, K_{cr}, be inversely related to the crack width, w_o.

$$K_{cr} = (1/\beta)K_n + K_d \qquad \text{(III.1.2)}$$

where K_n is the extensional crack stiffness due to reinforcement,

K_d is the dowel stiffness, and

$\beta = 6.24\ w_o$ or $\beta = w_o^{1.637}$

The "βG" approach can also be extended to include cracks in multiple, nonorthogonal directions by using the concept of seperating crack strain and concrete strain after the method of De Borst and Nauta [III.16]. The relationship between the incremental stress and the incremental strain in the cracked concrete can be written as follows:

$$d\sigma = \left\{ D_{co} - D_{co}\, N\, [D_{cr} + N^T\, D_{co}\, N]^{-1}\, N^T\, D_{co} \right\} d\epsilon \qquad \text{(III.1.3)}$$

where D_{co} is the material matrix of uncracked concrete,

D_{cr} is the material matrix of cracks, relating cracked stresses to "smeared" crack strains.

N is the transformation matrix.

It should be noted that as long as the constitutive matrices D_{co} and D_{cr} remain symmetric, the stress-strain matrix relating the incremental

stress and the incremental strain in the cracked concrete also remains symmetric.

Representing the interface shear stiffness as a function of the crack width certainly results in better treatment of the interface shear transfer problem. However, even after this modification, such an approach is still inadequate since it does not account for the frictional nature or the shear dilatancy problem of IST. This fact is likely to be important for transverse shear problems since in combined bending and shear, the area below the neutral axis will have limited shear capacity because the ability of the reinforcement to induce normal compressive stress across the crack will be reduced by flexure.

The poor representation of the frictional aspect of IST is due to the lack of off-diagonal terms in the crack rigidity matrix. This was recognized by Bazant and Gambarova [III.17] who approached the shear dilatancy problem by introducing a stress-displacement relation in which the off-diagonal terms of the crack stiffness matrix are non-zero.

$$\begin{Bmatrix} d\sigma_{nn}{}^{cr} \\ d\sigma_{nt}{}^{cr} \end{Bmatrix} - \begin{vmatrix} B_{nn} & B_{nt} \\ B_{nt} & B_{tt} \end{vmatrix} \begin{Bmatrix} d\delta_n \\ d\delta_t \end{Bmatrix} \qquad \text{(III.1.4)}$$

In this study, cracks were assumed to be composed of many equally spaced, parallel microcracks and the reinforcing bars were assumed to be sufficiently densely distributed and carry only axial forces. Dowel action across the crack and bar kinking were neglected. The coefficients B_{nn}, B_{nt} and B_{tt} of the crack stiffness matrix were determined by employing an empirical stress-displacement relation. This relation was obtained by optimizing the fits of Paulay and Loeber's experimental data [III.1]. The total strain $d\epsilon$ was decomposed into two components, the

strain in the crack $d\epsilon^{cr}$ and the strain in the solid concrete between the cracks $d\epsilon^{sc}$.

$$d\epsilon = d\epsilon^{cr} + d\epsilon^{sc} \qquad \text{(III.1.5)}$$

where $d_\epsilon{}^{cr}$ is the crack strain.

$d_\epsilon{}^{sc}$ is the strain in the solid concrete between cracks.

The averaged strains due to smeared cracks are related to crack displacements by:

$$\epsilon_{nn}{}^{cr} = \frac{\delta_{nn}}{s}, \qquad \gamma_{nt}{}^{cr} = 2\,\epsilon_{nt}{}^{cr} = \frac{\delta_{nt}}{s} \qquad \text{(III.1.6)}$$

where s is the averaged crack spacing.

Strains due to a crack may then be related to the stresses by inverting the relationship between the incremental stresses and the crack strains, yielding a relationship of the form:

$$\begin{Bmatrix} d\epsilon_{nn}{}^{cr} \\ d\epsilon_{tt}{}^{cr} \\ d\gamma_{nt}{}^{cr} \end{Bmatrix} = \begin{vmatrix} F_{nn}s^{-1} & 0 & F_{nt}s^{-1} \\ 0 & 0 & 0 \\ F_{tn}s^{-1} & 0 & F_{tt}s^{-1} \end{vmatrix} \begin{Bmatrix} d\sigma_{nn}{}^{cr} \\ d\sigma_{tt}{}^{cr} \\ d\sigma_{nt}{}^{cr} \end{Bmatrix} \qquad \text{(III.1.7)}$$

or, $$\{d\epsilon^{cr}\} = [F^{cr}]\,\{d\sigma^{cr}\} \qquad \text{(III.1.8)}$$

where $[F^{cr}]$ is the flexibility matrix of crack.

Strains in solid concrete between the crack can also be related to stresses in incremental form as:

$$\begin{Bmatrix} d_\epsilon n_n{}^{sc} \\ d\epsilon_{tt}{}^{sc} \\ d\gamma_{nt}{}^{sc} \end{Bmatrix} = \begin{vmatrix} E^{-1} & -\nu E^{-1} & 0 \\ -\nu E^{-1} & E^{-1} & 0 \\ 0 & 0 & G^{-1} \end{vmatrix} \begin{Bmatrix} d\sigma_{nn}{}^{cr} \\ d\sigma_{tt}{}^{cr} \\ d\tau_{nt}{}^{cr} \end{Bmatrix} \qquad \text{(III.1.9)}$$

or, $\{d\epsilon^{sc}\} = [F^{sc}]\ \{d\sigma^{cr}\}$ (III.1.10)

where $[F^{sc}]$ is the flexibility matrix of solid concrete.

Finally, the relationship between stress and total strain in cracked concrete can be obtained by adding the flexibility matrices of the solid concrete and the crack.

$$\{d\epsilon\} = \{d\epsilon^{cr}\} + \{d\epsilon^{sc}\} = [\ F^{cr} + F^{sc}\ ]\ \{d\sigma^{cr}\} \quad \text{(III.1.11)}$$

where $\{d\epsilon\}$ is the total strain in cracked concrete.

A simpler and conceptually more appealing smeared crack model, to compare with the more complicated model presented earlier by Bazant and Gambarova [III.17], was introduced a little later by Bazant and Tsubaki [III.18]. In this model, the interface shear transfer problem was treated by introducing the concepts of the friction coefficient and the dilatancy ratio for crack slip. The methods for handling cracks in multiple nonorthogonal directions as well as the inclusion of reinforcement were also presented in this study. Concrete was assumed to have no tensile strength and to contain one or two systems of straight, parallel, equidistant and continuous cracks. The spacing of the reinforcing bars as well as the spacing of cracks were assumed to be sufficiently dense so that the change of internal forces from one bar to the next or from one crack to the next would be negligible. The averaged strains in cracked concrete and in the reinforcing net was assumed to be the same.

For slipping frictional cracks of one direction, the following friction and dilatancy laws were assumed:

$$\sigma_{nt}^{cr} = -k\,\sigma_{nn}^{cr} + c \quad \text{for} \quad \sigma_{nn}^{cr} \le 0 \quad \text{(frictional slip)} \quad \text{(III.1.12)}$$

$$\delta_n = \alpha_d|\delta_t| + e \quad \text{for} \quad \delta_n \le 0 \quad \text{(dilatancy)} \quad \text{(III.1.13)}$$

In which k is the friction coefficient, c is cohesion, α_d is the dilatancy ratio, and e is expansion or initial dilatancy.

By expressing the total strains of concrete as the sum of crack strains and concrete strains,and by assuming the stresses in concrete between the cracks must be the same as the stresses transmitted across the crack, also by letting s be the mean spacing between parallel cracks, a relationship between the stress in the uncracked concrete and the total strain was obtained:

$$\{ \sigma^{cr} \} = \{ D\epsilon \} + \{f\} \qquad \text{(III.1.14)}$$

where

$$D = E^* \begin{vmatrix} 1 & \nu & \alpha_d \\ \nu & \dfrac{E_c}{E^*} + \nu^2 & \alpha_d \\ k & k\nu & (\alpha_d)(k) \end{vmatrix}; \quad f = \begin{Bmatrix} g_1 E^* \\ g_1 E^* \\ k g_1 E^* \; c \end{Bmatrix}$$

$$(E^*)^{-1} = \frac{1-\nu^2}{E_c} + \frac{1}{G_c}(\alpha_d)(k); \quad g_1 = \frac{1}{G_c}(\alpha_d)(c) - \frac{e}{s}$$

Matrix D represents the stiffness matrix of concrete containing slipping closely spaced parallel cracks. Although it is singular, it is not a problem since the addition of the stiffness due to the reinforcement results in a nonsingular matrix for the composite material.

The authors concluded that by using this concept of secant friction coefficient k and dilatancy ratio α_d, the interface shear transfer problem is more realistically treated as it accounts for friction and dilatancy of the cracks. However, they also acknowledged that accurate material matrix D can only be obtained if realistic values of k and α_d are known. In this study, due to the lack of experimental information, crude estimates of values of k and α_d had to be made for numerical calculation (k=1.7 and α_d=1.0). The inequality of the dilatancy ratio

and the friction coefficient caused the material matrix to be nonsymmetric. This is a significant problem since most solvers are based on symmetric matrices. A further problem is that a D matrix for the cracks cannot be obtained by this approach. Instead the combined D matrix for cracked concrete must be derived by algebraic manipulation. Thus the method devised by de Borst and Nauta [III.16] for multiple cracks cannot be used. Further, only an elastic material matrix for the solid concrete can be used.

III.2 DEVELOPMENT OF THE SOFT-DILATANCY INTERFACE SHEAR TRANSFER MODEL

III.2.1 INTRODUCTION

From the results of the experimental studies on interface shear transfer (IST), it became apparent that the nonlinear, post-cracking behavior of reinforced concrete subjected to transverse shear is caused primarily by the roughness of the cracked concrete surfaces. Such behavior can only be properly characterized by an IST model which correctly represents the friction/dilatancy behavior of interface shear transfer. The problem is more complicated when steel reinforcement is included. The presence of steel reinforcement in cracked concrete would result in an interaction between concrete and steel reinforcement that would increase the shear carrying capacity and the ductility of the concrete structures. This interaction is even more complex in plate and shell structures than in beams. It is still rather difficult to assess the effects of this interaction on the overall behavior of reinforced concrete structures and the current ACI building code still regards the shear strength of reinforced concrete as the sum of two independent quantities, the shear strength provided by concrete V_c and the shear strength provided by shear reinforcement V_s. It is clear that adequate IST and steel models are required for finite element analysis of shear in deep beams or thick plates and shells before this complex interaction can be accurately determined.

In the sections to follow, an explicit relationship between the incremental crack stress and incremental crack strain will be derived using the concepts obtained from the experimental studies reviewed in chapter III.1. A material model for uncracked concrete will be selected,

and then both the material matrices for cracks and for concrete will then be used to develop a general constitutive matrix for reinforced cracked concrete.

III.2.2 BASIC CONCEPTS

The concepts used in developing the analytical IST models in this study are based largely on the results and observations obtained from direct shear tests conducted by Walraven [III.5] and Paulay and Loeber [III.1].

Figures III.12 and III.13 show typical crack opening paths and the combination of shear and normal stresses versus shear slip observed by Walraven. The crack opening path, which characterizes the shear dilatancy, was influenced by different amounts of external restraint stiffness suggesting that if the restraint were reduced to near zero, a "zero restraint" dilatancy law could be obtained. The amount which the crack opening path deviates from the zero restraint dilatancy law would depend on the deformability of the surface roughness on either side of the crack. This deformability logically would be composed both of shear deformability and compressive deformability; that is, if the crack were subjected to shear slip and then subjected to a compressive stress, the 'in contact' crack width would decrease. Both the shear and compressive deformabilities on the cracked surface can be idealized by springs in directions paralell and normal to the cracked plane as shown in Figure III.14. This two spring model can be simplified to a one spring model as shown in Figure III.15 if the compressibility of the surface roughness is ignored. The remaining spring will represent the shear deformability of the surface roughness. The spring constant k_s of the spring that models the shear deformability can be determined using the results of the constant crack width tests such as those performed by Paulay and Loeber.

From Paulay and Loeber's results, which were shown in Figure III.1, the slope of the experimentally determined shear stress versus shear displacement relationship is plotted versus the crack width in Figure III.16. The apparently linear relationship suggests that k_s is inversely proportional to the crack width.

III.2.2.1 Dilatancy Law

The typical crack opening path for the case of zero initial crack width observed by Walraven (see Figure III.12) can be reasonably fit by the following functional relationship, with coefficient A arbitrarily selected (A = 3.2)

$$\delta_t = A(\delta_n)^2 \qquad \text{(III.2.1)}$$

where δ_t and δ_n are the shear slip and the crack width, respectively.

The above expression can then be used to establish a functional relationship between the normal and tangential crack strains, ϵ^{cr} and γ^{cr}, for a single crack by assuming that cracks are in the form of many equally spaced, paralell microcracks with a mean crack spacing s. The consequences of such assumption are the deformations due to cracks may be considered continuously distributed and the crack strains can be averaged over the crack spacing s as follows:

$$\epsilon^{cr} = \frac{\delta_n}{s} \; ; \qquad \text{and} \quad \gamma^{cr} = \frac{\delta_t}{s} \qquad \text{(III.2.2)}$$

The relationship between the normal and tangential crack strains can be obtained by replacing the crack width δ_n and the shear slip δ_t in expression (III.2.1) by ϵ^{cr} and γ^{cr}.

$$\gamma^{cr} = b(\epsilon^{cr})^2 \quad \text{,where} \quad b = A \times s \qquad \text{(III.2.3a)}$$

This expresssion represents the dilatancy law of cracks. A value of b=800 (corresponding to a mean crack spacing s of 250 mm) appears to

fit reasonably well with Walraven's data. Another possible crack dilatancy law could be obtained with a similar but more complete polynomial, such as:

$$\gamma^{cr} = a\epsilon^{cr} + b(\epsilon^{cr})^2 \qquad \text{(III.2.3b)}$$

where a and b are coefficients which can be arbitrarily selected to fit the experimental data.

III.2.2.2 Stress Ratio Law

Beside the "zero restraint" dilatancy law revealed in Walraven test results, a "stress ratio" law can be derived from tests with different external restraint stiffness also performed by Walraven. Shown in Figure III.13 is the typical combination of shear stress and normal stress versus shear slip for a certain concrete compressive strength. From these results, the ratio of the shear to normal stress can be determined and plotted against the shear slip (see Figure III.17) for three different compressive strength concretes. A constant stress ratio τ/σ of 1.45 for all three concretes was obtained for values of slip greater than 1.0 mm. For values of slip that are smaller than 1.0 mm, the stress ratio is found to increase with decreasing slip and very high values of stress ratio are obtained for values of slip less than 0.5 mm. The high value of τ/σ for low slips is probably due to the good 'fit' of the opposing crack surfaces. The mode of shear transfer in that case is basically one of direct bearing of surface irregularities against each other. For larger slips, the perfect match between opposing crack surfaces is lost and the stress ratio deteriorates to a value for a random fit between opposing crack surfaces, with the mode of shear transfer being primarily friction.

The above observations suggest that for realistic representation of IST, the models are required to conform to both the dilatancy and the

stress ratio laws. The candidate behavioral model suggested earlier, the one-spring model, is proposed in this study in order to generate functional relationship between incremental stress and strain of crack that satisfies both dilatancy and stress ratio laws. Such functional relationship will then be used to derive the material property of crack.

III.2.3 PROPOSED CRACK MODEL

III.2.3.1 The One-Spring Crack Model

In this model, the IST behavior is represented by pushing a block on a frictional, deformable hill as shown in Figure III.18. A spring with constant spring stiffness k_s is attached to the hill to represent the shear deformability of crack. The total horizontal displacements of the block and the slope can be thought of as the relative shear slip between the two opposing cracked surfaces, and the normal displacement of the block can be thought of as the crack opening or crack width. The hill has a constant friction coefficient μ and a slope $d\epsilon^{cr}/d\gamma^{cr}$. This friction coefficient μ is not necessarily the friction coefficient of concrete, it is rather an arbitrary quantity chosen so that both the stress ratio and the dilatancy laws can be satisfied. As stated, the spring stiffness k_s is inversely proportional to the crack width δ_n.

Call N and μN the stresses acting the crack surface, these stresses can be resolved into the normal and tangential stresses σ and τ as shown in Figure III.19.

$$\sigma = \mu N(d\epsilon^{cr}/ds^{cr}) - N(d\gamma^{cr}/ds^{cr}) \qquad \text{(III.2.4)}$$

$$\tau = \mu N(d\gamma^{cr}/ds^{cr}) + N(d\epsilon^{cr}/ds^{cr}) \qquad \text{(III.2.5)}$$

Define $R = \sigma/\tau$, then R can be written in terms of the incremental normal and tangential crack strains by replacing σ and τ by expressions (III.2.4) and (III.2.5) as follows:

$$R = \frac{\mu d\epsilon^{cr} - d\gamma^{cr}}{\mu d\gamma^{cr} + d\epsilon^{cr}} \qquad \text{(III.2.6)}$$

From the dilatancy law described in expression (III.2.3a), a functional relationship between the incremental normal and tangential crack strains can be obtained as:

$$d\gamma^{cr} = 2b\epsilon^{cr}d\epsilon^{cr} \qquad \text{(III.2.7a)}$$

A similar relationship can also be obtained if the dilatancy law described by expression (III.2.3b) is used:

$$d\gamma^{cr} = a + 2b\epsilon^{cr}d\epsilon^{cr} \qquad \text{(III.2.7b)}$$

R can then be rewritten based on expression (III.2.7a) as:

$$R = \frac{\mu - 2b\epsilon^{cr}}{2\mu b\epsilon^{cr} + 1} \qquad \text{(III.2.8a)}$$

or based on expression (III.2.7b) as:

$$R = \frac{\mu - (a + 2b\epsilon^{cr})}{\mu(a + 2b\epsilon^{cr}) + 1} \qquad \text{(III.2.8b)}$$

Expressions (III.2.8a and b) represent the analytical stress ratio derived using the one-spring model and the proposed dilatancy law. The model can be calibrated by plotting the inverse of the analytical stress ratio $(1/R)$ against the shear slip and then comparing this relationship with the experimentally determined stress ratio law in Figure III.17. A graph of 1/R according to expression (III.2.8a) versus shear slip δ_t is shown in Figure III.20 for b = 800 and μ = 0.9. The inverses of the analytical stress ratio according expression (III.2.8b) with different value of a and b are also plotted against the shear slip in Figure III.20. It can be seen that these plot compares favorably with results obtained from Walraven's data where crack slip δ_t is converted to tangential crack strain by assuming a mean crack spacing of 250 mm

(approximately 10 in). However, it should be noted that the analytical stress ratios can not be quantified when slip is small, due to lack of experimental data with small shear slip. R is affected very little by the change of the mean crack spacing s since the crack coefficient b is present in both the numerator and denominator of expressions (III.2.8a and b). The value of b may depend on the concrete being used, while the coefficient μ is probably nearly independent of the concrete mix design.

III.2.3.2 Incremental Crack Stress-Crack Strain Relationship

For the one-spring model, the shear stress on the cracked surface can be computed using the relationship between the normal and tangential crack strains derived in expression (III.2.3a) as follows:

$$\tau = k_s \gamma^1 = k_s(\gamma^{cr} - b\epsilon^{cr2}) \qquad \text{(III.2.9)}$$

Where γ^1 is the difference between the true tangential crack strain and the proposed tangential crack strain obtained from the "zero" dilatancy law. k_s is the constant spring stiffness determined from Paulay and Loeber's data.

Also since $\sigma = R\tau$, the normal crack stress can also be written in terms of the normal and tangential crack strains, ϵ^{cr} and γ^{cr}, by using expression (III.2.8a) for the stress ratio R.

$$\sigma = \frac{2b\epsilon^{cr} - \mu}{2\mu b\epsilon^{cr} + 1} k_s(\gamma^{cr} - b\epsilon^{cr2}) \qquad \text{(III.2.10)}$$

Expressions (III.2.9) and (III.2.10) can be used to establish the relationship between the crack stresses and crack strains in the incremental form for unreinforced crack as follows:

$$\begin{Bmatrix} d\sigma \\ d\tau \end{Bmatrix} = [D^{cr}] \begin{Bmatrix} d\epsilon^{cr} \\ d\gamma^{cr} \end{Bmatrix} \qquad \text{(III.2.11)}$$

$$\text{Where} \quad D^{cr} = \begin{vmatrix} d\sigma/d\epsilon^{cr} & d\sigma/d\gamma^{cr} \\ d\tau/d\epsilon^{cr} & d\tau/d\gamma^{cr} \end{vmatrix} \qquad \text{(III.2.12)}$$

Differentiating expressions (III.2.9) and (III.2.10) with respect to ϵ^{cr} and γ^{cr} yields:

$$d\sigma/d\epsilon^{cr} = \frac{2bk_s}{2\mu b\epsilon^{cr} + 1} \quad \frac{(1 - \mu^2)(\gamma^{cr} - b\epsilon^{cr2})}{(2\mu b\epsilon^{cr} + 1)} - \epsilon^{cr}(2b\epsilon^{cr} - \mu)$$

$$d\sigma/d\gamma^{cr} = k_s \quad \frac{-2b\epsilon^{cr} + \mu}{2\mu b\epsilon^{cr} + 1}$$

$$d\tau/d\epsilon^{cr} = - 2bk_s\epsilon^{cr}$$

$$d\tau/d\gamma^{cr} = k_s$$

Thus, in matrix form, the incremental crack stress and incremental crack strain can be related by the following D^{cr} matrix:

$$\frac{2b}{2\mu b\epsilon^{cr}+1} \quad \frac{(1-\mu^2)(b\epsilon^{cr2}-\gamma^{cr})}{(2\mu b\epsilon^{cr}+1)} - \epsilon^{cr}(\mu-2b\epsilon^{cr}) \qquad - \frac{2b\epsilon^{cr} + \mu}{2\mu b\epsilon^{cr} + 1}$$

$$D^{cr} = k_s \qquad \text{(III.2.13a)}$$

$$- 2b\epsilon^{cr} \qquad\qquad 1$$

For the case of slipping-crack ($\mu = 0$), D^{cr} simplifies to:

$$D^{cr} = k_s \begin{vmatrix} 4b^2\epsilon^{cr}2 & -2b\epsilon^{cr} \\ -2b\epsilon^{cr} & 1 \end{vmatrix} \qquad \text{(III.2.14a)}$$

A similar procedure can be used to obtain the material matrix D^{cr} when the second crack dilatancy law (expression (III.2.3b) is used. In that case, the D^{cr} matrix is as follows:

$$D^{cr} = \begin{vmatrix} \frac{d\sigma}{d\epsilon^{cr}} & \frac{d\sigma}{d\gamma^{cr}} \\ \frac{d\tau}{d\epsilon^{cr}} & \frac{d\tau}{d\gamma^{cr}} \end{vmatrix} \qquad \text{(III.2.13b)}$$

where,

$$\frac{d\sigma}{d\epsilon^{cr}} = \frac{K_s}{\mu(a+2b\epsilon)+1}\left|\left\{(a+2b\epsilon)(a+2b\epsilon-\mu)\right\} + \frac{2b(1+\mu^2)(a\epsilon+b\epsilon^2-\gamma)}{\mu(a+2b\epsilon)+1}\right|$$

$$\frac{d\sigma}{d\gamma^{cr}} = K_s\left|\frac{\mu-(a+2b\epsilon)}{\mu(a+2b\epsilon)+1}\right|$$

$$\frac{d\tau}{d\epsilon^{cr}} = -K_s(a+2b\epsilon)$$

$$\frac{d\tau}{d\gamma} = K_s$$

The preceding D^{cr} matrices represent explicitly the relationship between the incremental crack stresses and incremental crack strains of a single crack. This would allow the total strain increment of cracked concrete to be decomposed into two components, the strain increment of uncracked concrete between the cracks and the strain increment of the crack. Such decomposition enables the non-linear material models for the uncracked concrete between the cracks to be conveniently incorporated. It should be noted that the two off-diagonal terms in the D^{cr} matrix are non-zero, which implies that the coupling between the normal crack stress increment and the tangential crack strain increment, or between the tangential crack stress increment and the normal crack strain increment is taken into account. However, the general form of the D^{cr} matrices (expressions III.2.13a and b), which is required for the case of slipping-frictional crack, can be seen to be non-symmetric. Thus, when employed for general cases, the unsymmetric D^{cr} would result in a non-symmetric stiffness matrix. This represents a problem since most equation solvers used in finite element analysis require the stiffness matrix to be symmetric. In this study, this problem is dealt with by assuming that the D^{cr} matrix is symmetric in the stiffness phase of the analysis and then using the true D^{cr} matrix in the stress phases to recover the stresses and strains and the unbalanced forces.

III.2.4 CONCRETE MODEL

As stated earlier, the explicit relationship of the incremental crack stresses and incremental crack strains, represented by the material matrix of crack D^{cr} (expressions III.2.13 and III.2.14), enables the decomposition of the total strains in cracked concrete into the crack strains and the strains of uncracked concrete between the crack. Such decompositon facilitates the development of the constitutive matrix for

cracked concrete by using the method devised by De Borst and Nauta (expression III.1.3).

Expression (III.1.3) shows that the constitutive matrix for cracked concrete is composed basically of two independent material matrices, the material matrix for cracks D^{cr} and the material matrix for uncracked concrete D^{co}. The D^{cr} matrix has been derived in the previous section using the one-spring model (expressions III.2.13 and III.2.14). The material matrix for uncracked concrete, D^{co}, is described in this section.

A sophisticated concrete model might not be necessary in problems where nonlinear behavior is dominated by cracking of concrete under low tensile stresses. Thus in this present study, a relatively simple nonlinear-elastic concrete model will be used to described the biaxial stress state of concrete. The model was proposed by Darwin and Pecknold [III.19].

According to Darwin and Pecknold, the orthotropic incremental constitutive relationship for the biaxial stress conditions can be expressed as:

$$\begin{Bmatrix} d\sigma_1 \\ d\sigma_2 \\ d\tau_{12} \end{Bmatrix} = \frac{1}{(1 - \nu^2)} \begin{vmatrix} E_1 & \nu\sqrt{E_1E_2} & 0 \\ \nu\sqrt{E_1E_2} & E_2 & 0 \\ 0 & 0 & \dfrac{E_1+E_2-2\nu\sqrt{E_1E_2}}{4} \end{vmatrix} \begin{Bmatrix} d\epsilon_1{}^{co} \\ d\epsilon_2{}^{co} \\ d\gamma_{12}{}^{c} \end{Bmatrix} \quad \text{(III.2.15)}$$

The incremental stress-strain relation in the global coordinate system can be obtained by transforming expression III.2.15 to the global coordinate axes x,y:

$$\{ d\sigma \} = [D^{co}] \{ d\epsilon^{co} \} \quad \text{(III.2.16)}$$

where

$$\{ d\sigma \}^T = \{ d\sigma_x,\ d\sigma_y,\ d\tau_{xy} \}$$

$$\{ d\epsilon \}^T = \{ d\epsilon_x,\ d\epsilon_y,\ d\gamma_{xy} \}$$

and

$$[D^{co}] = \begin{vmatrix} E_1C^2+E_2S^2 & \nu\sqrt{E_1E_2} & 1/2(E_1-E_2)CS \\ & E_1S^2+E_2C^2 & 1/2(E_1-E_2)CS \\ \text{Sym.} & & \dfrac{E_1+E_2-2\nu\sqrt{E_1E_2}}{4(1-\nu^2)} \end{vmatrix} \qquad \text{(III.2.17)}$$

where $C = \cos\theta$ $S = \sin\theta$, with θ is the angle between the x-axis and the orthotropic 1-direction.

A total stress-strain relation can be derived for each orthotropic direction of the biaxial stress state using an equivalent uniaxial stress-strain curve. A typical curve is shown in Figure III.21.

The equivalent uniaxial stress-strain curve relates the total stress σ_i in the orthotropic i-direction to the total equivalent uniaxial strain ϵ_{iu} in the compression regime of the curve as follows:

$$\sigma_1 = \frac{E_o\epsilon_{iu}}{1 + \left(\dfrac{E_o}{E_s} - 2\right)\left(\dfrac{\epsilon_{iu}}{\epsilon_{ic}}\right) + \left(\dfrac{\epsilon_{iu}}{\epsilon_{ic}}\right)^2} \qquad \text{(III.2.18)}$$

In the tension regime, concrete is characterized as linear-elastic with limited tensile strength:

$$\sigma_1 = E_o\epsilon_{iu} \quad \text{when } \sigma_i \le \sigma_{it} \qquad \text{(III.2.19)}$$

where $E_s = \sigma_{ic}/\epsilon_{ic}$, is defined as the secant elastic modulus of concrete,

E_o is the tangent elastic modulus of concrete,

σ_{ic}, ϵ_{ic} are the maximum compressive stress and the corresponding strain in the orthotropic i-direction, and

σ_{it} is the concrete tensile strength in the orthotropic i-direction.

The total equivalent uniaxial strain ϵ_{iu} in expressions III.2.18 and III.2.19 may be computed as the sum of the incremental equivalent uniaxial strain $d\epsilon_{iu}$ as follow;

$$\epsilon_{iu} = \Sigma\, d\epsilon_{iu} = \Sigma\, (d\sigma_i/E_i) \qquad \text{(III.2.20)}$$

E_i is the modulus of elasticity in the orthotropic i-direction. In the compression regime, E_i can be obtained by differentiating expression III.2.18 with respect to ϵ_{iu} as:

$$E_i = \frac{\partial \sigma_i}{\partial \epsilon_{iu}} = \frac{E_o(1 - q^2)}{1 + \left[\frac{E_o}{E_s} - 2\right] q + q^2} \qquad \text{(III.2.21)}$$

where $q = \epsilon_{iu}/\epsilon_{ic}$.

In the tension regime with $\sigma_i \leq \sigma_{it}$, $E_i = E_o$ (III.2.22)

III.2.5 MATERIAL MODEL FOR CRACKED CONCRETE

III.2.5.1 Incremental Stress-Strain Relation Of Unreinforced Cracked Concrete

De Borst and Nauta's method for handling multi-directional cracks in concrete requires two conditions for equilibrium to be satisfied. The first condition, which has already been stated, is that the total strain of concrete containing many smeared cracks, ϵ, is equal to the sum of the strain in uncracked concrete between the cracks ϵ^{co} and the crack strain ϵ^{cr}. In incremental form, this condition can be written as:

$$\{d\epsilon\} = \{d\epsilon^{co}\} + \{d\epsilon^{cr}\} \qquad \text{(III.2.23)}$$

Where $\{d\epsilon\}^T = \{d\epsilon_x, d\epsilon_y, d\gamma_{xy}\}$ are the global incremental strains in cracked concrete,

$\{d\epsilon^{co}\}^T = \{d\epsilon_x^{co}, d\epsilon_y^{co}, d\epsilon_{xy}^{co}\}$ are the global incremental strains of uncracked concrete between the cracks, and

$\{d\epsilon^{cr}\}^T = \{d\epsilon_x^{cr}, d\epsilon_y^{cr}, d\epsilon_{xy}^{cr}\}$ are the global incremental crack strains.

The second equilibrium condition requires that the stresses that are being transmitted across the cracks must be the same as the stresses in concrete between the cracks. Again, in incremental form, this equilibrium condition can be written as:

$$\{d\sigma\} = [D^{co}]\{d\epsilon^{co}\} \qquad \text{(III.2.24)}$$

where $[D^{co}]$ is the material matrix of the uncracked concrete as described in expressions (III.2.16) and (III.2.17), and $\{d\sigma\}^T = \{d\sigma_x, d\sigma_y, d\tau_{xy}\}$ is the global incremental stresses in concrete.

The global incremental stresses and strains can be related to the local incremental stresses and strains through the use of the transformation matrix N, so that the crack properties matrix D^{cr}, derived in the local coordinate as in expressions (III.2.13) or (III.2.14), can be incorporated.

Call $\{ds^{cr}\}$ and $\{de^{cr}\}$ the local incremental stresses and strains in cracked concrete. $\{ds^{cr}\}^T = \{d\sigma, d\tau\}$ and $\{de^{cr}\}^T = \{d\epsilon^{cr}, d\gamma^{cr}\}$ as defined in expressions (III.2.2) and (III.2.11). Then:

$$\{d\epsilon^{cr}\} = [N]\{de^{cr}\} \qquad \text{(III.2.25)}$$

and

$$\{ds^{cr}\} = [N]^T\{d\sigma\} \qquad \text{(III.2.26)}$$

where [N] is the 3x2 transformation matrix. If θ is the angle between the normal to the crack and the x-axis in the global coordinate, then N will read:

$$N^T = \begin{vmatrix} \cos^2\theta & \sin^2\theta & 2\sin\theta\cos\theta \\ -\sin\theta\cos\theta & \sin\theta\cos\theta & \cos^2\theta - \sin^2\theta \end{vmatrix} \quad \text{(III.2.27)}$$

Substituting $\{d\epsilon^{co}\}$ in expression (III.2.24) by expressions (III.2.23) and (III.2.25) gives:

$$\{d\sigma\} = D^{co}(d\epsilon - Nde^{cr}) \quad \text{(III.2.28)}$$

Replacing $\{d\sigma\}$ in expression (III.2.26) by expression (III.2.28) gives,

$$\{ds^{cr}\} = N^T D^{co}(d\epsilon - Nde^{cr}) \quad \text{(III.2.29)}$$

By inserting $\{ds^{cr}\} = D^{cr}\{de^{cr}\}$ from expression (III.2.11) into expression (III.2.29), we have

$$D^{cr}\{de^{cr}\} = N^T D^{co}(d\epsilon - Nde^{cr}) \quad \text{(III.2.30)}$$

or,

$$\{de^{cr}\} = [(D^{cr} + N^T D^{co} N)^{-1} N^T D^{co}]\, d\epsilon \quad \text{(III.2.31)}$$

Replacing $\{de^{cr}\}$ in expression (III.2.28) by expression (III.2.31) yields the incremental stress-strain relationship for cracked concrete in the global coordinate system:

$$\{d\sigma\} = [\, D^{co} - D^{co}N(\, D^{cr} + N^T D^{co} N)^{-1}\, N^T D^{co}\,]\{d\epsilon\} \quad \text{(III.2.32)}$$

The global stress-strain relationship described in expression (III.2.32) allows the crack properties matrix, D^{cr}, derived using the dilatancy and stress ratio laws (expressions (III.2.13) and (III.2.14)) to be conveniently incorporated. Furthermore, any material models for the uncracked concrete can be employed by modifying the concrete material matrix D^{co}. This relationship also allows easy handling of more than one open crack by modifying the transformation matrix N and the crack properties matrix D^{cr}.

The transformation matrix N and the crack properties matrix D^{cr} will read as follows for n open cracks:

$$N = \begin{vmatrix} \cos^2\theta_1 & -\sin\theta_1\cos\theta_1 & \ldots\ldots & \cos^2\theta_n & -\sin\theta_n\cos\theta_n \\ \sin^2\theta_1 & \sin\theta_1\cos_{\theta 1} & \ldots\ldots & \sin^2\theta_n & \sin\theta_n\cos\theta_n \\ 2\sin\theta_1\cos\theta_1 & \cos^2\theta_1-\sin^2\theta_1 & \ldots & 2\sin\theta_n\cos\theta_n & \cos^2\theta_n-\sin^2\theta_n \end{vmatrix} \quad \text{(III.2.33)}$$

and,

$$D^{cr} = \begin{vmatrix} D^{cr} & 0 & \ldots\ldots & 0 \\ 0 & D^{cr} & \ldots\ldots & 0 \\ \vdots & \vdots & & \vdots \\ 0 & 0 & \ldots\ldots & D^{cr} \end{vmatrix} \quad \text{(III.2.34)}$$

III.2.5.2 Incremental Stress-Strain Relation Of Reinforced Cracked Concrete

The inclusion of steel reinforcement on the crack surfaces provides the cracks with increased extensional and shear stiffnesses, and thus improves their ability to transmit interface shear forces. The effectiveness of the steel reinforcement in increasing the interface shear and extensional stiffnesses depends on two factors. The first is the bond/slip relationship between the reinforcing bars and the concrete being used. The second factor is the state of local stress. Incorporating these highly nonlinear behavior into an analytical model so that the interaction between the reinforcing bars and the cracked concrete can be truly represented is rather difficult. The difficulty involves the development of a general mathematical representation that can be implemented by the finite element techniques.

$$\{d\sigma\} = \left| [D^{co} - D^{co}N(D^{cr} + N^{T}D^{co}N)^{-1}N^{T}D^{co}] + [S] \right| \{d\epsilon\} \quad \text{(III.2.37)}$$

Expression (III.2.37) represents the incremental stress-strain relationship for reinforced cracked concrete.

III.2.6 SUMMARY

This chapter focuses on the development of a material model for cracks. The model, represented by the incremental crack stress-crack strain relation (expressions III.2.13a and b, and III.2.14), was derived based on the experimentally-observed dilatancy and stress ratio laws. The explicit incremental stress-strain relation of cracks allows the method developed by De Borst and Nauta to be used in developing general material matrices for both unreinforced and reinforced cracked concrete (expressions III.2.32 and III.2.37). The uncracked concrete in both cases was modeled by using the nonlinear-elastic equivalent uniaxial stress-strain curve to represent the stress-equivalent strain relation in each orthotropic direction of the biaxial stress state. Perfect compatibility in strains between the steel reinforcement and the concrete was assumed to allow simple incorporation of the extensional and shear stiffnesses provided by the reinforcement.

III.3 COMPUTER IMPLEMENTATION AND NUMERICAL STUDIES

III.3.1 INTRODUCTION

This chapter outlines the implementation of the cracked concrete model developed in this study into a general purpose computer program using the finite element techniques. The failure criteria selected for the concrete and the steel reinforcement will also be discussed. Numerical results obtained from analyzing concrete structures which have experimentally tested using the proposed model are presented. Finally, merits and shortcomings of the proposed cracked concrete model are discussed.

III.3.2 FAILURE CRITERIA

III.3.2.1 Failure Criteria Of Concrete

In this study, the failure criteria of concrete under biaxial stress state are selected using the Kupfer and Gerstle biaxial strength envelope [III.20]. A typical biaxial strength envelope is shown in Figure III.22.

The strength envelope divides the stress state in concrete into two main regions. The region within the envelope represents the states of stresses of undamaged concrete. Within this region, concrete is modeled as nonlinear elastic in compression and linear elastic in tension. The incremental stress-strain relation in this region follows that described in expressions (III.2.16) and (III.2.17), and the total stress-strain relation can be obtained using expressions (III.2.18) and (III.2.19). The region outside the envelope represents the states of stresses that cause either crushing or cracking in concrete.

The line that seperates these two regions represent the ultimate stress state. This line can be mathematically described for three different stress conditions: (1) both principle stresses are in

compression, (2) one principle stress is in compression, the other is in tension, and (3) both principle stresses are in tension. The mathematical representations of the ultimate stress states of these three regimes and the corresponding failure criteria selected for the concrete in this study are as follows:

1. Compression-Compression (σ_1 and $\sigma_2 \leq 0$)

$$\left(\frac{\sigma_1}{f'_c} + \frac{\sigma_2}{f'_c} \right)^2 + \frac{\sigma_1}{f'_c} + 3.65 \frac{\sigma_2}{f'_c} = 0 \qquad \text{(III.3.1)}$$

where f'_c is the uniaxial compressive strength of concrete.

When both principle stresses are in compression and the state of stress is such that expression (III.3.1) is satisfied (≤ 0), then crushing failure of concrete is considered to have occurred.

2. Compression-Tension ($\sigma_1 > 0$ and $\sigma_2 < 0$)

Cracking is considered to have occurred in this regime when the principle stresses satisfy the following two conditions:

$$\frac{\sigma_2}{f_t} \geq 1 + 0.8 \frac{\sigma_1}{f'_c} \qquad \text{(III.3.2)}$$

and,

$$\frac{\sigma_2}{\sigma_1} \leq -0.165 \qquad \text{(III.3.3)}$$

Crushing failure occurs in this regime when expression (III.3.2) and the following expression are satisfied:

$$\frac{\sigma_2}{\sigma_1} > -0.165 \qquad \text{(III.3.4)}$$

3. Tension-Tension (σ_1 and $\sigma_2 > 0$)

In this regime, cracking is allowed when either one of the principle stresses exceeds the tensile strength of concrete:

$$\sigma_1 \text{ or } \sigma_2 \geq f_t \qquad \text{(III.3.5)}$$

III.3.2.2 Failure Criteria Of Reinforcement

In this study, steel reinforcement is modeled as linear elastic prior to yielding to simplify the problem. Yielding in the reinforcement occurs when the uniaxial tensile strain in the reinforcement reachs 2,000 microstrain.

III.3.3 COMPUTER IMPLEMENTATION

III.3.3.1 General

A finite element program, coded in Fortran 77, was developed to study the effectiveness of the proposed IST model in predicting the structural response of shear critical concrete beams. A quadrilateral 4-noded plane-stress element was used in this program. The solution procedure employed in this program is incremental, whereby the slope of the load-deformation increment is allowed to change progressively following the "modified Newton-Raphson" method (see Figure III.23) Computationally, this means the load-deformation matrix (or stiffness matrix) is continually changed after every load increment; thus, the nonlinearity of the load-deformation history can be modelled in greater detail if the load increment are kept small.

Beside the new IST model developed in this study, a "βG" model was also implemented in the same program to check the validity of the method of separating crack strains and concrete strains, which is widely employed in this study, and to compare the results of the two models.

In the "βG" approach, uncracked concrete is treated exactly the same way as in the case of the new IST model, i.e. the incremental and total

concrete stress-strain relations follow expressions (III.2.16 to III.2.19). However, the incremental crack stress-crack strain relation of the "βG" model is arbitrarily selected as:

$$D^{cr}_{(\beta)} = \begin{vmatrix} \alpha E & 0 \\ 0 & \beta G \end{vmatrix} \qquad \text{(III.3.6)}$$

where α is an arbitrary value and β is the shear retention factor, also selected arbitrarily.

The incremental stress-strain relations of cracked concrete in the "βG" model thus have the same form as in expressions (III.2.32) and (III.2.37), except that the D^{cr} matrix in those expressions is replaced by $D^{cr}_{(\beta)}$ (expression III.3.6).

III.3.3.2 Iteration Scheme

Before describing the steps involved in the implementation of these models, two points need to be mentioned:

1. First, the incremental crack stress-crack strain relation of the proposed IST model, represented by the D^{cr} matrix in expression (III.2.13), is non-symmetric. Thus, when D^{cr} is employed in the finite element program, a non-symmetric stiffness matrix would result. Since most equation solvers used in finite element analysis require the stiffness matrix to be symmetric, the incremental D^{cr} matrix in this study will be assumed to be symmetric in the stiffness phase of the analysis ($D^{cr}_{(1,2)} = D^{cr}_{(2,1)}$). The true D^{cr} matrix will then be used in the stress phase to recover the stresses and strains and the unbalanced forces.

2. Second, the total stress-strain relation for cracked reinforced and unreinforced concrete is not yet developed since the total crack stress-crack strain relation does not exist. Thus in the process of recovering stress and strain, a total crack stress-crack strain relation and a total stress-strain relation of cracked concrete will have to be assumed. The total crack stress-crack strain relation in this phase will have the following form:

$$D^{cr}{}_{total} = \begin{vmatrix} \dfrac{\sigma^{cr}}{\epsilon^{cr}} & 0 \\ 0 & \dfrac{\tau^{cr}}{\gamma^{cr}} \end{vmatrix} \qquad \text{(III.3.7)}$$

in which ϵ^{cr} and γ^{cr} are the total crack normal and shear strains, updated to the current iteration step.

The total cracked concrete stress-strain material matrix will have the following form:

$$D^{total} = \begin{vmatrix} \dfrac{\sigma_x{}^{total}}{\epsilon_x} & 0 & 0 \\ 0 & \dfrac{\sigma_y{}^{total}}{\epsilon_y} & 0 \\ 0 & 0 & \dfrac{\tau_{xy}{}^{total}}{\gamma_{xy}} \end{vmatrix} \qquad \text{(III.3.8)}$$

The iteration scheme used in this program can be better explained by the following step-by-step procedure employed for each increment of load. The program flow chart is shown in Figure III.24.

1. Form the incremental global stiffness matrix K_u from the incremental element stiffness matrix KM, where KM is computed as:

$$KM = \iint B^T D B \, dxdy \qquad \text{(III.3.9)}$$

or in numerical form,

$$KM = DET * \sum_{1}^{GP} \sum_{1}^{GP} K1 * K2 * (B^T D B)_{I,J} \qquad \text{(III.3.10)}$$

where K1 and K2 are Gaussian multipliers,

DET is the determinant of the Jacobian matrix,

B is the strain-displacement matrix which contains the derivatives of the shape functions in the local coordinate system.

D is the incremental material matrix according to either expression (III.2.32) or expression (III.2.37). When a crack does not yet exist in the current element, D is reduced to the incremental material matrix suggested by Darwin and Pecknold (expression III.2.17).

2. Solve $[K_u]\{d\delta\} = \{dP\}$ for the incremental displacement vector $\{d\delta\}$. $\{dP\}$ is the preselected incremental load vector.

3. Compute the incremental strain vector for each element from the element displacement vector, and sum incremental strains of all previous load steps to obtain total strain vector for each element:

$$\{d\epsilon\}_{ele.} = [B]\{d\delta\}_{ele.} \qquad \text{(III.3.12)}$$

$$\{\epsilon\}^{total} = \sum \{d\epsilon\} \qquad \text{(III.3.13)}$$

where $\{d\epsilon\}^T_{ele.} = \{d\epsilon_x, d\epsilon_y, d\gamma_{xy}\}$

4. Compute total global and principle stresses in each element using the total stress-uniaxial strain relations in expressions (III.2.18) and (III.2.19).

5. Check status of each element using the stress criteria from the biaxial strength envelope (expressions (III.3.1) to (III.3.5)). If the criteria for cracking are not met in an element, repeat steps 1 to 5. If the criteria for cracking are met in an element, then the following iterative step will be followed:

6. Assume the total strains due to cracks in an element equal to the total strains in expression (III.3.13).

$$\begin{Bmatrix} \epsilon^{cr} \\ \gamma^{cr} \end{Bmatrix} = [\ N\ ]^T \begin{Bmatrix} \epsilon_x{}^{total} \\ \epsilon_y{}^{total} \\ \gamma_{xy}{}^{total} \end{Bmatrix} \qquad \text{(III.3.14)}$$

7. Compute crack normal and shear stresses σ^{cr} and τ^{cr} following stress ratio law (expressions (III.2.9) and (III.2.10)), then rotate to the global coordinates to obtain total global stresses $\sigma_x{}^{total}$, $\sigma_y{}^{total}$, and $\tau_{xy}{}^{total}$.

8. Assume the total crack material matrix $D^{cr}{}_{total}$ as in expression (III.3.7), using σ^{cr} and τ^{cr} obtained from step 7. Also assume the total cracked concrete stress-strain relation, D^{total}, as in expression (III.3.8), using $\sigma_x{}^{total}$, $\sigma_y{}^{total}$, and $\tau_{xy}{}^{total}$ from step 7.

9. Compute new total stress in the cracked element using either expression (III.2.32) or expression (III.2.37) with D^{cr} replaced by the assumed $D^{cr}{}_{total}$ and D^{co} replaced by D^{total}.

10. If the difference between the total stress vector $\{\sigma^{total}\}$ in step 9 and that in step 7 meet the convergence criteria (0.1% in this study), integrate total stresses in step 9 to obtain the equivalent element nodal load vector and then assemble to obtain the true nodal force vector. If the convergence criteria is not satisfied, the next few steps will have to be taken:
11. Compute total global strains for concrete $\{\epsilon^{co}\}$ using $\{\sigma^{total}\}$ in step 9 and the assumed D^{total} as in expression (III.3.8).
12. Compute crack strains as the balance between the total strain $\{\epsilon^{total}\}$ and the assumed $\{\epsilon^{co}\}$ in step 11:

$$\{\epsilon^{cr}\} = \{\epsilon^{total}\} - \{\epsilon^{co}\}$$

13. Repeat steps 7 to 10 until the convergence criteria is satisfied.

III.3.4 NUMERICAL STUDIES

The results of finite element analyses of four shear critical reinforced concrete beams are presented in this section. Two of the four beams, XOB-1 and OC-1, contained only tension reinforcement, the other two, XB-1 and CC-1, contained both tension, compression, and shear reinforcements. These beams were experimentally studied by Bresler and Scordelis and the test results are given in reference [III.21].

Each test beam was analyzed using the same finite element program developed in this study using three different crack models. The three model used includes:

1. The one-spring IST model, developed using the crack dilatancy law as described by expression III.2.3a, with the D^{cr} matrix as in expression III.2.13a. In all the analyses with this model, the dilatancy coefficients b and μ were selected as 800 and 0.9, respectively.

2. The same one-spring IST model but the crack dilatancy law follows expression III.2.3b and the D^{cr} matrix is as in expresion III.2.13b. The dilatancy coefficients a, b and μ in expression III.2.13b were selected as 0.5, 800, and 0.9 in all the analyses with this model.
3. The βG model where the D^{cr} matrix follows expression (III.3.6) and β was kept constant in each analysis.

The same iteration scheme was used for all three models, and only one set of crack was allowed to open in each element in the current analyses.

III.3.4.1 Beams Without Shear Reinforcement

a) Beam XOB-1

This beam was reinforced by 4 #9 rebars placed along the bottom layer. Figure III.25 shows the dimensions and material properties of the beam and the finite element mesh. In all the analyses, the steel reinforcement was smeared out and distributed evenly onto the elements in the layer that contained reinforcement. The results of the finite element analyses are presented in the form of the load-center deflection curves and are compared with the experimental results as shown in Figure III.26.

Prior to cracking, the results from both IST models and the βG model agree closely with the experimental load-deflection curve. Initiation of cracks was indicated by all three models at 7.6 kips. However, the load-deflection behavior of the beam after cracking was different for each model. The load-deflection behavior of the IST model which was derived from the simple dilatancy law ($\gamma^{cr} = b(\epsilon^{cr})^2$, expression [III.2.3a]) appeared to become slightly stiffer immediately after cracking occurred. As the load increased beyond the cracking load level

and more cracks developed in other elements, a gradual degradation of the beam stiffness was seen. This degradation of stiffness became more significant as ultimate load was approached. A load drop off was finally obtained at 58.3 kips. This is in close agreement with the measured ultimate load of this beam (57.5 kips).

The load-deflection response of the IST model that follows the more complete dilatancy law ($\gamma^{cr} = a\epsilon^{cr} + b(\epsilon^{cr})^2$, expression III.2.3b) was similar in trend. Increased stiffness immediately after first cracks initiated and gradual degradation of stiffness at higher load were also observed, although the after-crack-stiffness of the beam was less than that indicated by the first model. The ultimate deflection was almost two times those of the first model and the experimental results.

The load-deflection responses obtained from the βG model with β equal 0.5 and 0.1 were also plotted. The response for the case β equal to 0.5 was in close agreement with the response obtained from the first model and ultimate load for this case was only slightly higher (59.4 kips).

b) Beam OC-1

OC-1 contained 2 #9 bars as tension reinforcement. This beam was analyzed with the same finite element mesh as shown in Figure III.25. The dimensions and material properties of this beam are shown in Figure III.27. The experimental load-deflection behavior and those obtained from the current analyses are shown in Figure III.28.

Both IST models overpredicted the ultimate capacity of this beam (34.9 kips). The load-deflection reponses of both of these two crack dilatancy models were in good agreement and similar in trend. Increased stiffness shortly after cracking was seen in both models, and degradation of stiffness due to increasing load was also observed. Good agreement

between experimental and analytical results can be seen prior to cracking. Both IST models predicted an ultimate load of about 42 kips. The βG model also predicted a similar ultimate load with β equals 0.5. However, different from the previous case, the load-deflection response for the βG approach where β equals 0.5 indicated a larger-after crack-stiffness than for the case of the first IST model. Significant reduction in strength was predicted when β was reduced to 0.1.

III.3.4.2 Beams With Shear Reinforcement

a) Beam CC-1

Beam CC-1 differs from beam OC-1 by the inclusion of flexural reinforcement in the compression zone and the addition of web shear reinforcement. The material properties and dimensions of this beam are given in Figure III.29. The load-deflection reponses of this beam according to the three crack models are given in Figure III.30.

Similar to beam OC-1, the responses obtained from the two IST model were in very close agreement. Even though these responses did not exactly duplicate the experimental load-deflection behavior, their predictions regarding the beam ultimate load and maximum center deflection agreed very closely with the experimental results. Both models yielded an ultimate load of about 44 kips and a center deflection of 0.42 in to compare with 49.5 kips and 0.39 in obtained from test. The βG model with β of 0.5 was able to match the experimental load-deflection behavior up to 20 kips (half of ultimate load). However, the βG prediction became less accurate when load is increased beyond this load level. Better results may be obtained for the βG approach if the shear retention factor is varied with increasing load.

b) Beam XB-1

Beam XB-1 also contained shear and compression reinforcement. Figure III.31 shows the material properties and dimensions of this beam, and Figure III.32 shows the experimental and the analytical load-deflection responses.

As seen on Figure III.32, the first IST model predicted well the load-deflection behavior of this beam up to 30 kips. Beyond this load level, experimental results indicate that the real beam was more flexible than the prediction of this model. The increased stiffness shortly after cracking, as seen in all other beams analyzed thus far, was also observed. The second IST model also indicates this change of beam stiffness. Further, the response predicted by the second IST model was more flexible and did not yield similar ultimate load and maximum center deflection at failure. The βG model with β of 0.5 appears to predict well the load-deflection behavior, even though it could not predict very accurately the failure load and deflection of this beam.

III.3.5 SUMMARY

This chapter described the concrete failure criteria selected for the finite element analysis and iteration scheme developed for implementing both the improved crack material models (IST models) proposed in this study and the βG model. This iteration scheme allows the handling of the non-symmetric incremental crack material matrix and the lack of the total (or secant) crack material matrix.

Even though only one set of cracks was allowed to open in each element, which is unrealistic in real beams, moderate success in predicting responses of reinforced concrete beams tested by Bresler and Scordelis was obtained using the proposed models, and one model can be more successful in one beam than in another. The βG model with different

values of β was also used in analyzing these beams. The analytical load-deflection responses with β equals 0.5 appear to match well with the experimental responses at low load level (but beyond cracking load). Better results may be obtained by allowing the shear retention factor to vary with the strain or crack conditions in an element.

III.4 SUMMARY AND CONCLUSIONS OF ANALYTICAL STUDY

III.4.1 SUMMARY

The ability of cracks to transfer shear force was represented in the improved 2-dimensional crack material model developed in this study. Two new models based on the concept of crack dilatancy and quantified by experimental results from other researchers, constitute the first step toward achieving the total goal of developing a general, computer-based, 3-dimensional model capable of analyzing more complex transverse shear problems such as the punching shear problem in reinforced concrete plates and shells. The mechanics of punching shear in lightweight concrete plates and shells were investigated experimentally and reported in the first part of this dissertation.

In the proposed models, incremental interface crack stresses were related explicitly to incremental interface crack strains, thus allowing the method developed by De Borst and Nauta to be used in deriving the material matrix for cracked concrete. This material matrix was then incorporated into a finite element program employing 4-noded quadrilateral plane stress elements to analyze shear critical reinforced concrete beams. The concrete condition of each element in this program was determined using the Kupfer's biaxial strength criteria. Steel reinforcement was smeared throughout an element and bonding between the steel and the concrete in the region near the cracks was assumed to be perfect.

Due to the nonsymmetry of the incremental crack material matrix D^{cr} and the lack of a total crack stress-crack strain relation, an iteration scheme was used so that the incremental D^{cr} matrix can be assumed to be

symmetric in the stiffness phase of the analyses. The full, non-symmetric D^{cr} matrix was used in the stress phase to recover stress and the unbalanced forces.

Four concrete beams tested by Bresler and Scordelis were analyzed using the two proposed IST models and the βG model where the shear retention factor β was kept constant throughout the loading history. Reasonably good predictions of the load-center deflection responses, along with ultimate load and maximum center deflection were obtained for beams XOB-1, OC-1, and CC-1 using the two proposed models. However, these models yielded different results in beam XB-1. The βG model produced good load-deflection behavior up to half of the loading history in beams XB-1 and CC-1 with constant β equal to 0.5. Reducing β with increasing load may yield better results.

III.4.2 CONCLUSIONS

The following conclusions were drawn for the analytical part of this dissertation in light of the results of numerical analyses:

1. Both IST material models proposed in this study were able to predict with some accuracy the nonlinear behavior of cracked beams. Expansion of these models to allow more than one set of cracks to develop in an element, along with better representation of bond/slip in the reinforcement, may lead to better results.

2. The increase in beam stiffness shortly after cracking developed, as seen on the load-deflection responses of the proposed IST material models, may be the result of the analytical stress ratios (expressions III.2.8a and III.2.8b). These analytical stress ratios become very large or change sign when shear slip approaches 0 as seen on Figure III.17 and could not be

quantified by experimental results since data of direct shear test with very small shear slip is not available.

3. A β value of 0.5 in the constant βG model in most cases produced good agreement with the two IST material models and the experimental results at lower load. As more cracks develop due to increasing load, the βG model become less accurate and reduction of the β value is needed to improve accuracy.

Table II.1 Similitude Requirements for Reinforced Concrete Modeling

QUANTITY	DIMENSION	SCALE FACTOR FOR PRACTICAL TRUE MODEL
Concrete stress	FL^{-2}	1
Concrete strain	—	1
Modulus of concrete	FL^{-2}	1
Poisson's ratio	—	1
Mass density	FL^{-3}	$1/S_\ell$
Reinforcing stress	FL^{-2}	1
Reinforcing strain	—	1
Modulus of reinforcing	FL^{-2}	1
Bond stress	FL^{-2}	1
Linear dimension	L	S_ℓ
Displacement	L	S_ℓ
Angular displacement	—	1
Area of reinforcement	L^2	S_ℓ^2
Concentrated load	F	S_ℓ^2
Line load	FL^{-1}	S_ℓ
Pressure	FL^{-2}	1
Moment	FL	S_ℓ^3

Table II.2 Lightweight Concrete Mix Design

MATERIAL FOR 1 CY. MIX			MIX # 6
Portland Cement type I (lbs)			805.7
Solite Aggregate (lbs) 1/2 in. max. size			1025
Sand (lbs)			1076
Corrocem (lbs)			96 **
Water (lbs)			210.4
Daravair AEA (Oz.)			30
MEASUREMENT	Slump (in.)		8.0
	Air content (%)		7.5
	Standard Unit Weight(pcf)		115

Specimen No.	Thickness (IN.)	Area of Loading, (IN^2)	Shear Reinforcing Ratio (%)	Flexural Reinforcing Ratio (%)	Prestress (500 psi)	R/t Ratio	Geometry
FP1	7	50	0.22	1.75	NO	-	Single-Span Plate
FP2-1	7	50	0	1.75	NO	-	Three-Span Plate
FP2-2	7	50	0	1.75	NO	-	Three-Span Plate
FP3	7	50	0.22	1.75	NO	-	Three-Span Plate
FP4	7	50	0.44	1.75	NO	-	Three-Span Plate
FP5	7	50	0.22	1.75	One-Way	-	Three-Span Plate
FP6	7	50	0.22	1.75	Two-Way	-	Three-Span Plate
IFP2-1	7	138	0	2.50	NO	-	Three-Span Plate
IFP2-2	7	100	0	2.50	NO	-	Three-Span Plate
AS7	5	50	0.24	1.75	NO	12	Arched Shell
AS8	5	50	0	1.75	NO	6	Arched Shell
AS9	5	50	0	1.75	NO	12	Arched Shell
AS10	5	50	0.24	1.75	One-Way	12	Arched Shell
AS11	5	50	0.48	1.75	NO	12	Arched Shell
AS12	5	50	0.24	1.75	NO	6	Arched Shell

Table II.3 Descriptions of Test Specimens

Specimen No.	Compressive Strength (psi)	Initial cracking load P_{cr} (Kips)	V_{cr}	Ultimate load P_u (Kips)	Normalized shear strength $V_{test} = P_u/bod$
FP1	7780	76	3.4 $\times\sqrt{f'_c}$	216.8	9.8 $\times\sqrt{f'_c}$
FP2-1	9010	90	3.8	114.9	4.8
FP2-2	8810	98	4.2	126.9	5.4
FP3	9320	90	3.7	195.1	8.0
FP4	8810	100	4.2	251.9	10.7
FP5	8610	87	3.7	202.2	8.7
FP6	8610	85	3.6	221.3	9.5
AS7	7790	93	7.2	190.6	14.7
AS8	7310	108	8.6	152.0	12.1
AS9	7030	92	7.5	124.3	10.1
AS10	6750	87	7.2	152.1	12.6
AS11	7200	95	7.6	192.4	15.4
AS12	6010	106	9.3	170.1	14.9

Table II.4 Summary of Test Results

Item	Provision	Reference Section
location of critical section	d/2 from perimeter of load	11.11.1.2
critical perimeter, b_o	$\pi(D_L + d)$	11.11.1.2
shear strength of concrete without shear reinforcement	$V_c = (2 + 4/\beta_c)\sqrt{f'_c}\, b_o d \leq 4\sqrt{f'_c}\, b_o d$ where β_c = aspect ratio of load	11.11.2.1
shear strength of concrete with shear reinforcement	$V_c = 2\sqrt{f'_c}\, b_o d$	11.11.3.4
shear strength of concrete with two-way prestress and without shear reinforcement	$V_c = (3.5\sqrt{f'_c} + 0.3f_{pc})\, b_o d + V_p$ $f'_c \leq 5000$ psi; 125 psi f_{pc} 500 psi	11.11.2.2
extent of shear reinforcement	d	11.5.3
area of shear reinforcement, ΣA_v	$A_v(D_L + d)\, d = \rho_v b_o d$	
shear strength of shear	$V_s = A_v f_y$, $f_y \leq 60{,}000$ psi	11.11.3.5, 11.5.2
factor on f'_c term for lightweight concrete	0.75 for all-lightweight concrete 0.85 for sand-lightweight concrete	11.2.1.2
code specified nominal nominal shear strength	$V_n = V_c + V_s$	11.11.1
limitations	$V_n \leq 6\sqrt{f'_c}\, b_o d$ for bar reinforcement	11.11.3.2

Table II.5 Summary of the ACI 318-83 Provisions for Punching Shear

Table II.6 Predicted Component and Nominal Shear Strength for Test Specimens According to ACI

	PERMISSIBLE STRESSES BY ACI		
Specimen No.	$V_{c_{ACI}}$	$V_{s_{ACI}}$	$V_{n_{ACI}}$
FP1	1.7	1.36	3.06
FP2-1	3.4	0	3.4
FP2-2	3.4	0	3.4
FP3	1.7	1.36	3.06
FP4	1.7	2.73	4.43
FP5	1.7	1.36	3.06
FP6	1.7	1.36	3.06
AS7	1.7	1.36	3.06
AS8	3.4	0	3.4
AS9	3.4	0	3.4
AS10	1.7	1.36	3.06
AS11	1.7	2.73	4.43
AS12	1.7	1.36	3.06

Specimen No.	$\frac{V_{Test}}{V_{nACI}}$	$\frac{V_c}{V_{cACI}}$	$\frac{V_s}{V_{sACI}}$
FP1	3.2	3.0	3.46
FP2-1	1.4	1.4	——
FP2-2	1.6	1.6	——
FP3	2.6	3.0	2.1
FP4	2.4	3.0	2.1
FP5	2.8	3.0	2.6
FP6	3.1	3.0	3.2
AS7	4.8	5.9	3.4
AS8	3.6	3.6	——
AS9	3.0	3.0	——
AS10	4.1	5.9	1.9
AS11	3.5	5.9	1.9
AS12	4.9	7.1	2.1

Table II.7 Ratios of Measured versus Code-Predicted Shear Strength

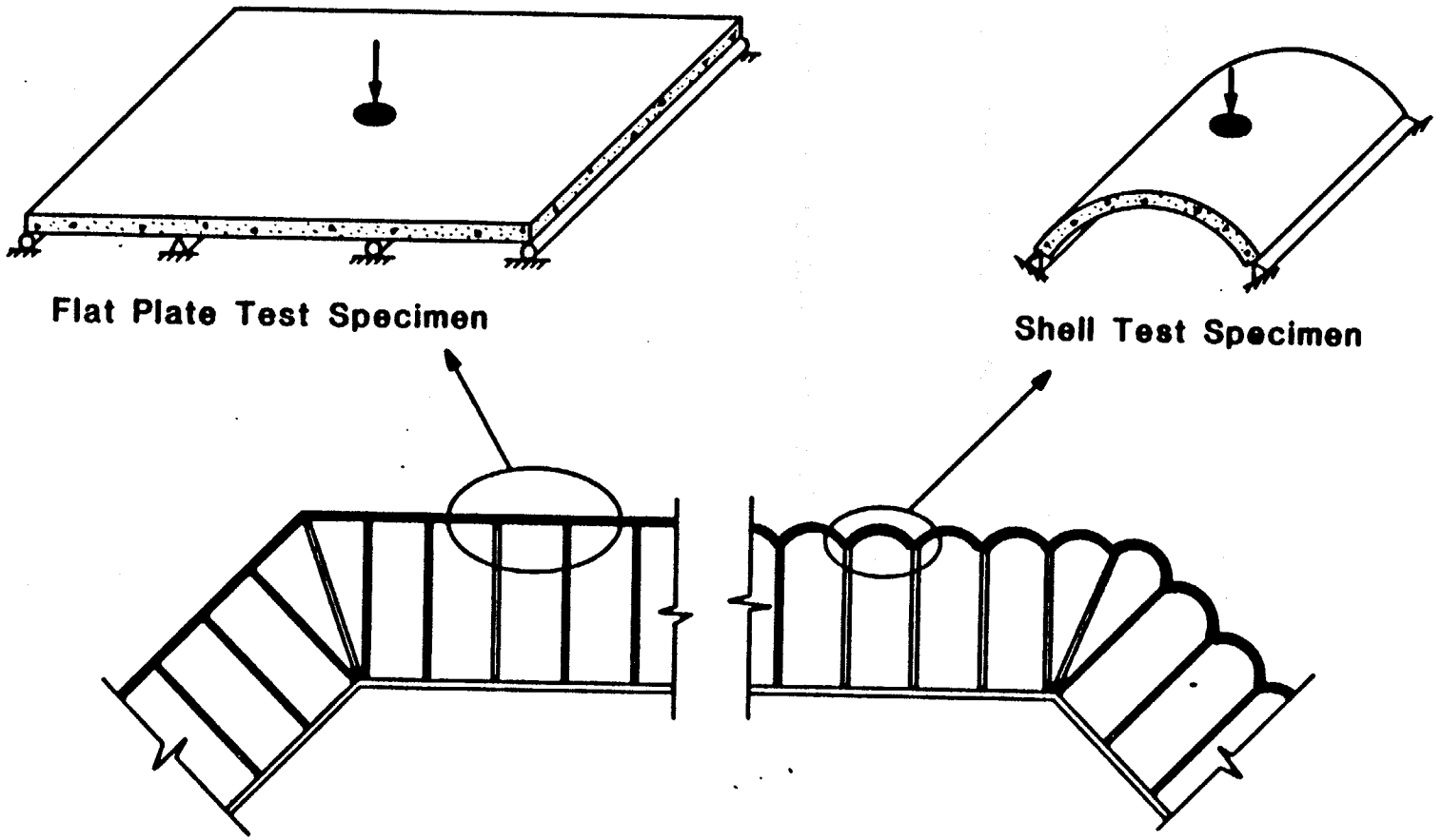

Figure II.1 Typical Ice Wall Configurations

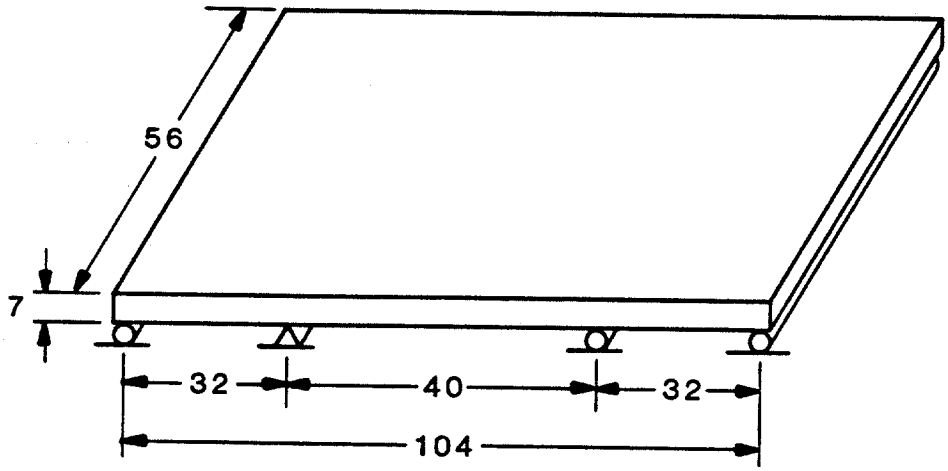

(1) Three-span continuous model

All dimensions in inches

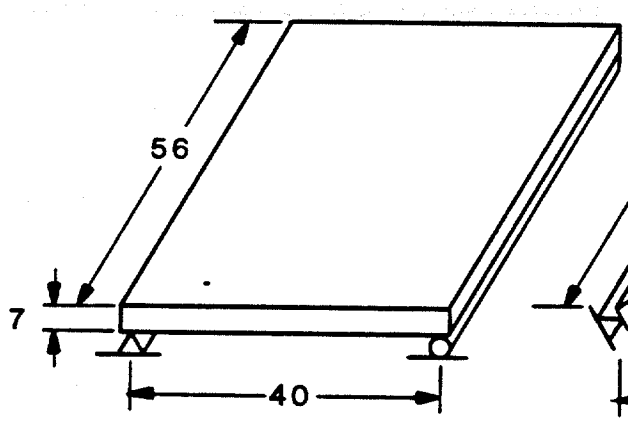

(2) Single span model

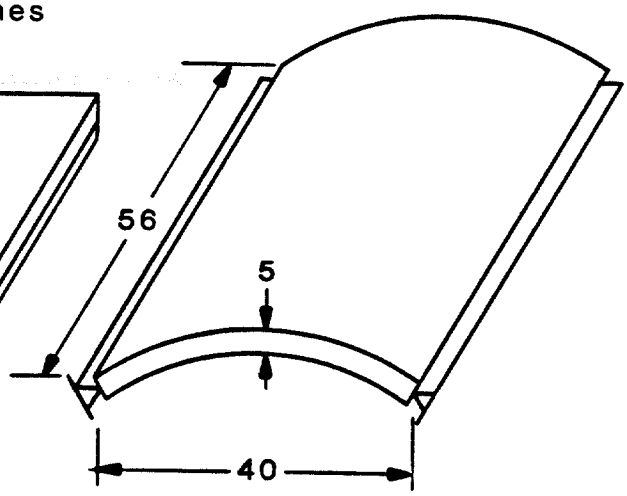

(3) Arched shell model

Figure II.2 Geometries and Dimensions of the 1/6-Scale Specimens.

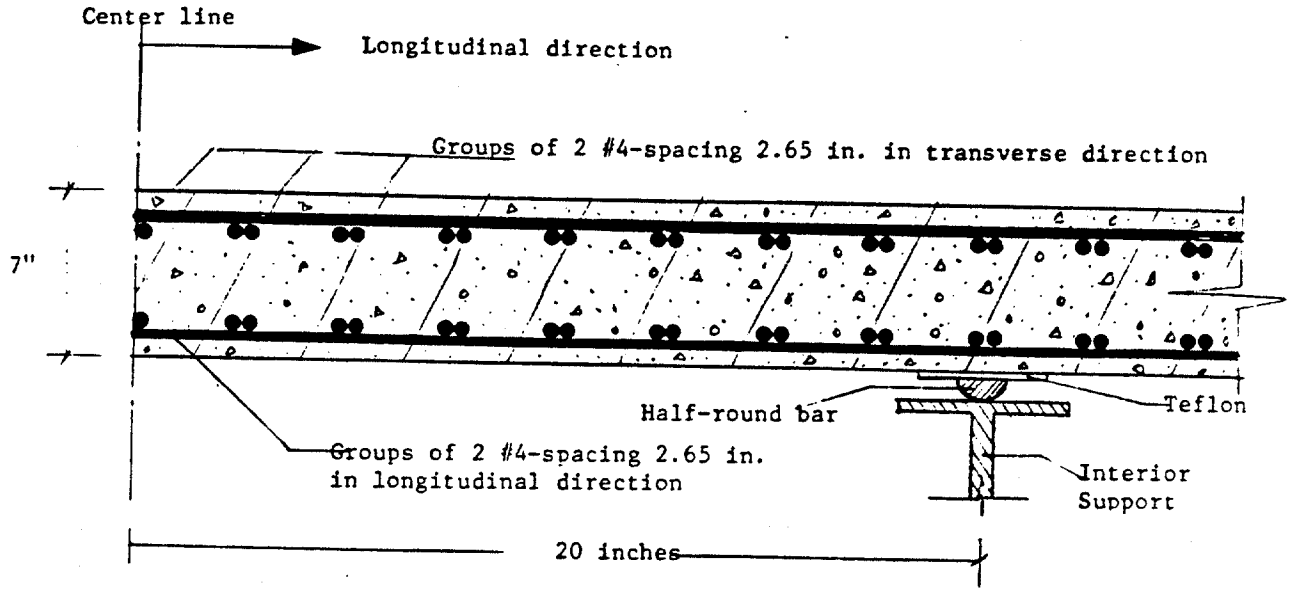

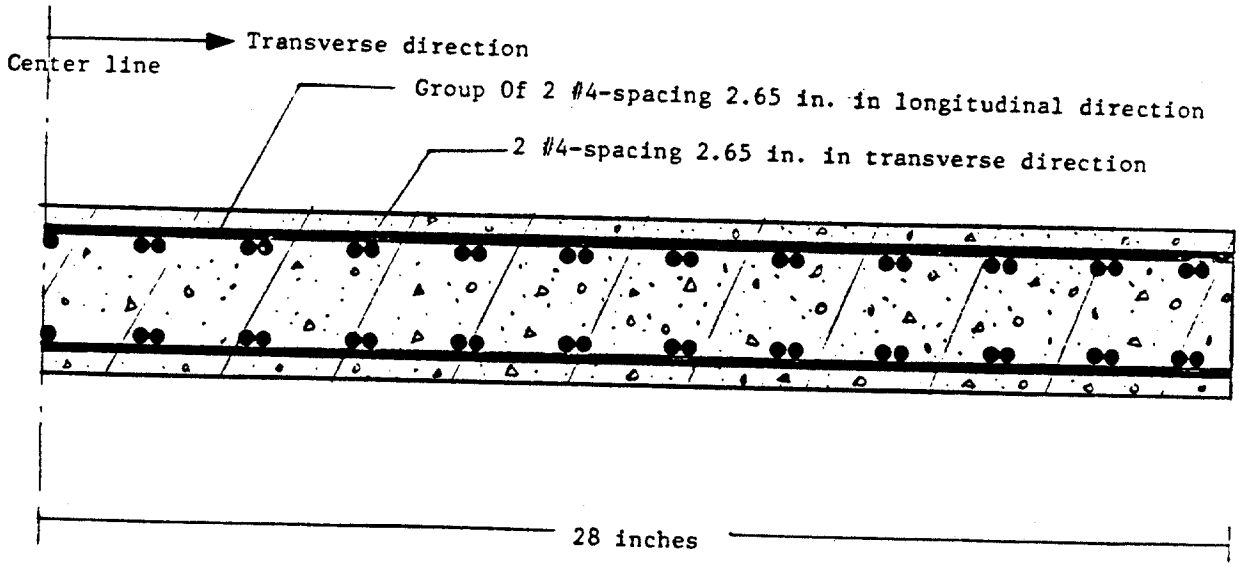

Figure II.3 Reinforcement Arrangements

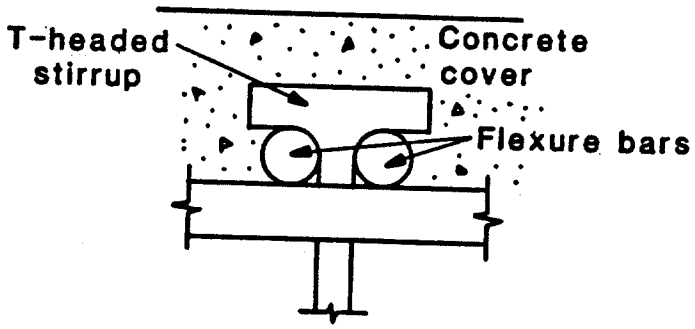

Figure II.4 Arrangement of Shear Reinforcement

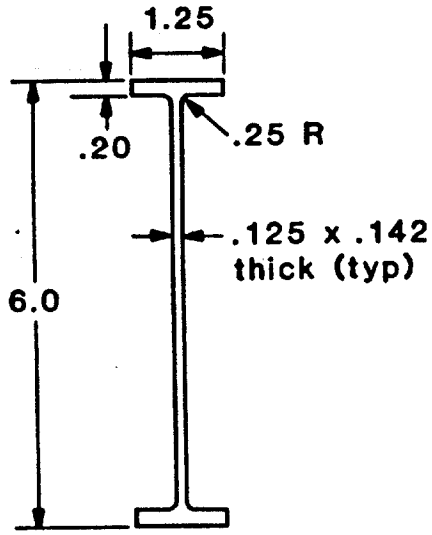

All dimensions in inches

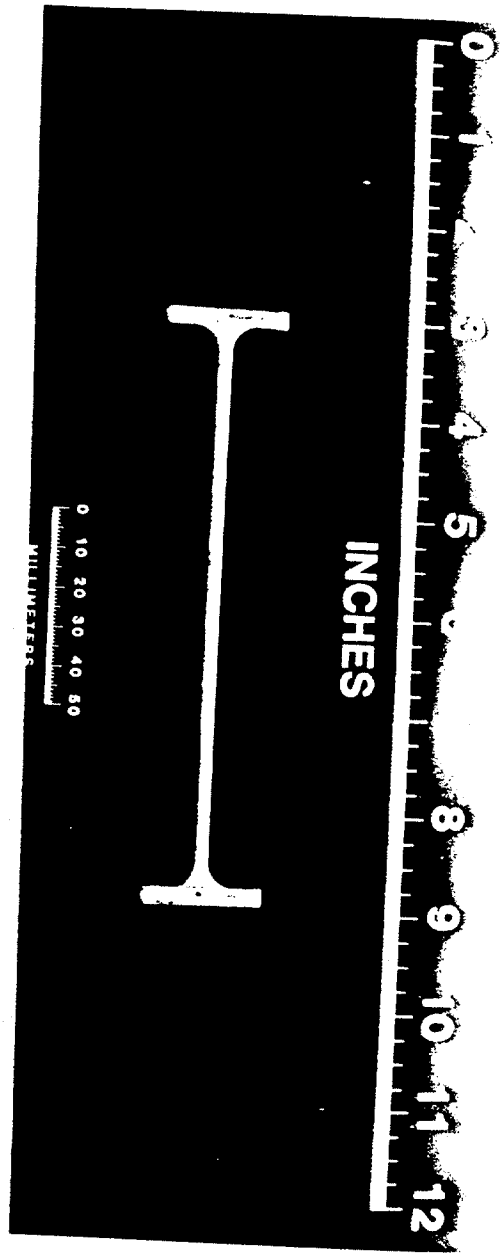

Figure II.5 Dimensions of the T-Headed Shear Bar

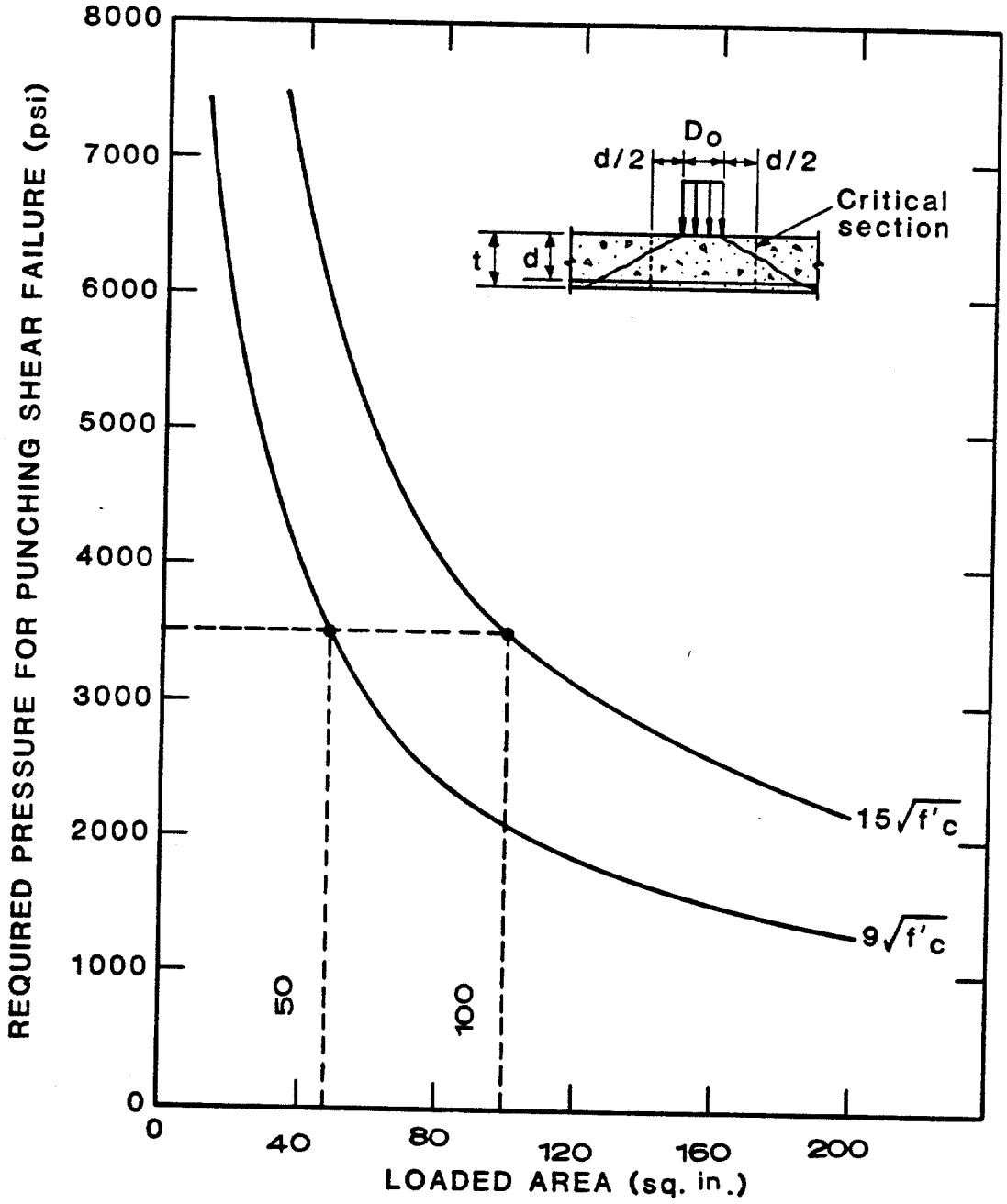

Figure II.6 Punching Shear Pressure versus Loaded Area

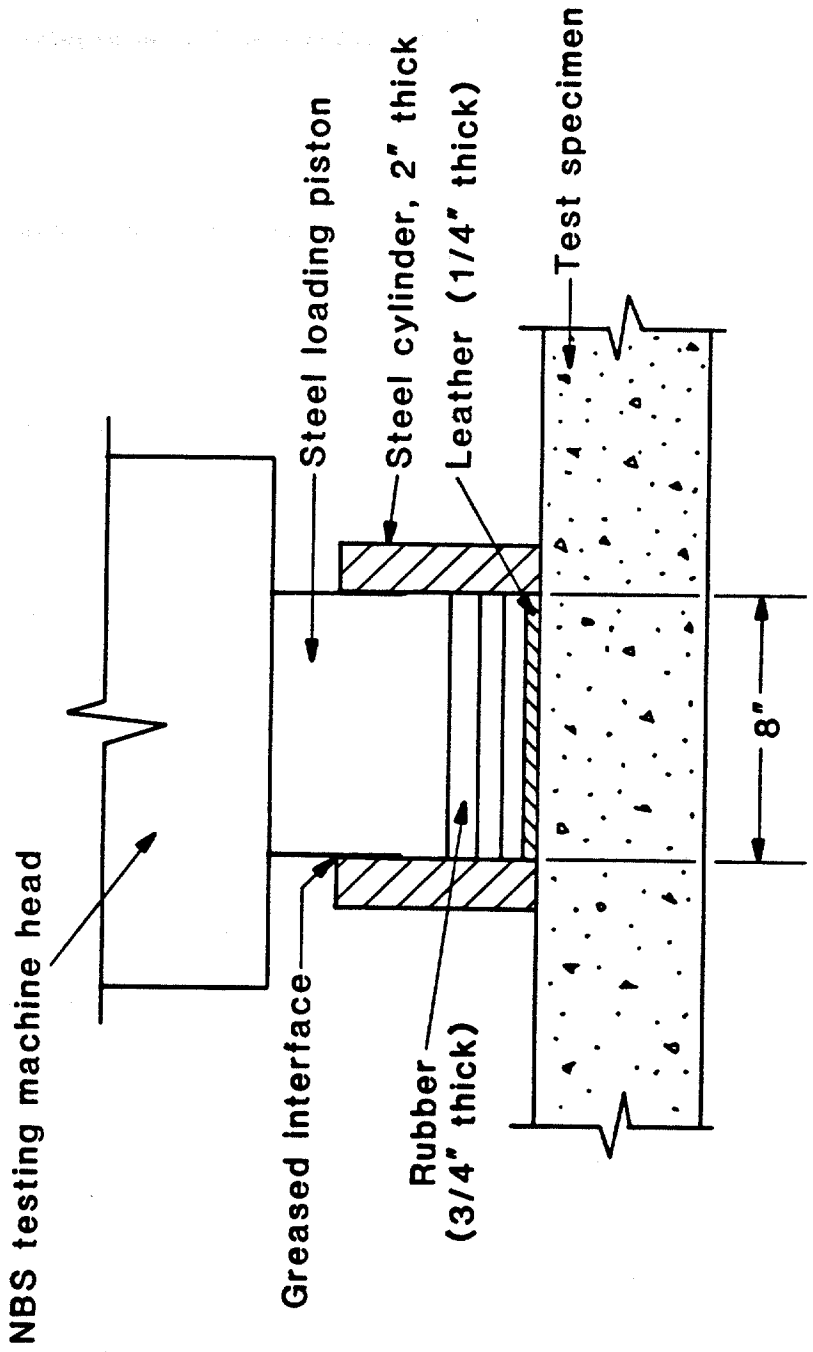

Figure II.7 Loading System

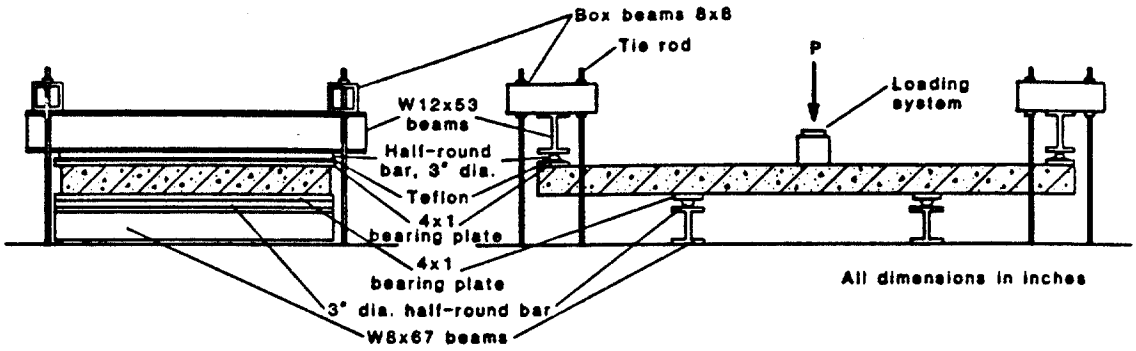

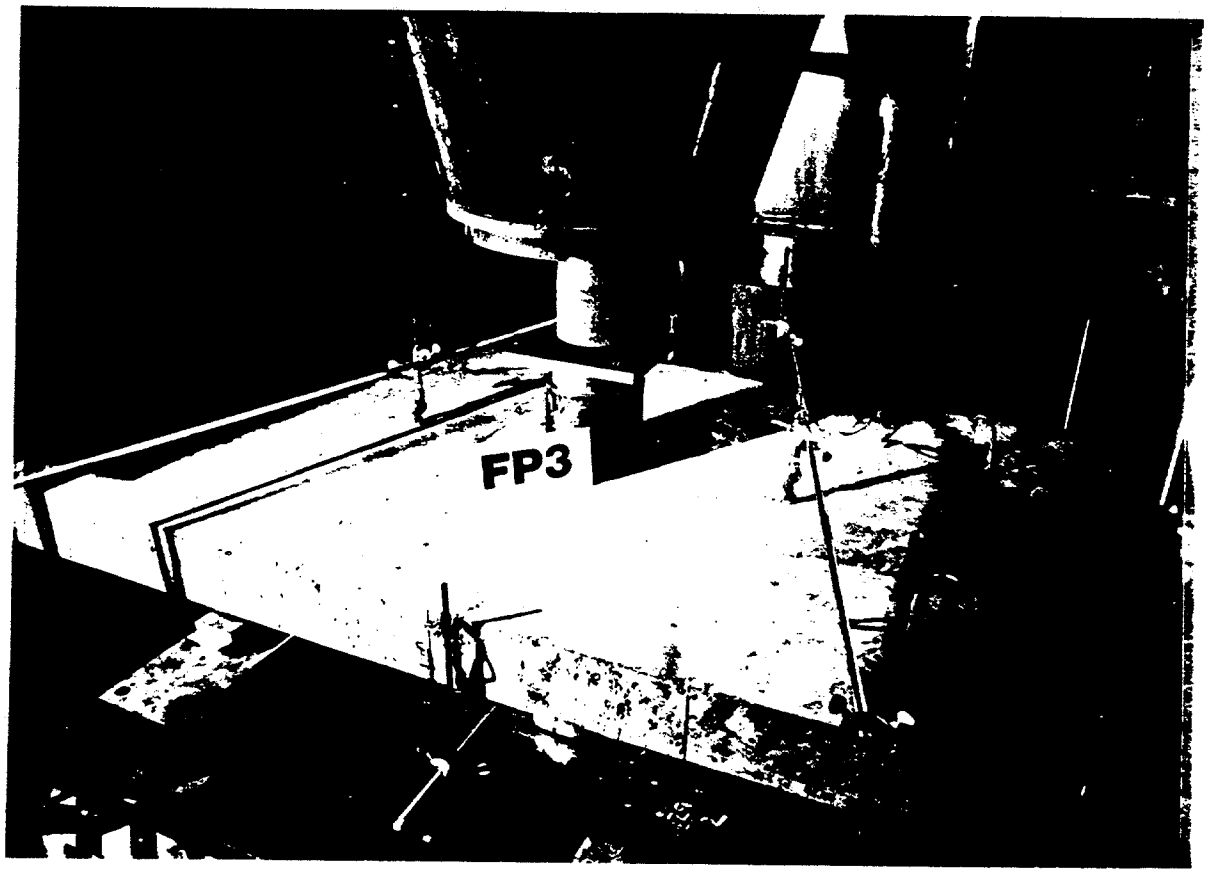

Figure II.8 Flat Plate Test Setup

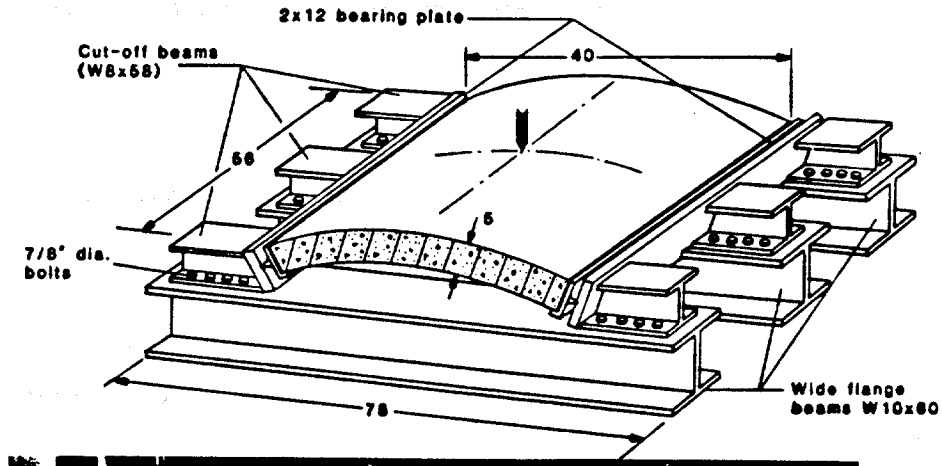

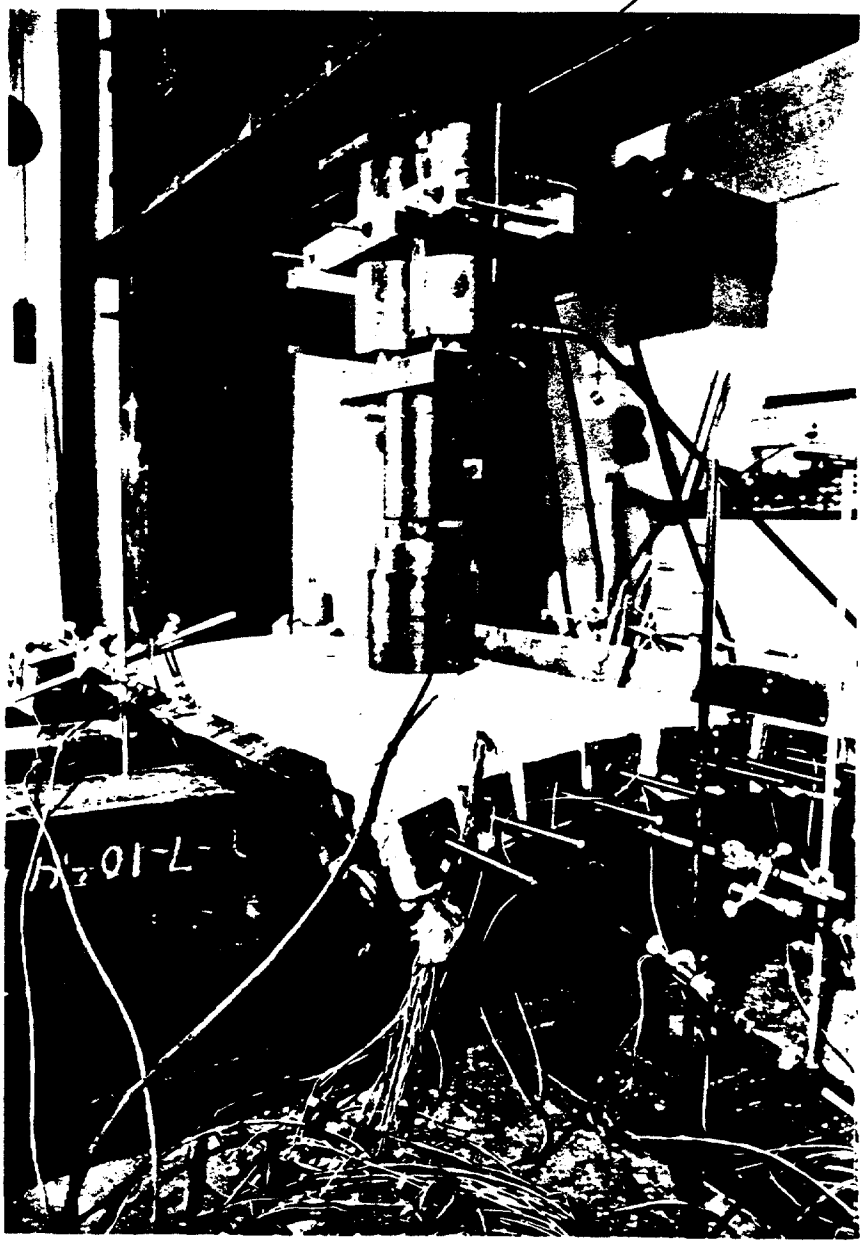

Figure II.9 Arched Shell Test Setup

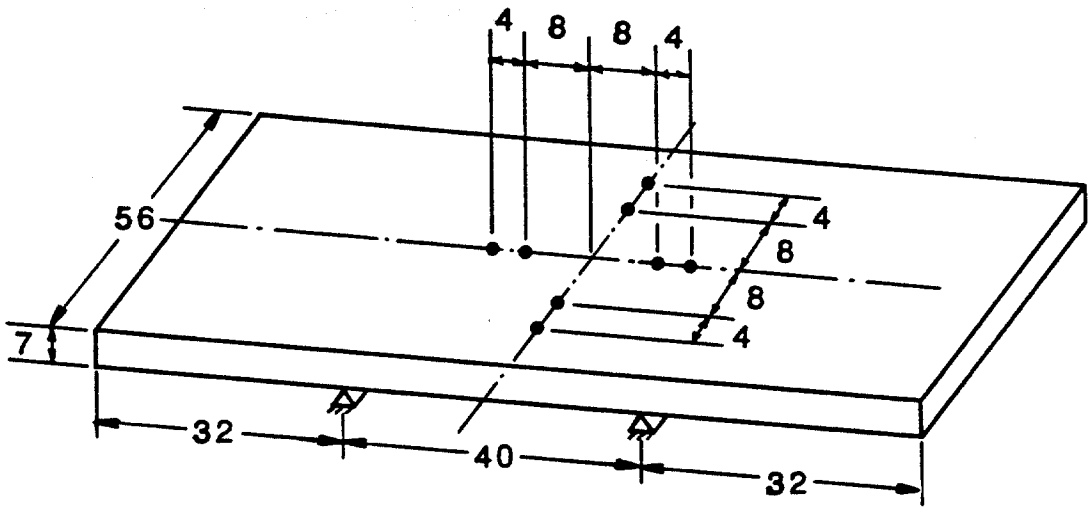

All dimensions in inches

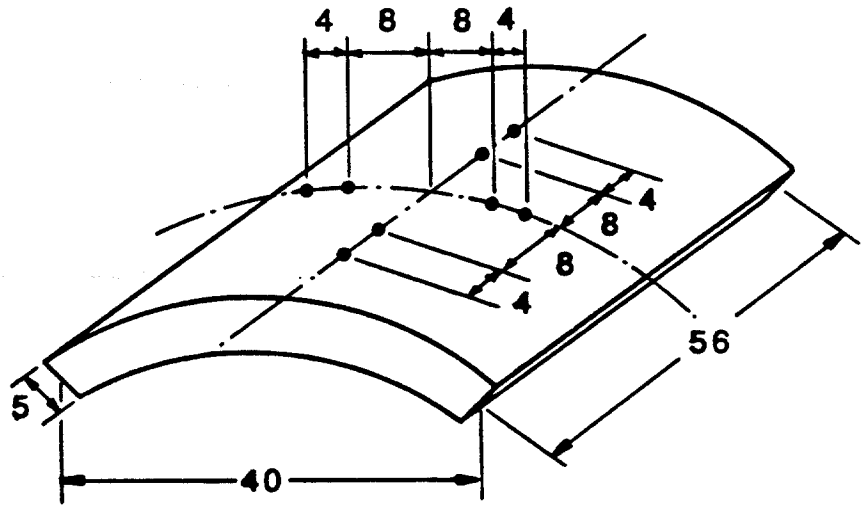

Figure II.10 Locations of Gaged Shear Bars

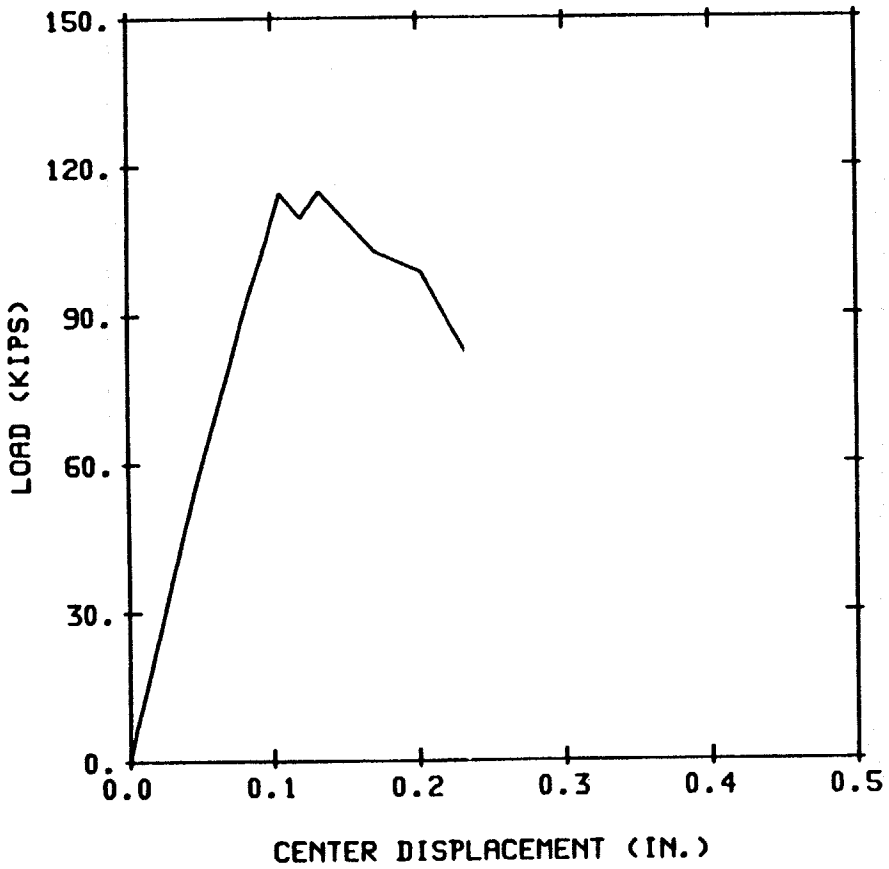

Figure II.11 Load-Center Deflection Curve of FP2-1

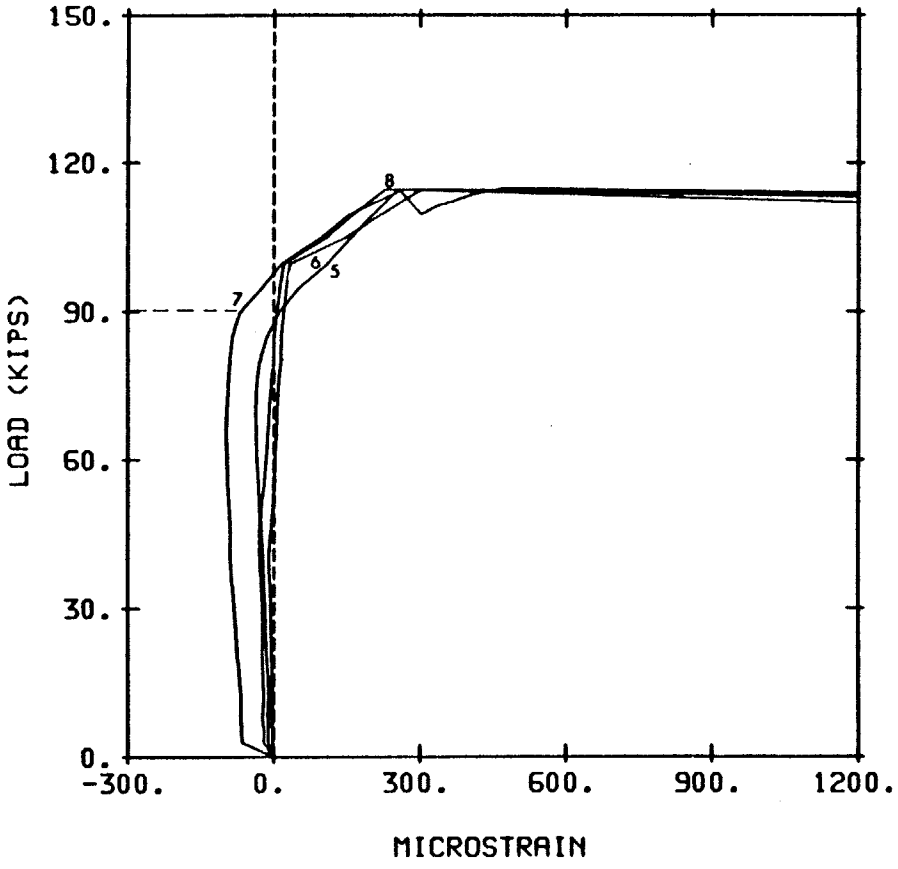

Figure II.12 Load-Strain Curves for Gaged Shear Bars in FP2-1

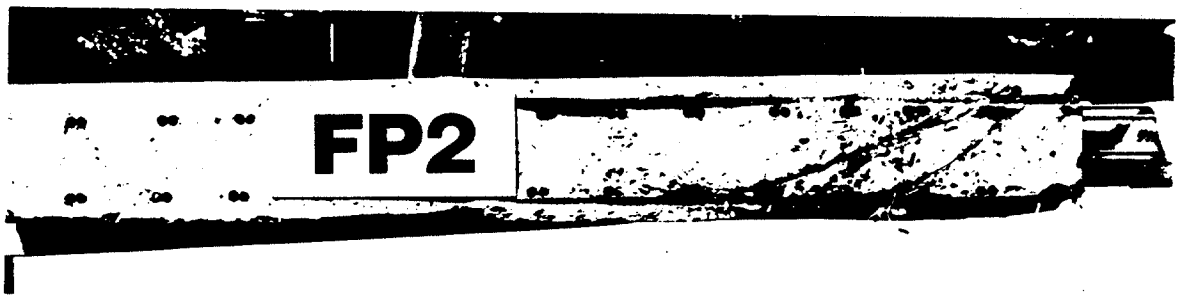

a

b

Figure II.13 Crack Patterns in FP2-1
a) Span Cross-Section
b) Transverse Cross-Section

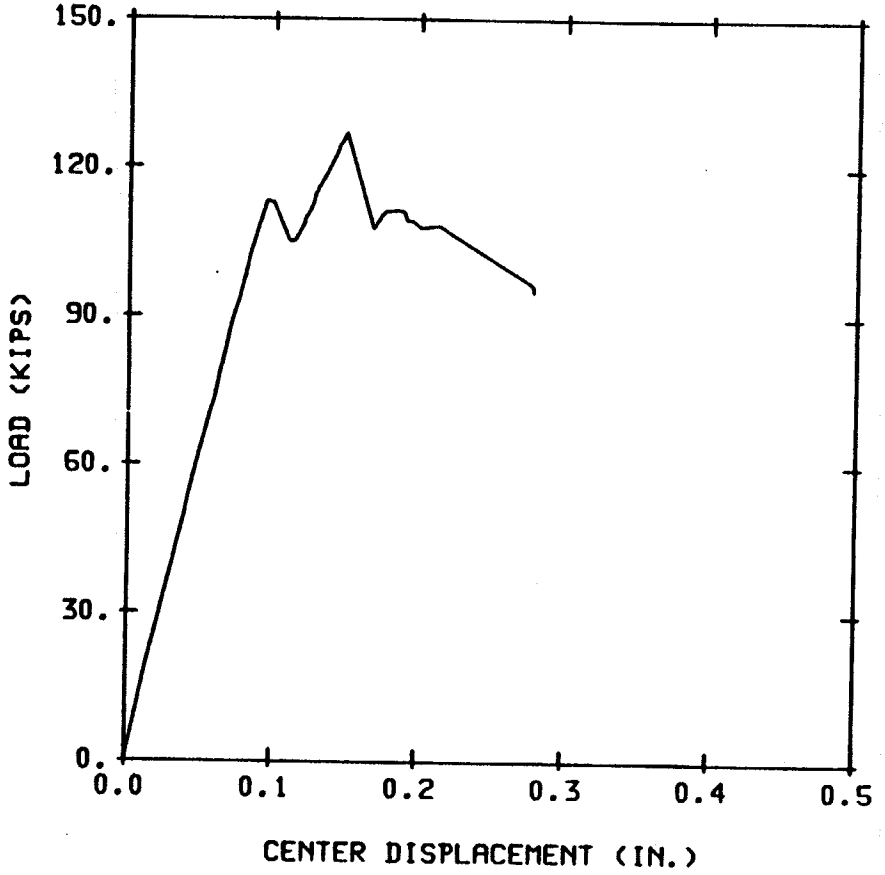

Figure II.14 Load-Center Deflection Curve of FP2-2

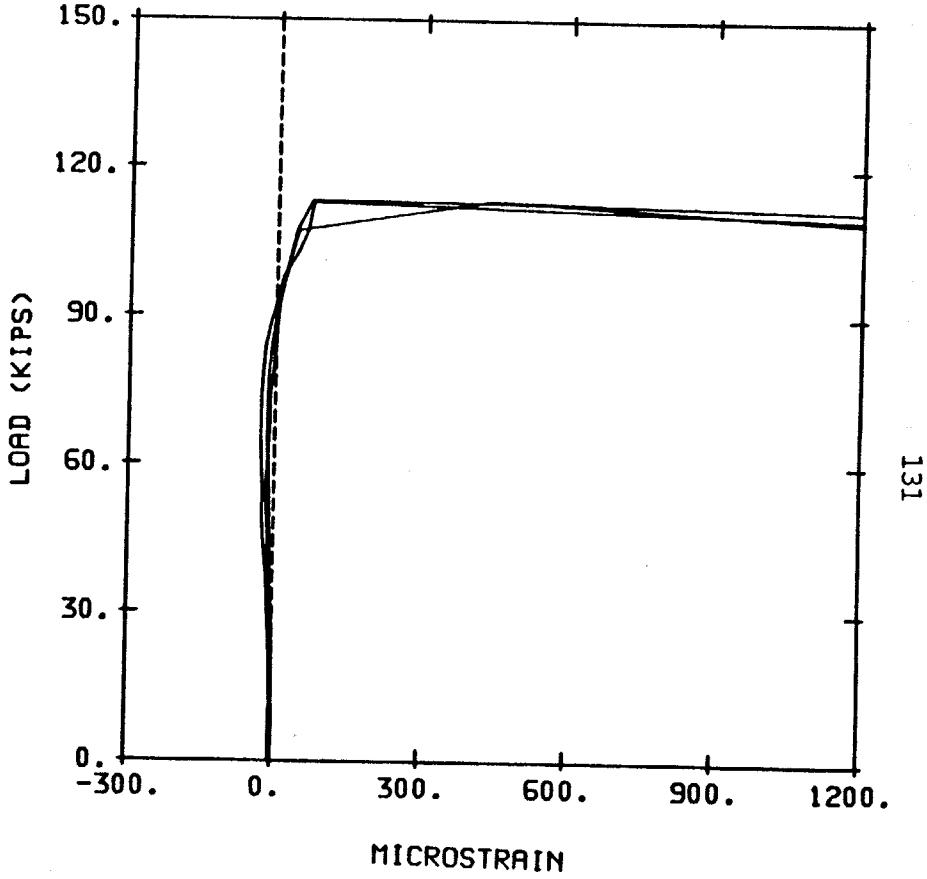

Figure II.15 Load-Strain Curves for Gaged Shear Bars in FP2-2

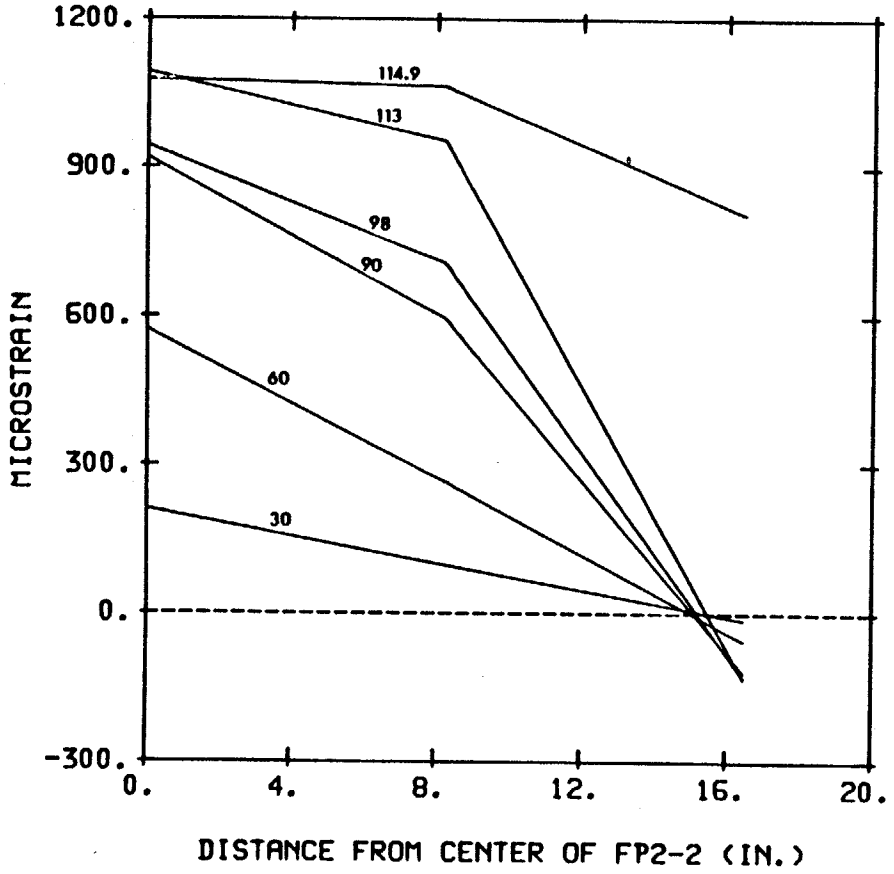

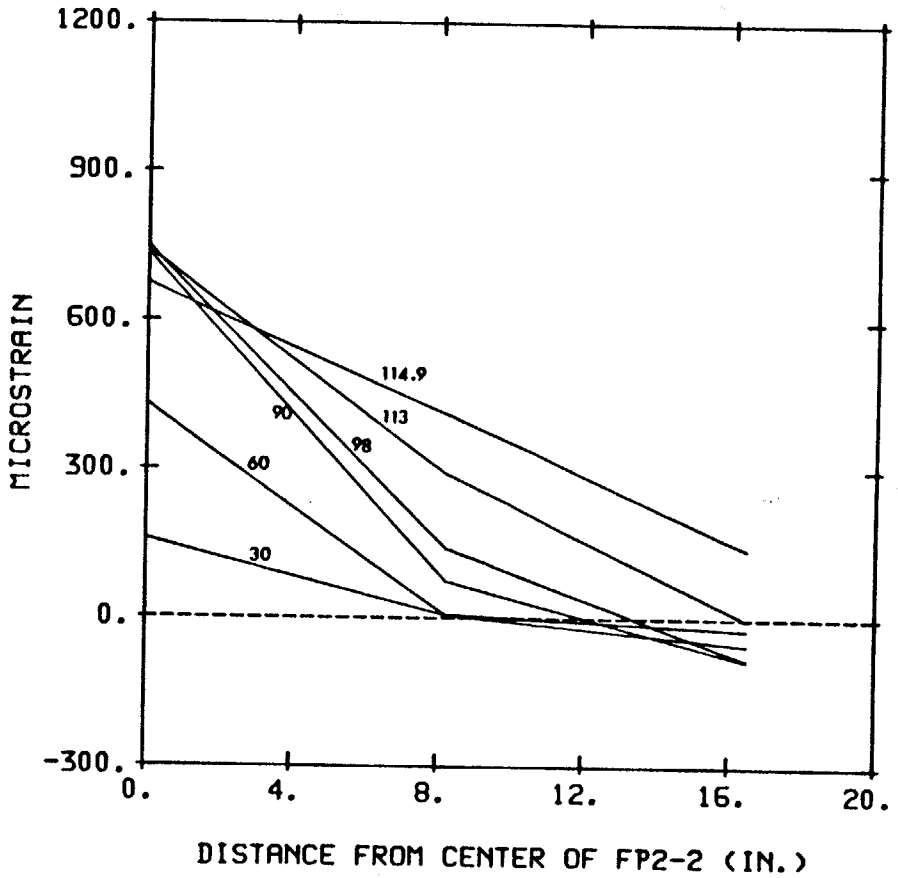

Figure II.16 Flexural Strain Profiles of FP2-2
a) in Span Tension Reinforcement
b) in Transverse Tension Reinforcement

a

b

c

Figure II.17 Crack Patterns in FP2-2
a) Underside
b) Span Cross-Section
c) Transverse Cross-Section

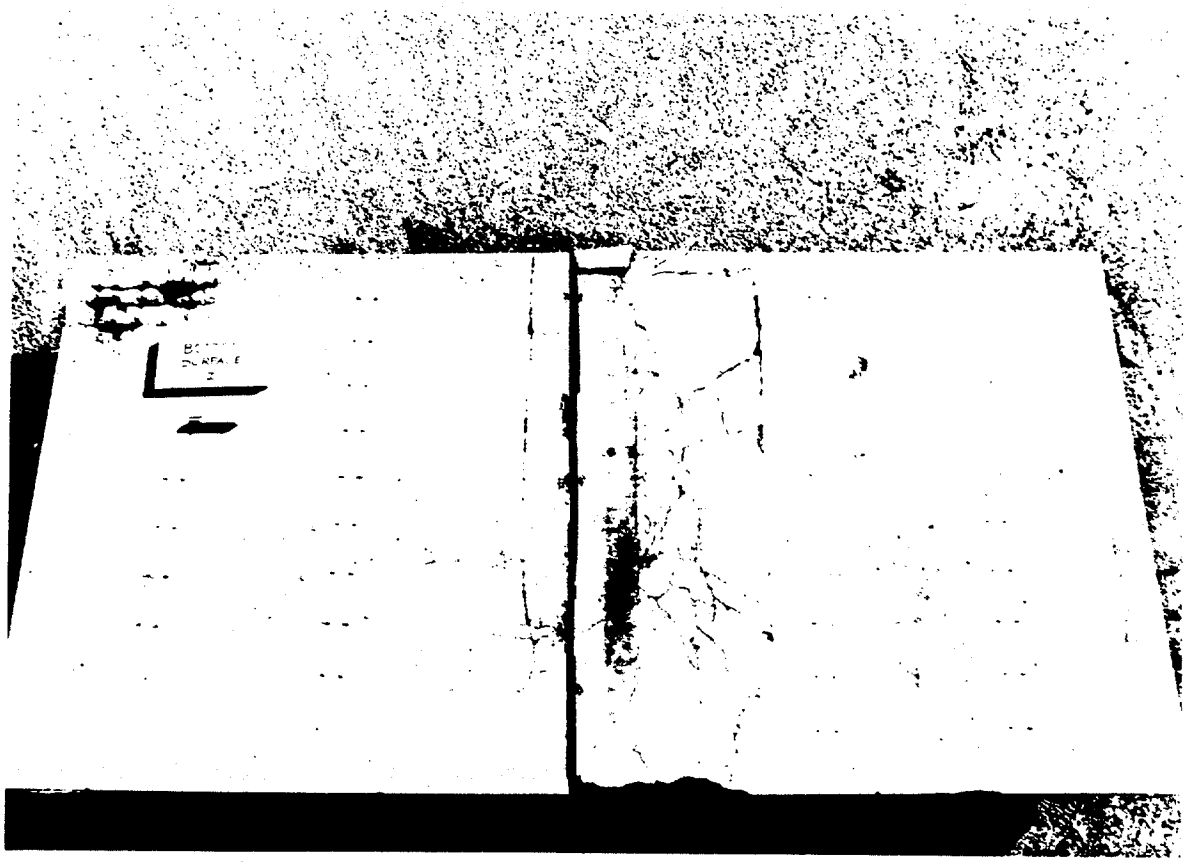

a

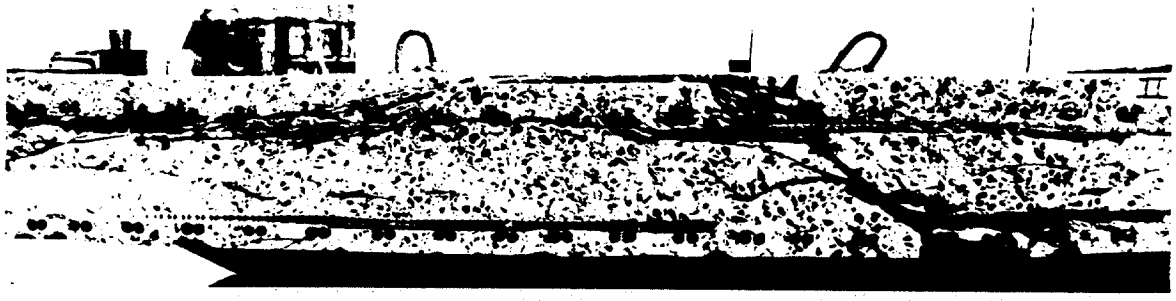

b

Figure II.18 Crack Patterns in IFP2-2
a) Underside

b) Transverse Cross-Section

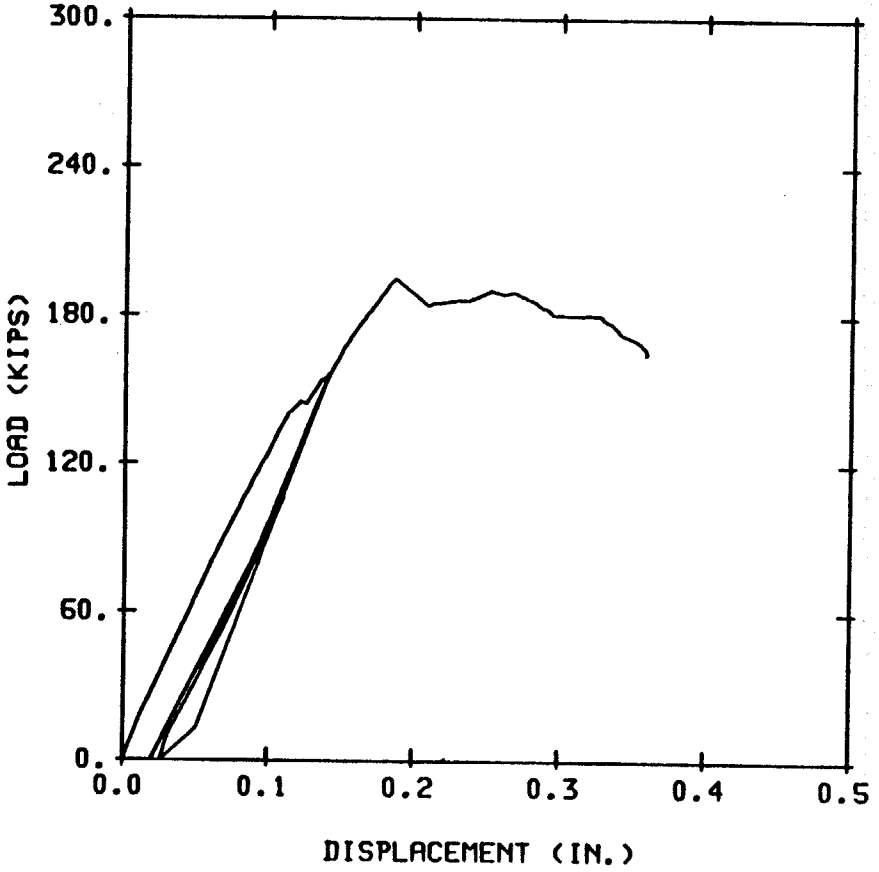

Figure II.19 Load-Center Deflection in FP3

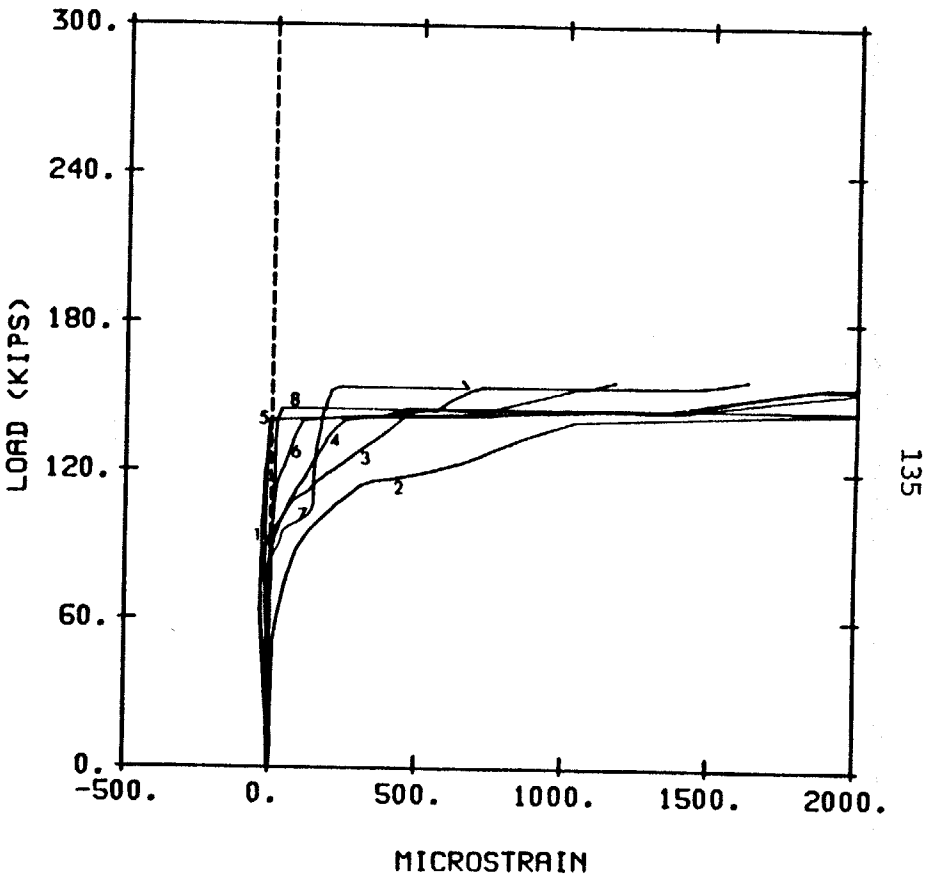

Figure II.20 Load-Strain in Gaged Shear Bars in FP3

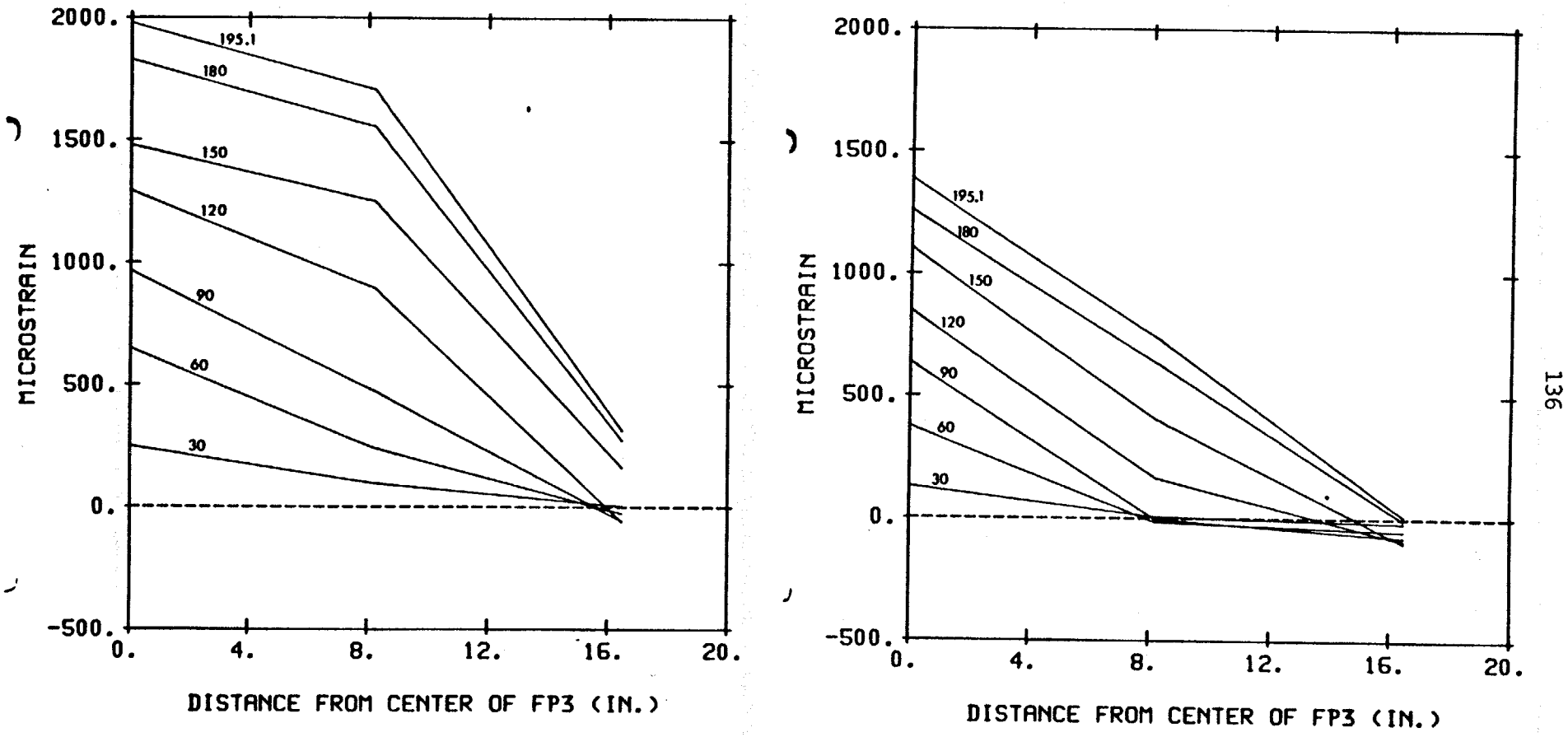

Figure II.21 Flexural Strain Profiles of FP3
a) in Span Tension Reinforcement
b) in Transverse Tension Reinforcement

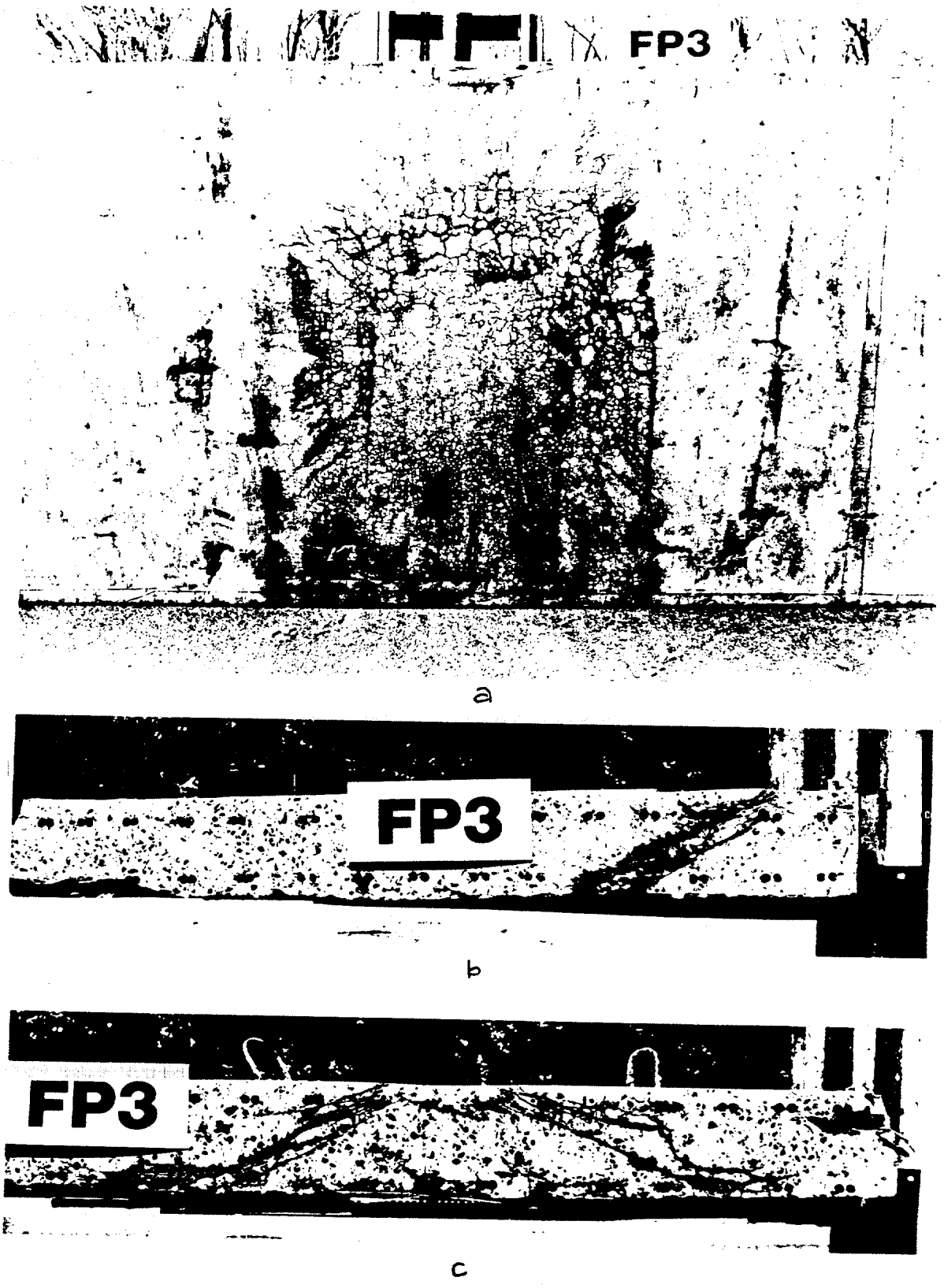

Figure II.22 Crack Patterns in FP3
a) Underside
b) Span Cross-Section
c) Transverse Cross-Section

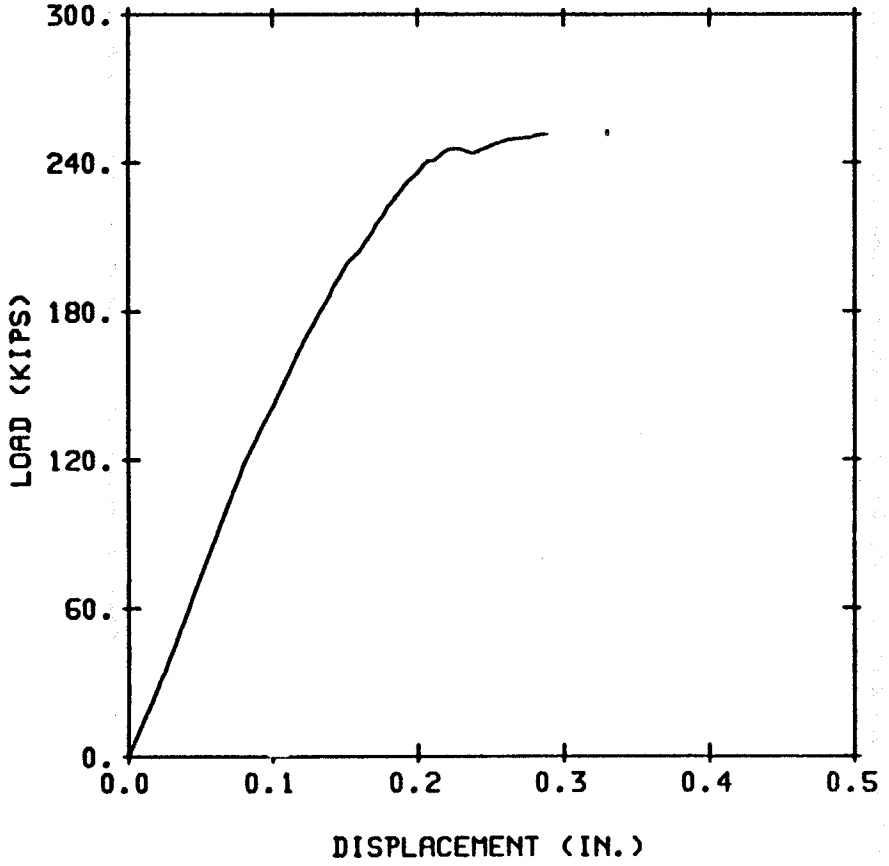

Figure II.23 Load-Center Deflection in FP4

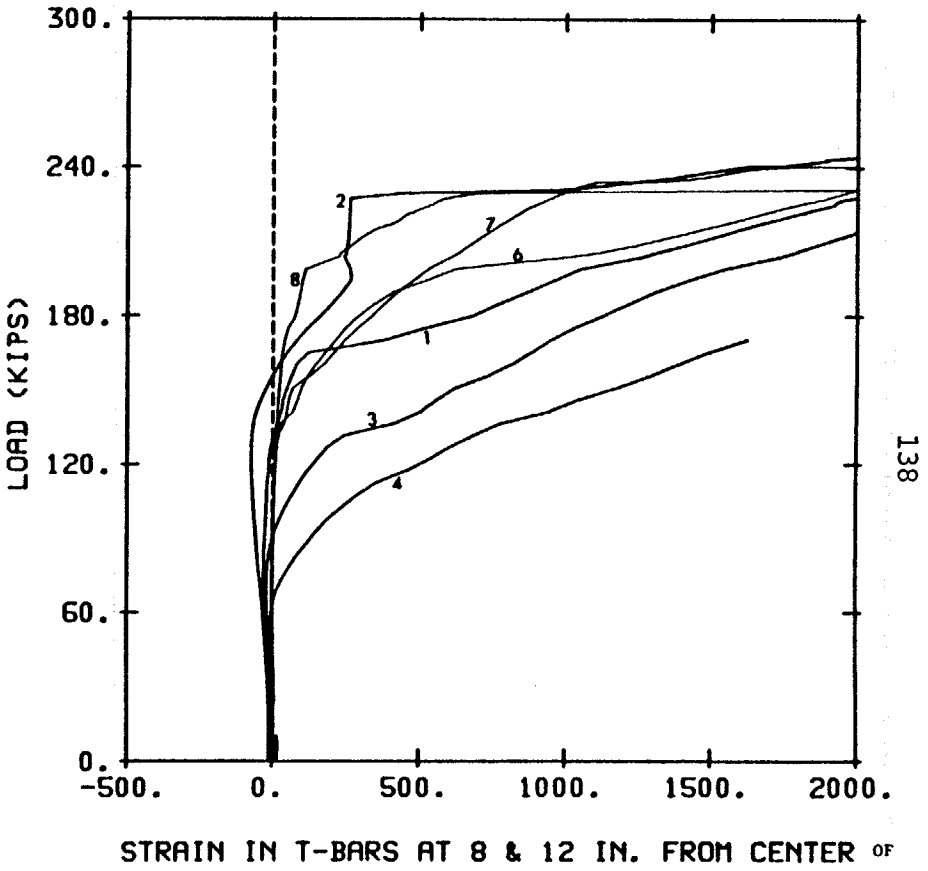

Figure II.24 Load-Strain in Gaged Shear Bars in FP4

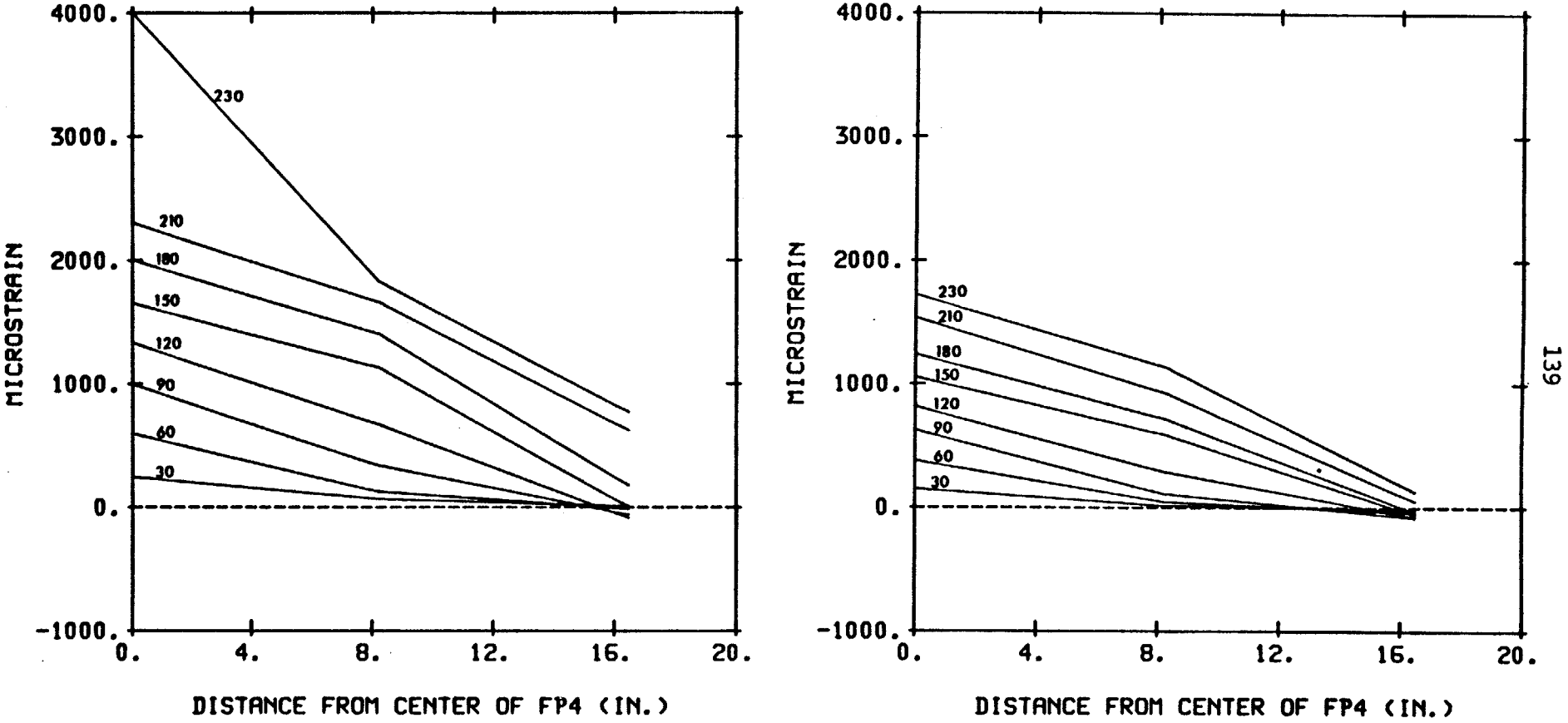

Figure II.25 Flexural Strain Profiles of FP4
a) in Span Tension Reinforcement
b) in Transverse Tension Reinforcement

a

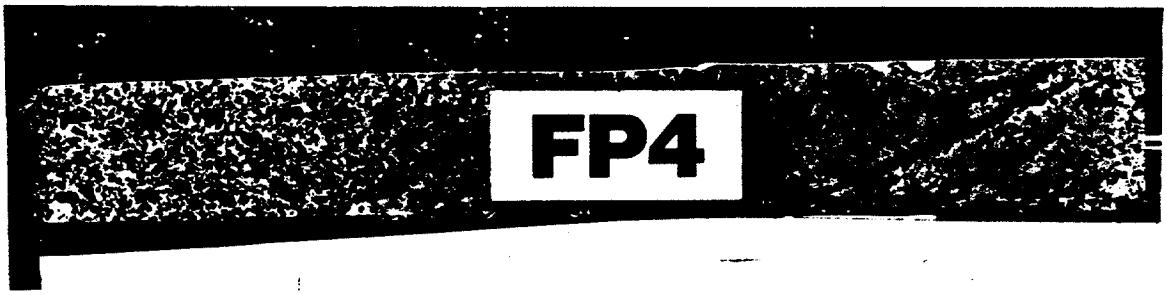

b

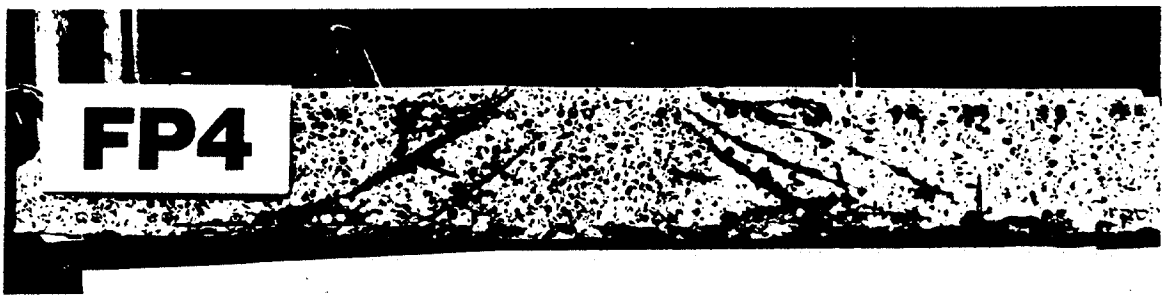

c

Figure II.26 Crack Patterns in FP4
a) Underside
b) Span Cross-Section
c) Transverse Cross-Section

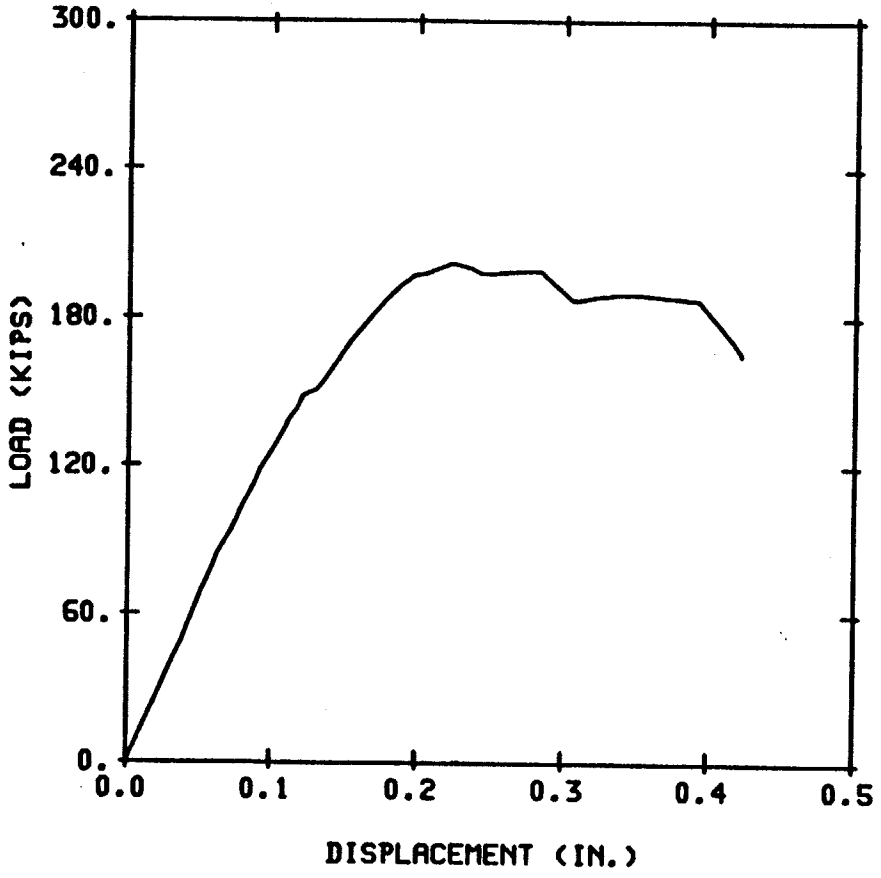

Figure II.27 Load-Center Deflection curve in FP5

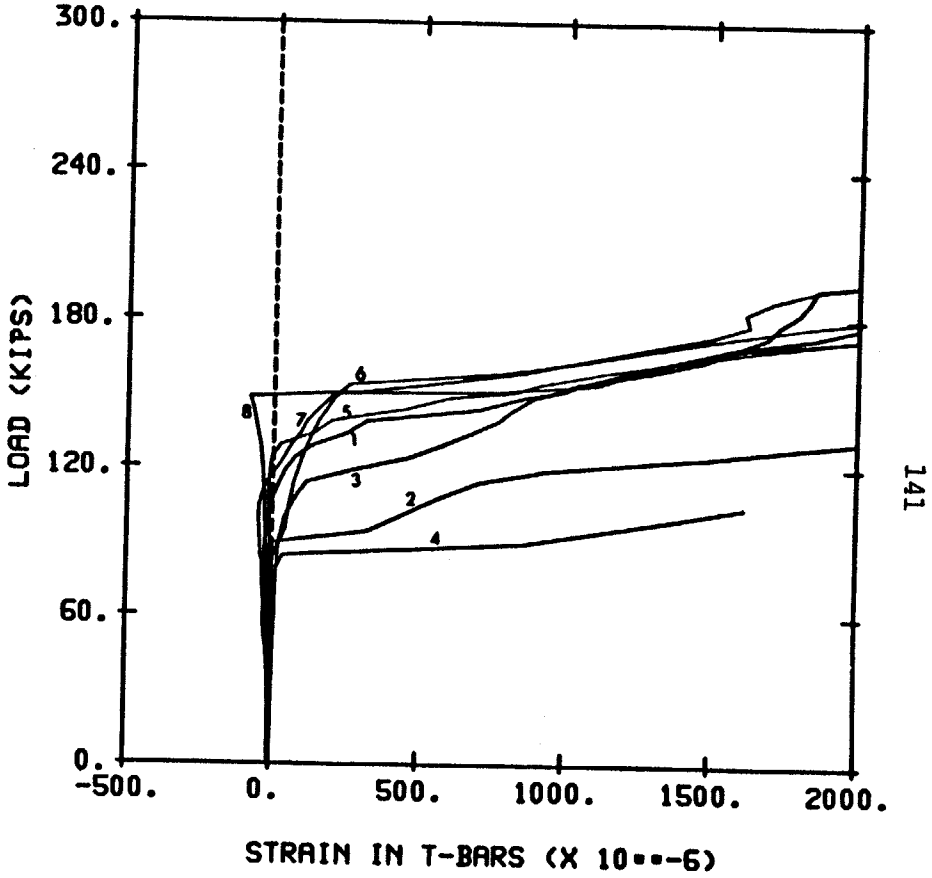

Figure II.28 Load-Strain Curves in Gaged Shear Bars in FP5

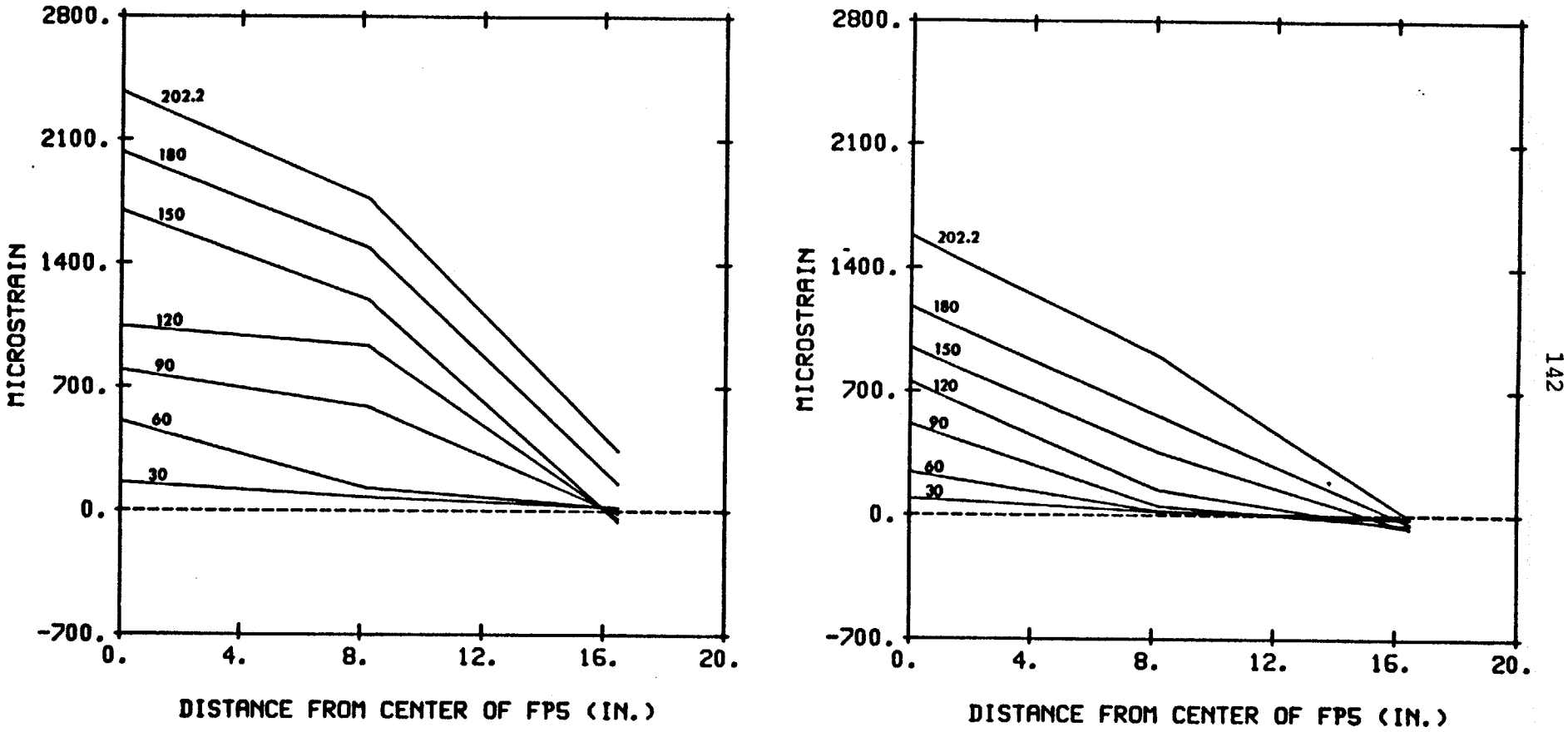

Figure II.29 Flexural Strain Profiles of FP5
a) in Span Tension Reinforcement
b) in Transverse Tension Reinforcement

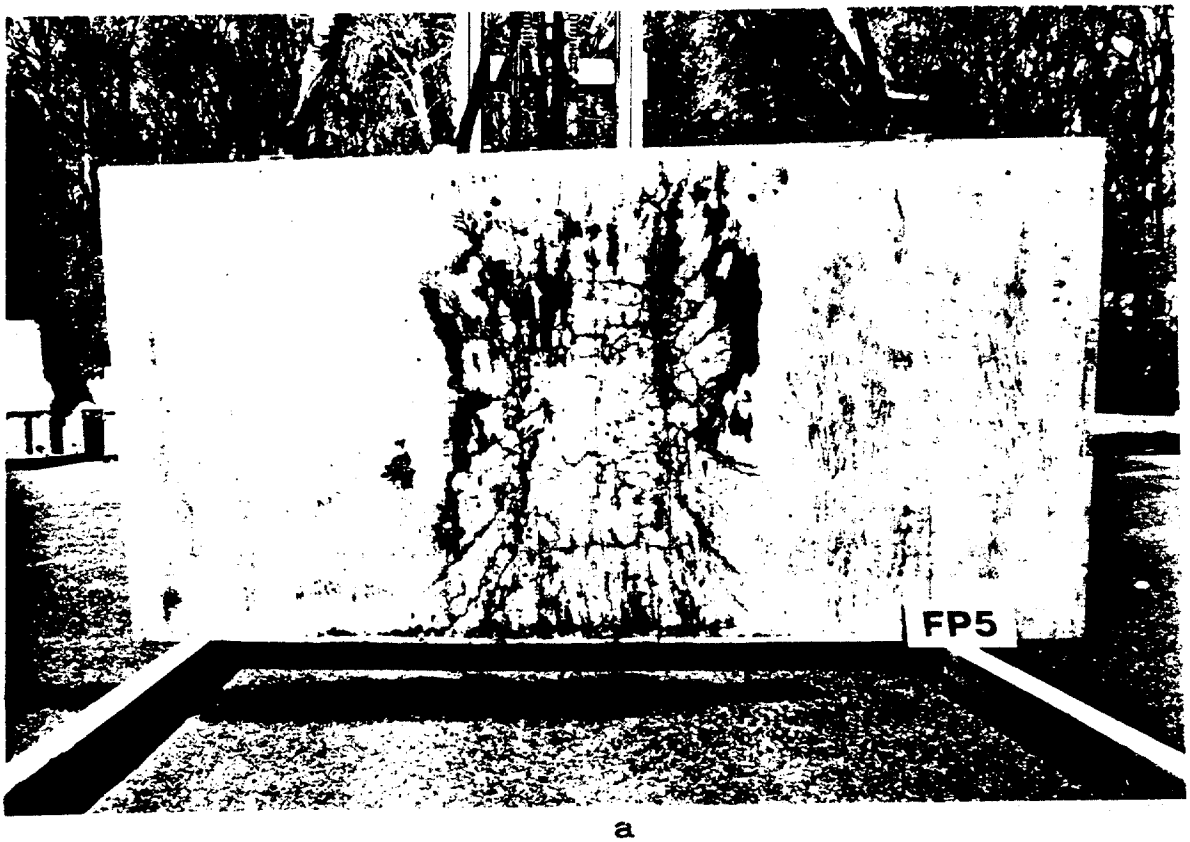

a

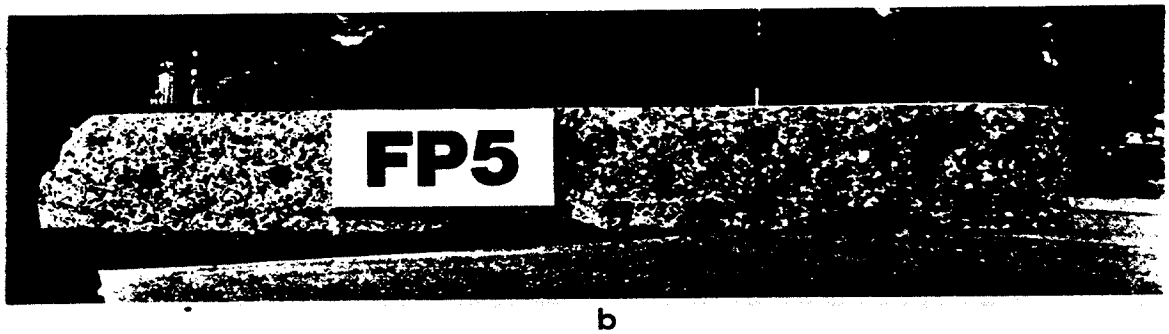

b

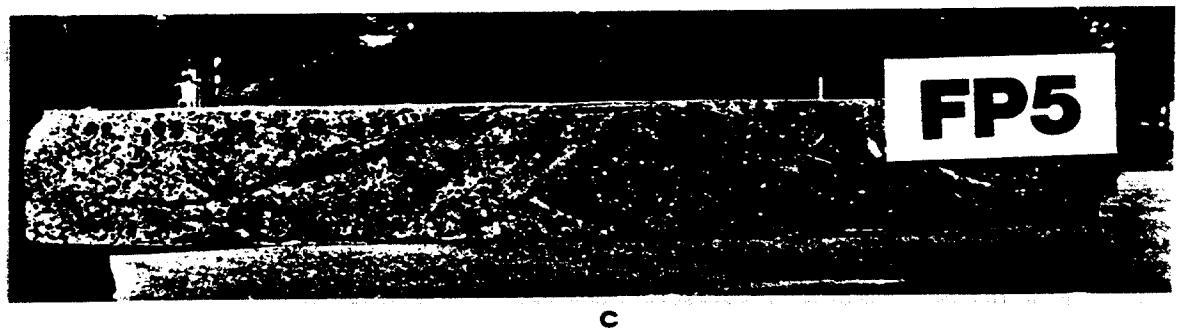

c

Figure II.30 Crack Patterns in FP5
a) Underside
b) Span Cross-Section
c) Transverse Cross-Section

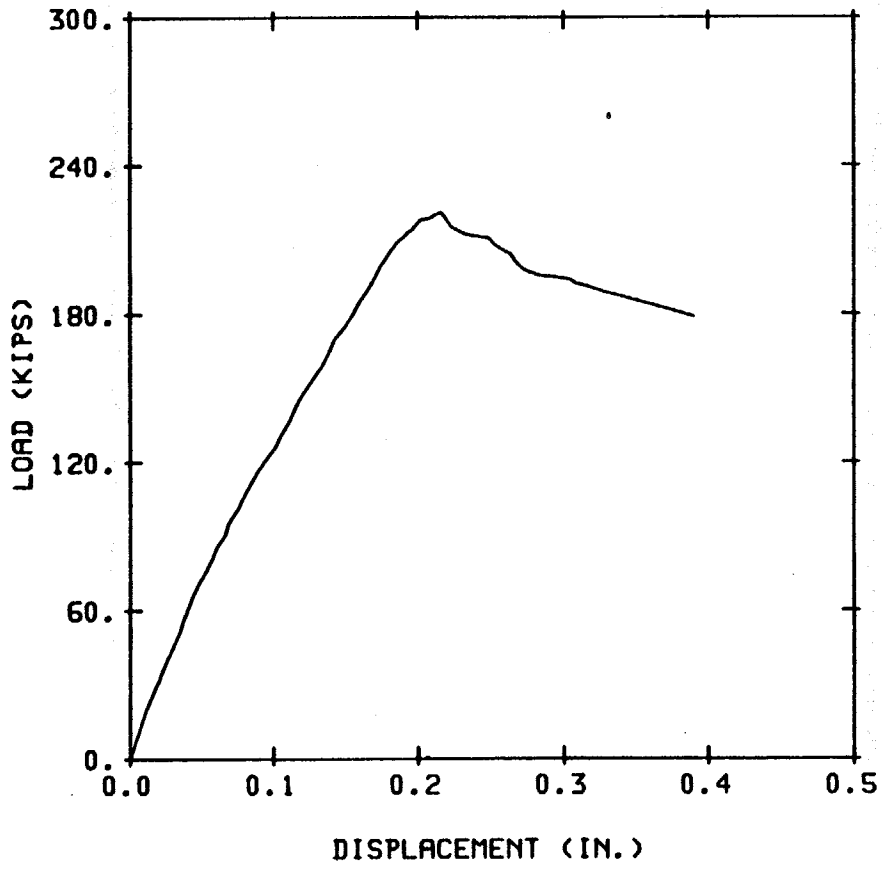

Figure II.31 Load-Center Deflection Curve in FP6

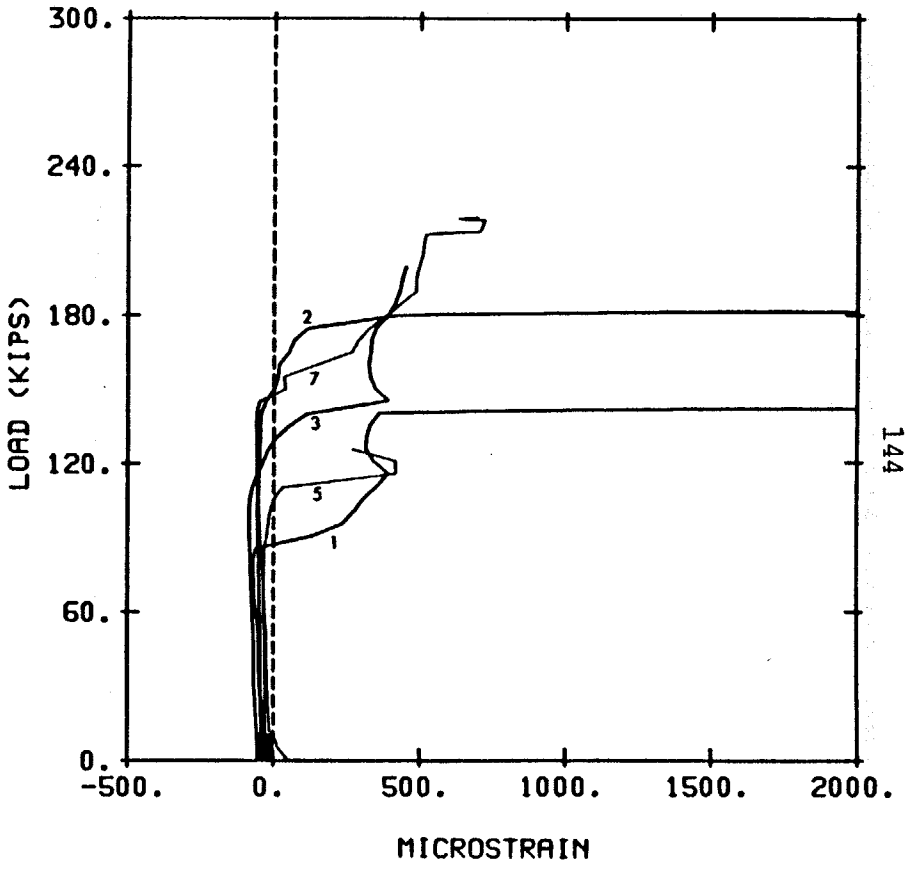

Figure II.32 Load-Strain Curves in Gaged Shear Bars in FP6

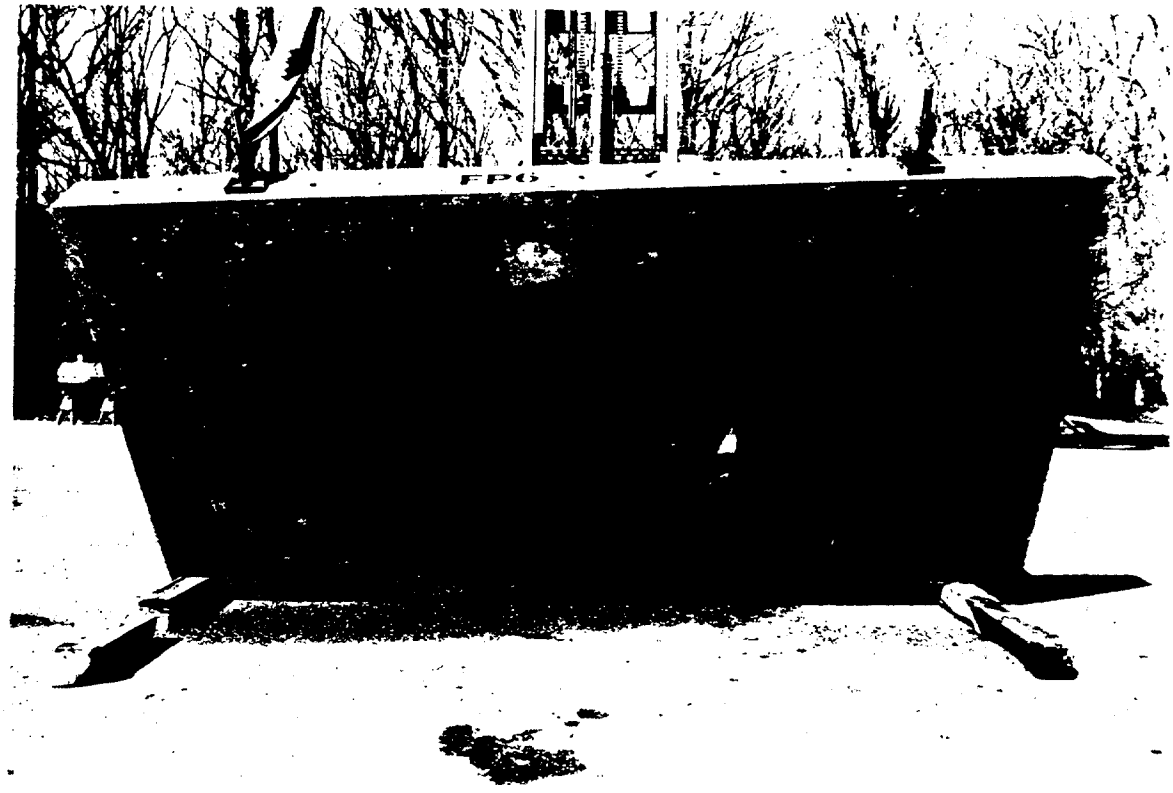

a

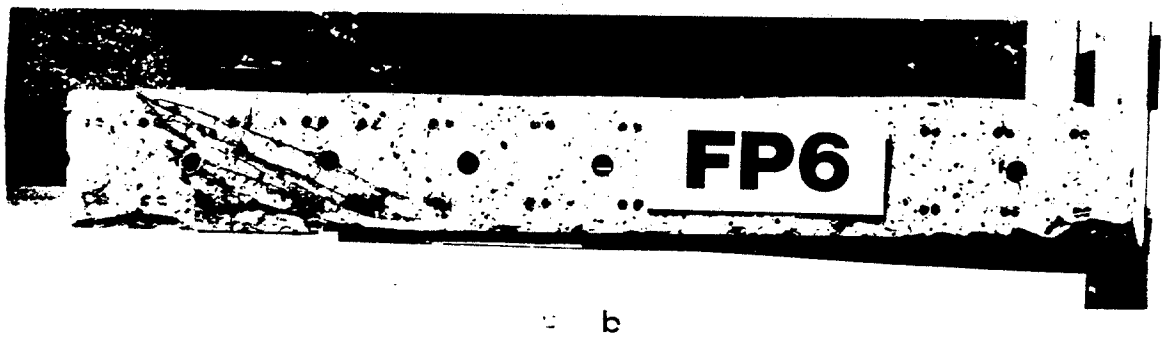

b

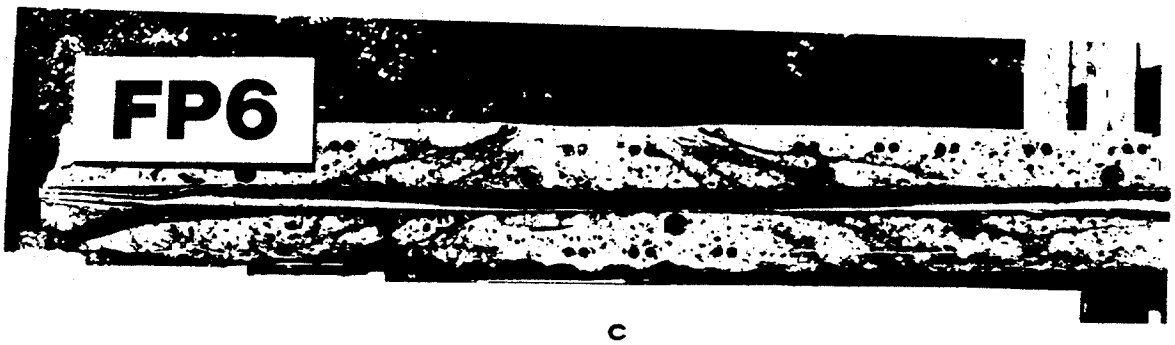

c

Figure II.33 Crack Patterns in FP6
a) Underside
b) Span Cross-Section
c) Transverse Cross-Section

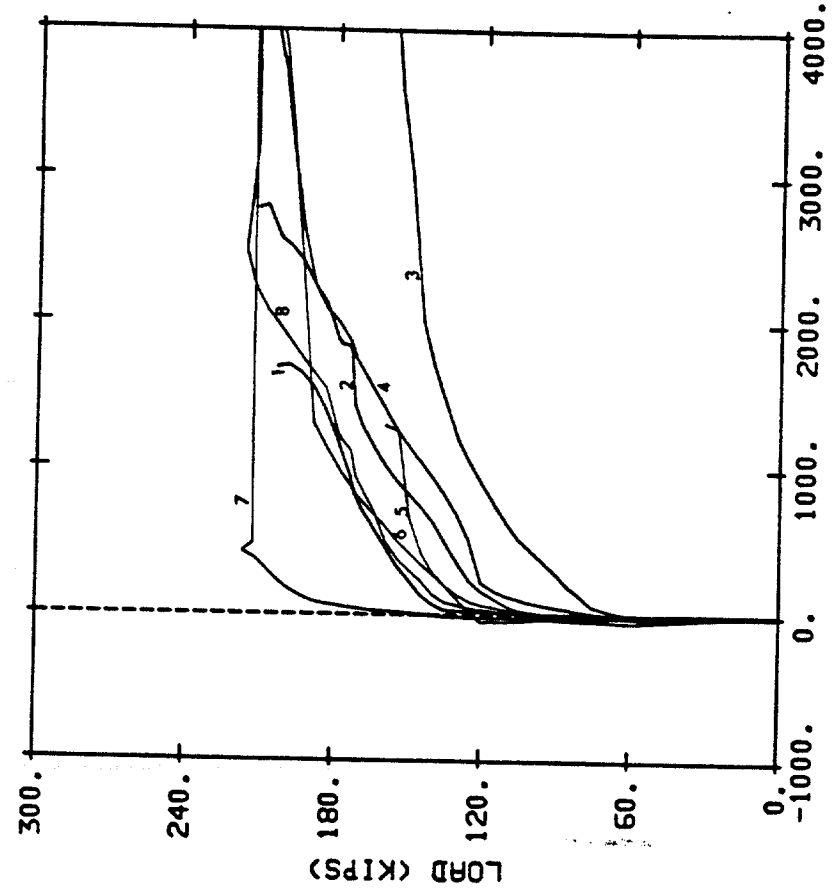

Figure II.35 Load-Strain Curves in Gaged Shear Bars in FP1

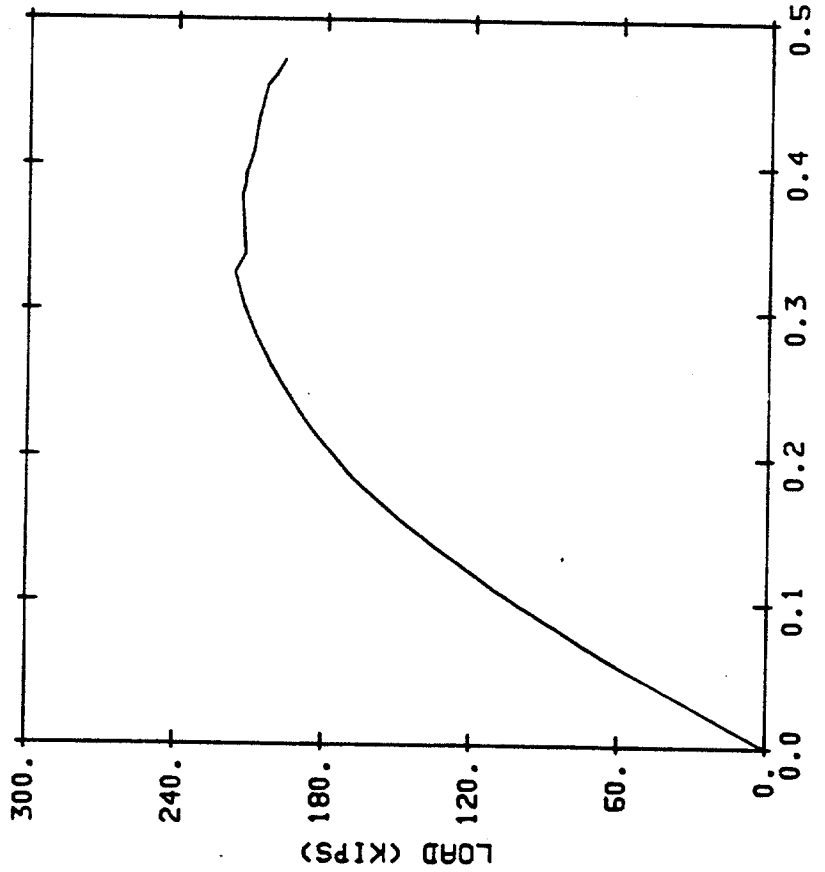

Figure II.34 Load-Center Deflection Curve in FP1

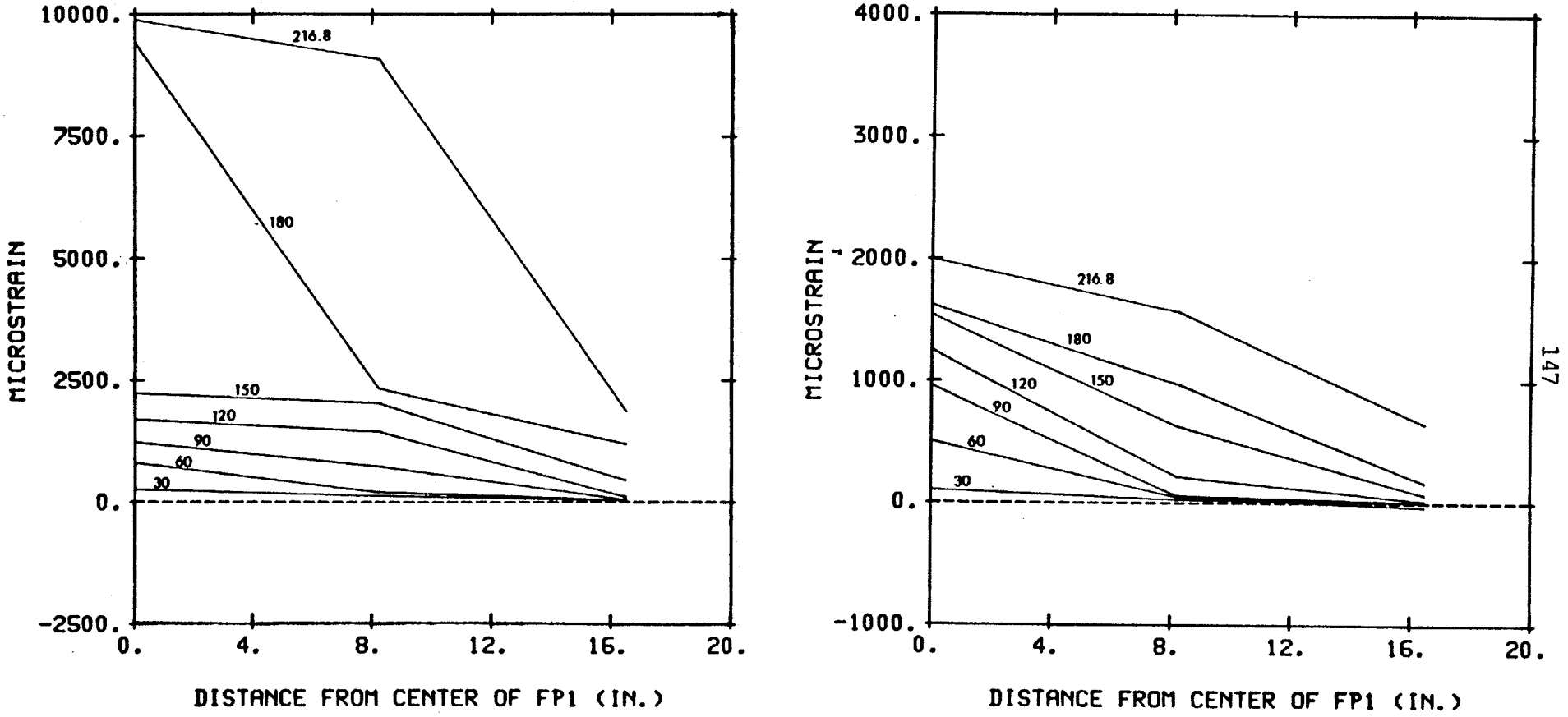

Figure II.36 Flexural Strain Profiles of FP1
a) in Span Tension Reinforcement
b) in Transverse Tension Reinforcement

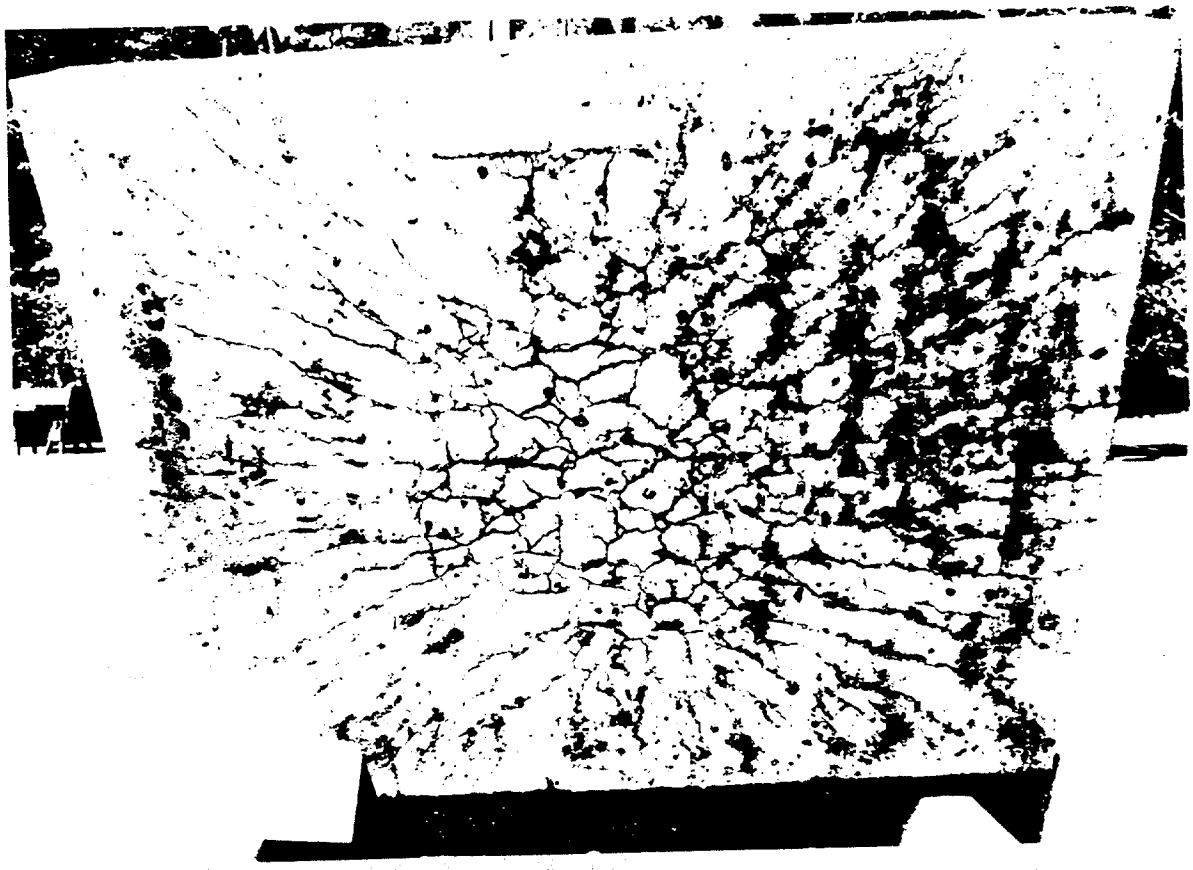

a

b

Figure II.37 Crack Patterns in FP1
a) Underside

b) Transverse Cross-Section

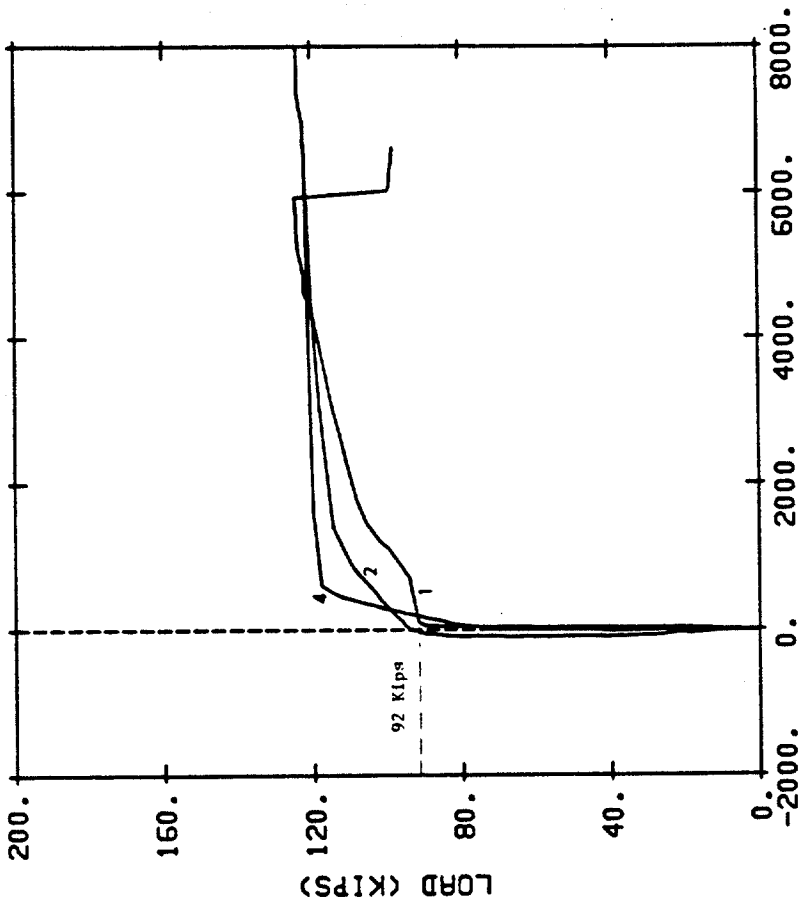

Figure II.39 Load-Strain Curves in Gaged Shear Bars in AS9

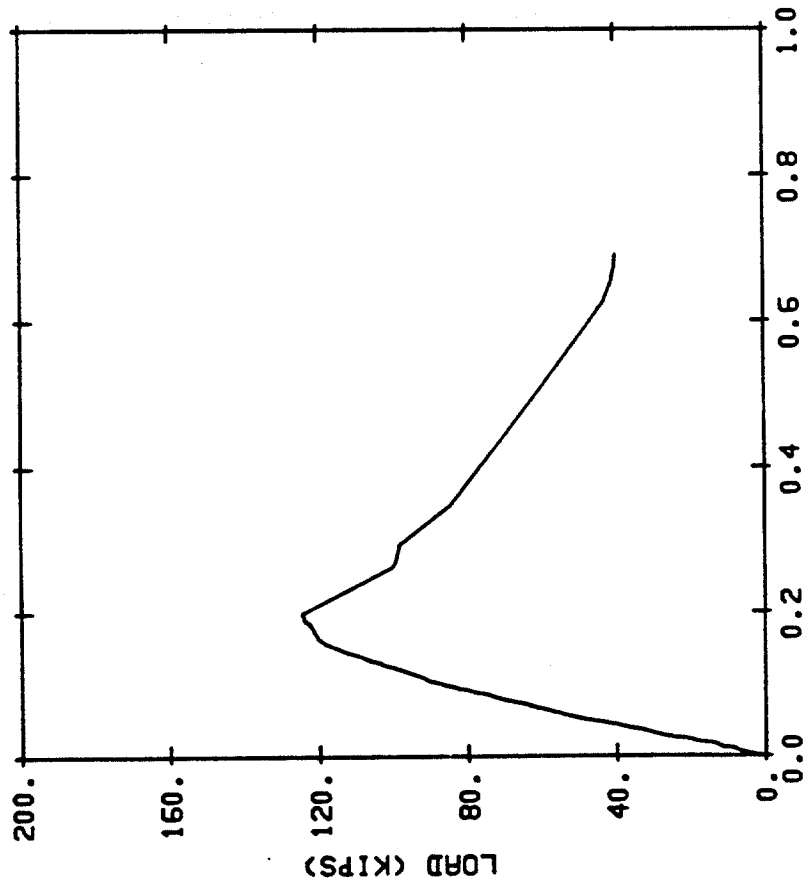

Figure II.38 Load-Center Deflection Curve in AS9

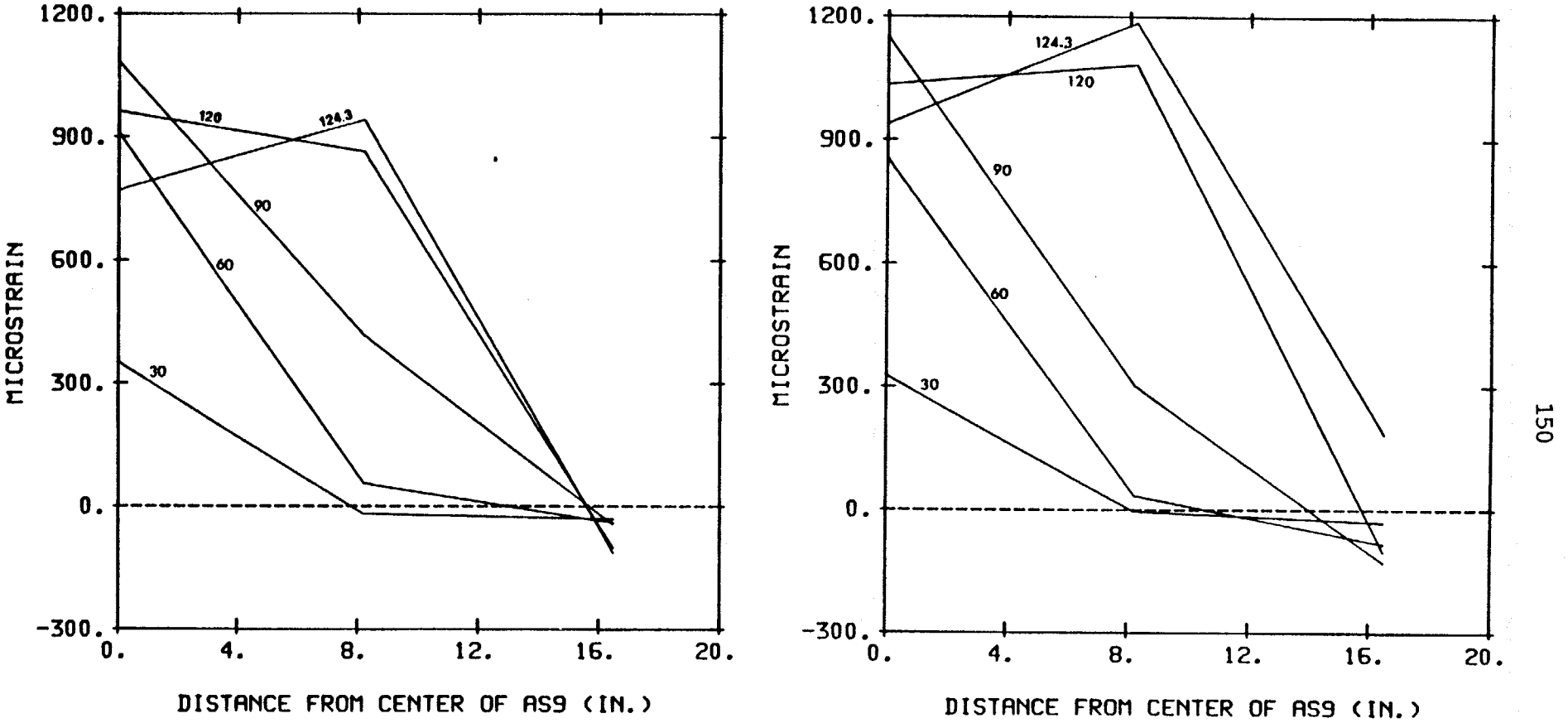

Figure II.40 Flexural Strain Profiles of AS9
a) in Span Tension Reinforcement
b) in Transverse Tension Reinforcement
c) in Span Compression Reinforcement

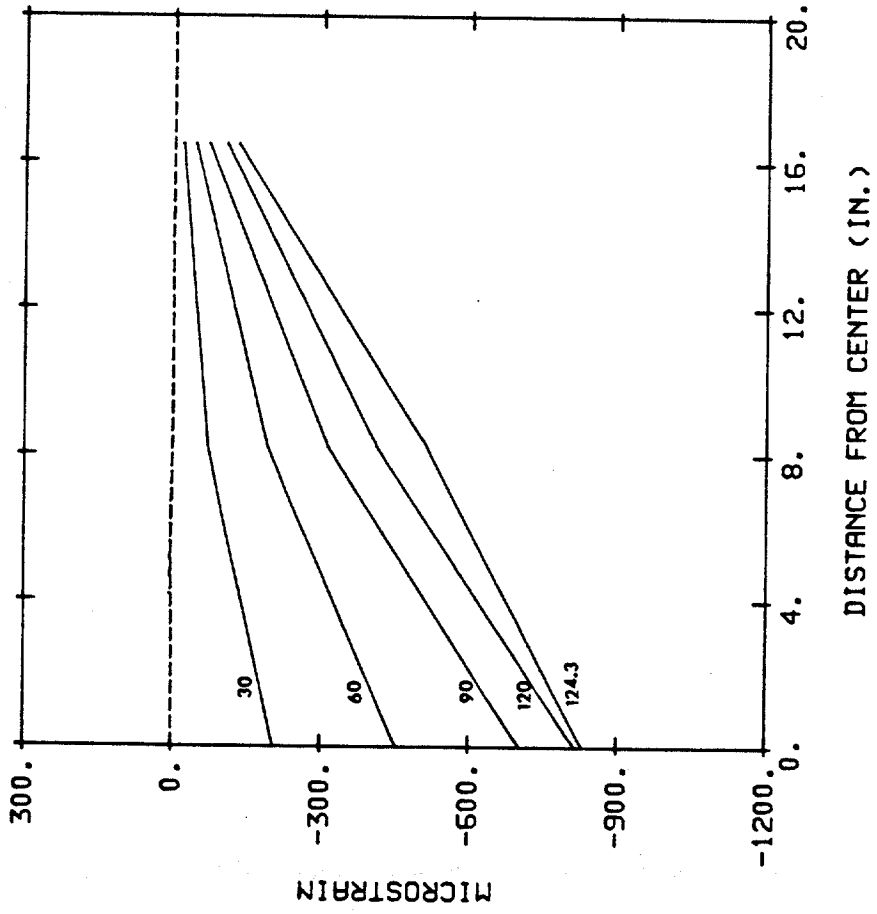

Figure II.40 (continued)

a

b

c

Figure II.41 Crack Patterns in AS9
a) Underside
b) Span Cross-Section
c) Transverse Cross-Section

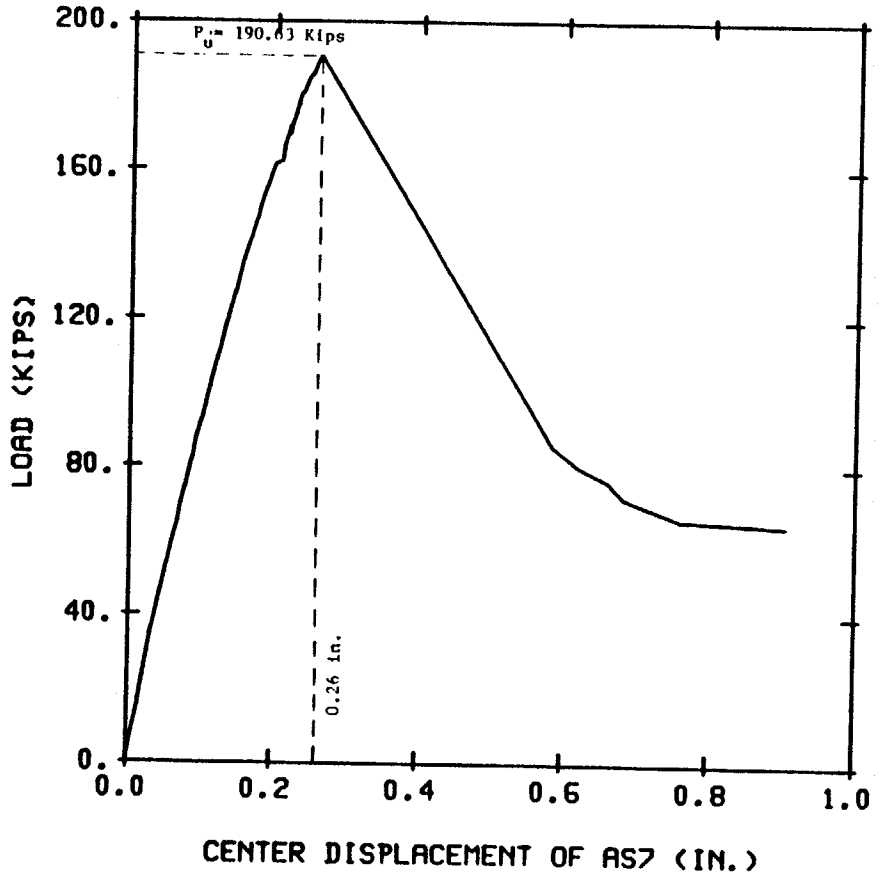

Figure II.42 Load Center Deflection Curve in AS7

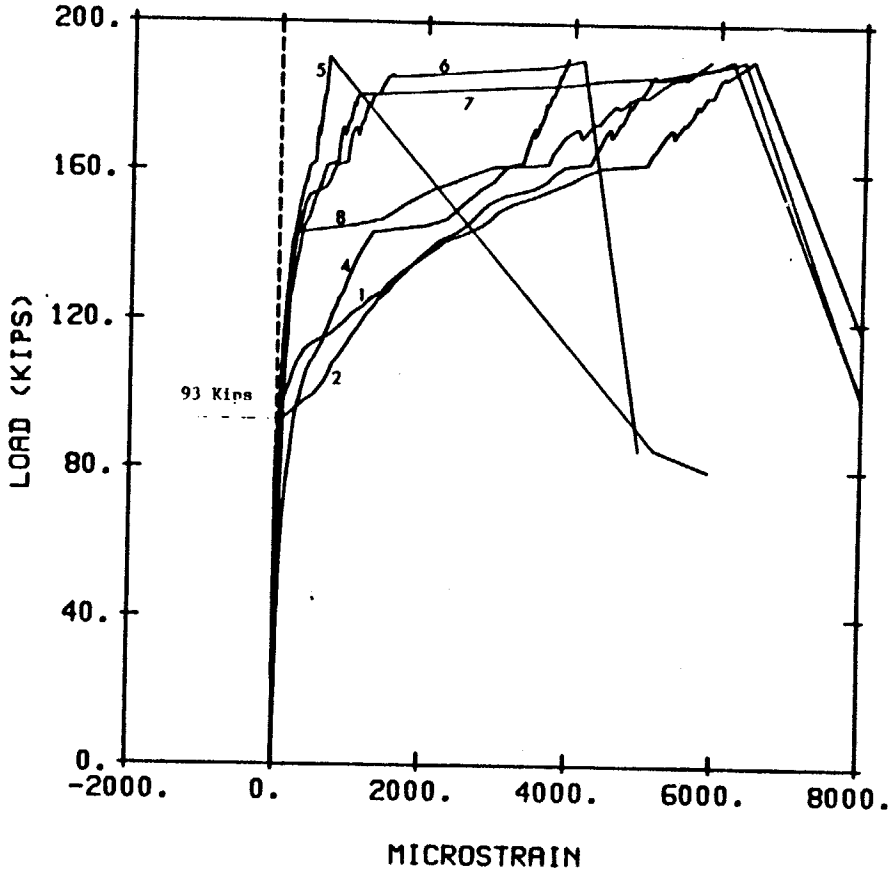

Figure II.43 Load-Strain Curves in Gaged Shear Bars in AS7

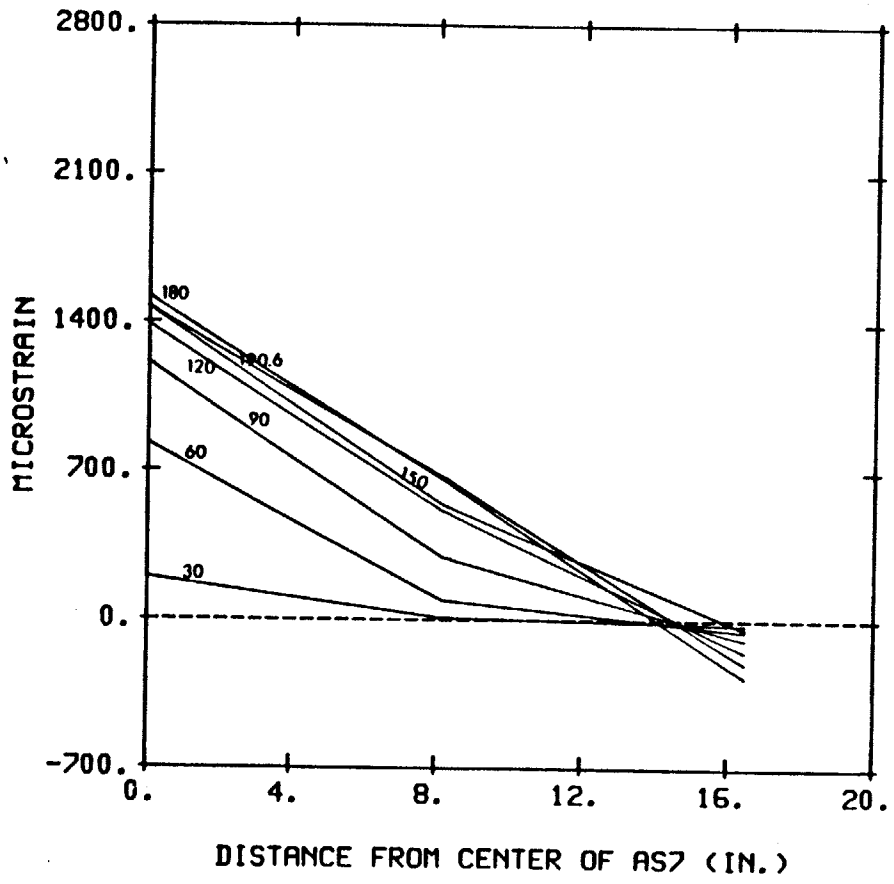

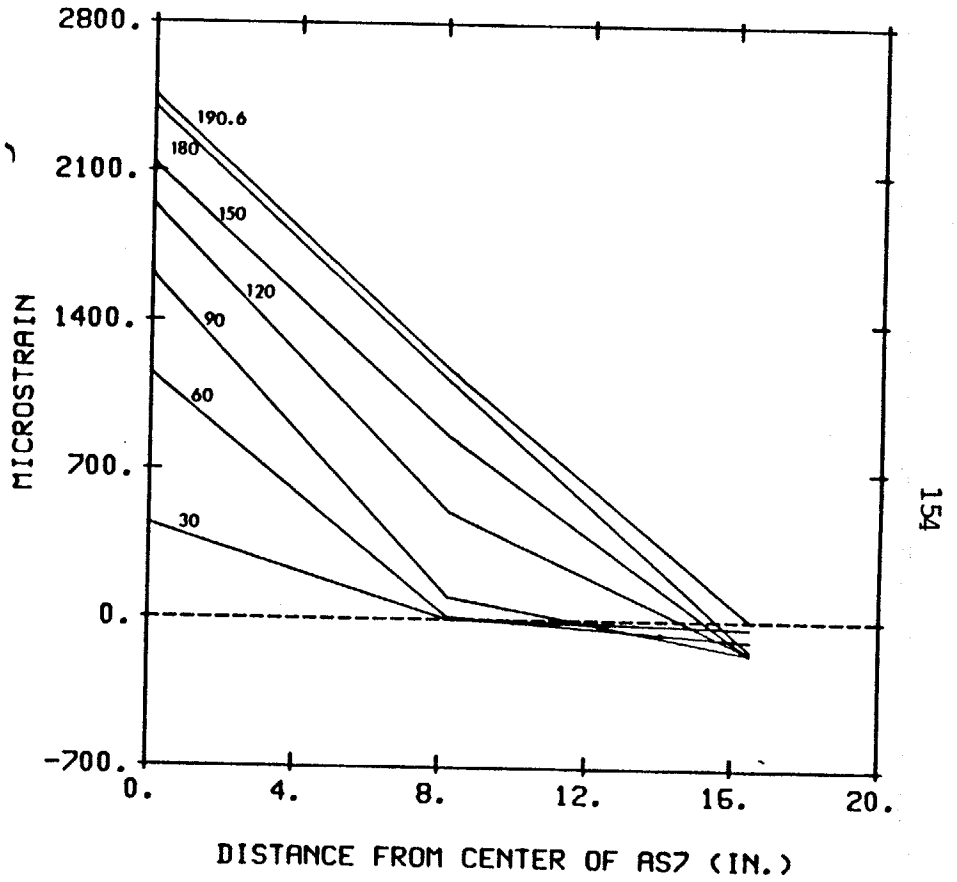

Figure II.44 Flexural Strain Profiles of AS7
a) in Span Tension Reinforcement
b) in Transverse Tension Reinforcement
c) in Span Compression Reinforcement

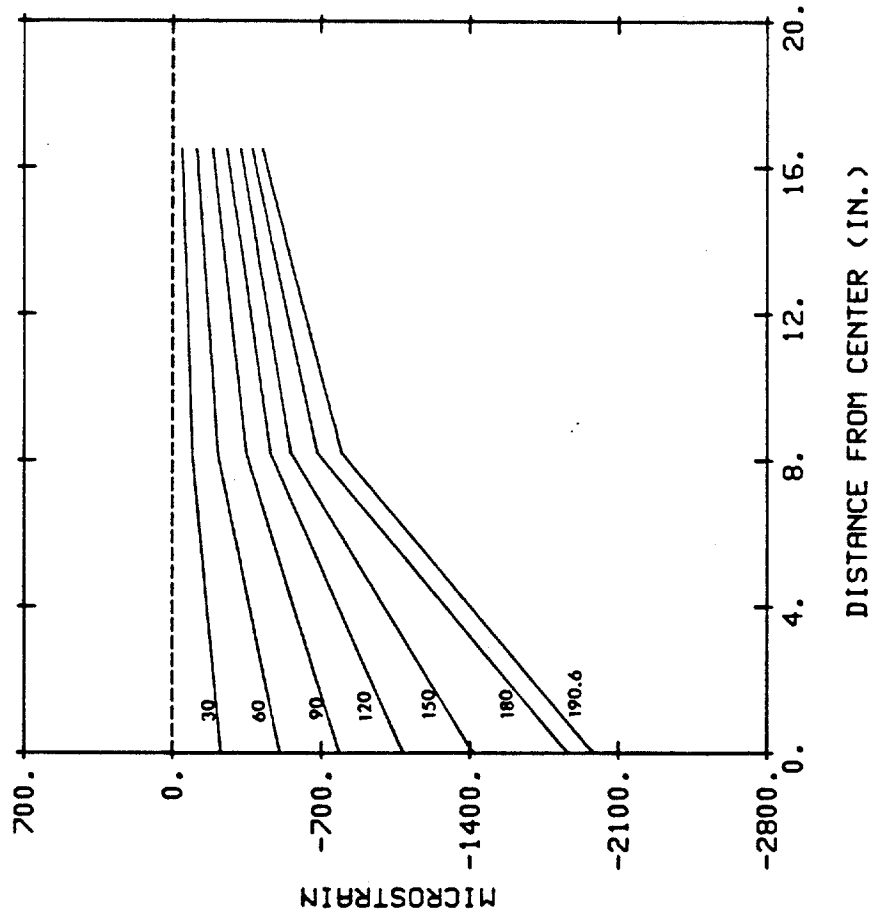

Figure II.44 (continued)

a

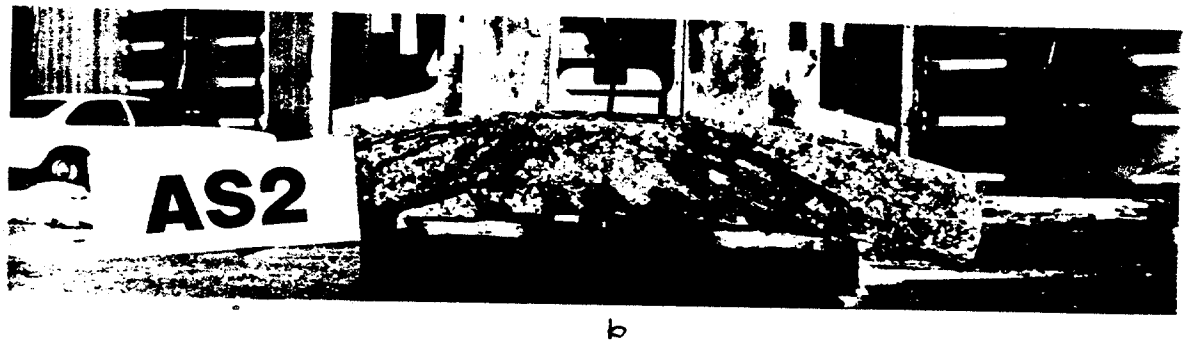

b

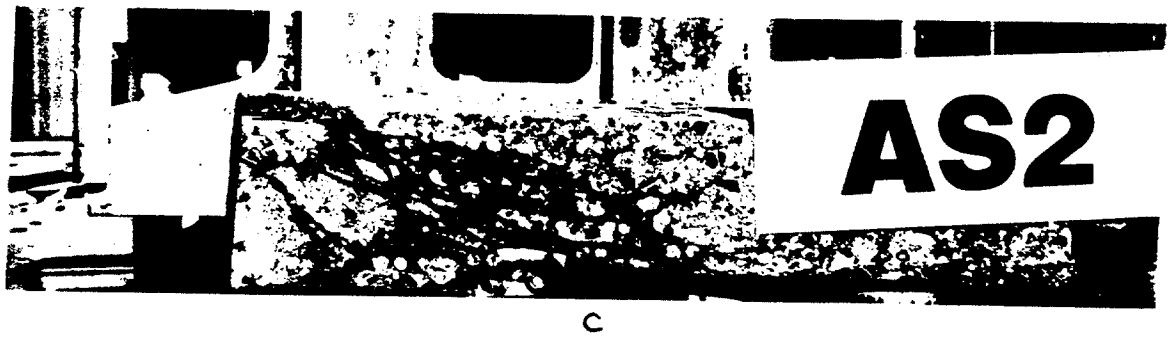

c

Figure II.45 Crack Patterns in AS7
a) Underside
b) Span Cross-Section
c) Transverse Cross-Section

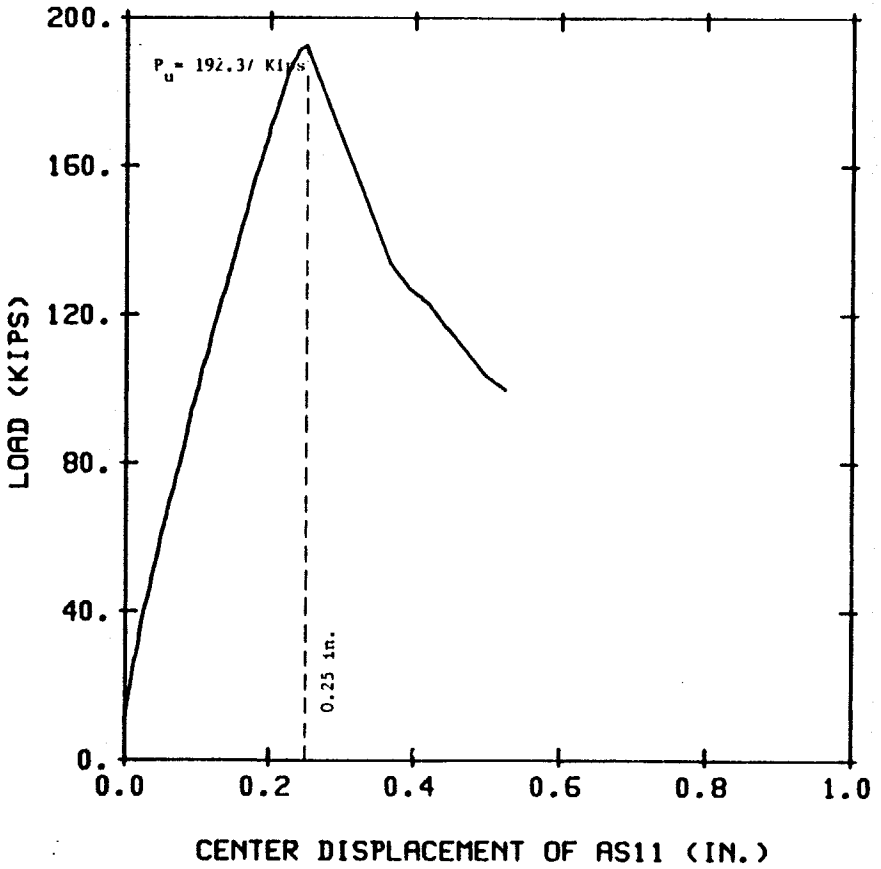

Figure II.46 Load-Center Deflection Curve in AS11

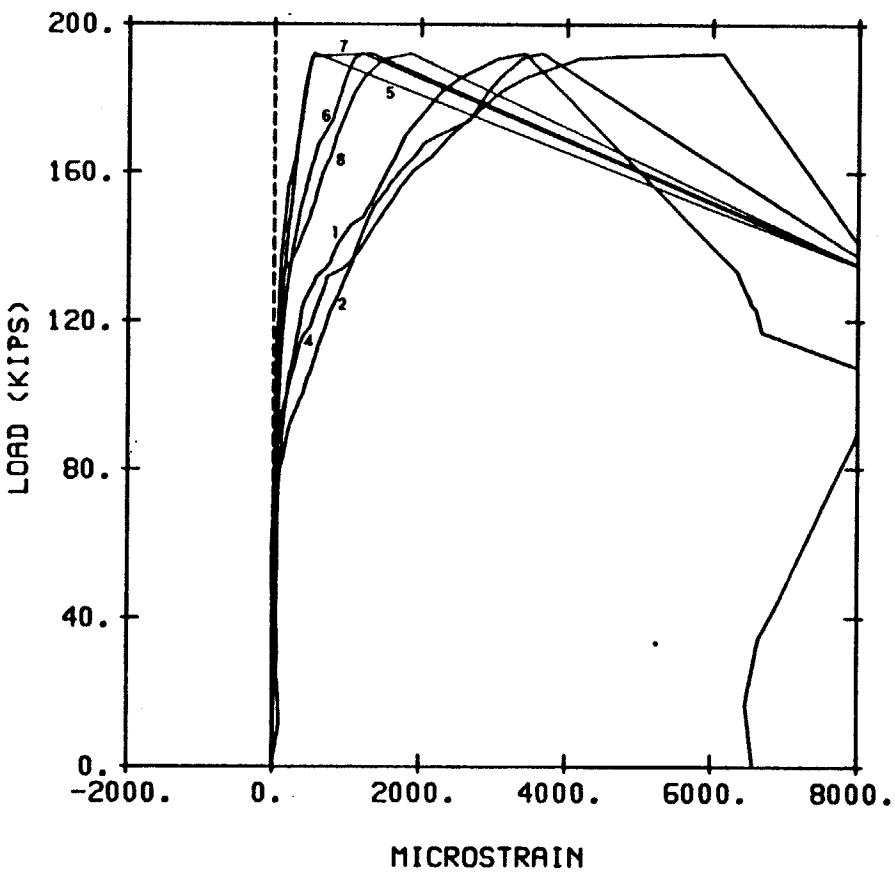

Figure II.47 Load-Strain Curves in Gaged Shear Bars in AS11

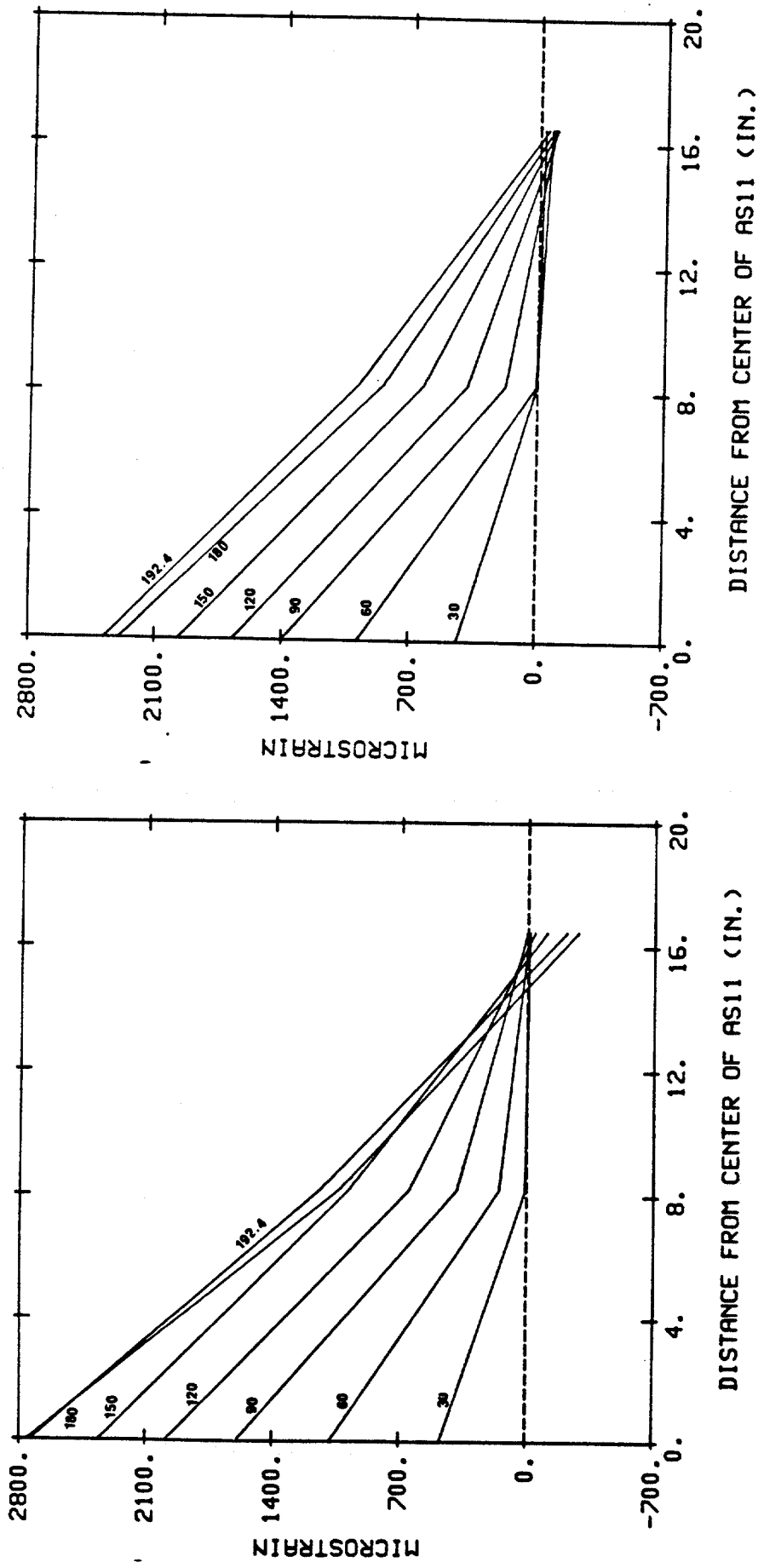

Figure II.48 Flexural Strain Profiles of AS11
a) in Span Tension Reinforcement
b) in Transverse Tension Reinforcement
c) in Span Compression Reinforcement

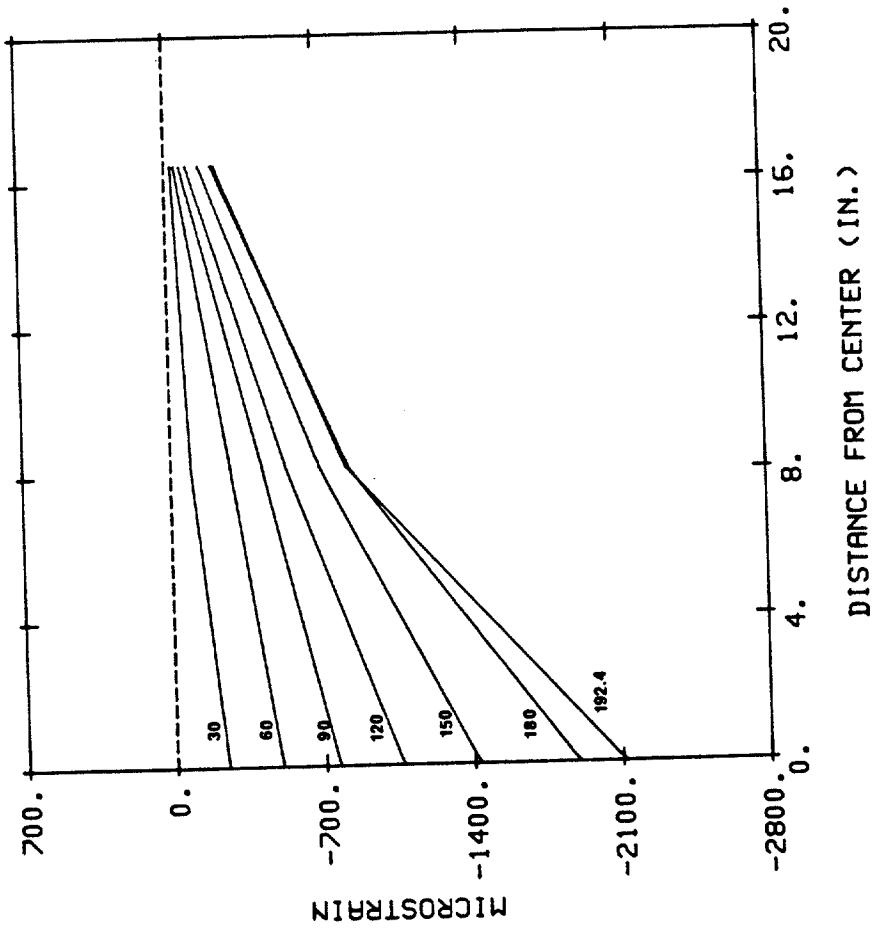

(e)

Figure II.48 (continued)

a

b

Figure II.49 Crack Patterns in AS11

a) Span Cross-Section
b) Transverse Cross-Section

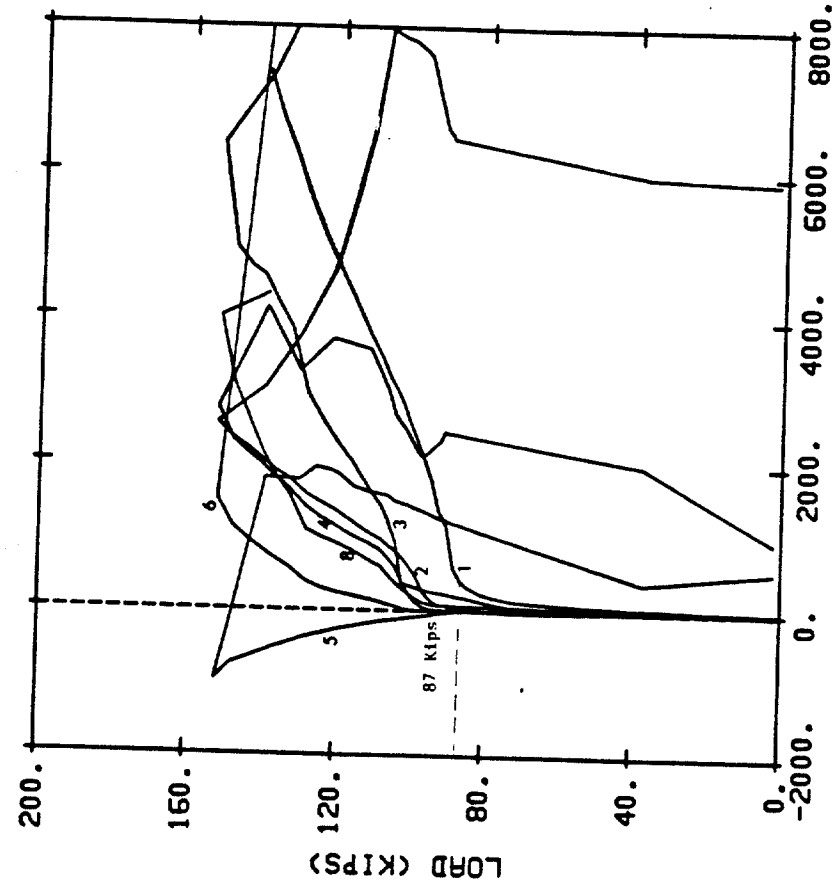

Figure II.51 Load-Strain Curves in Gaged Shear Bars in AS10

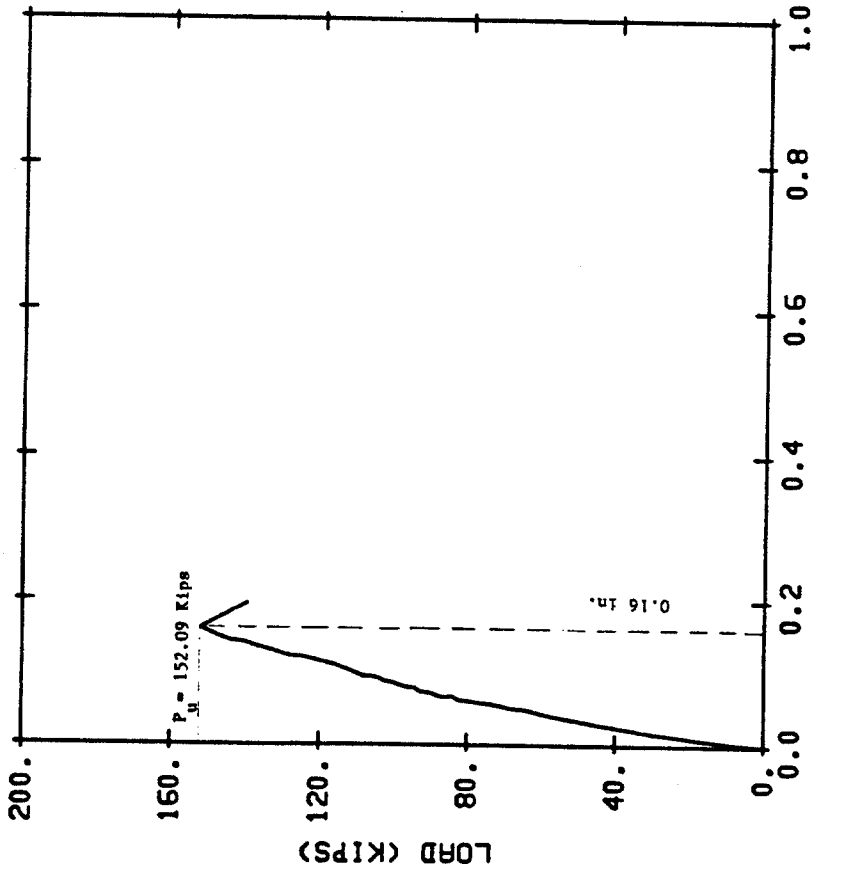

Figure II.50 Load-Center Deflection Curve in AS10

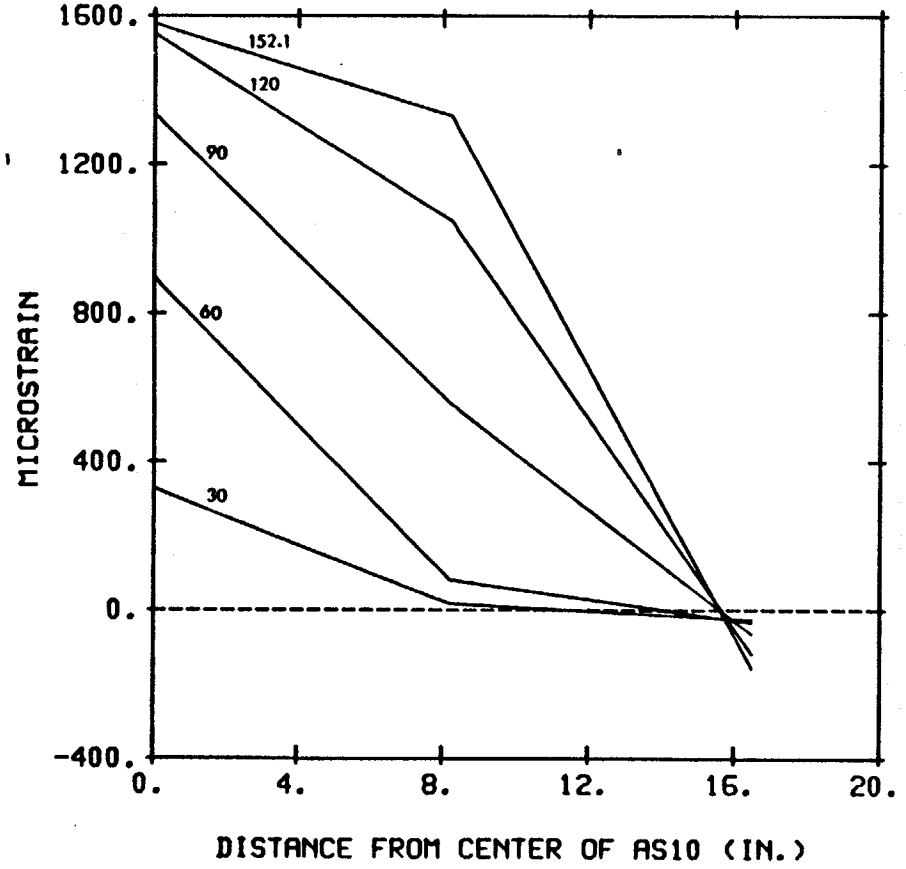

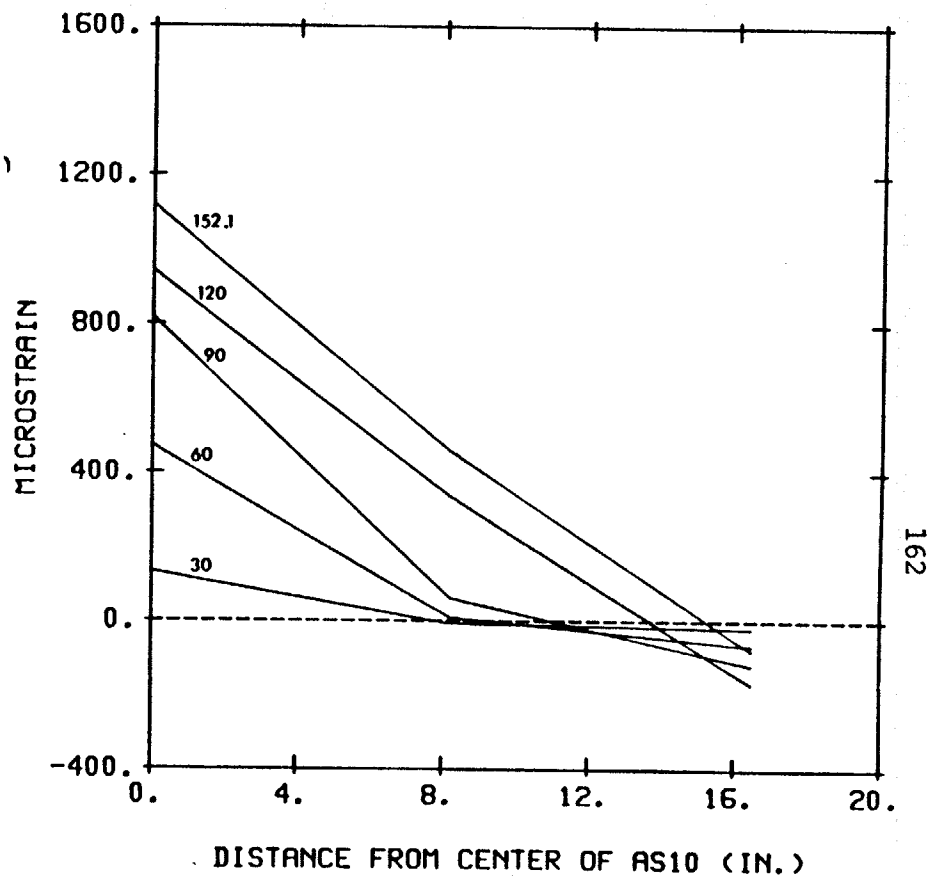

Figure II.52 Flexural Strain Profiles of AS10
a) in Span Tension Reinforcement
b) in Transverse Tension Reinforcement
c) in Span Compression Reinforcement

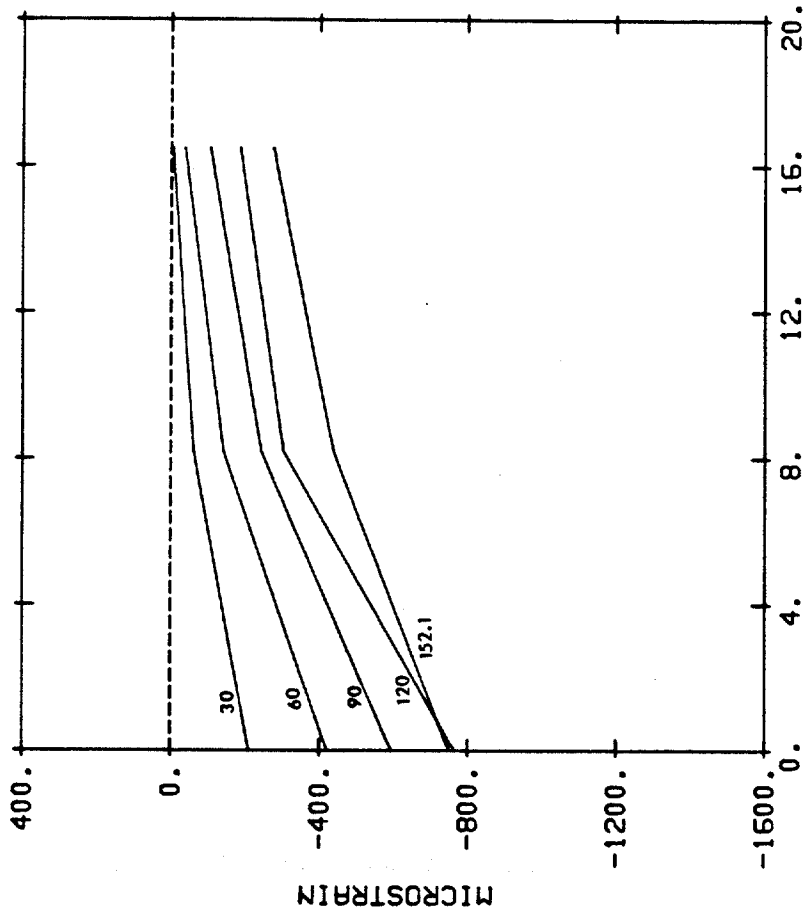

(e)

Figure II.52 (continued)

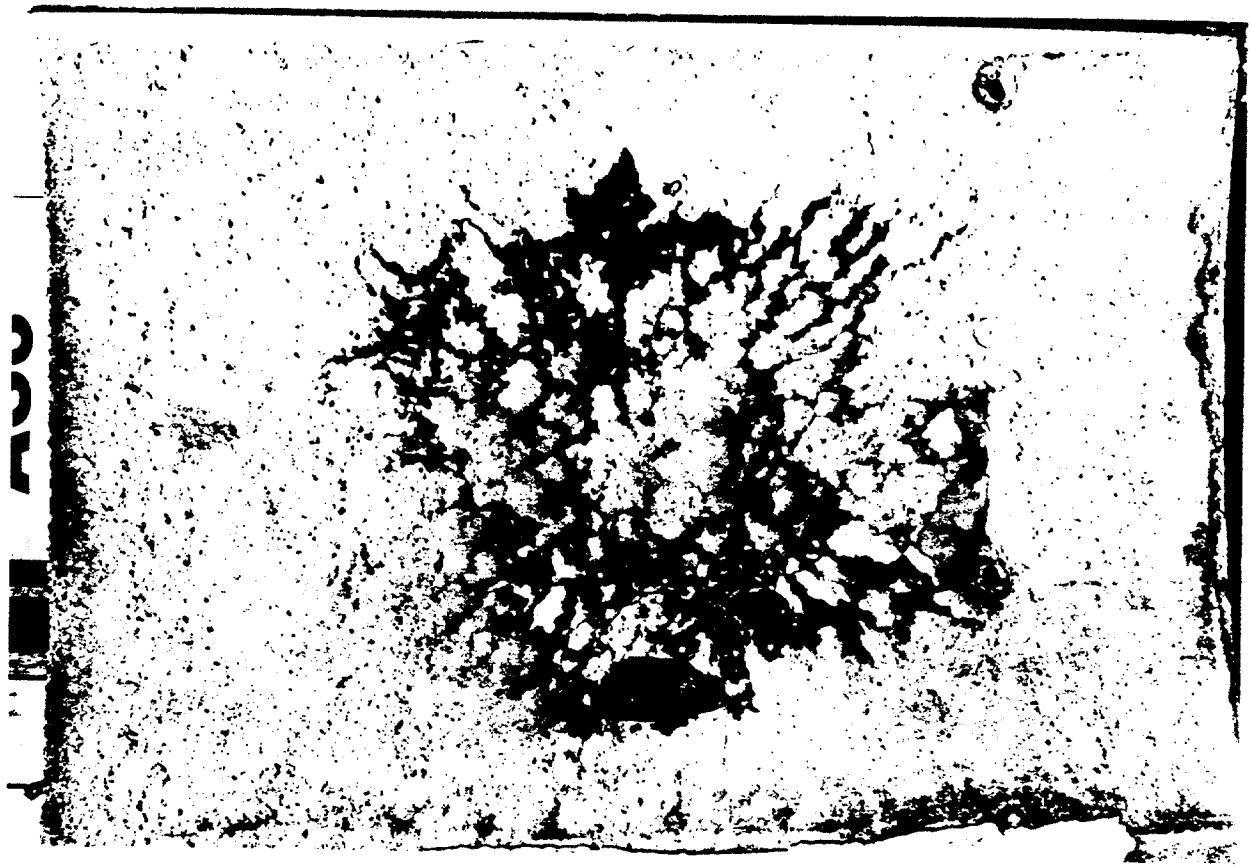

a

b

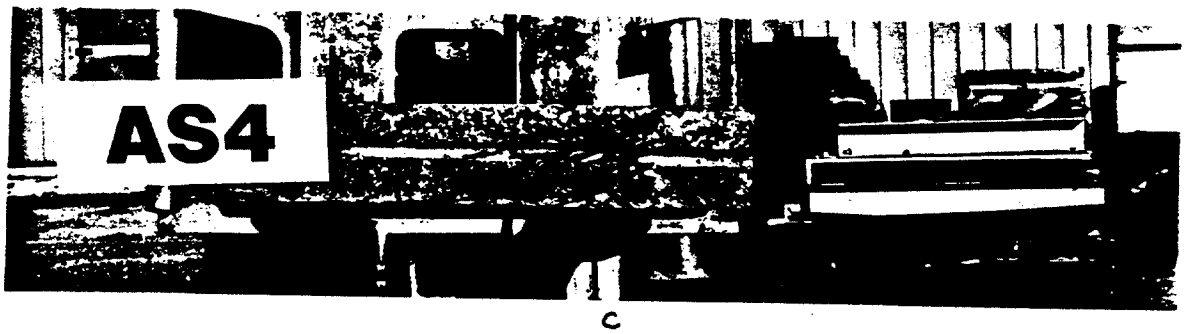

c

Figure II.53 Crack Patterns in AS10
a) Underside
b) Span Cross-Section
c) Transverse Cross-Section

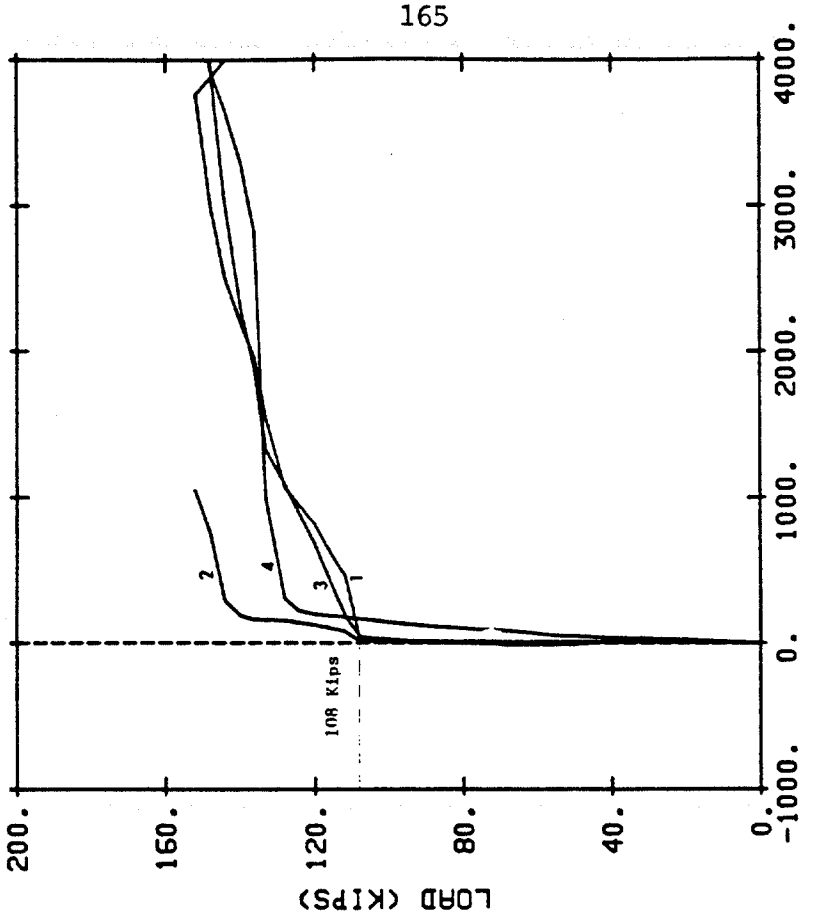

Figure II.55 Load-Strain Curves in Gaged Shear Bars in AS8

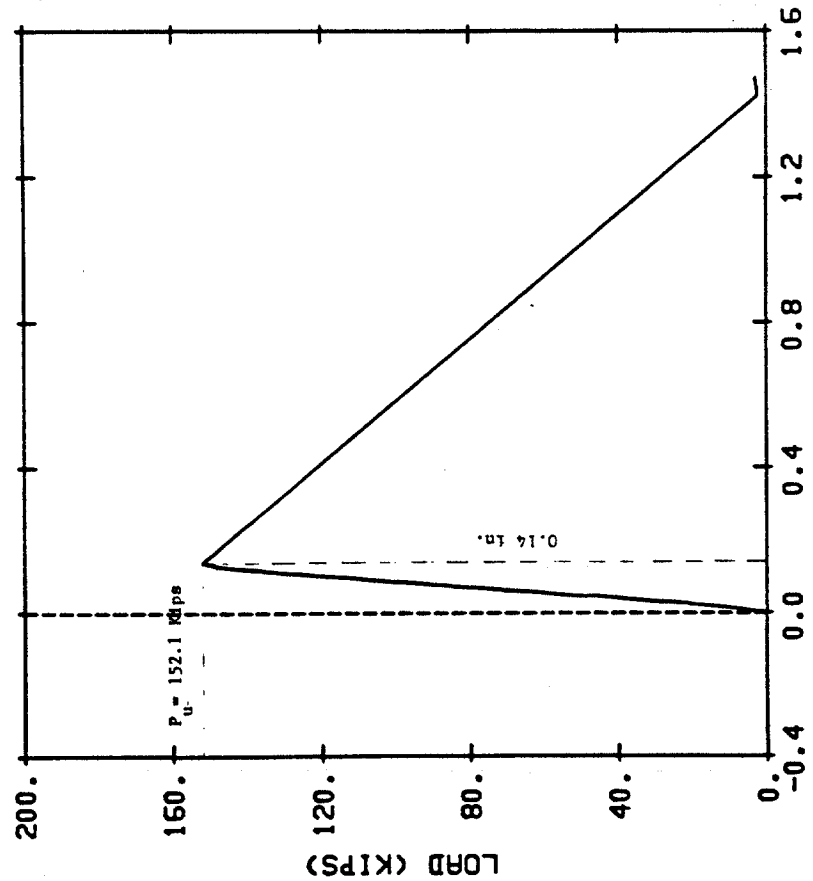

Figure II.54 Load-Center Deflection Curve in AS8

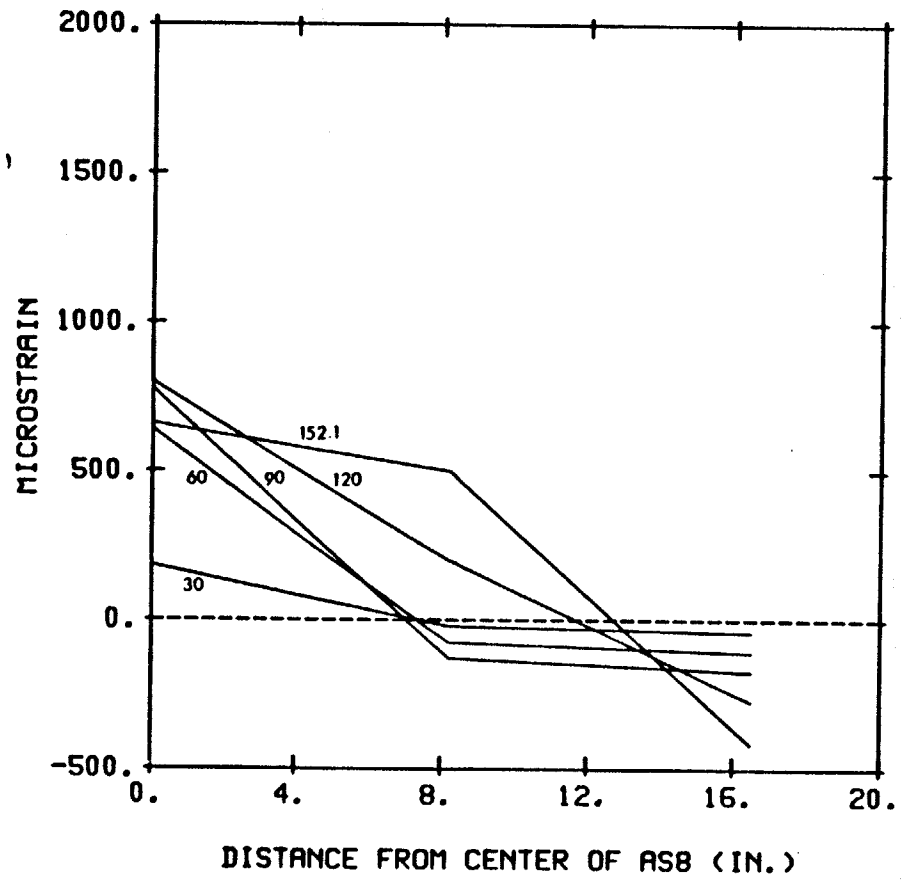

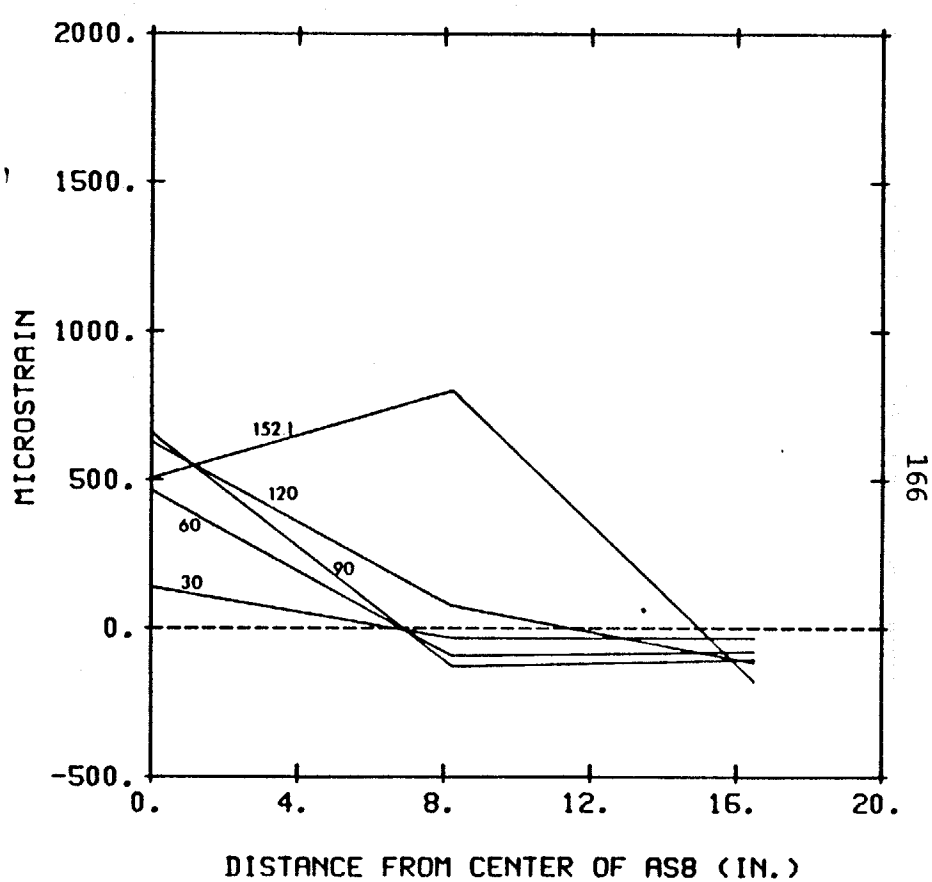

Figure II.56 Flexural Strain Profiles of AS8
a) in Span Tension Reinforcement
b) in Transverse Tension Reinforcement
c) in Span Compression Reinforcement

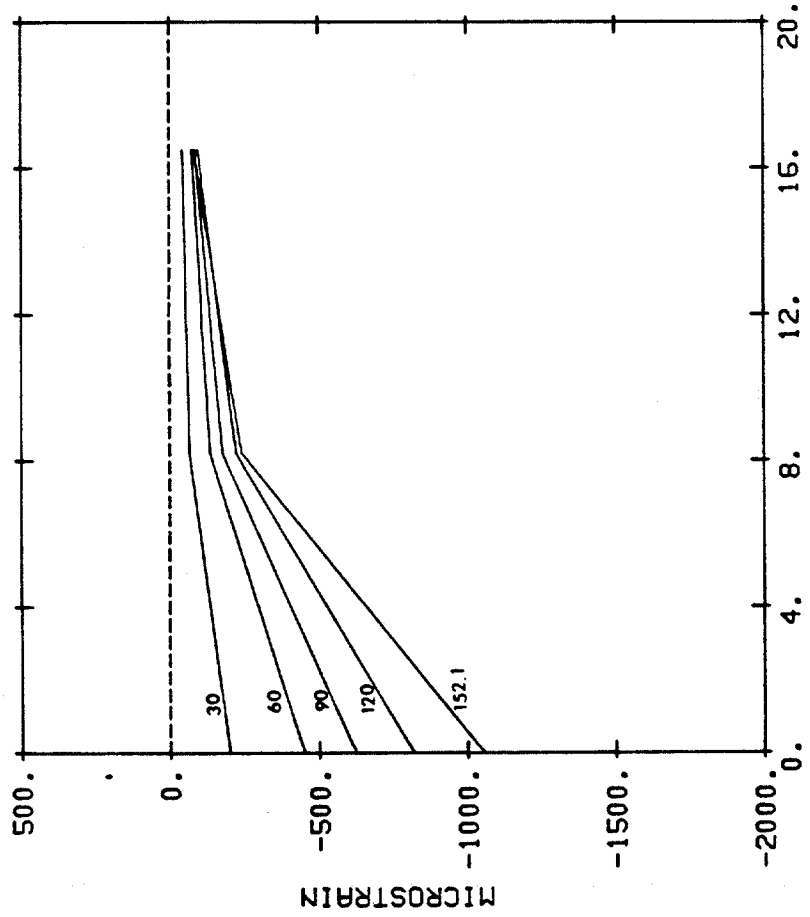

(e)

Figure II.56 (continued)

Figure II.57 Crack Patterns on the Underside of AS8

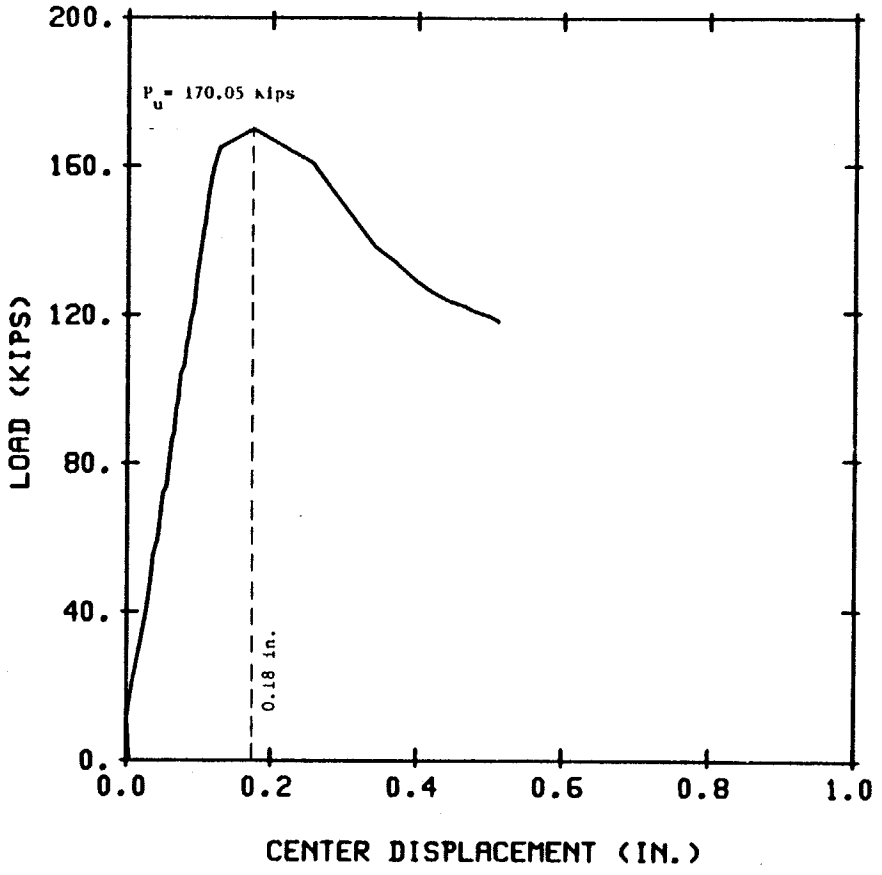

Figure II.58 Load-Center Deflection Curves in AS12

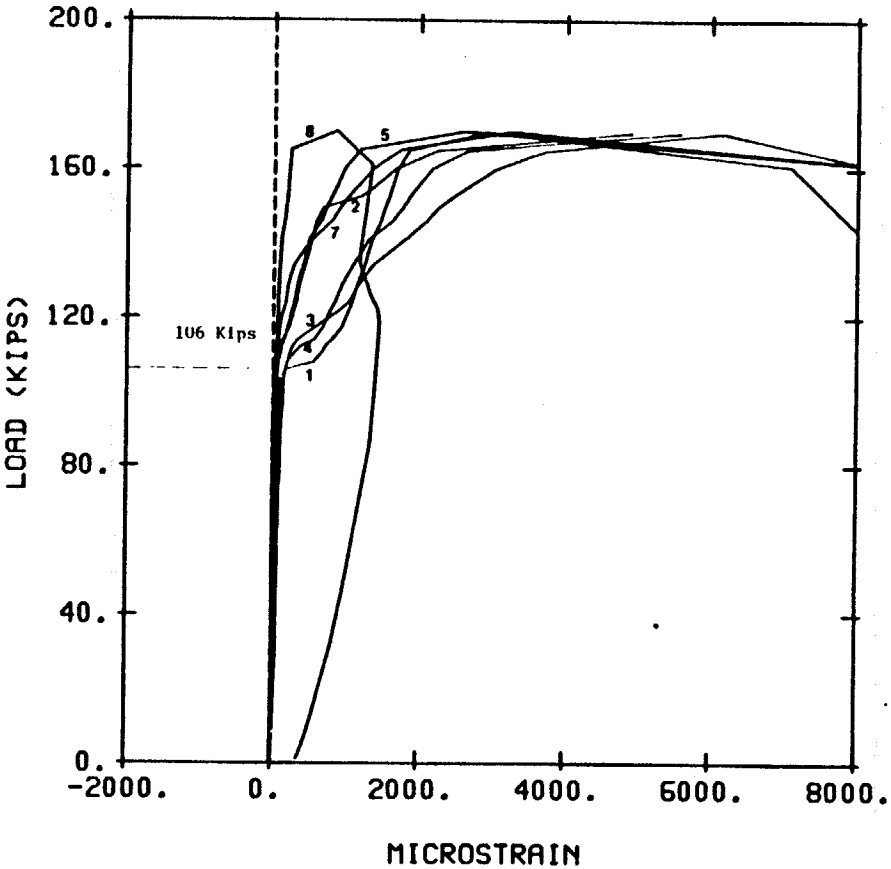

Figure II.59 Load-Strain Curves in Gaged Shear Bars of AS12

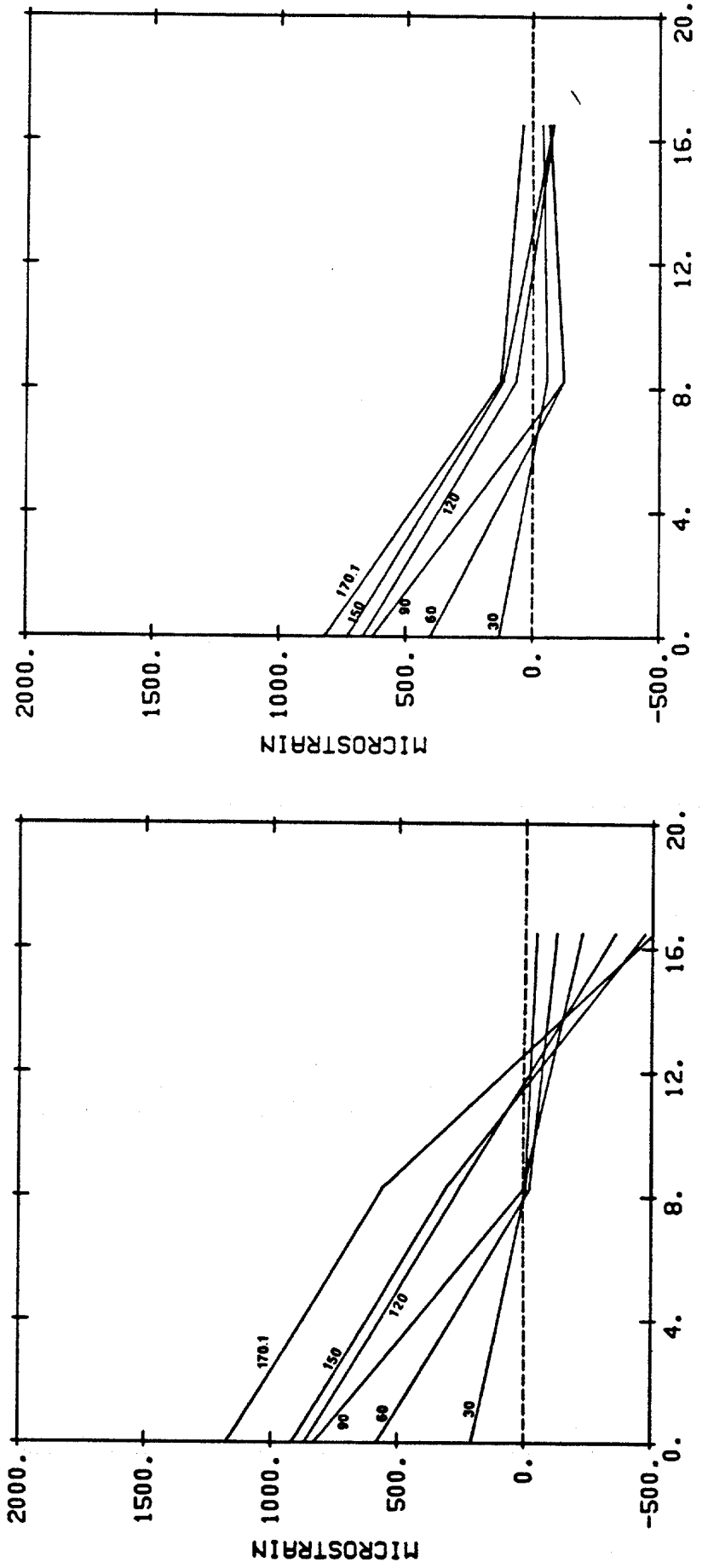

Figure II.60 Flexural Strain Profiles of AS12
a) in Span Tension Reinforcement
b) in Transverse Tension Reinforcement
c) in Span Compression Reinforcement

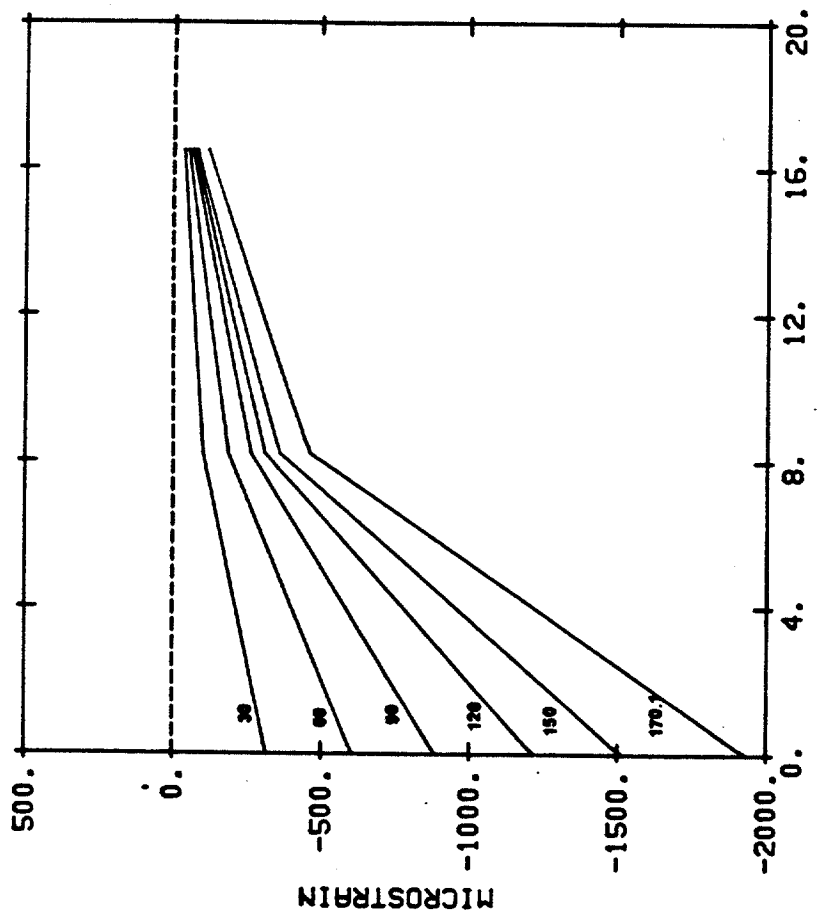

(e)

Figure II.60 (continued)

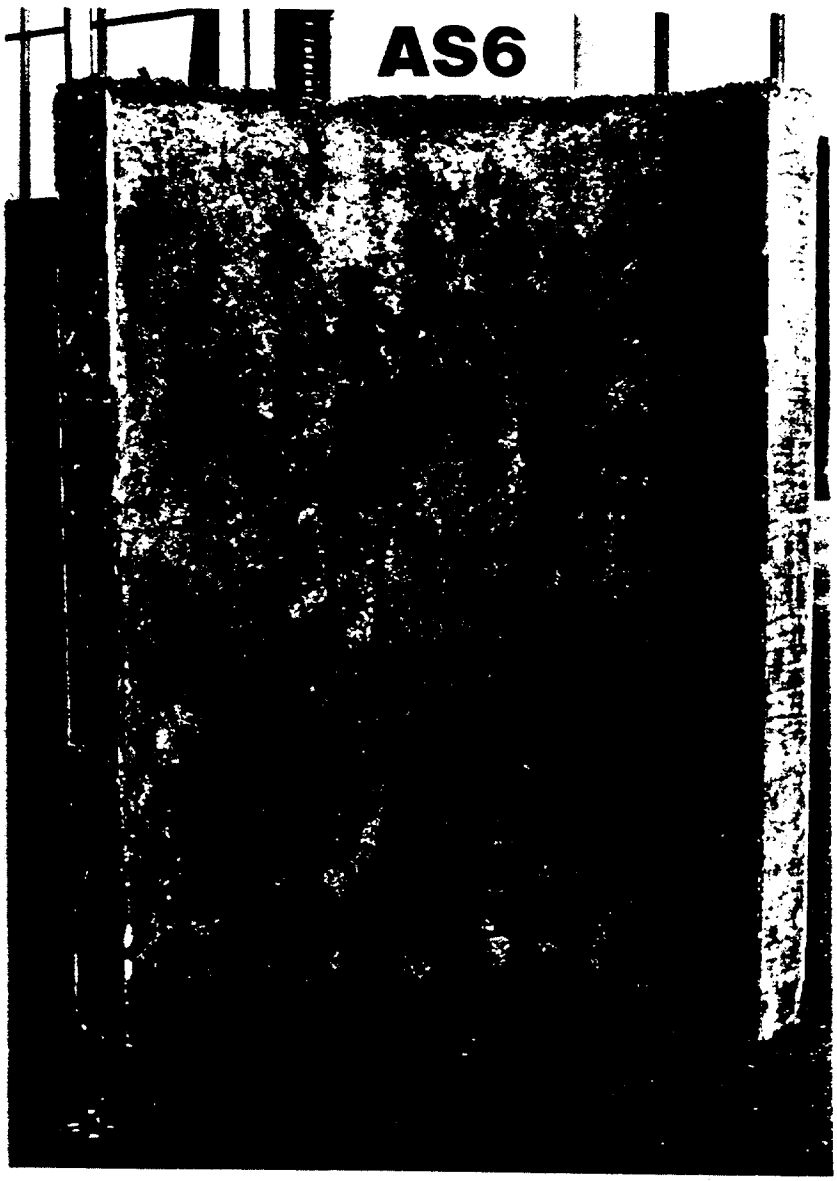

Figure II.61 Crack Patterns on the Underside of AS12

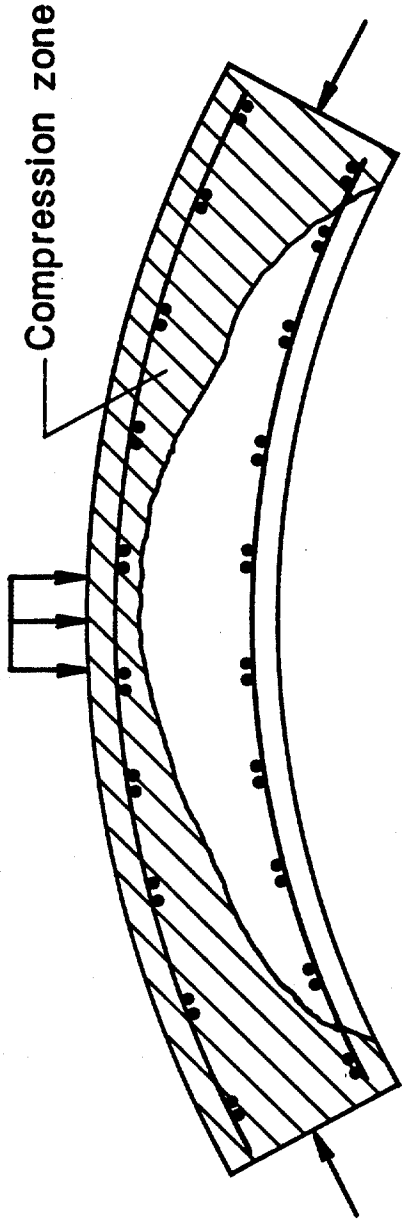

Figure II.62 Idealized Compression Zone in Shell Specimens

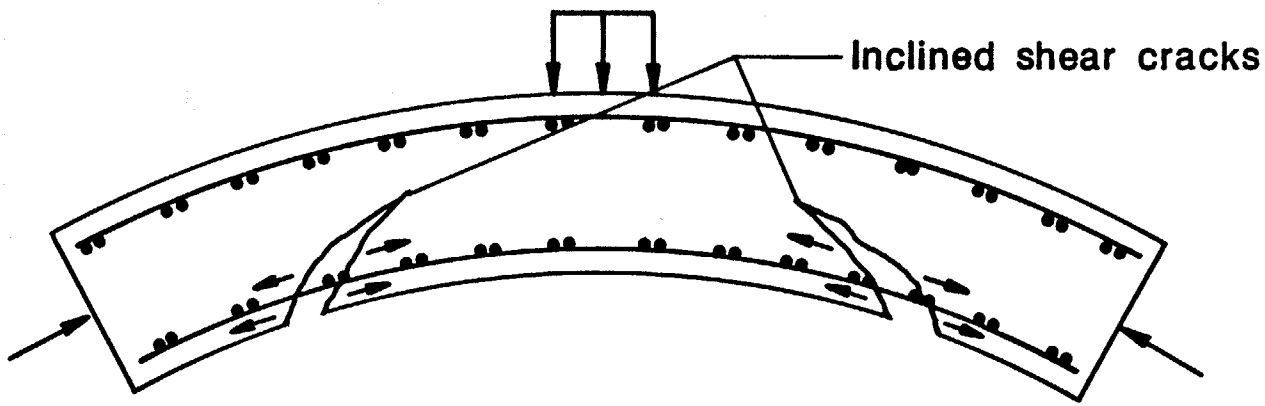

Figure II.63 Effect of Inclined Shear Cracks in Shells

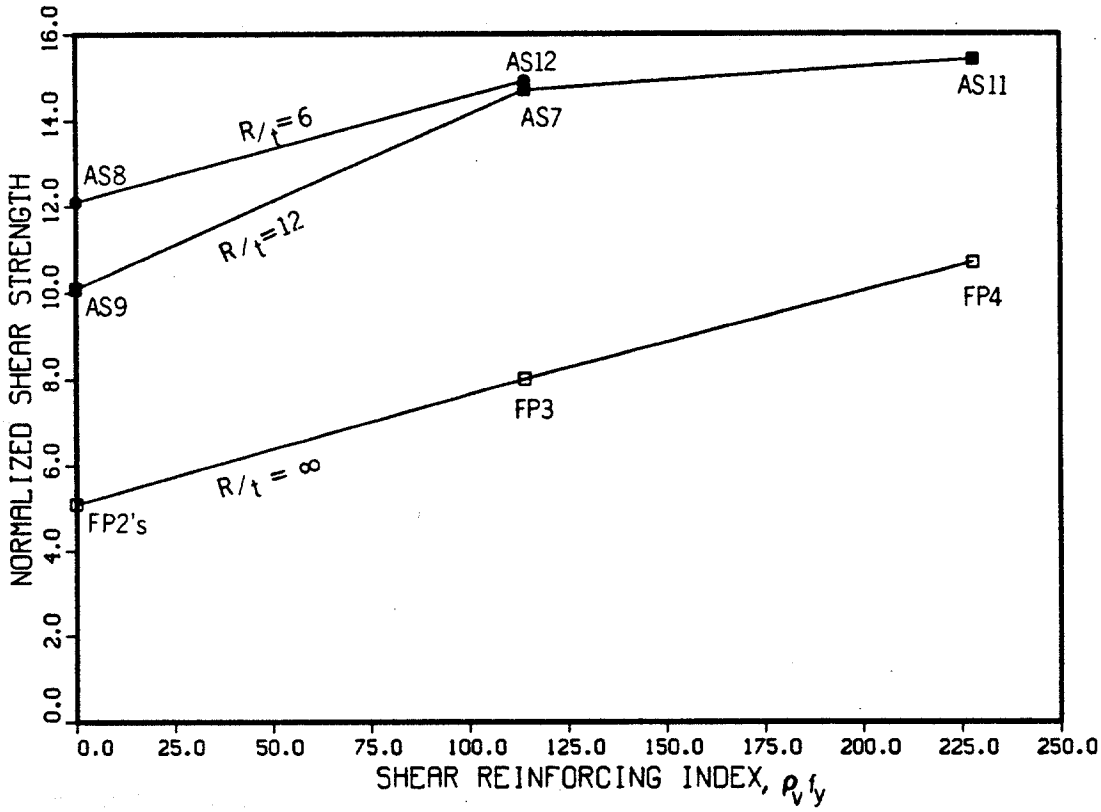

Figure II.64 Normalized Shear Strength versus Shear Reinforcement Index

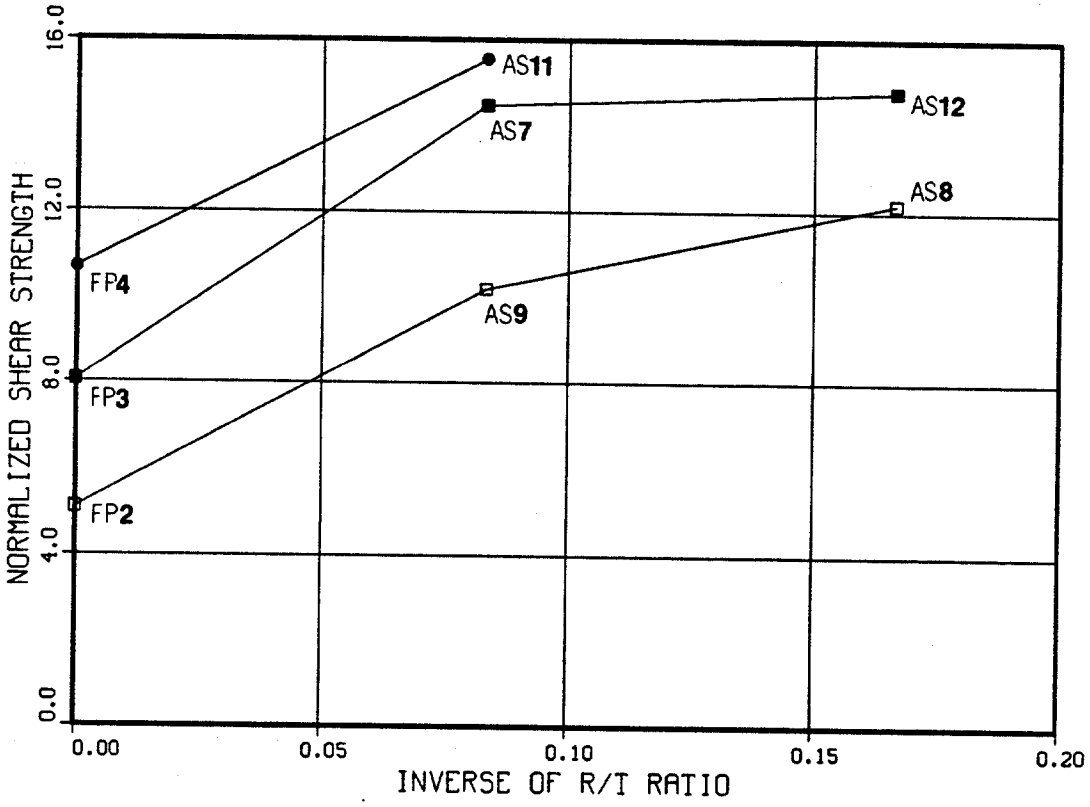

Figure II.65 Normalized Shear Strength versus Inverse of R/t Ratios

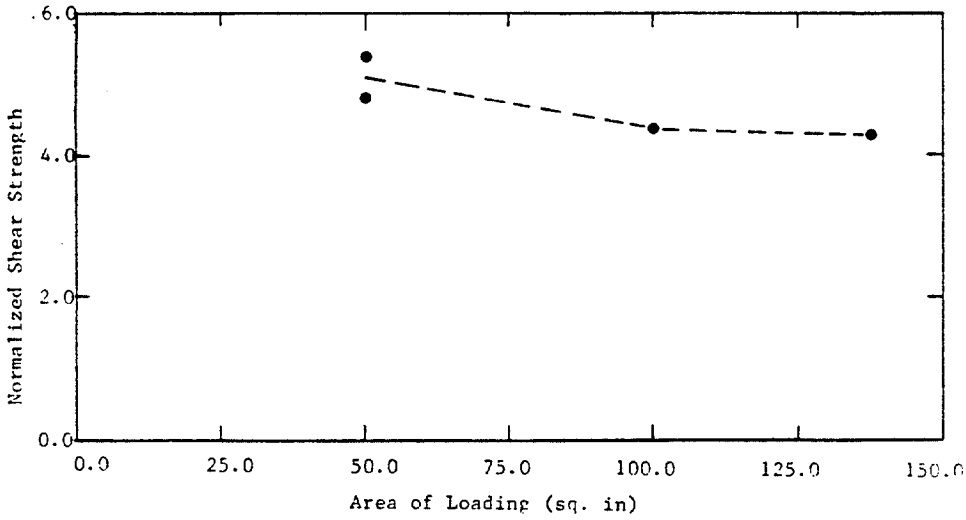

Figure II.66 Normalized Shear Strength versus Area of Loading

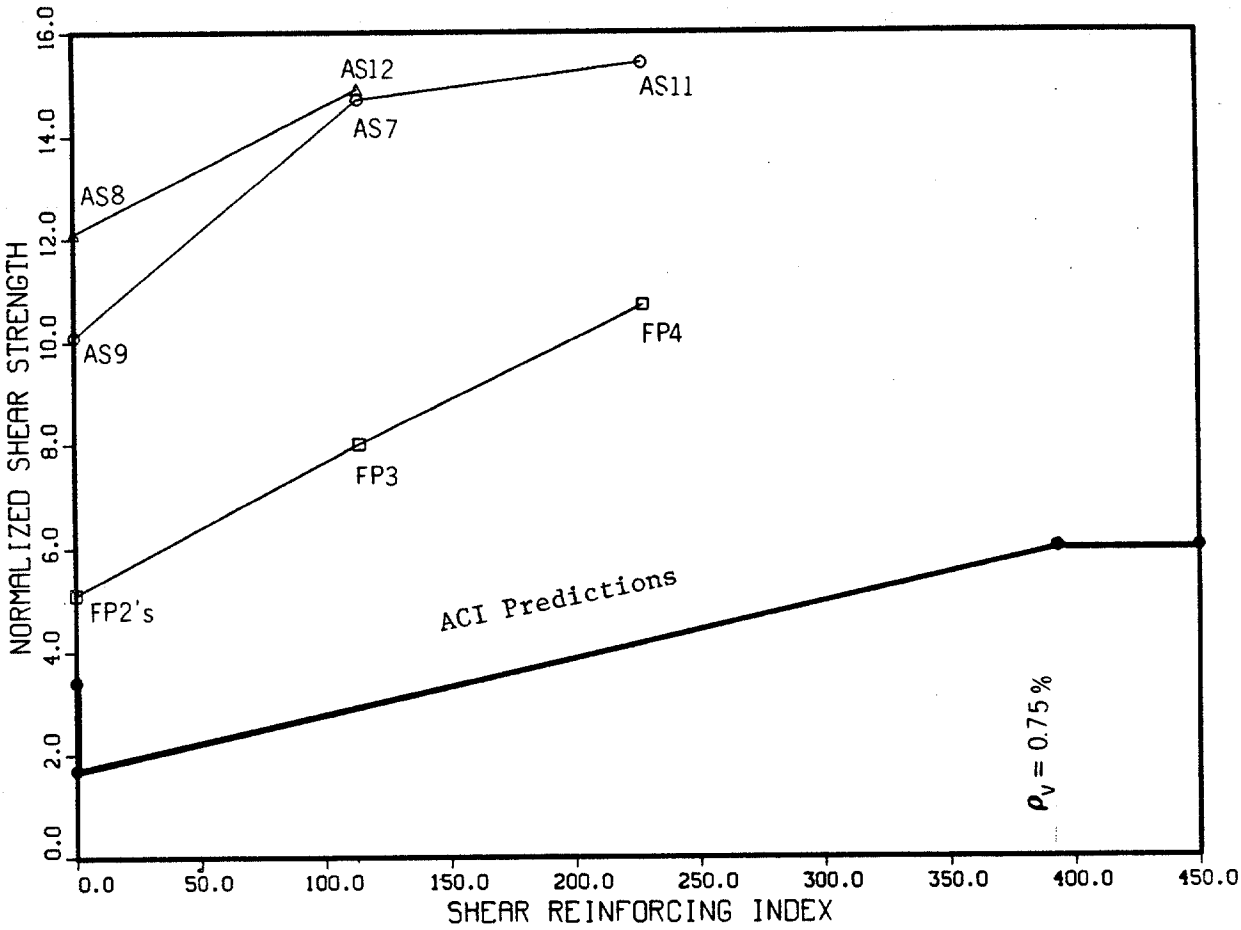

Figure II.67 Comparison of Test Results and the ACI Predictions

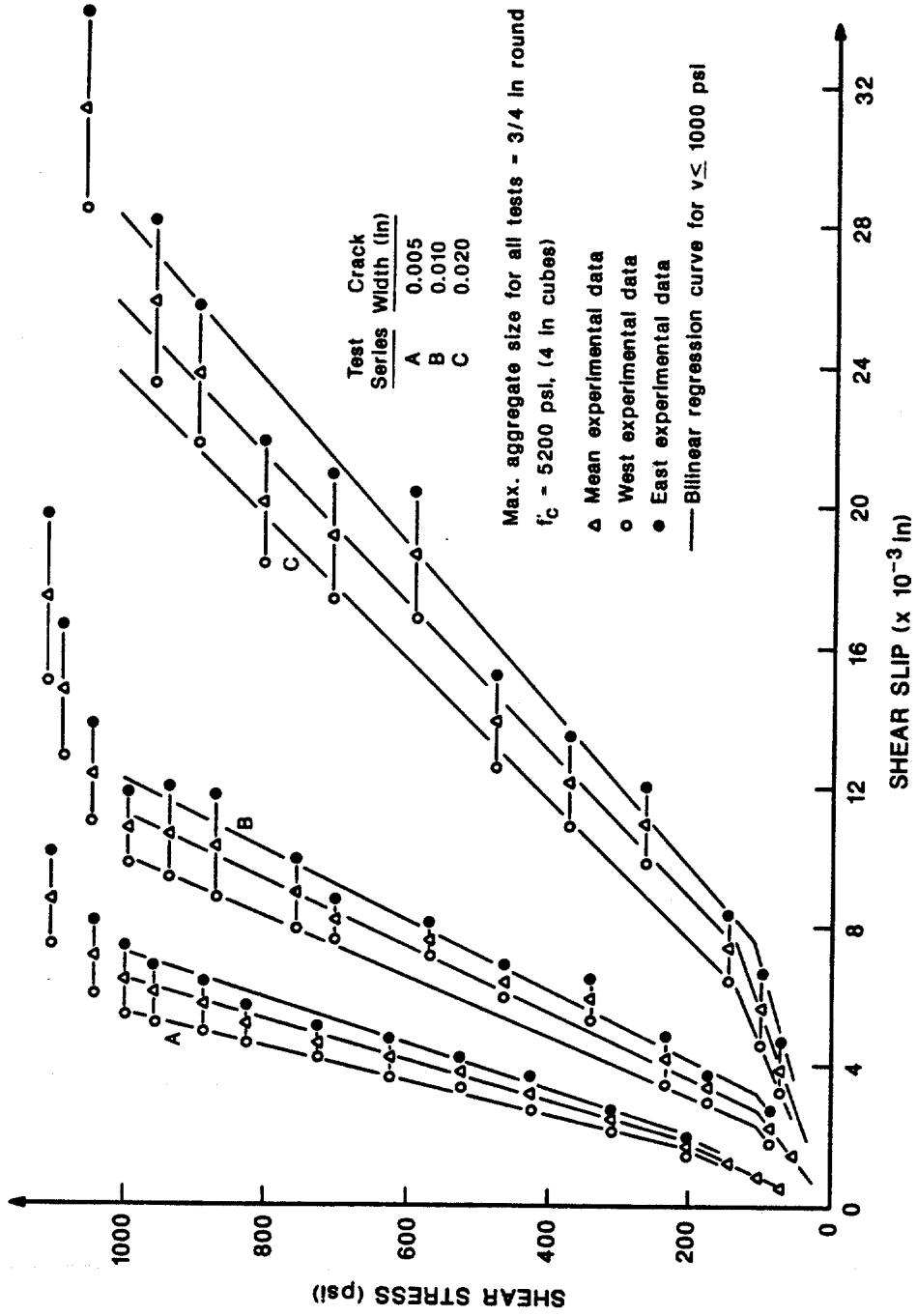

Figure III.1 Typical Shear Stress-Shear Slip Relationships for Different Crack Widths (after Paulay and Loeber)

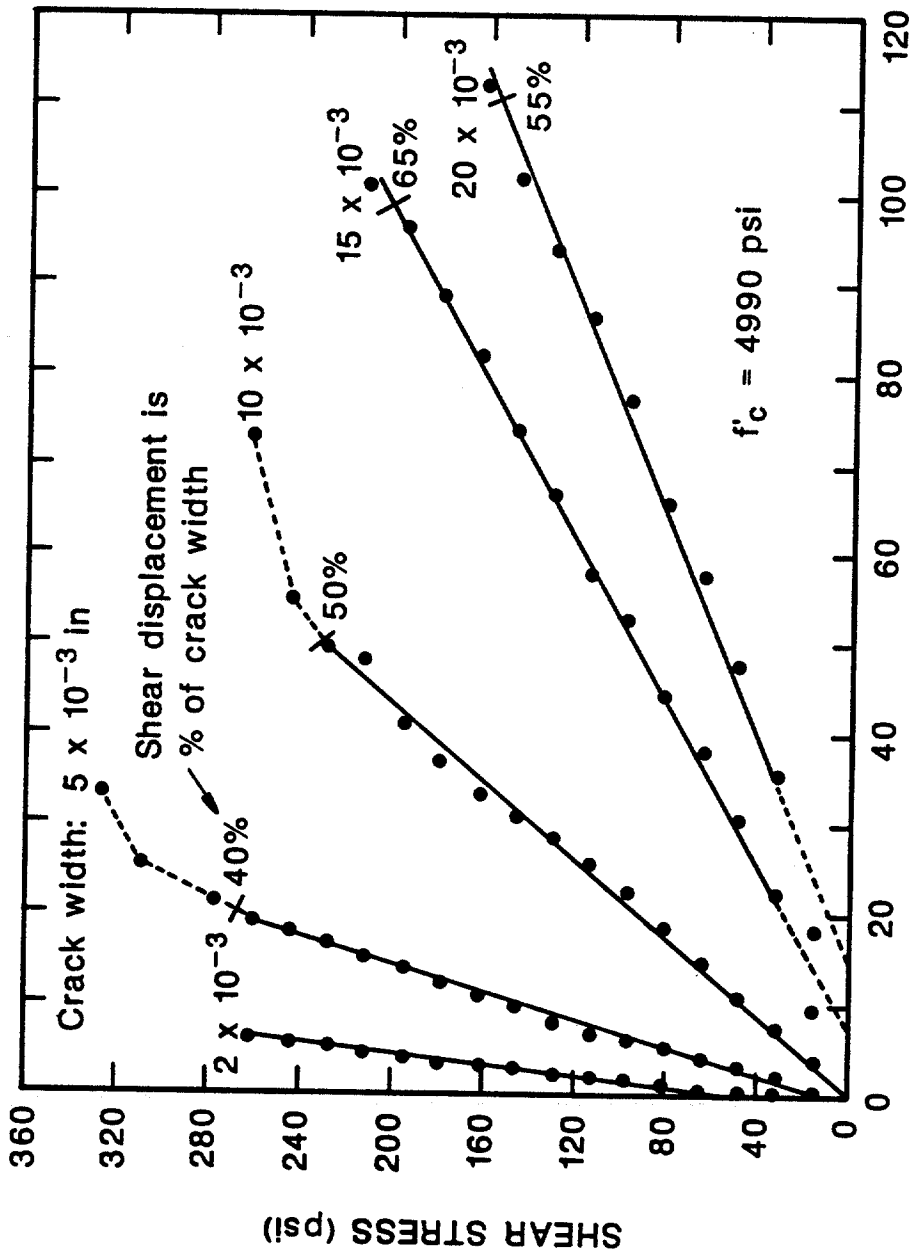

Figure III.2 Typical Shear Stress-Shear Slip Relationships for Different Crack Widths (after Houde and Mirza)

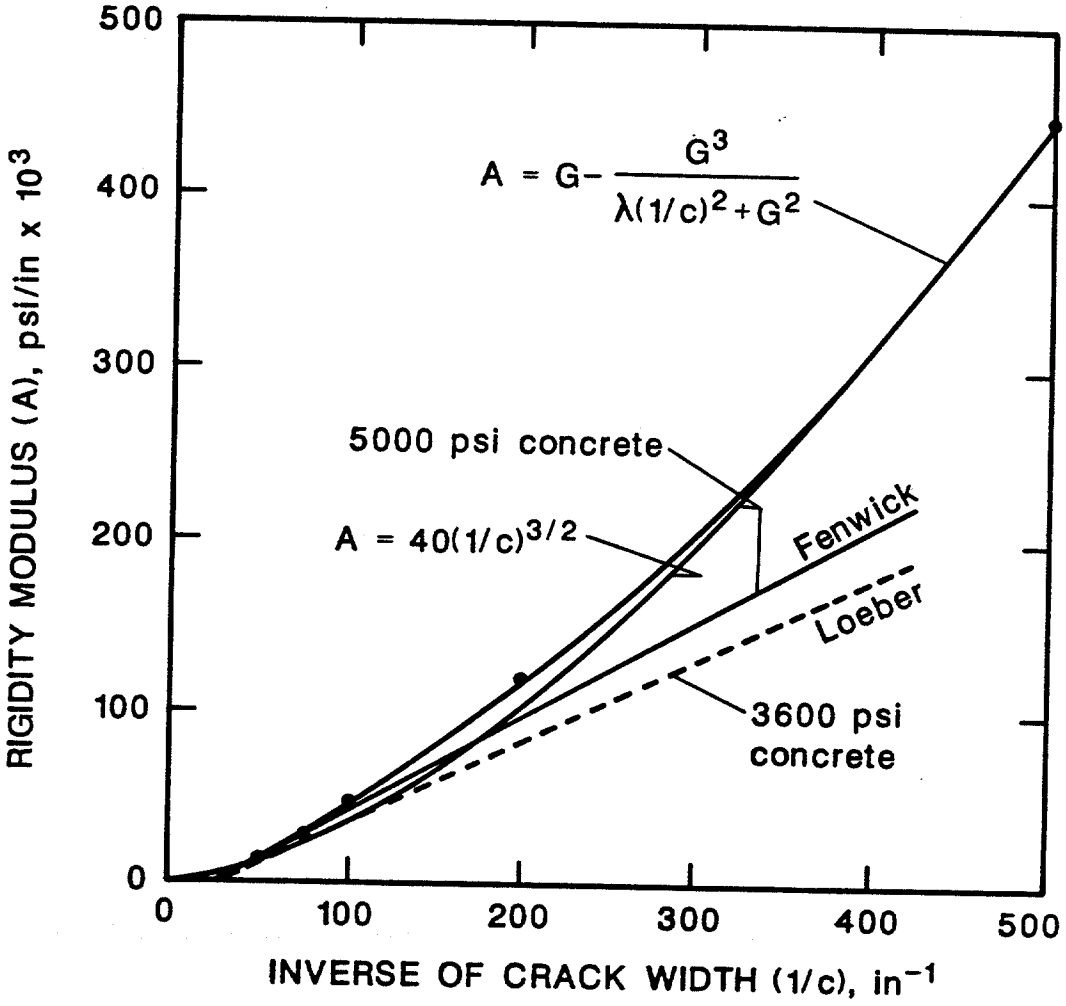

Figure III.3 Crack Shear Stiffness versus Inverse of Crack Widths (after Houde and Mirza)

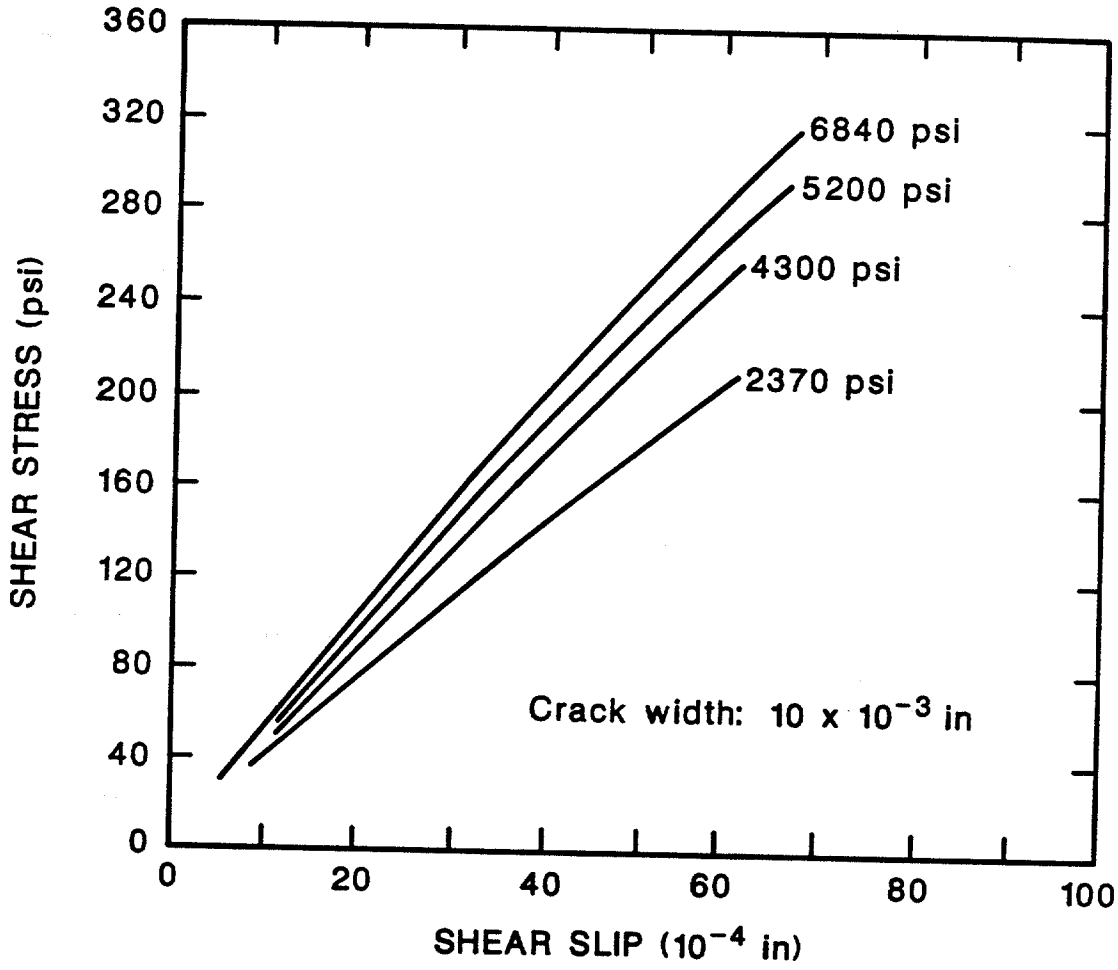

Figure III.4 Shear Stress versus Shear Slip for Concrete with Different Compressive Strength (Houde and Mirza)

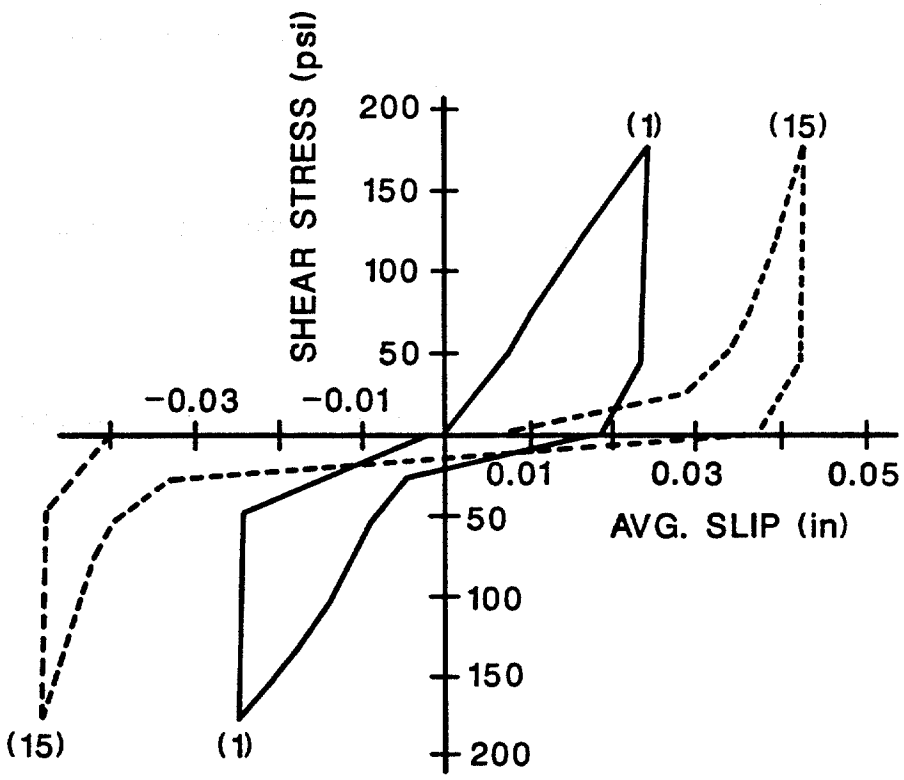

Figure III.5 Typical Shear Stress-Shear Slip Relationship for Cyclic Loading (after Laible)

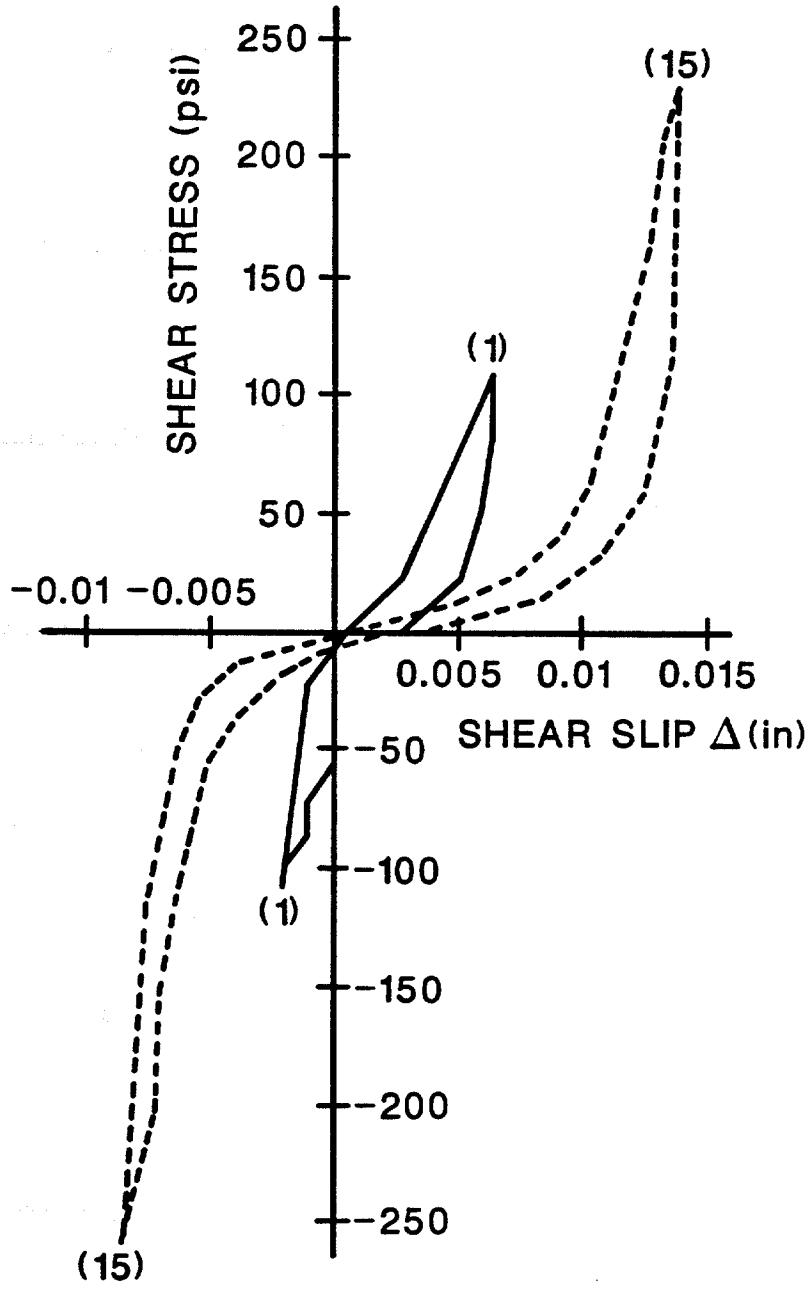

Figure III.6 Typical Shear Stress-Shear Slip relationsahips for Cyclic Loading (after Jimenez-Peres et al)

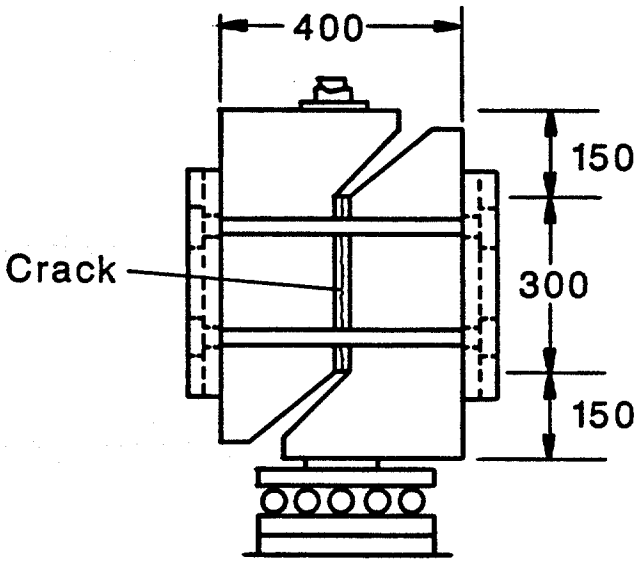

Figure III.7 Walraven's Test Specimen

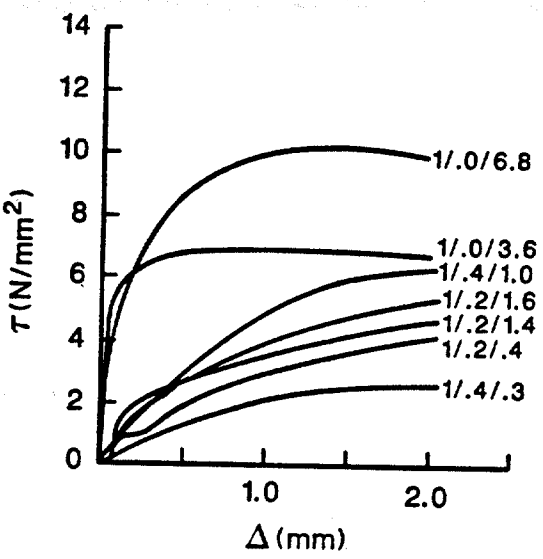

Figure III.8 Typical Shear Stress-Shear Slip Relationship For Different Restraining Stiffness (after Walraven)

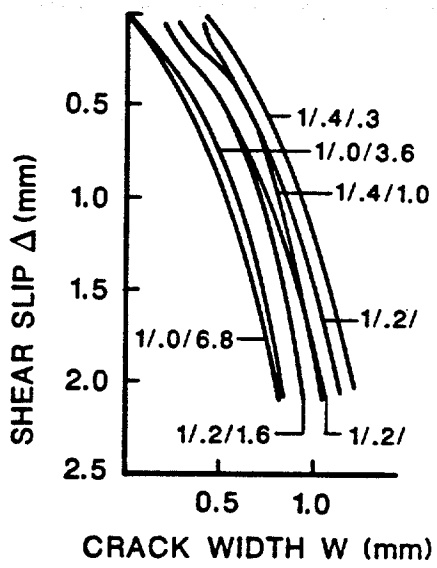

Figure III.9 Typical Shear Stress-Crack Width Relationships (after Walraven)

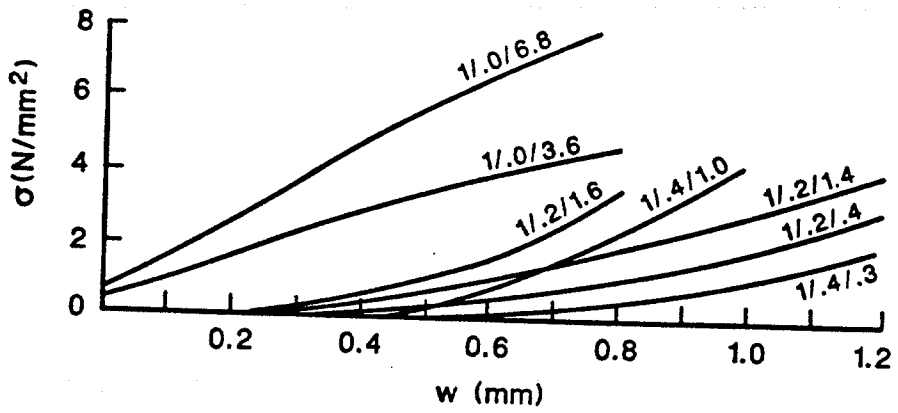

Figure III.10 Typical Normal Stress-Crack Width Relationship (after Walraven)

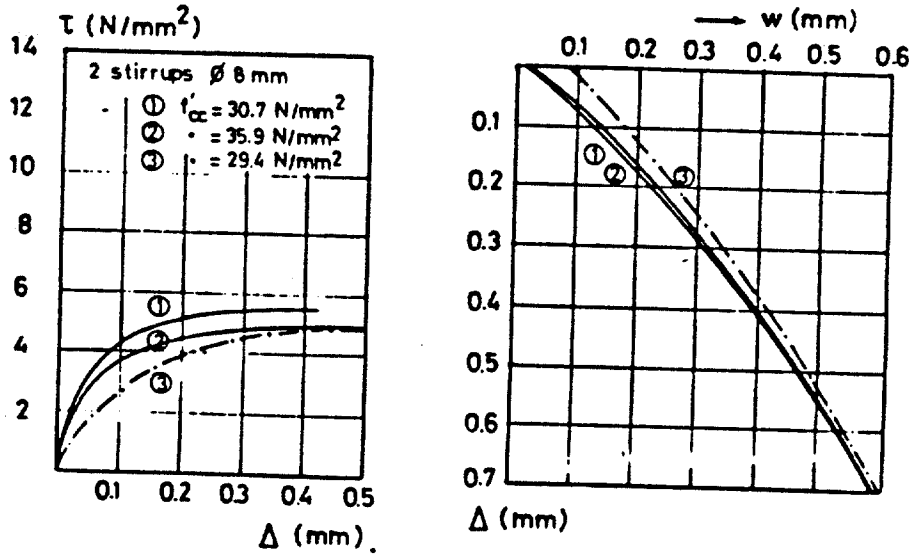

Figure III.11 Results of Tests With Embedded Bars (after Walraven)

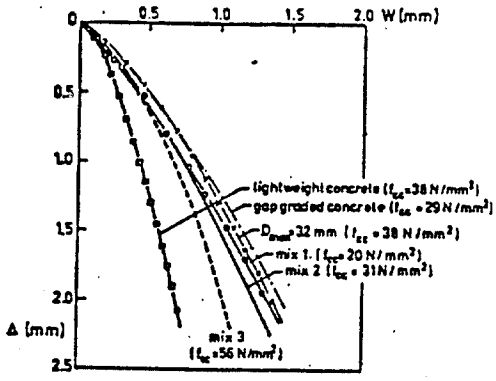

Figure III.12 Typical Crack Opening Paths (after Walraven)

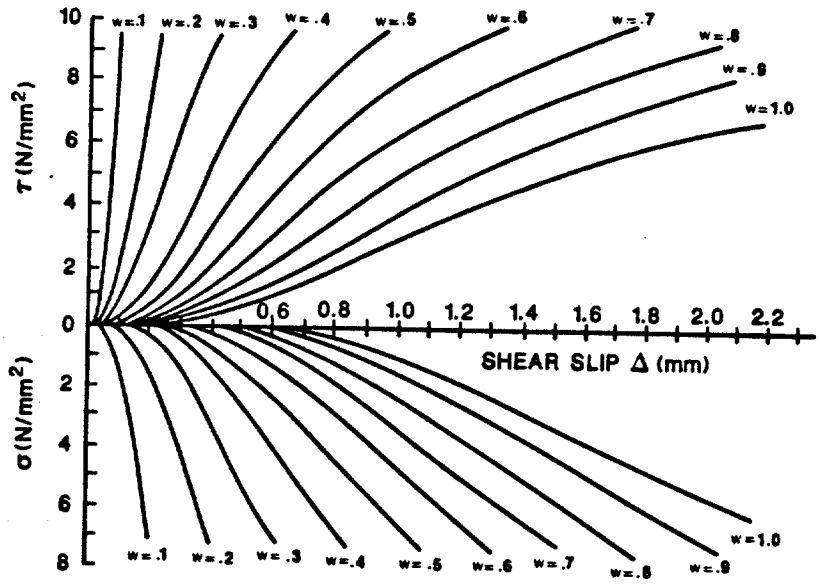

Figure III.13 Combinations of Shear and Normal Stresses versus Shear Slips (after Walraven)

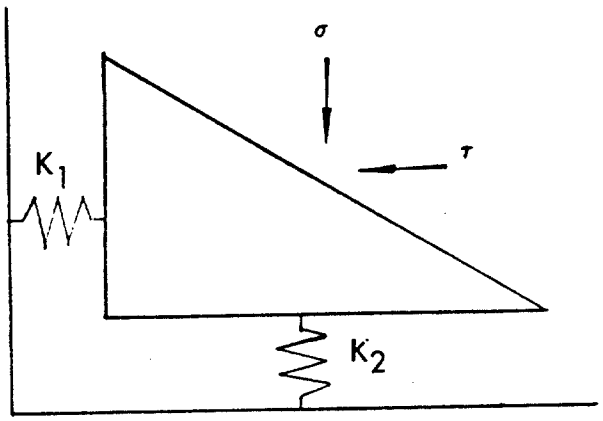

Figure III.14 Idealization of Crack Shear and Compressive Deformabilities by the Two-Spring Concept

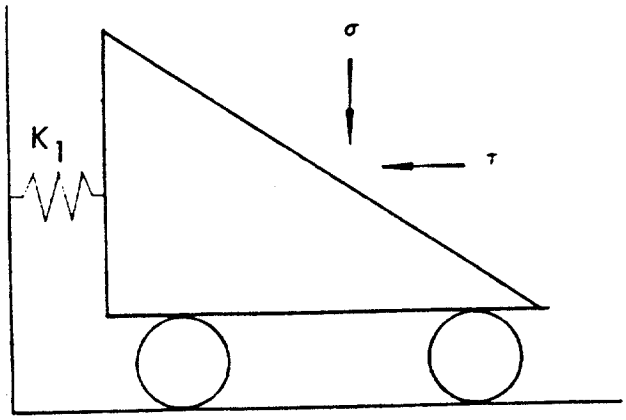

Figure III.15 The One-Spring Concept, Ignoring Crack Compressibility

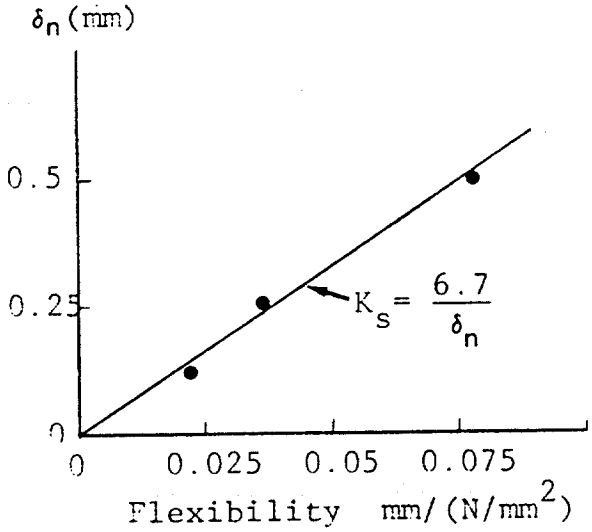

Figure III.16 Crack Shear Stiffness

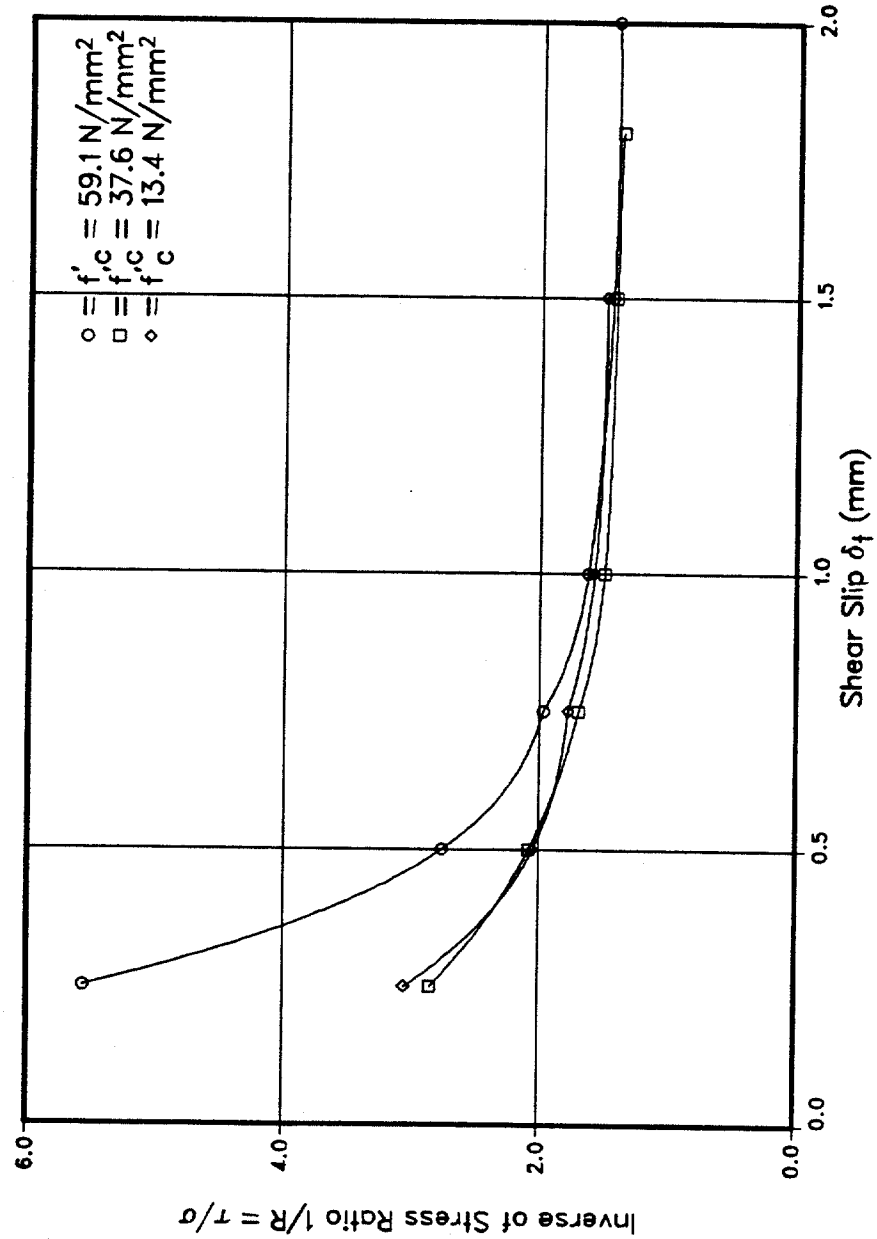

Figure III.17 Stress Ratio Law (Derived from Experimental Results Obtained by Walraven)

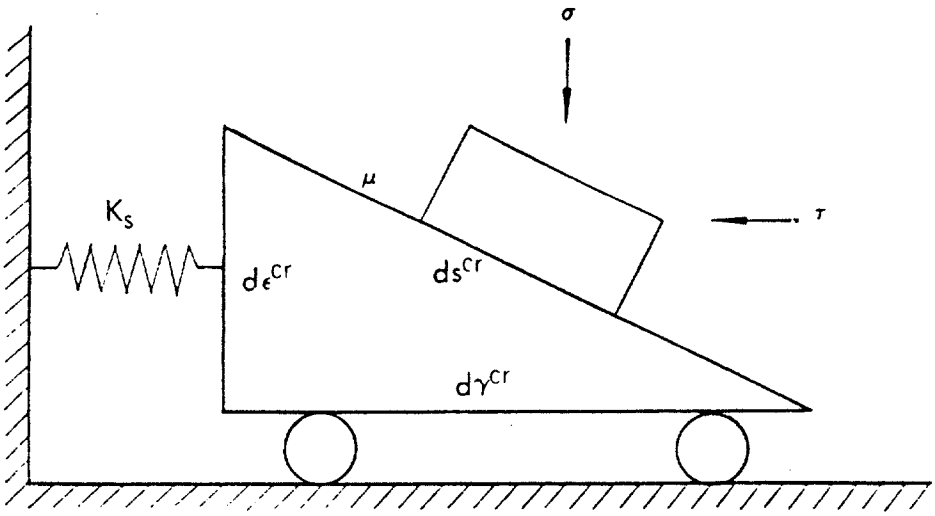

Figure III.18 The One-spring model.

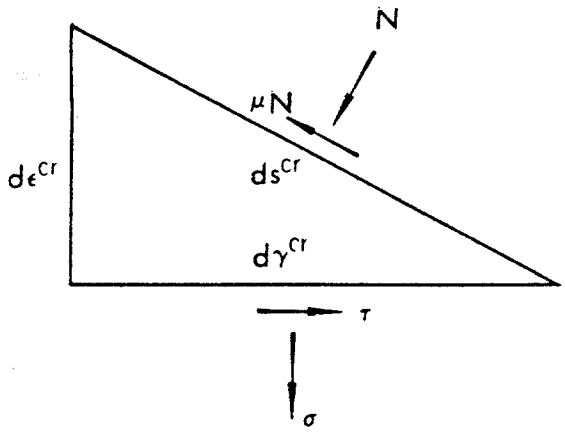

Figure III.19 Force equilibrium on the one-spring model.

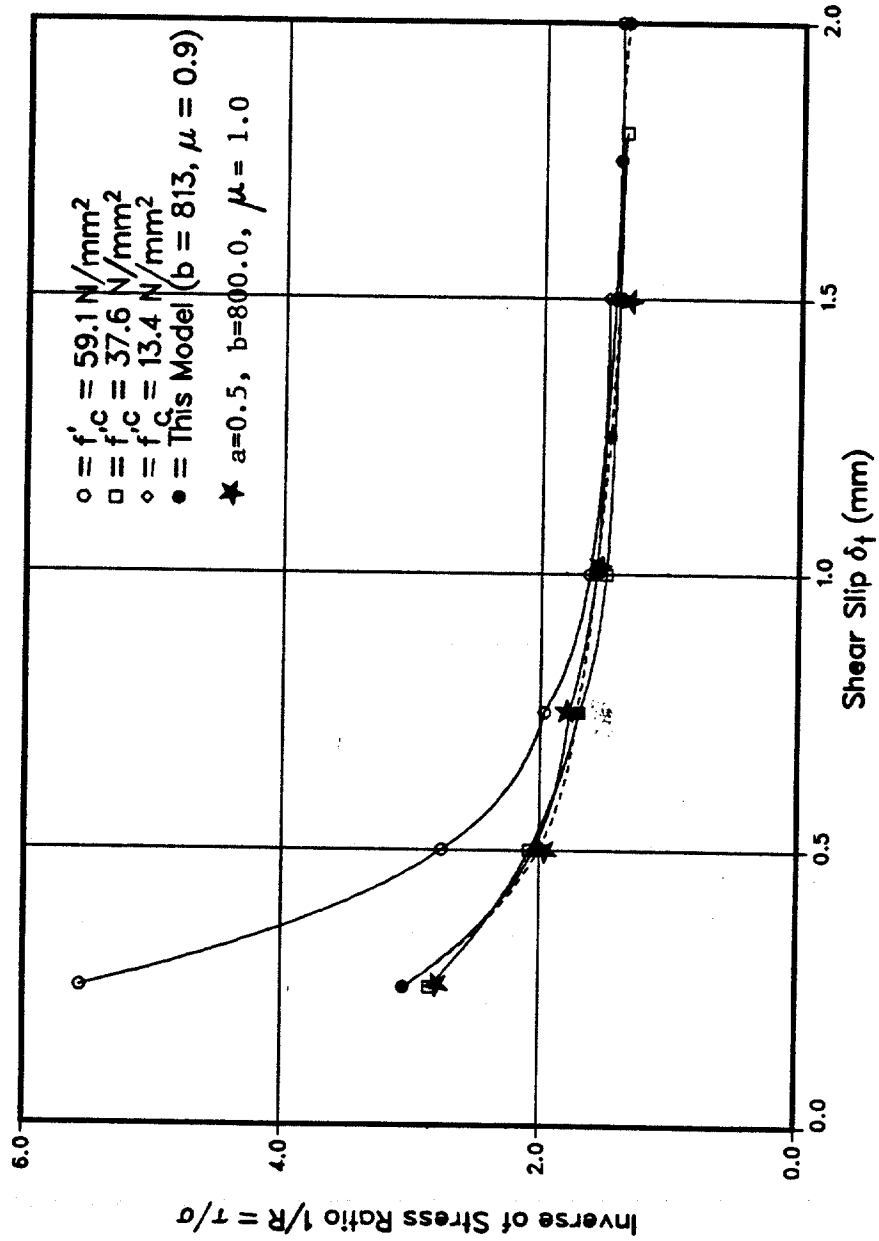

Figure III.20 Qualification of the One-Spring Model by Experimental Stress Ratio Law

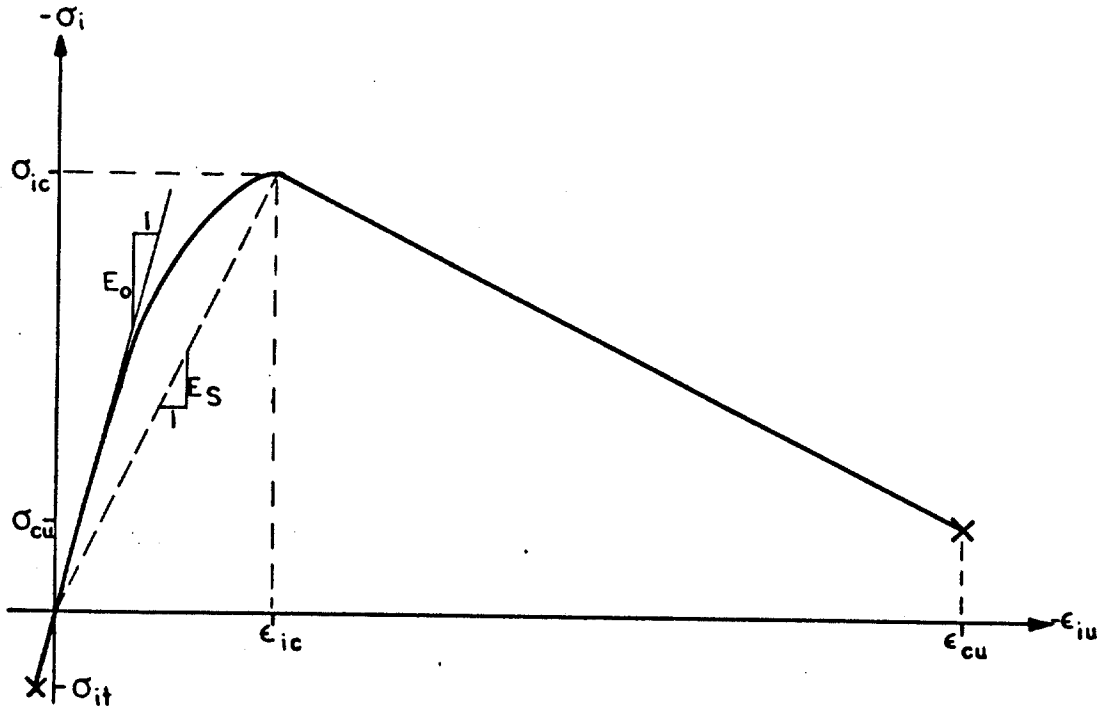

Figure III.21 Stress-Equivalent Uniaxial Strain Relationship (after Darwin and Pecknold)

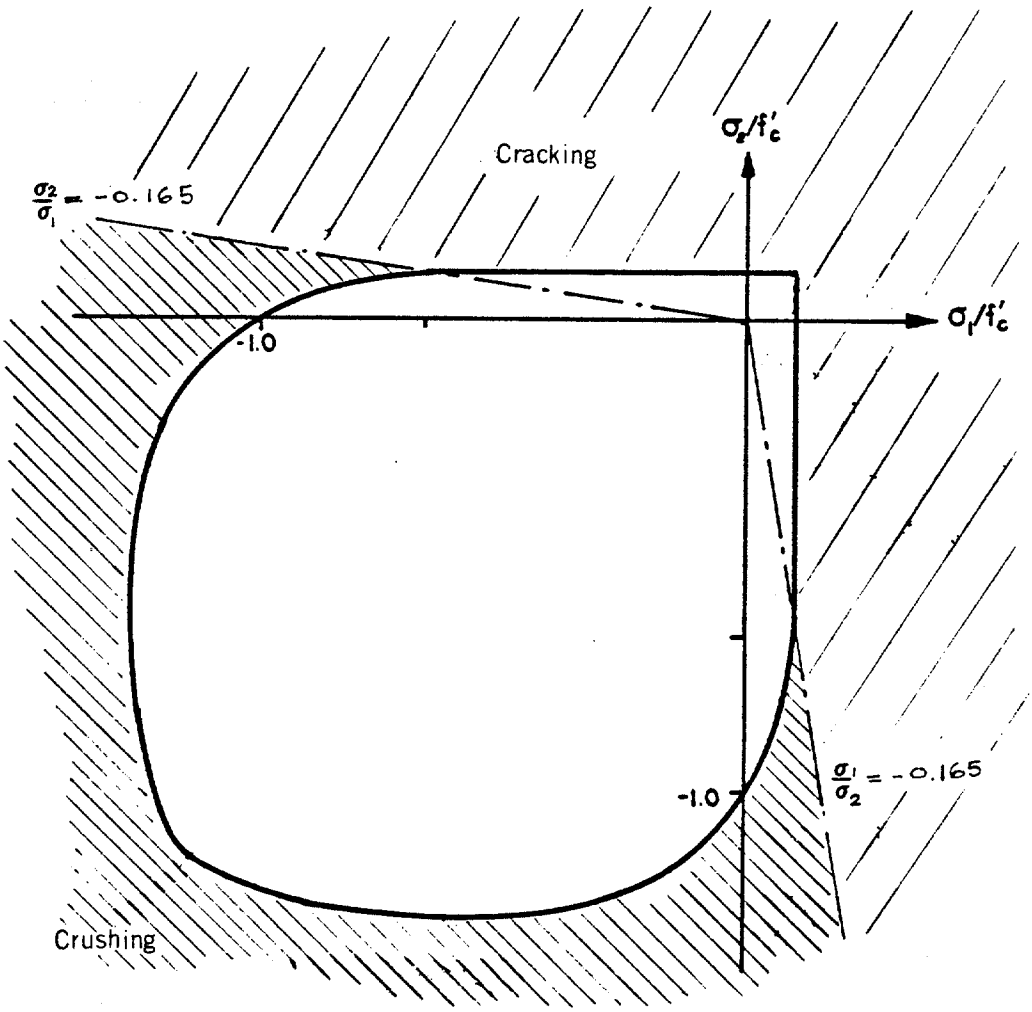

Figure III.22 Biaxial Strength Envelop
(after Kupfer and Gerstle)

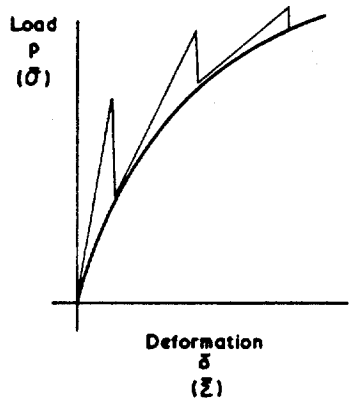

Figure III.23 "Modified Newton-Raphson" Iteration Scheme

Figure III.24 Program Flow Chart

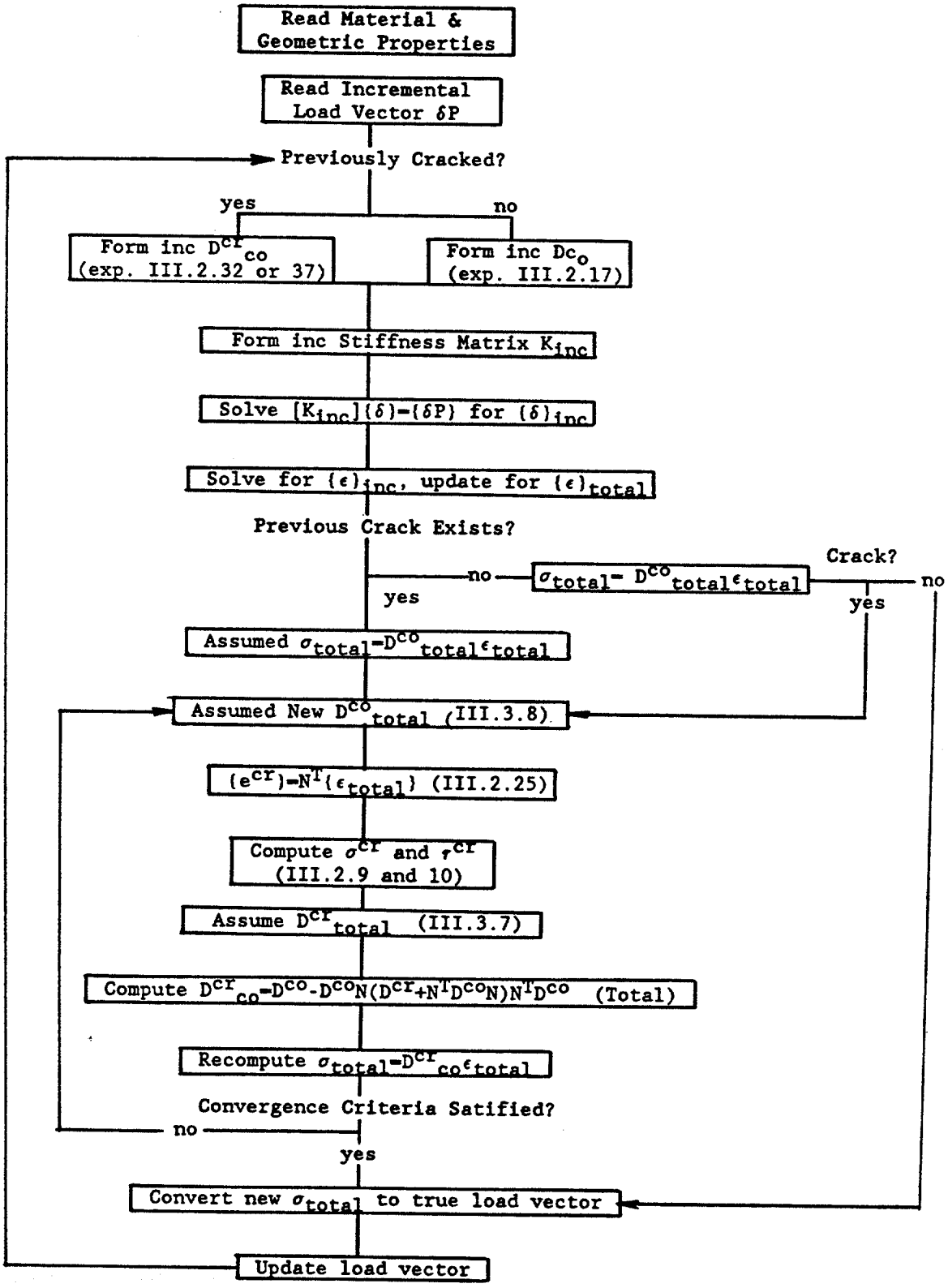

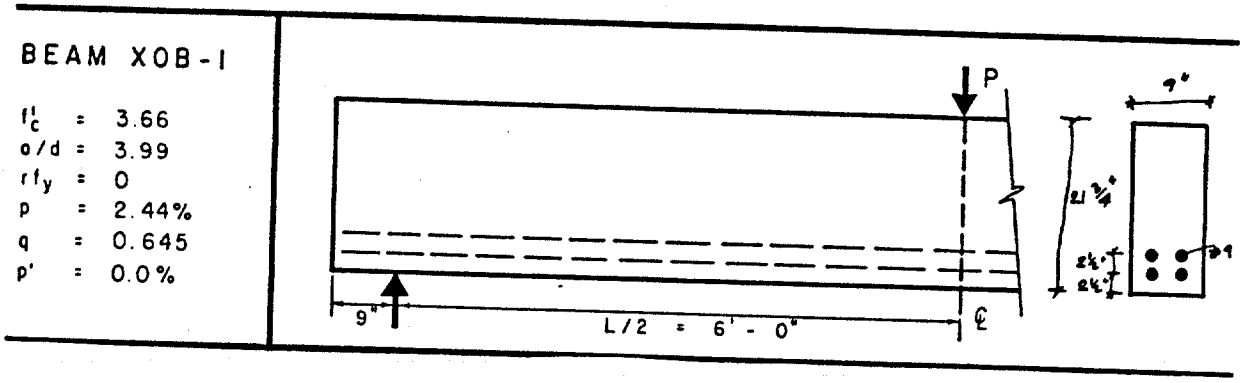

Figure III.25 Dimensions and Material Properties of Beam XOB-1

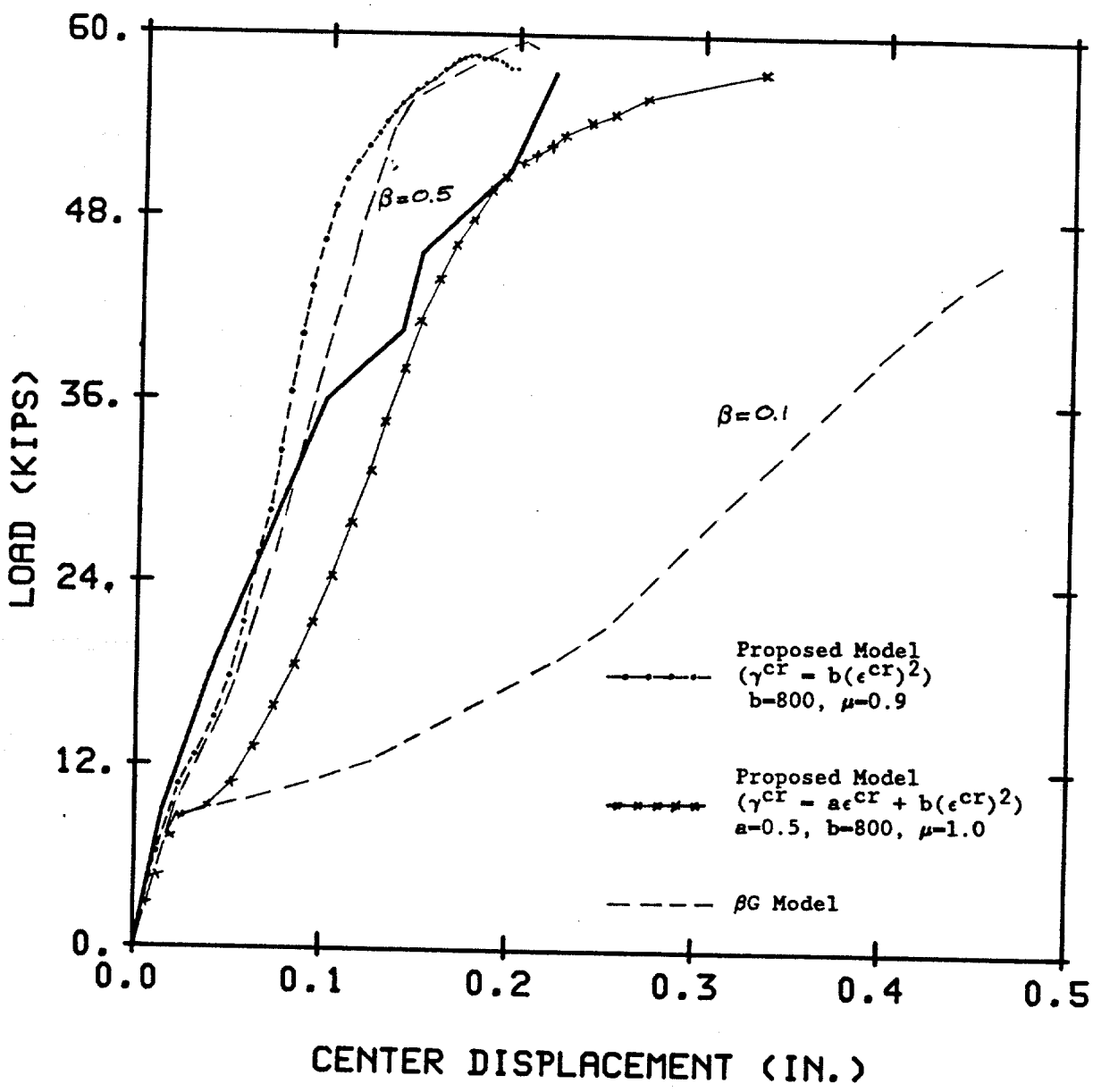

Figure III.26 Load-Center Deflection Curves of Beam XOB-1

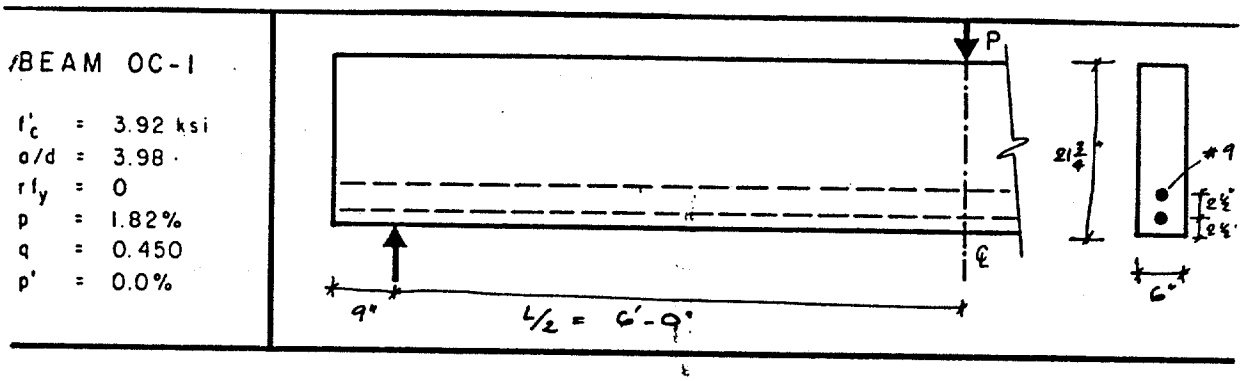

Figure III.27 Dimensions and Material Properties of Beam OC-1

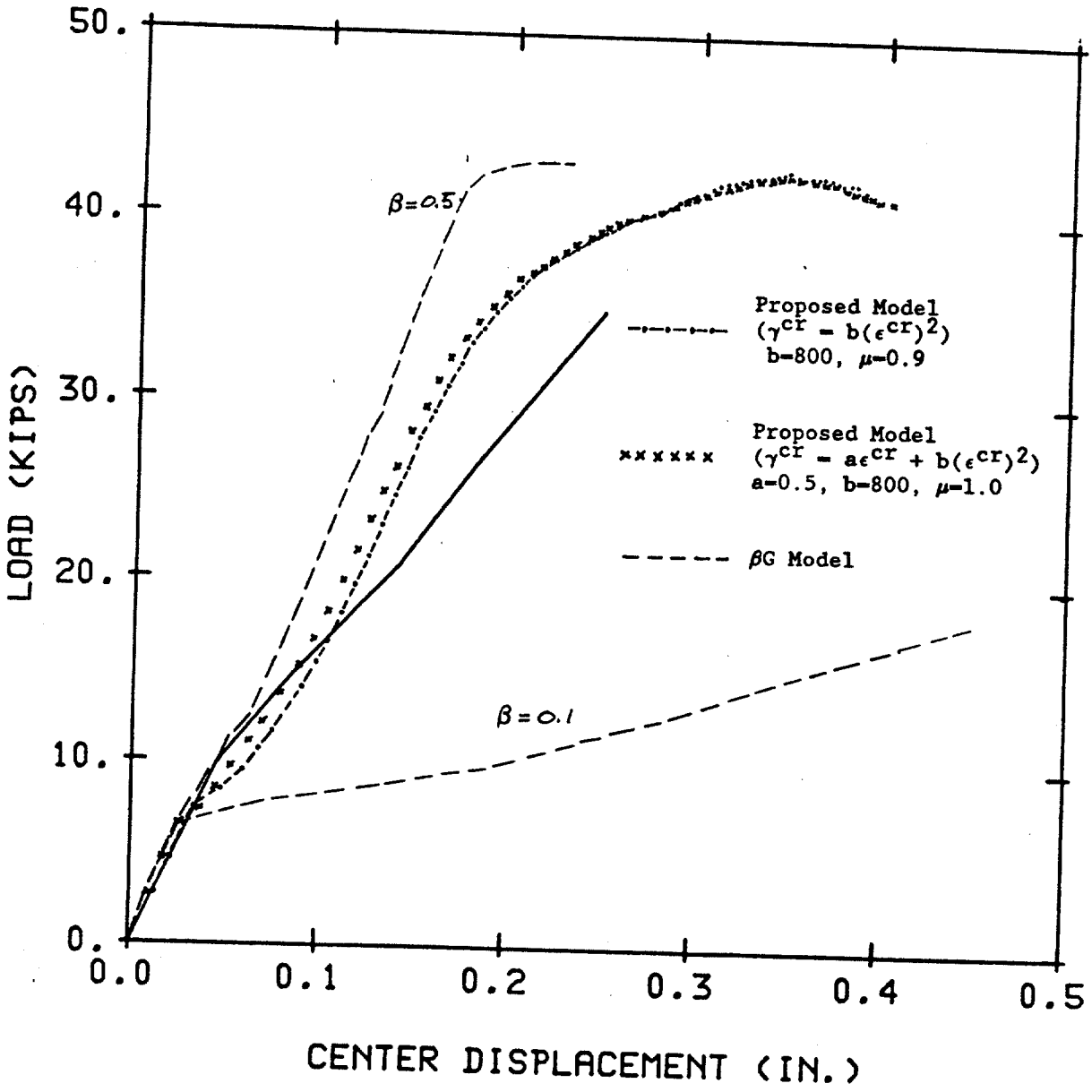

Figure III.28 Load-Center Deflection Curves of Beam OC-1

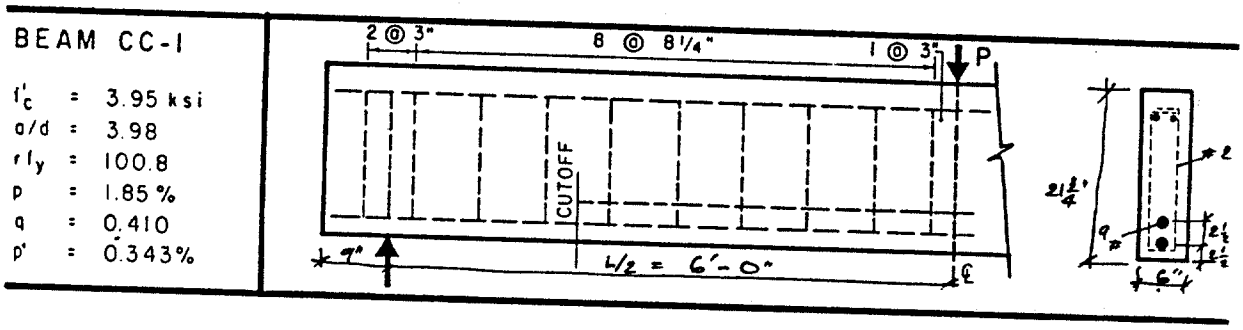

Figure III.29 Dimensions and Material Properties of Beam CC-1

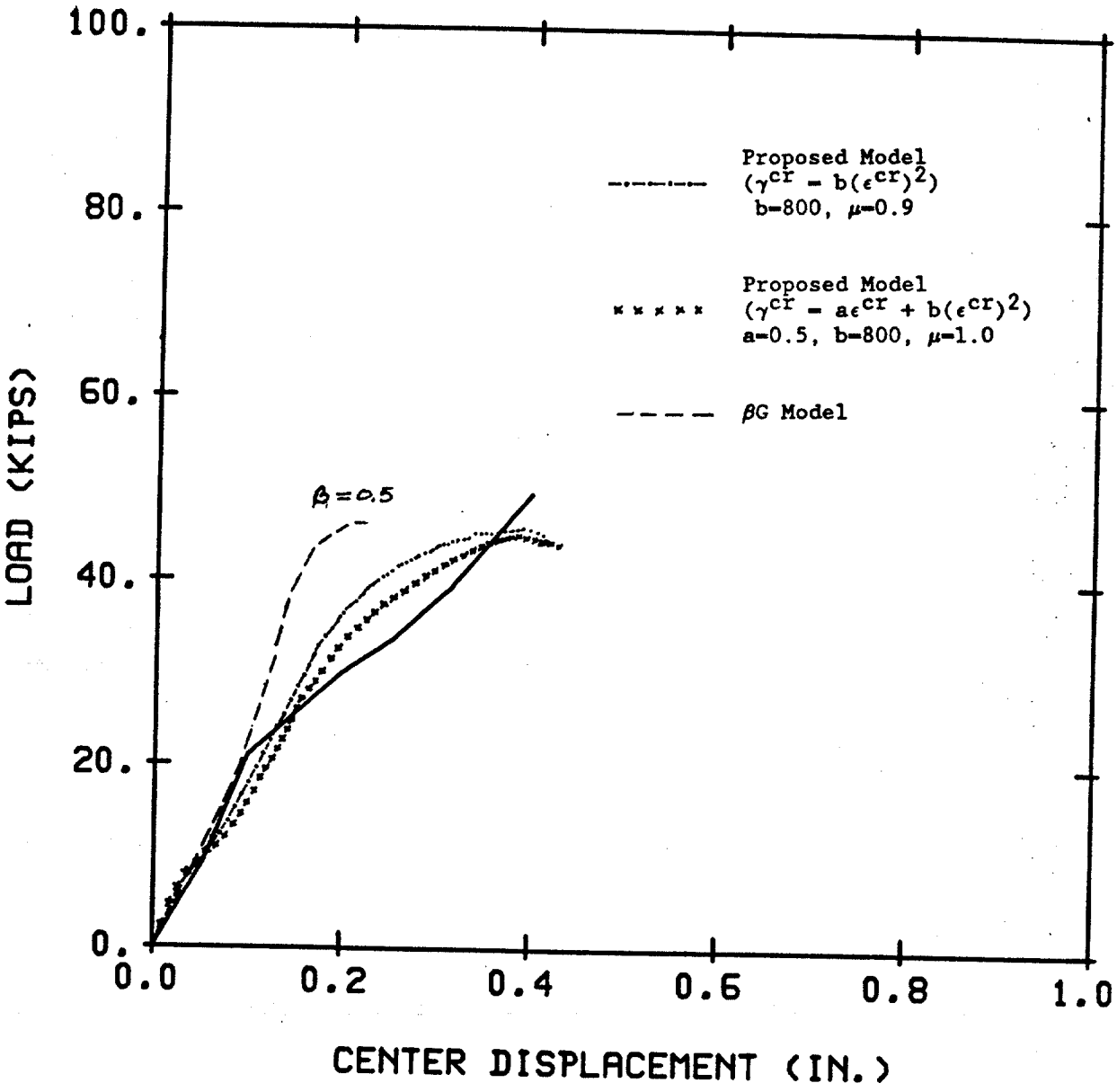

Figure III.30 Load-Center Deflection Curves of Beam CC-1

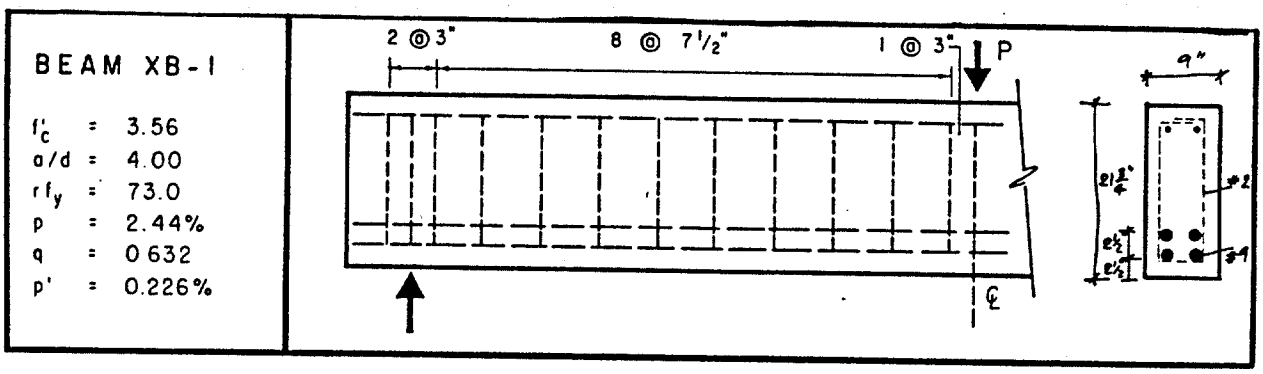

Figure III.31 Dimensions and Material Properties of Beam XB-1

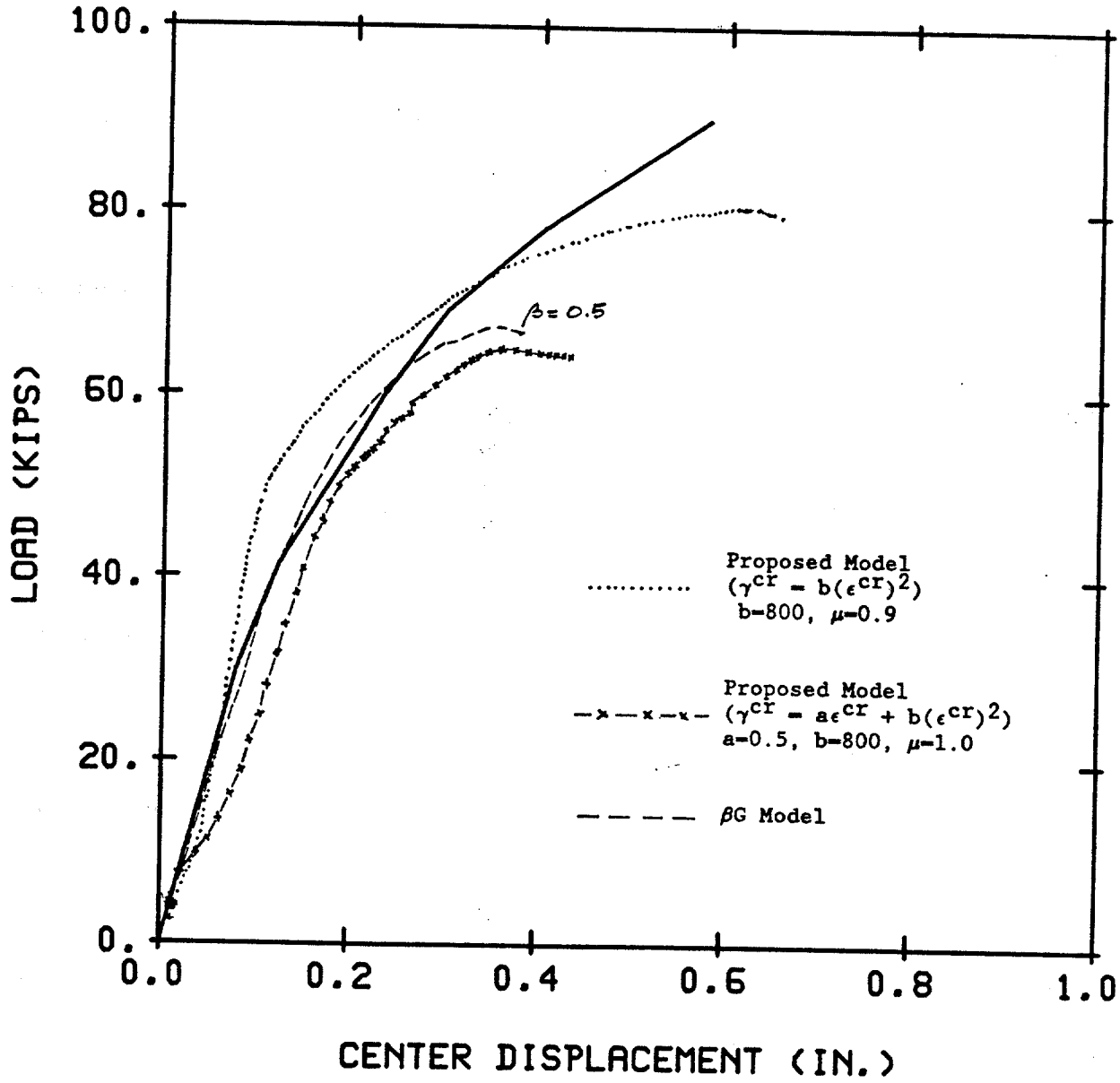

Figure III.32 Load-Center Deflection Curves of Beam XB-1

IV. BIBLIOGRAPHY

II.1.1 Mclean, D.I., Lew, H.S., Phan, L.T. and Sansalone, M., "Punching Shear Resistance of Lightweight Concrete Offshore Structures for the Arctic: Literature Review", NBSIR 86-3388, National Bureau of Standards.

II.1.2 Phan, L.T., Lew, H.S., Mclean, D.I., "Punching Shear Resistance of Lightweight Concrete Offshore Structures for the Arctic: Planning of Experimental Study", NBSIR 86-3440, National Bureau of Standards.

II.1.3 Sabnis, G.M., Harris, H.G., White, R.N. and Mirza, M.S., "Structural Modeling and Experimental Techniques", Prentice-Hall, 1983.

II.1.4 Harris, H.G., "Use of Structural Models as an Alternative to Full Scale Testing", Full-Scale Load Testing of Structures, ASTM STP 702, Shriever, W.R., Ed., American Society for Testing and Materials, 1980, pp. 25-44.

II.1.5 American Concrete Institute Committee 444, "Models of Concrete Structure", SP-24, ACI, Detroit, Mich., 1970.

II.1.6 Bhula, D.N., Birdy, J.N. and Bruen, F.J., "Design of Concrete Gravity Structures to Withstand Concentrated Ridge and Flow Impact Loads". Proceedings 1984 Offshore Technology Conference, OTC 4708, Houston, Texas.

II.1.7 "Experimental Work on Punching Shear Resistance of Concrete Structures for the Arctic", Brian Watt Associates, Inc. AOGA project no. 152.

III.1 Paulay, T. and Loeber, P.T., "Shear Transfer by Aggregate Interlock". Special Publication SP-42, American Concrete Institute, 1976, pp. 1-15.

III.2 Houde, J. and Mirza, M.S., "Investigation of Shear Transfer Across Cracks by Aggregate Interlock". Department of Civil Engineering, Structures Division, Ecole Polytechnique De Montreal, August 1972.

III.3 Laible, J.P., "An Experimental Investigation of Interface Shear Transfer and Applications in the Dynamic Analysis of Nuclear Containment Vessels". Ph.D. Thesis, Cornell University, August, 1973.

III.4 Jimenez-Perez, R., Gergely, P. and White, R.N., "Shear Transfer Across Cracks in Reinforced Concrete", Report 78-4, Department of Structural Engineering, Cornell University, August, 1978.

III.5 Reinhardt, H.W. and Walraven, J.C., "Cracks in Concrete Subject to Shear". Journal of the Structural Division, Proceeding of the American Society of Civil Engineers, ASCE, Vol. 108, No. ST1, January, 1982.

III.6 Ngo, D. and Scordelis, A.C., "Finite Element Analysis of Reinforced Concrete Beams", Journal of the American Concrete Institute, Vol. 64, No. 3, March, 1967, pp. 152-163.

III.7 Ngo, D., Scordelis, A.C. and Franklin, H.A., "Finite Element Study of Reinforced Concrete Beams With Diagonal Tension Cracks". UC-SESM Report No. 79-19, University of California at Berkeley, December,1970.

III.8 Nilson, A.H., "Nonlinear Analysis of Reinforced Concrete by the Finite Element Method". Journal of the American Concrete Institute, Vol. 65, No. 9, September, 1968, pp. 757-766.

III.9 Mufti, A.A., Mirza, M.S., McCutcheon, J.O. and Houde, J., "A Study of the Behavior of Reinforced Concrete Elements". Proceeding of the Specialty Conference of Finite Element Method in Civil Engineering, Montreal, Canada, June, 1972.

III.10 Al-Mahaidi, "Nonlinear Finite Element Analysis of Reinforced Concrete Deep Members". Research Report No. 79-1, Department of Structural Engineering, Cornell University, January, 1979.

III.11 Saouma, V.E. and Ingraffea, A.R., "Fracture Mechanics Analysis of Discrete Cracking". Proceedings, IABSE Colloquium on Advanced Mechanics of Reinforced Concrete, Delft, June, 1981.

III.12 Fenwick and Paulay, "Mechanisms of Shear Resistance of Concrete Beams". Journal of the Structural Division, ASCE, Vol. 94, No. ST10, Proc. pp. 2325, October, 1968, pp. 2325-2350.

III.13 Hand, F.R., Pecknold, D.A. and Schnobrich, W.C., "Nonlinear Layered Analysis of Reinforced Concrete Plates and Shells". Journal of the Structural Division, Vol. 99, No. ST7, July, 1973, pp.1491-1505.

III.14 Suidan, M. and Schnobrich, W.C., "Finite Element Analysis of Reinforced Concrete". Journal of the Structural Division, Vol. 99, No. ST10, October 1973, pp. 2109-2122.

III.15 Leombruni, P., Buyukozturk, O. and Connor, J.J., "Analysis of Shear Transfer in Reinforced Concrete With Application to Containment Wall Specimens". Report MIT-CER 79-26, Department of Civil Engineering, Massachusetts Institute of Technology, June, 1979.

III.16 De Borst, R. and Nauta, P., "Non Orthogonal Cracks in Smeared Finite Element Models". Engineering Computation, Vol. 2, March 1985.

III.17 Bazant, P. and Gambarova, P., "Rough Cracks in Reinforced Concrete". Journal of the Structural Division, Vol. 106, No. ST4, April, 1980, pp. 819-842.

III.18 Bazant, P. and Tsubaki, T., "Slip-Dilatancy Model for Cracked Reinforced Concrete". Journal of the Structural Division, Vol. 106, No. ST9, September, 1980, pp. 1947-1966.

III.19 Chen, A.C.T. and Chen, W.F., "Constitutive Relations for Concrete", Journal of the Engineering Mechanics Division, ASCE, Vol. 101, No. EM4, Proc. Paper 11529, Aug., 1975, pp. 465-481.

III.20 Kupfer, H. and Gerstle, K., "Behavior of Concrete Under Biaxial Stress", Journal of the Engineering Mechanics Division, ASCE, Vol. 99, No. EM4, Proc. Paper 9917, Aug. 1973, pp. 852-866.